High-Q AlN Contour Mode Resonators with Unattached, Voltage-Actuated Electrodes

Robert Schneider

Electrical Engineering and Computer Sciences
University of California at Berkeley

Technical Report No. UCB/EECS-2016-4
http://www.eecs.berkeley.edu/Pubs/TechRpts/2016/EECS-2016-4.html

January 6, 2016

High-Q AlN Contour Mode Resonators with Unattached, Voltage-Actuated Electrodes

by

Robert Anthony Schneider

A dissertation submitted in partial satisfaction of the

requirements for the degree of

Doctor of Philosophy

in

Engineering–Electrical Engineering and Computer Sciences

in the

Graduate Division

of the

University of California, Berkeley

Committee in charge:

Professor Clark T.-C. Nguyen, Chair
Professor Kristofer S. J. Pister
Professor Liwei Lin

Fall 2015

High-Q AlN Contour Mode Resonators with Unattached, Voltage-Actuated Electrodes

Abstract

High-Q AlN Contour Mode Resonators with Unattached, Voltage-Actuated Electrodes

by

Robert Anthony Schneider

Doctor of Philosophy in Engineering–Electrical Engineering and Computer Sciences

University of California, Berkeley

Professor Clark T.-C. Nguyen, Chair

High-Q narrowband filters at ultra-high frequencies hold promise for reducing noise and suppressing interferers in wireless transceivers, yet research efforts confront a daunting challenge. So far, no existing resonator technology can provide the simultaneous high-Q, high electromechanical coupling (k_{eff}^2), frequency tunability, low motional resistance (R_x), stop-band rejection, self-switchability, frequency accuracy, and power handling desired to select individual channels or small portions of a band over a wide RF range. Indeed, each technology provides only a subset of the desired properties.

Recently introduced "capacitive-piezoelectric" resonators, i.e., piezoelectric resonators with non-contacting transduction electrodes, known for achieving very good Q's, have recently emerged (in the early 2010's) as a contender among existing technologies to address the needs of RF narrowband selection. Several reports of such devices, made from aluminum nitride (AlN), have demonstrated improved Q's over attached electrode counterparts at frequencies up to 1.2 GHz, albeit with reduced transduction efficiency due to the added capacitive gaps. Fabrication challenges, while still allowing for a glimpse of the promise of this technology, have, until now, hindered attempts at more complex devices than just simple resonators with improved Q's.

This thesis project demonstrates several key improvements to capacitive-piezo technology, which, taken together, further bolster its case for deployment for frequency control applications. First, new fabrication techniques improve yields, reliability, and performance. Second, design modifications now allow k_{eff}^2's on par even with attached-electrode contour-mode devices, while most importantly, achieving unprecedented Q-factors for AlN. Third, a new electrode-collapse based resonance-quenching capability allows ON/OFF switching of resonators and filters, such as would be useful for a bank of parallel filters. Fourth, an integrated voltage-controlled gap-reduction-based frequency tuning mechanism permits wide frequency tuning of devices and thus much improved frequency accuracy. Gap actuation also allows for the decoupling of filters in the OFF state. And fifth, switchable and tunable capacitive-piezo narrow-band filters are demonstrated for the first time.

This thesis is divided into eight parts. In the first chapter, context is provided to demonstrate the purpose of this work. RF channel selection is introduced and a survey of currently available technology is presented. The second chapter explains key operating principles for MEMS resonators so a novice reader can be better equipped to fully understand the design choices made in later chapters. Chapter 3, on high-performance capacitive-piezo disk resonators, introduces the fundamental device of this thesis, providing examples of performance and design optimization, experimental results, simulation methods, and modeling. Chapter 4 introduces capacitive-piezoelectric disk arrays as a method to increase the area and thereby reduce the motional resistance of the unit disk resonator. Chapter 5 discusses voltage controlled gap actuation of the capacitive piezoelectric transducer's top electrode, which enables voltage controlled frequency tuning and on/off switching. Chapter 6 takes a thorough look at the fabrication technology needed to make capacitive-piezo devices, including lessons learned on how to avoid certain pitfalls. Chapter 7, on filters, contains both theory and measurement results of filters. Chapter 8 concludes the thesis by summarizing the key achievements of Chapters 3 through 7, highlighting key areas needing further development, and discussing implications of this technology for the future.

For my family.

Contents

List of Figures

List of Tables

Acknowledgments

First and foremost, I am deeply grateful for my PhD advisor, Prof. Clark Nguyen, who has sparked my healthy obsession with the burgeoning field of micro-electro-mechanical systems. Without his generous financial support, our many spirited discussions, and his thoughtful feedback, I would not have been able to meet my research goals. His wisdom and passion for the field are unmatched. I am thankful to have had the opportunity to attend UC Berkeley under his guidance.

I appreciate my qualifying exam and dissertation committee members, Professors Nguyen, Kris Pister, Liwei Lin, and Tsu-Jae King-Liu, for their time and assistance in guiding my research project and reviewing this dissertation. I also acknowledge the funding support of the United States Defense Advanced Research Projects Agency (DARPA) through the Chip Scale Spectrum Analyzer (CSSA) and Optical Radiation Cooling and Heating in Integrated Devices (ORCHID) programs of the Microsystems Technology Office.

As a member of the Berkeley Sensor & Actuator Center (BSAC), I am all the more enlightened to have attended six years worth of BSAC lunch seminars and BSAC industrial advisory board research review meetings. I appreciate the BSAC staff, the faculty co-directors, and BSAC's industrial sponsors who continue to make much of our research possible and relevant.

Within the Nguyen research group, I acknowledge the leadership and contributions of post-doctoral researchers Bongsang Kim, Tommi Riekkinen, and Tristan Rocheleau. Current and former graduate students, Henry Barrow, Li-Wen Hung, Mehmet Akgul, Yang Lin, Wei-Chang Li, Thura Lin Nang, Brian Pepin, Lingqi Wu, Turker Beyazoglu, Ilya Gurin, Jalal Naghsh Nilchi, Ruonan Liu, Alper Ozgurluk, and Divya Kashyap, have always kindly offered their friendship, cooperation, and expertise. I also appreciate Zeying Ren for her assistance as a fab engineer in the Nanolab.

I enjoyed serving as a member of the Berkeley Electrical Engineering Graduate Student Association (EEGSA) and am thankful to have worked with other students to help make our department a more open, functional, happy, and healthy community. Our social hours, bar nights, barbecues, and many other events truly brought people together. Thank you to Kevin for serving as co-president with me from 2011 to 2012, and also to Neel, Matt, Zach, Josh, Gireeja, Claire, Aaron, multiple Dans, Joey, Katie, Ankur, Samarth, James, Stephen, Rikky, Austin, and others.

Working in the Marvell Nanofabrication Laboratory has been an enjoyable source of hands-on learning. I appreciate the staff members for their support for the many complicated pieces of equipment in the lab. Thank you to Dr. Jeffrey Clarkson, Ryan Rivers, Richeleau Hemphill, Joe Donnelly, Jay Morford, Greg Mullins, Kim Chan, Marilyn Kushner, and Dr. Evan Stateler, for answering my questions and helping me achieve my goals.

Before coming to Berkeley, I was fortunate to have had many caring teachers who taught me to think in new ways: Charlotte Akin, Roger Fisher, Norm Friehauf, Ernie Santner, Bill Delaney, Jason Schultz, Steve Getsinger, Tammi Howe, Patti McMaster, Larry Asher, Prof. Stuart Reges, Prof. Steve Sefcik, Prof. Brian Otis, Prof. Lih Lin, Prof. Babak Parviz,

and especially Prof. Evan Goldstein. Outside of an academic environment, I wouldn't be where I am today without the inspiration and guidance from Er-Juan Feng, Yam Poon, Jay Shin, Joseph Mitchell, Mark Dollevoet, Yu-Chin Jou, Thi Nguyen, Peter Kersten, Jared Millington, Alan and Lori Campbell, Paul Limpf, and Air Force Capt. Chris Stover.

Above all, I thank my beloved friends and family. To my mom, my dad, my step dad, and grandma, thank you for nurturing my desires to learn, grow, and enjoy all life has to offer. To my Bay Area friends, thank you for the laughs, mischief, and adventures. Most especially, Katie, my beautiful wife, thank you for bringing me immeasurable fulfillment and happiness. Thank you also for your patience during my extended stint in graduate school. Finally, to our newborn twin daughters, Madeline and Eleanor, thank you for your precious smiles. You are the best motivation to complete a dissertation that anyone could ask for.

-R. S. (11/18/15)

Chapter 1

Introduction

To motivate developing new microelectromechanical system (MEMS) resonator components for radios, this chapter introduces key concepts related to radios and MEMS filters. Section 1.1 highlights applications of radio communication, explains fundamental operating principles for radios, and reviews operating requirements necessary for a reliable radio link. We also examine a typical receiver to determine which (typically off-chip) components are potentially replaceable by on-chip MEMS components. Section 1.2 examines the feasibility and benefits of integrating high-Q resonant elements on-chip to reduce off-chip part counts and improve performance. For example, narrowband filtering at RF offers benefits of suppressing interferers, relaxing linearity requirements, and reducing power consumption in a receiver. Section 1.3 provides a survey of existing radio front end filter technologies to examine the suitability of each for achieving high selectivity, preferably on chip, with an emphasis on MEMS devices. We aim to highlight that new MEMS resonator technologies, offering both integration and higher Q's, will enable improvements in single-chip multi-mode UHF receivers that consume very little power and occupy a tiny form factor.

1.1 Radios for Wireless Communication

Radio-based communication allows untethered connectivity and information transfer in a manner not possible using wired systems, thus enabling applications such as wireless local area networks (Wi-Fi), cell phone networks, wireless sensor networks, wireless health monitoring, radio-frequency identification (RFID), air- and space-craft communication, cordless computer interface devices, keyless entry, wireless personal area networks (Bluetooth), AM/FM/TV broadcasting, and the global positioning system (GPS). Indeed, society has come rapidly to rely on a large variety of radio devices. What's more, looking forward, new frontiers in wireless research continue to seek out entirely new applications for radio. Integrating the high-Q passives that a receiver uses onto a single chip is one path forward towards enabling the transformative reductions in size, power consumption, and cost that are desired for next-generation radios.

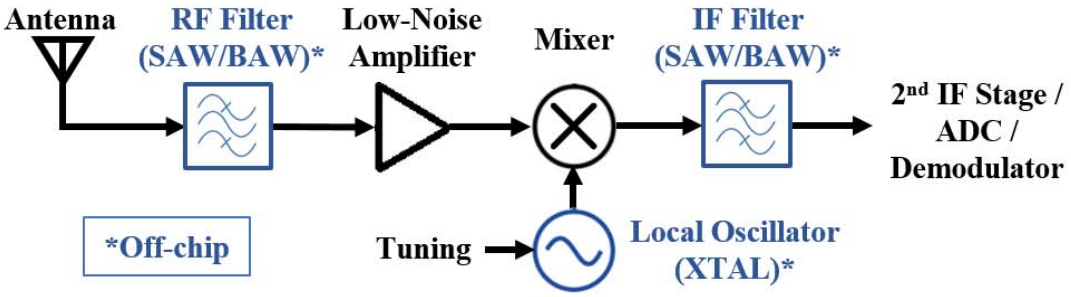

Figure 1.1: Block diagram of a common heterodyne architecture for a radio receiver. The frequency control elements shown in blue commonly use high-Q off-chip components.

Operating Principles

Radios operate through sending and receiving wireless signals between a transmitter and one or more receivers. Such signals are carried by electromagnetic waves. Electromagnetic waves can move at a speed of up to 300 million m/s, thus they are capable of spreading information nearly instantaneously over non-astronomical length scales. Radio communication signals commonly span frequencies ranging from under 1 MHz up to several 10's of GHz. Here, optimal frequency of operation depends on the application, but higher frequencies are often preferred to allow for high data rates (bandwidths) and small size.

To transmit data wirelessly, one can encode an information signal onto a single tone carrier wave and then transmit the modulated signal by driving a proportional current on an antenna, thus creating electromagnetic waves. Some basic modulation schemes include modulating a carrier's amplitude (AM), modulating its frequency or phase (FM/PM), or keying it on and off (OOK). More elaborate modulation schemes, such as gaussian minimum shift keying (GMSK) or n-point quadrature amplitude modulation (n-QAM), are often used to maximize the bandwidth efficiency of digital signals. Regardless of the modulation method used, fundamentally, the amount of data one can send, in bits/second, is limited by the bandwidth of the communication channel and its signal to noise ratio [1].

A receiver's job, of course, is to detect the transmitted signal at a remote location and demodulate it. Although several other receiver architectures exist, the heterodyne architecture, which employs frequency mixing to an intermediate frequency, is by far the most widespread in modern radios due to its strong selectivity.

Heterodyne Receiver Architecture

Figure 1.1 presents a block diagram of a common heterodyne architecture for a radio receiver. Here, energy received from an antenna is passed through an RF filter centered around the carrier frequency to eliminate out-of-band interferers. The signal is then strengthened using an amplifier that ideally adds little to no noise. A mixer, which can here be considered a simple analog multiplier, multiplies the received signal with a local oscillator (LO) tone at

the carrier frequency to produce a copy of the received signal at a lower, intermediate frequency (IF). Here, the translated signal is then filtered using a smaller bandwidth than that of the RF filter, thus suppressing in-band interferers. From this point, an optional second IF stage may be used for more frequency downconversion. Eventually, the signal is passed to either an analog to digital converter (ADC) or a demodulator to extract the modulating signal from the carrier.

Notably, the components of fig. 1.1 drawn in blue are commonly implemented using *off-chip* components, typically surface acoustic wave (SAW) or bulk acoustic wave (BAW) filters, and quartz crystal resonators (XTAL) are used. These devices can meet performance specifications that typically cannot be met using the passive components available in a standard CMOS process. For the filters, the ability to strongly discriminate nearby signals demands very high Q's. For the oscillator, the synthesized frequency must be set by an accuracy within several parts per million, even as temperature varies. This oscillator must also exhibit low phase noise, and thus also have high Q. Quartz crystals readily meet these demands [2]. Despite the good performance of these devices, to reduce size and costs, it is desirable to migrate these functions on chip using MEMS devices, if possible. In section 1.2, we will take a closer look at how this might be feasible.

Although several receiver architectures are possible, in practice, almost all receivers are made using the same heterodyning architecture of fig. 1.1, the defining feature of which is using an intermediate frequency (IF) filter for channel selection [3]. One alternative is a direct conversion architecture which mixes directly to baseband and thus requires RF channel selection, which is filtering a very narrow channel that is centered at high frequencies. This is desirable in principle, as we will show, but can require prohibitively high Q's, e.g., ranging between values of 10^4 and 10^7, depending on a channel's fractional bandwidth. On the other hand, filtering at IF, instead of at RF, solves this problem, as doing so allows one to use more than one filter with each having easily realizable Q's, e.g., 10^2 to 10^4. For the IF filter, required Q is proportional to the chosen IF frequency and inversely proportional to the channel bandwidth. Regardless of whether a heterodyning or a direct conversion architecture is used, high Q is universally desired in filters. Higher Q always enables improved noise figure as is shown mathematically in section 1.2. Because Q is so important, radio architectures are essentially determined by available filter technology [4].

Requirements For a Radio Link

To allow an operational radio link, a number of necessary but not sufficient conditions must be met related to signal power strength, noise levels, avoiding or suppressing interferers, and available bandwidth. These requirements are highlighted below.

Operate on an Unoccupied Channel

For wireless communication to take place, a desired channel must not be occupied by another user (interferer). To illustrate the environment in which a receiver operates, fig. 1.2

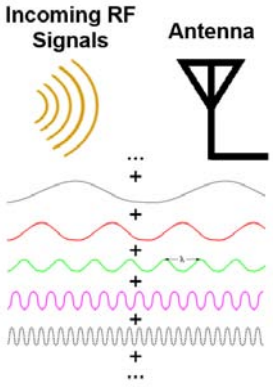

(a) A spectrum of electromagnetic waves received by an antenna.

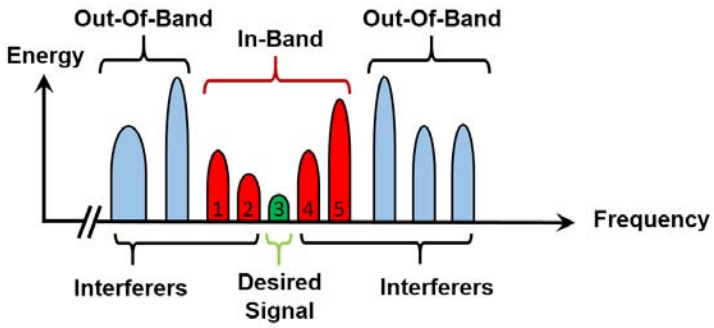

(b) In the frequency domain, a channel of interest (green) is surrounded by unwanted interferers, both in-band (red) and out-of-band (blue).

Figure 1.2: Illustration of a typical RF environment in which an antenna is presented with many incoming signals at different frequencies, of which only one is of interest.

presents a typical RF environment in which a receiver's antenna is presented with many incoming signals, each having a different carrier frequency. Figure 1.2b presents a frequency domain plot illustrating a spectrum of received signals having different power spectral densities, in which a desired open channel (Ch. 3) now has become occupied by a signal of interest shown in green. Immediately surrounding the signal of interest are in-band interferers shown in red (Chs. 1, 2, 4, and 5), while out-of-band interferers are shown in blue. The function of a radio receiver operating in such an environment is to select the desired signal from among all others, even if it is relatively weak, as is shown, and mix it down to baseband and demodulate it to extract its content. In this example, if Ch. 3 were occupied by an interferer, no channels would be available for communication.

Especially in densely populated locations, available bandwidth among users can become scarce. It may become impossible to provide service for all users. To facilitate efficient sharing of the wireless spectrum, organizations such as the Federal Communications Commission mandate that radio transcievers operate within purpose-specific frequency bands. Within a band, users share bandwidth through communicating on individual channels, of which about 5 to 100 might typically exist within a band. For example, LPD433 (low power device 433 MHz), ranging from 433.075 MHz to 434.775 MHz, is a radio band dedicated to industrial/scientific/medical (ISM) purposes. LPD433 is subdivided into 69 channels, of 25 kHz bandwidth each, among which many users can operate. Such channel sizes at this frequency represent a narrow 0.006% fractional bandwidth (FBW). Larger channel sizes exist in other bands, e.g., Bluetooth 4.0 at 2.4 GHz uses 2 MHz channels with fractional bandwiths of about 0.08%. Within a band, channel hopping and/or time divided access are often used to accommodate more users. Channel selection in a heterodyne receiver occurs through tuning the LO frequency so that $f_{RF} - f_{LO} = f_{IF}$.

Meet Signal to Noise Demands

For any radio link, the power of a transmitted signal must be large enough so that the incident signal power that reaches an intended receiver's antenna is greater than that of its minimum detectable signal (MDS). Signal to noise requirements set the maximum distance over which one can transmit information for a given transmitted signal power. The link strength is further dependent on wavelength (λ), antenna efficiency, and environmental factors. Fundamentally, incident power density on an antenna depends inversely on the square of the distance from the source in the radiative far field region, i.e., beyond several wavelengths. Absorption of RF power by air can further limit link distance, particularly at very high frequencies, e.g., 60 GHz. Obstacles between transmitter and receiver, e.g., buildings, also hinder signal transmission through absorption, reflection, and multi-path effects. Minimum detectable signal further depends on antenna design in the receiver. For example, a guideline for efficient antenna design is that the size of an antenna should ideally be close to the wavelength of operation, e.g., a quarter-wave monopole is a common antenna design for mobile communications systems [5]. Directionality of an antenna's radiation pattern also affects a wireless link's strength. Conjugate impedance matching is needed for maximum power transfer.

The minimum amount of signal power a receiver can detect depends on the noise performance and capability of the radio receiver itself. In particular, if the noise figure of a receiver's front end RF filter can be reduced, its MDS requirement becomes more relaxed, thus enabling detection of weaker signals. Noise performance of subsequent components in the receive signal path such as the low noise amplifier (LNA) and mixer must be optimized as well, but the noise performance of these components is not more critical than that of the front end filter due to the manner in which noise figure is calculated.

Suppress and Manage Interferers

In a typical RF environment, a signal of interest is present among undesirable nearby signals (interferers) due to other users of the spectrum. A receiver remains able to extract a desired carrier's data as long as the interferers are not too powerful. In an example of blocker analysis to quantify permitted signal strengths in interferers, a design specification for an integrated GSM receiver by J. Rudell et al. provides limits for tolerable interference levels in a receiver at various frequency offsets from the carrier [6]. Above certain tolerable levels, disruptive interference occurs that prevents a signal from being detected. The maximum permissible interferer tone powers are smallest for frequencies closest to the carrier. Beyond the most obvious interference situation of an interferer sharing a desired carrier's frequency, two indirect interference mechanisms are of concern. First, amplifier gain compression can occur due to a strong undesired signal that drives a receiver's amplifier into its non linear region, thus decreasing SNR for the signal of interest. A second type of potentially disruptive interference is intermodulation distortion, which is the generation of additional signals at new frequencies due to amplitude modulation of two or more strong interferers, which can occur

through a nonlinear amplifier. The most sinister form of intermodulation distortion is that which occurs from the third order nonlinear component. To illustrate, consider two large interferers at $f_c + \Delta f$ and $f_c + 2\Delta f$. These two signals can combine through a third order nonlinearity to generate many sum and difference products, e.g., $2\omega_1 - \omega_2$, thus including a signal at f_c, potentially disrupting communication. For example, in fig. 1.2b, if the signals occupying channels 4 and 5 were very large, a significant intermodulation product could arise in channel 3, thus increasing the bit error rate. In view of these considerations, it is highly desirable to suppress nonlinearities and interferers in a receiver through maximizing the third order intercept point of the RF filter and LNA. Reducing the bandwidth of the RF filter that precedes the low noise amplifier in the signal path of a receiver's front end is one way to suppress such interferers. Such bandwidth reduction requires high Q.

Avoid Jammers

Deliberately and maliciously using a powerful radio signal to disrupt radio communications is called jamming. In the U.S., use of RF jammers to disrupt authorized RF communication is illegal [7]. Such jammers can disrupt critical communications such as emergency calls to first responders. Nonetheless, some totalitarian governments jam radio broadcasts to censor opposition and free expression. When a very strong jammer is present, little can be done to retain a radio link except change operating frequency.

1.2 On-chip High-Q Filters and Oscillators for Radio

While any radio must meet each of the aforementioned basic operating requirements, a designer also desires decreased cost, power consumption, and size. Integrating various radio components onto a single chip is one way to attain such improvements. As was touched upon in fig. 1.1 and section 1.1, radios typically require a number of off-chip components due to a lack of an adequately performing on-chip counterparts. These items include (a) an accurate frequency reference, e.g. a quartz crystal, for the local oscillator, and (b) RF and IF filters, e.g., surface or bulk acoustic wave (SAW/BAW) filters. On-chip CMOS-based LC resonators generally exhibit inadequate Q's, e.g. less than 100, and poor frequency accuracy, e.g., worse than 1%. However, high Q MEMS components, possibly having many different frequencies on a single chip, that can be co-fabricated over CMOS, or otherwise attached through wafer level bonding, alternatively offer compelling performance and cost advantages. Multi-frequency switchable and tunable MEMS resonators open the door for integrated band- and channel-hopping to avoid jammers and interferers in a spectrum-constrained environment, with both the small sizes and high Q's desired for low power operation.

MEMS as a Quartz Alternative for Local Oscillators

Single chip wireless motes are of great interest particularly for wireless sensor networks, for which ubiquitous deployment requires a very low mote unit cost. Reducing PCB size and

the number of off-chip parts is thus essential. Unfortunately, quartz (crystalline SiO_2) cannot be deposited in thin-film form on a wafer– if it is to be eliminated from the mote, alternative measures must be taken to ensure operation. As an example of one effort to explore quartz-crystal-oscillator-free communication using the IEEE 802.15.4 protocol for wireless sensor networks, the work of [8] developed a frequency error detection and correction algorithm to synchronize a receiver to a transmitter with greatly relaxed frequency error requirements, of ± 1000 ppm, representing a $25\times$ increase, between a transmitter and a receiver. The relaxed requirement comes with added performance penalties related to packet error rates and sensitivity. The work proposes using an LC resonator as a reference, but an on-chip, high-Q MEMS resonator would offer better reliability if the marginal cost increase were tolerable. As an added bonus, if an integrated CMOS/MEMS process were used, MEMS based RF and IF filters would also be available for little to no added cost.

Commercially available MEMS oscillators already (as of 2015) achieve absolute frequency accuracies better than ± 10 ppm at 220 MHz or higher over a wide temperature range, e.g., [9] from SiTime. Such performance is attained through the aid of advanced temperature sensing and a phase locked loop (PLL) based synthesizer [10]. To change channels, one can tune the local's oscillator's frequency (LO=RF-IF) within the band of interest. For ultra-low-power operation, a designer may decide to eliminate the PLL to reduce power consumption by several milliwatts, in which case direct synthesis at close to RF is needed. Frequency accuracy would drop for a PLL-less system.

Phase noise performance of MEMS oscillators has been shown to be very good. In fact, when normalized by power consumption, MEMS based oscillators offer the best phase noise figure of merit for oscillators. For example, the work of [11] uses a capacitive-gap transduced wineglass resonator to meet Global System for Mobile Communications (GSM) phase noise specs with a power consumption of only 78μW.

In 1993, Nguyen and Howe proved that monolithic MEMS over CMOS integration was possible through demonstrating a micro mechanical comb drive resonator built directly over a sustaining amplifier, using a fabrication process that combined a planar CMOS process with surface micromachining [12]. Integrated system design approaches that combine relaxing accuracy requirements for proper operation with efforts to bring high Q passives on chip through using low cost MEMS should enable high-Q integrated local oscillators for radio.

The Importance of Resonator Q in Local Oscillators

An ideal spectrum for an oscillator would contain energy at only one frequency, resembling a dirac delta function. Real oscillators exhibit phase noise. They have nonzero noise power at small offsets from f_0 in the frequency domain. A simple model for the phase noise of an oscillator was first described by David Leeson in 1966 [13]. Based on this work, a semi-empirical model for phase noise, $\mathcal{L}(\Delta\omega)$, summarized by Hajimiri and Lee [14] is given by:

$$\mathcal{L}(\Delta\omega) = 10\log_{10}\left\{\frac{2Fk_BT}{P_s}\left[1+\left(\frac{\omega_0}{2Q_L\Delta\omega}\right)^2\right]\left(1+\frac{\Delta\omega_{1/f^3}}{|\Delta\omega|}\right)\right\} \tag{1.1}$$

Where F is an empirical parameter, k_B is Boltzmann's constant, T is temperature in Kelvin, P_s is the average power dissipated in the resistive part of the tank, ω_0 is the oscillation frequency, and Q_L is the effective quality factor of the tank with all the loadings in place, $\Delta\omega$ is the offset from the carrier, and $\Delta\omega_{1/f^3}$ is the frequency of the corner between the $1/f^3$ and $1/f^2$ regions.

Thus, phase noise is inversely proportional to Q_L^2. Clearly, in addition to increasing signal power of the oscillator, one should maximize resonator Q as much as possible. Another reason to maximize Q is to minimize the required amplifier gain to sustain oscillation and thus reduce power consumption.

On-Chip High Q MEMS Filters

Just like with oscillators, replacing the off-chip high-Q RF and IF filters of a radio receiver with on-chip counterparts would reduce cost and size for radios. Additionally, maximizing the Q's of such filters would enable either one or both of the following: (a) narrower fractional bandwidths for improved interferer rejection, or, (b) lower insertion losses for better sensitivity.

High-Q Narrowband Filters for Improved Rejection of Interferers

In section 1.1, we explained why attenuating strong interferers relaxes linearity requirements on subsequent radio stages, such as the low noise amplifier (LNA) at the output of the RF filter. Tolerating interferers is a requirement for proper operation. In this section, we will examine the tradeoffs inherent to deciding on the best bandwidth of an RF filter to use and show why high resonator Q enables small bandwidths.

Figure 1.3 depicts how reducing the fractional bandwidth of an RF filter affects the strength and presence of interferers. In fig. 1.3a, a band select filter, here shown as having a 1.0% fractional bandwidth (FBW), is depicted as rejecting out-of-band interferers in the same RF environment as is shown in fig. 1.2. The filter shown passes all channels over which the transceiver operates, even though only one channel is desired at any one time. If strong enough, a nearby transmitter on an adjacent channel might disrupt communications through down-mixed local oscillator phase noise or the interference mechanisms previously mentioned. The majority of heterodyne receivers operate in this manner. On the other hand, RF channel selection with a narrower filter, as is shown in fig. 1.3b seems more ideal. Here, the depicted channel-select filter is shown to have a 0.2% fractional bandwidth, though true RF channel selection might require much tighter filtering, e.g., 0.001%. Here, we assume that insertion loss in the filter is the same as that shown in fig. 1.3a. Clearly, all in-band interferers are suppressed and the LNA is presented with a spectrum which varies over a much smaller dynamic range, as is desired.

If the post-RF-filter spectrum of fig. 1.3b is most desirable, one might ask, "Why don't heterodyne receivers use RF channel selection?" Indeed, for optimal performance, an RF filter would ideally be very narrow, selecting only the signal of interest and rejecting all

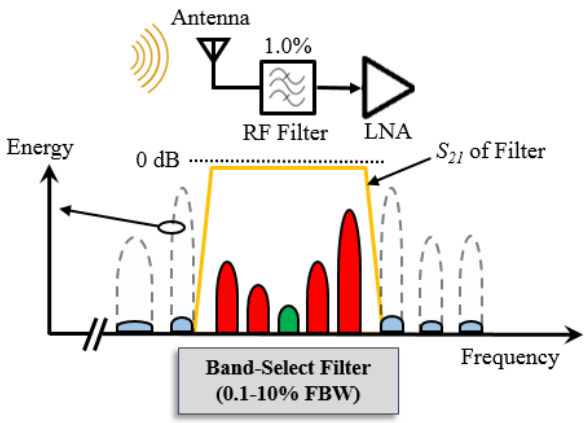

(a) A band-selecting RF filter attenuates out-of-band interferers while permitting in-band interferers.

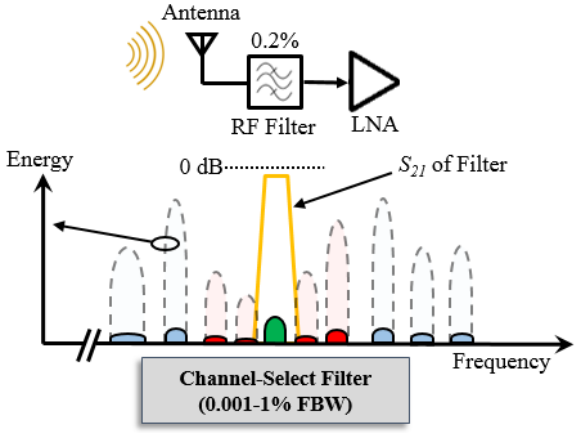

(b) A channel-selecting RF filter attenuates in-band interferers, but requires proportionately higher Q.

Figure 1.3: A comparison between RF band selection and RF channel selection as presented to the input of a receiver's LNA.

others. Yet, very tight RF filtering is not always feasible as it can require prohibitively high Q's. For many designers, band selection at RF with channel selection at IF using LO tuning is the most suitable receiver architecture considering present-day hardware constraints. In addition to the Q requirement, with RF channel selection, one also would in almost all likelihood need a way to change the filter's frequency to channel hop to other frequencies outside of the very narrow filter's passband. This is usually, but not always, necessary. As a counterexample, some very low bandwidth applications do use just a single channel over their lifetime. For example, some one-way pagers utilize a single SAW narrowband filter in their receiver.

RF Channel Selection Requires Switchability and/or Tunability

If one seeks to channel hop within a frequency band using an RF channel selecting front end, one requires either a tunable narrowband RF filter or, alternatively, a bank of switchable narrowband RF filters at different frequencies. The first of these alternatives would need only one filter, which is desirable, but would require a frequency tuning method capable of tuning over the entire band. The switchable filter bank is perhaps a more realistic approach, but of course requires numerous individual switched filters. Through batch fabrication, some filter technologies are amenable to this approach, allowing for multiple microscale devices on the same substrate, while others are not.

High-Q Resonators for Low Insertion Loss

Insertion loss (IL), defined as the reduction in transmitted signal level due to the insertion of a device in a signal path, is an important figure of merit for filters, as one can show that any insertion loss in the passband of a front end filter directly degrades overall noise figure, and hence sensitivity, by the same amount. Thus, to preserve signal to noise ratio, insertion loss must be minimized, e.g., to 3 dB or less, for an RF filter. Insertion loss, in terms of the 2-port scattering parameters transmission factor S_{21}, is defined as follows:

$$IL\ (\text{dB}) = -20\log_{10}(S_{21}) \tag{1.2}$$

For the purpose of intuitive illustration, if one assumes that a filter, in its passband, is represented by a single series resistance, R_{filter}, linking the non grounded terminals of the input and output ports having termination resistances of R_{T1} and R_{T2}, rather than its more complex, and more correct, full two-port network representation, S_{21} in the passband will simply be given by:

$$S_{21} = \frac{R_{T1} + R_{T2}}{R_{filter} + R_{T1} + R_{T2}} \tag{1.3}$$

Since an S_{21} magnitude close to unity, i.e., 0 dB, is desired, low insertion loss is achieved through reducing a filter's resistance (damping) relative to input and output termination resistance. Intuitively, since resonator motional resistance R_x is inversely proportional to Q, higher Q always translates to less insertion loss holding all else constant. As a sidenote, one might be tempted just to increase terminating resistors to arbitrarily high values to achieve lower insertion loss; however, doing so overloads the Q's of the resonators and decreases stop band rejection.

To highlight the importance of using high-Q resonators in a filter, fig. 1.4 presents a simulated comparison of 0.2% bandwidth filters, of 2nd, 3rd, and 4th order, made from lower Q (2.1k) and higher Q (8.8k), constituent resonators. Here, order n refers to the number of constituent resonators in the filter. One can clearly see that lower insertion loss is achieved using high-Q resonators, and that the most marked improvement in insertion loss is for the four resonator filter.

It is also instructive to examine why the Q needed for a given insertion loss increases linearly as fractional bandwidth decreases because it explains why narrowband filter's require higher Q's than do wideband filters.

High-Q Resonators for Narrow Fractional Bandwidths and Steep Rolloff

The insertion loss of a multipole bandpass filter is a function of both fractional bandwidth and Q, but also strongly depends on the number of (complex conjugate pairs of) poles in the transfer function n, the pole locations in complex frequency space, and the terminating impedances, which must have specific values to achieve minimum insertion loss in the passband for a given filter. Larger values of n allow for steeper stop band rolloff and thus better

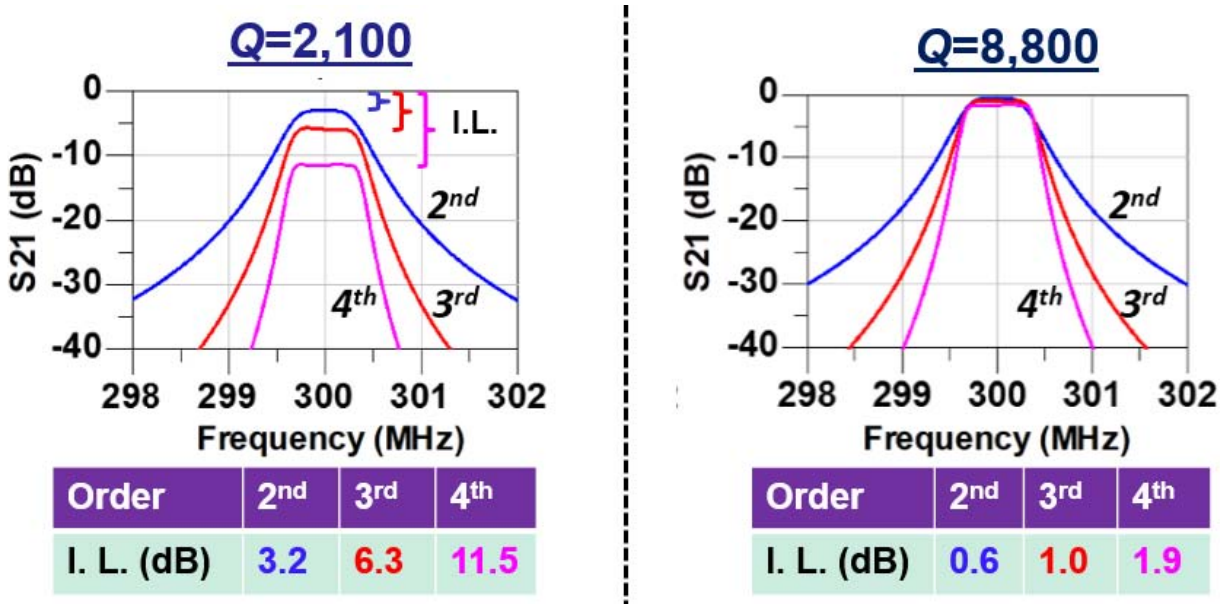

Figure 1.4: Comparison of 0.2% bandwidth filters, of 2nd, 3rd, and 4th order, made from lower Q (2.1k) and higher Q (8.8k), constituent resonators.

rejection of in-band interferers, as fig. 1.4 shows. The classic filter design text by Zverev [15] defines a normalized resonator quality factor, q_0, normalized by fractional bandwidth, that determines the amount of insertion loss for various types of properly terminated bandpass filters, e.g., Chebyshev, Bessel, etc., of varying orders, as follows:

$$q_0 = \frac{Q\Delta f_{3db}}{f_0} = Q \cdot FBW \tag{1.4}$$

Zverev further provides lookup tables that state insertion loss values for various values of q_0. These tables additionally contain the normalized design parameters that allow one to compute coupling strengths between resonators and the needed terminating impedances, for each combination of filter type and order, $n < 9$. As a guideline, $q_0 > 10$ will guarantee insertion losses of 3.0 dB or less for $n < 5$. Larger n values require higher q_0, and hence Q, to achieve the same insertion loss of a filter having smaller n. Equation (1.4) shows, for example, that if fractional bandwidth is halved, then required Q doubles to achieve the same q_0 and thus insertion loss.

Low Impedance Resonators for Low Termination Resistance

For most practical systems, the terminating resistances between an RF filter should range between about 50 and 500 Ω, e.g., to maximize power transfer between the filter and an antenna on one side and an LNA on the other in a receive chain. Matching networks may be used if needed to transform the terminating impedances to values that the filter requires.

In designing the filter, the motional resistances of the resonators comprising the filter should be comparable to this range as well, though their optimal values will depend on the design.

One common misconception is that a filter or resonator should be "matched" to its source and load resistance, i.e., be identical, for minimum insertion loss; however, insertion loss less than 3.5 dB is not possible unless the filter impedance's magnitude in the passband is smaller than that of the terminating resistors. In fact, based on eq. (1.3), we see that R_{filter} must approach zero to approach zero insertion loss.

Temperature Stability of Filters

As temperature changes, a filter's passband should remain stationary rather than shift significantly. Filters with large fractional bandwidths have less stringent temperature requirements than do narrowband filters. For example, a 100 ppm shift is much more detrimental to a 1,000-ppm-wide filter than to a 50,000-ppm-wide filter. Band-select filters with a buffer region on either side can tolerate shifts due to temperature without using any form of temperature compensation. A narrow channel-select filter, however, would certainly be required to correct for such shifts, which are on the order of 20 ppm/K for resonators made from materials such as silicon or AlN.

Minimized Capacitive Feedthrough for Strong Stopband Rejection

Lastly, for any filter, the port-to-port feedthrough capacitance must be minimized to ensure strong stop band rejection. The transmission through a 2-port network has a capacitive feedthrough floor which is proportional to both operating frequency and parasitic capacitance. More generally, any low impedance feedthrough path is harmful and should be eliminated as much as possible. Ground shielding between input and output is one useful method for suppressing feedthrough.

Additional Aspects of Filter Design

In this section, we have presented many of the basic performance requirements for bandpass filters, which we aim to bring on-chip. A more detailed treatment of filter design will be presented in chapter 7, focusing on novel capacitive-piezoelectric filters. We will include aspects of filter design not yet discussed, filter synthesis techniques, and measurements.

1.3 Survey of Band- and Channel-Select Filter Technologies at 100MHz-3GHz

Very high frequency (VHF) and ultra high frequency (UHF) filters are a key enabler for wireless transceivers and communications technology in general. They block out interfering signals to enable low power operation. There exist several mature technologies for

implementing low-loss bandpass filters, including the broad classes of surface acoustic wave (SAW) and bulk acoustic wave (BAW) resonators and filters, which both use piezoelectric material. BAW devices include solidly mounted resonators (SMR) and more recently introduced thin-film bulk acoustic resonators (FBAR). Newer filter technologies that target having multiple frequencies available on the same chip include piezoelectric contour mode and biased capacitive gap filters. To further improve performance, this thesis project seeks to introduce a new class of devices: capacitive-piezoelectric filters.

What each of these technologies shares in common are needs for high Q, power handling, frequency accuracy, strong stop band rejection, low insertion loss, low passband ripple, linearity, low motional resistance, low cost, and temperature stability. In this section, we look closely at each filter technology to examine its merits and drawbacks with regard to these metrics. We also evaluate each filter technology's suitability for implementing RF channel selection.

SAW Filters

Using interdigitated transducer (IDT) electrodes, one can excite and detect surface acoustic waves on a piezoelectric substrate, as was first demonstrated in 1965 by White and Vollmer [16]. SAW devices soon achieved commercial success serving as intermediate frequency (IF) filters for early televisions [17]. Unfortunately, early SAW filters had excessive insertion losses of 20 to 30 dB, but at IF, such losses were tolerable, as they did not significantly degrade signal to noise ratio (SNR). At RF, however, low insertion loss is essential as any loss directly reduces the SNR in superheterodyne receivers. Later, in 1982, a key innovation for implementing SAW filters with reduced insertion losses came with the introduction of the interdigitated interdigital transducer (IIDT) [17]. SAW filters then came to be used in cell phones, pagers, and satellite receivers [18].

More recently, passive SAW RF ID tags have emerged and can even be used for temperature sensing [19]. SAW resonators have also been commercialized to make oscillators for remote control applications such as keyless entry, home and car security systems, and medical alert devices [18]. SAW 2-port resonators, made on a quartz substrate, can achieve loaded Q's of 5,000 at 1 GHz with insertion losses of 15 dB using 50Ω terminations [18], and thus motional resistances of 460 Ω and unloaded Q's of 6,000.

SAW filters are commonly made on quartz, lithium niobate, or lithium tantalate piezoelectric substrates. Quartz is often used to achieve high Q and excellent temperature stability (using the AT-cut) [2]. Quartz resonators were first investigated almost a century ago by Walter Cady [20]. Alternatively, $LiNbO_3$ or $LiTaO_3$ is used when very wide bandwidths are needed due to its large SAW electromechanical coupling of about 6% [21], which directly determines maximum fractional bandwidth. $LiNbO_3$ and $LiTaO_3$ exhibit lower Q's than quartz, but high Q is not as essential for large bandwidth filters.

SAW filters are sold commercially at frequencies ranging from 10's of MHz to several GHz with fractional bandwidths ranging from less than 1000 ppm to 10%. To examine a list of a large variety SAW product offerings from a major manufacturer, refer to [22].

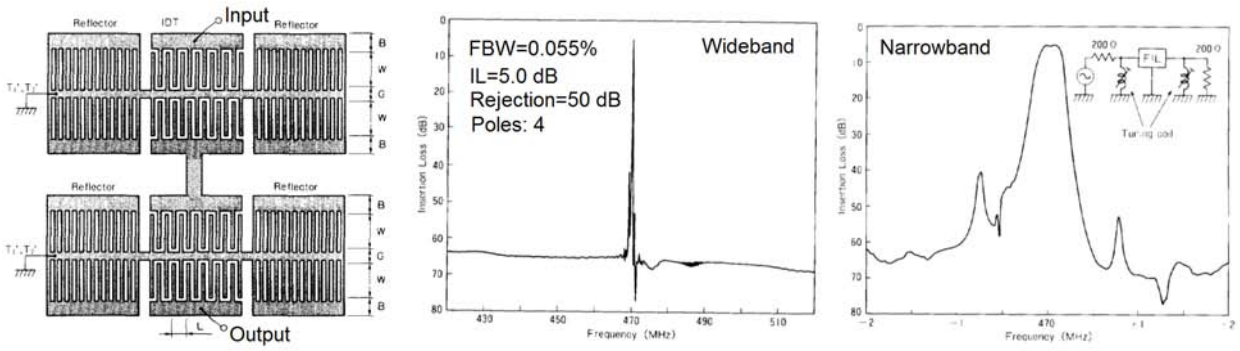

Figure 1.5: Device schematic and frequency responses (wideband and narrowband) of a 470 MHz 4-pole SAW filter made of quartz [23].

To highlight the RF channelizing capability of SAW filter technology, the work of [23] achieves an insertion loss of 5.0 dB with an extremely narrow fractional bandwidth of only 0.055%, with a four pole response at 470 MHz and 60 dB of out-of-band rejection. Smaller insertion losses of 1.6 dB were achieved by filtering the same bandwidth at 280 MHz. A 200 Ω termination was used with inductive tuning. A device schematic, wideband response, and narrowband response for the device is included in fig. 1.5. The device is a series cascade of two two-pole filters. To scale the device in frequency beyond 1 GHz, narrower linewidths below 0.5 μm are needed.

SAW devices have been widely commercially adopted and billions of them are produced each year. Advantages include low cost and high performance. They are not amenable to on-chip integration with circuitry, however. SAW filters require a piezoelectric substrate, precluding them from integration with CMOS devices. Additionally, multi-frequency capability on the same substrate is limited, as cross talk, i.e., energy leakage, between devices would occur.

MEMS-Based Quartz VHF and UHF Filters

The dominance of quartz as a resonator material for timing and frequency control has been established for decades, but emerging MEMS technologies are often advantageous due to their amenability to batch fabrication and extremely small size. Unfortunately, it is not feasible using current fabrication technology to directly grow or deposit quartz on a wafer to make quartz MEMS devices. It would be even more difficult to directly deposit a quartz film having an optimal orientation such as the temperature insensitive AT-cut.

As a workaround towards combining the favorable aspects of AT-cut quartz–which include high-Q and temperature insensitivity–with those of MEMS–which include CMOS integration, high frequencies, and small size–[24] reports a new technique for achieving VHF and UHF AT-cut quartz devices on a wafer, thus allowing for CMOS-quartz integration. The work utilizes an elaborate wafer bonding and thinning process using a quartz blank, a car-

rier wafer, and a host substrate. The quartz is thinned from an initial thickness of 300 μm down to less than 10μm after attachment to the handle wafer. Two wafer bonding steps are required. Ultimately, the resulting $f_0 \times Q$ product of 2.1 $\times 10^{13}$ Hz is the highest reported to date for any AT-cut quartz resonator, indicating very good performance.

Despite the high Q's achieved and the low motional resistances of about 100 Ω, the challenges of fabricating integrated resonators using bonded and thinned quartz–including using only a small 3" wafer, high expense, bonding stress variation, and quartz thickness variation control–make it quite difficult to offer an economically advantageous product over alternative resonator technologies.

BAW Filters

Bulk Acoustic Wave (BAW) thin-film piezoelectric resonators consist of two classes of devices: Solidly Mounted Resonators (SMRs), which are attached to the substrate and make use of Bragg reflectors for acoustic energy confinement [25], and thin-Film Bulk Acoustic Resonators (FBARs), which are substrate-isolated structures making use of either a small air gap between resonator and substrate or bulk etching of the substrate [26]. While the technologies have similar capabilities and performance, FBAR technology is preferred due to its marginally better acoustic confinement in the piezoelectric film and its simpler fabrication process, which does not require a reflector film stack [27]. Thus, we will limit our discussion of BAW filters to only those made from FBARs, though many of the points to be made are applicable to SMR filters as well.

For BAW devices, it is preferable to deposit the active material without wafer bonding to a crystal substrate. Sputter deposition is preferred. Aluminum nitride (AlN) is the piezoelectric material of choice due to its strong electromechanical coupling, which requires (a) a strong piezoelectric coefficient for electromechanical transduction and (b) a low electrical permittivity to minimize feedthrough capacitance.

FBAR Filters

AlN thin-Film Bulk Acoustic Resonators (FBARs) exhibit very low motional resistances of about 1Ω, strong electromechanical coupling C_x/C_0 of about 6%, resonance frequencies ranging from hundreds of MHz to several GHz, and Q's typically limited to about 2,500 [27]. They are exceptionally well-suited for wideband filters and can handle the large powers needed to drive a cell phone's antenna. For these devices, consisting of a (roughly) 1-μm-thick suspended AlN piezoelectric film sandwiched between top and bottom electrodes made of molybdenum, resonance frequency is inversely proportional to thickness.

Several BAW resonators can be arranged in a ladder topology to implement a high-order (multi-pole) band-select filter [29]. Avago Technologies has commercialized this technology through their production of duplexer filters, consisting of two such band-select filters, for wireless handsets. Billions of such devices have been sold in recent years, finding use in almost all modern smart phones. A typical frequency response for such a duplexer, as given

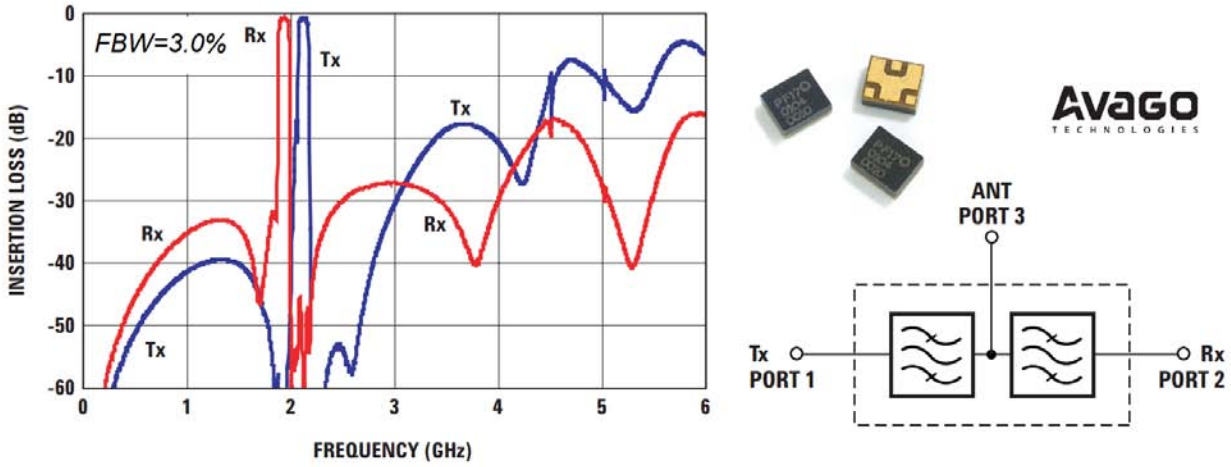

Figure 1.6: Receive (Rx) and transmit (Tx) frequency characteristics, device image, and functional block diagram, for a commercially available FBAR duplexer [28].

by its datasheet [28], is presented in fig. 1.6. This device interfaces between an antenna and a wireless transceiver's receive (Rx) and transmit (Tx) modulation electronics. Notably, the filters depicted have fractional bandwidths (FBW) of about 3% with insertion losses of 1.5 to 2.0 dB.

FBAR filters are effective for implementing RF band selection, however, their Q's are not as high as would be needed to implement RF channel selection with low insertion loss. As discussed in section 1.2, smaller fractional bandwidths require higher Q's to attain a given low insertion loss. Additionally, FBAR devices do not have CAD definable resonance frequencies, and are thus not amenable to cofabrication of many frequencies on the same die as is desired for RF channel selection. Lastly, since the fractional bandwidth for a ladder filter is defined by the spacing of series and parallel resonance frequencies, i.e., the electromechanical coupling C_x/C_0 or "k_t^2" of the device, bandwidth cannot be significantly reduced using a ladder topology to implement a channelizing filter unless parallel capacitance is introduced to each resonator.

Due to the CMOS-friendly (low) temperatures needed to perform sputter depositions, i.e., 300°C or less, FBARs can be succesfully integrated directly over CMOS [30]. FBAR's have also been used to synthesize novel radio components such as local oscillators with extremely low power consumption, e.g., 22μW [31], or which are tunable over a large 7,000 ppm range [32].

Contour Mode AlN Filters

"Contour mode" micromechanical piezoelectric resonators (CMR's), unlike BAW resonators, are those which vibrate in lateral mode shapes and thus vibrate at frequencies determined by lateral geometry [33]. Multiple frequencies are thus possible *on the same chip*

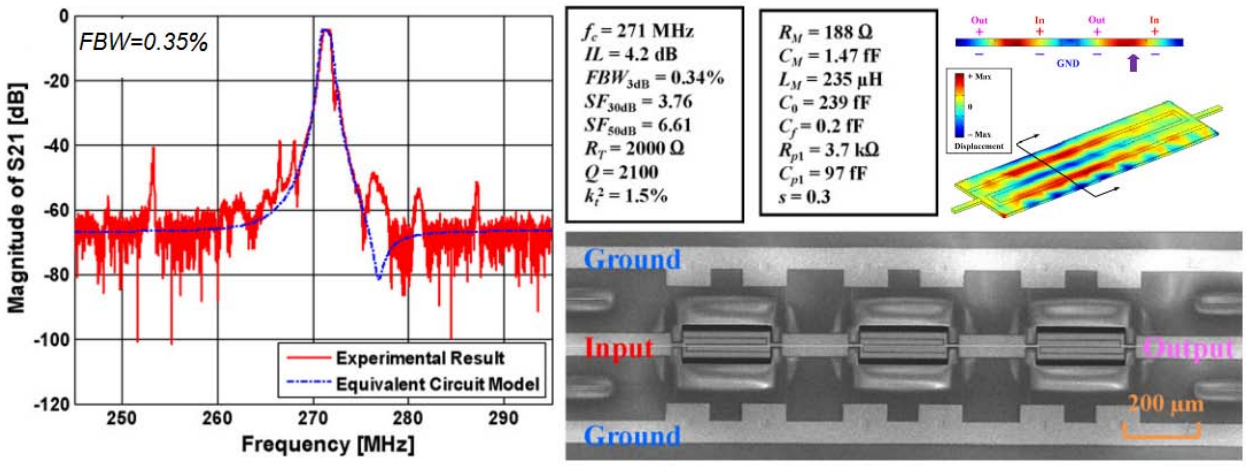

Figure 1.7: A VHF channelizing filter made from AlN contour mode resonators [37].

using CMR's. CMR's have other desirable capabilities, too. First, their resonance frequencies can span a very wide range: for example, filters have been made both at low frequencies, such as 13 MHz [34], and at super high frequencies (SHF), exceeding 3 GHz [35] using highly similar fabrication processes which typically use only 3 to 5 lithography steps. They are thus suitable for implementing oscillators and filters at both IF and RF. Secondly, they are fabricated at low enough temperatures to be integrated directly over CMOS. Lastly, due to the large number of mode shapes and geometries possible, the technology also allows for a more diverse range of resonator coupling techniques for filters, such as series capacitive coupling and mechanical coupling. Lastly, electrodes can be placed to allow for out of phase detection and excitation, allowing one to integrate single-ended to differential conversion into a filter with CMR's, eliminating the need for a balun [36].

To illustrate the RF channelizing capability of AlN contour mode resonators, fig. 1.7 presents the filter of [37], a 3rd order coupled-resonator piezoelectric filter utilizing capacitive coupling, offering insertion loss of 4.2 dB with a fractional bandwidth of 0.34%. Here, the insertion loss is due to the Q's of the comprising resonators of 2,100, offering a q_0 of 7.1. A second similar filter with a larger FBW of 0.53% had an improved insertion loss of 2.3 dB due to its increased q_0 of 11.1. These filters exhibit very strong stopband rejection of 60 dB.

AlN contour-mode technology has reduced electromechanical coupling strength compared to BAW devices– k_{eff}^2 is about 6% with BAW resonators and is 2% or less for CMR resonators due to the transverse nature of the transduction. Additionally, available power handling is reduced compared to with most BAW devices due to reduced area. These potential issues may not cause problems in targeted narrow band applications, however, the somewhat limited Q's of about 2,000 can cause significant insertion loss degradation for fractional bandwidths smaller than 0.5%. AlN CMR based filters thus adequately fulfill the needs of fractional bandwidths ranging from about 0.3% to 1.0%. At increased fractional bandwidths beyond about half of the electromechanical coupling, the shunt capacitances of the input

ports of the devices will degrade insertion losses unless an inductor matching network is used to resonate out the capacitance, as is done in [34] to achieve a much larger bandwidth of 4.0%.

Biased Capacitive-Gap Transduced Micromechanical Filters

Biased capacitive-gap transduced micromechanical resonators, or simply "capacitively" transduced resonators, are advantageous due to their demonstrated ultra-high Q's, their CAD-definable resonance frequencies, their electrical stiffness based tuning capability, their on-off switchability, their compact form-factors, and their amenability to on-chip integration when low-temperature-deposited materials are used. Interestingly, they have also been shown to perform integrated RF filtering and mixing in a single device [38].

The current challenge of using capacitively transduced resonator technology for RF channelizing filtering is *simultaneously* achieving sufficient electromechanical coupling, low enough motional resistance, good frequency accuracy (perhaps with some method for tuning frequency), good temperature stability, high fabrication yield, sufficient power handling, very small capacitive gaps (d_0's), and sufficient resistance to electrostatic pull-in at large bias voltages (V_p's).

Ultra-High Q Resonance

Micromechanical capacitive resonators, such as those reported in [39], [40], [41], or [42], made from doped polycrystalline silicon or diamond, can achieve very high quality factors (Q's) ranging from 10k to 100k+ at frequencies ranging from several kHz to several GHz. Such high Q's are attributable to several favorable factors, including minimized anchor losses, minimal surface losses, vacuum operation, and the use of low-loss acoustic materials. Since the only material requirement of a capacitively transduced resonator is that it be electrically conductive or otherwise chargeable, the available materials library for capacitive-gap transduced resonators is indeed much larger than that for piezoelectric devices.

The high Q's of micromechanical resonators made from non-piezoelectric materials have provided ample opportunities for experimental investigation, and elimination, of various resonator energy dissipation mechanisms. Quarter wavelength supports between anchors and resonators, which minimize displacement at anchor locations, have been shown to enable higher Q's [43]. Low anchor loss has enabled extremely high Q's, exceeding 360,000 in silicon at 60MHz, when cooled using liquid helium at 5K through the elimination of phonon-phonon-based Akhiezer damping [44]. Vacuum operation has been shown to increase the mechanical Q's of resonators through the elimination of gas damping, for example, as is needed to improve the phase noise of an optomechanical oscillator [45].

A Path Towards Stronger Electromechanical Coupling, $k_{eff}^2 = \frac{C_x}{C_0}$

While the Q's achieved by capacitive devices are admirable, their electromechanical coupling coefficients are often too small to permit their use in real-world applications when using very stiff structures at very high frequencies beyond 100 MHz. For example, using capacitive gaps of 75nm, the work of [39] achieves a record-high Q of 40,000 at 3.0 GHz but its demonstrated coupling is weak. For this device, $k_{eff}^2 = \frac{C_x}{C_0}$ is below 10^{-5}. Thus, to measure and even detect the resonance, a mixing measurement had to be used, the procedure for which was first described in [46]. Attaining sufficient motional-to-electrical capacitance ratios in capacitive transducer(s) is a critical task for VHF and UHF capacitive resonators and filters.

On the bright side, through the use of more aggressively scaled gaps and larger bias voltages, k_{eff}^2's can be dramatically improved. For example, in the recent work of [47], aggressive gaps of 39 nm and bias voltages of 14V are used to achieve $\frac{C_x}{C_0}$ levels of 0.1% at 223 MHz, representing a significant coupling improvement over previous efforts, such as [48], which required inductors to cancel unwanted capacitive reactance. Due to the strongly nonlinear V_p^2 and $1/d_0^3$ dependencies of electromechanical coupling in capacitive resonators, if fabrication allows, optimizing these two parameters may even lead to better coupling than piezoelectric counterparts.

A Path Towards Lower Motional Resistances

The motional resistances (R_x's) of capacitively transduced resonators are typically large due to limits on achievable gap sizes and bias voltages. Typical R_x values for capacitively transduced MEMS resonators range from 1kΩ to several MΩ. Common methods for reducing R_x include capacitive gap reduction, bias voltage maximization, increasing transduction area, and using array composite resonators [49]. Gap capacitance optimization is a highly effective way to increase coupling and reduce R_x. For example, in the work of [50], an R_x in the 100's of Ω's is achieved on a wineglass resonator through the use of atomic layer deposition (ALD) gap reduction. It should be noted that although parasitic trace resistance to the resonator prevented an accurate measurement of Q and R_x, the estimated values are nonetheless impressive. In the work of [51], capacitive gap sizes are reduced to record-low values, resulting in a reduction of R_x from 40.3kΩ to 1.26kΩ by shrinking gaps from 100nm to $\approx$10nm while maintaining a Q of 66k.

Another way to improve R_x is through the use of solid-gap transduction, where a dielectric gap is used instead of an air gap. Better yet, the work of [52] takes solid gap transduction a step-further, utilizing internal solid-gap transduction to create a very long serpentine transducer within the device. Such a method was used to demonstrate a motional resistance of 475Ω at 2.75 GHz with a Q of 7,200. The technique could readily be adapted to achieve even lower R_x, i.e., 50 Ω or less, through gap minimization and/or the use of higher-κ materials. This device in particular would also benefit from better isolation of the drive and sense transducers to achieve better stopband rejection.

Frequency Tuning

Capacitive-gap transduced micromechanical resonators possess the valuable capability to tune resonance frequency in a manner which does not depend on electromechanical coupling, thus allowing for potentially very wide tuning. Through the phenomenon of "electrical stiffness", which is a manifestation of the nonlinear voltage to force transfer function as a function of gap size, a "negative stiffness" acts to decrease resonance frequency as a function of tuning voltage. To highlight the effectiveness of this tuning method, the work of [53] achieves a -5.0% relative frequency shift using a tuning voltage of only 3.2V on a 32.768 kHz resonator. At higher frequencies for which coupling is weaker relative to mechanical stiffness, larger voltages are required, but they can nonetheless still have a strong effect on resonance frequency.

On/Off Switchability

The bias voltage dependent transduction strength of a biased capacitive gap transducer allows one to easily switch resonators and filters on and off through the introduction and removal of a polarizing voltage, V_p. In a parallel filter bank application, one can imagine numerous filters at different frequencies, each individually addressable through a control voltage which draws no current and thus consumes no quiescent power. The work of [54] demonstrates this concept through using multiple self-switched filters having settling times below 1 μs and with no added series switch insertion loss.

Channelizer Filters

Although several biased capacitive-gap transduced micromechanical filters [1] have been reported in the literature, examples of devices at very high frequencies are limited due to the aforementioned challenge of attaining sufficient electromechanical coupling. The first such VHF filter reported is the work of [48], which utilizes a differential disk array circuit consisting of 60 mechanically linked radial contour mode disks. Since it lacked sufficient electromechanical coupling and required large terminating impedances, inductors were needed to resonate out shunt input and output capacitance. Even though differential operation was used to suppress feedthrough by 20 dB, only 30 dB of stop band rejection was achieved. On a single ended device, deembedding was needed to see evidence of the filter characteristic, indicating that improved performance was needed.

Figure 1.8 presents the work of Akgul and Nguyen, which offers an improved, similar device through the use of 39 nm gaps and a V_p of 14V. Through the greatly improved electromechanical coupling of 0.1%, representing a 7× improvement, a much better frequency characteristic was achieved without the use of inductors, with better stop band rejection, better insertion loss, and with lower terminating resistance of 590 Ω. This device utilized

[1] Here, we refer to a filter as a system consisting of two or more coupled resonators, for which the transfer function has multiple left-hand-plane complex-conjugate pole pairs.

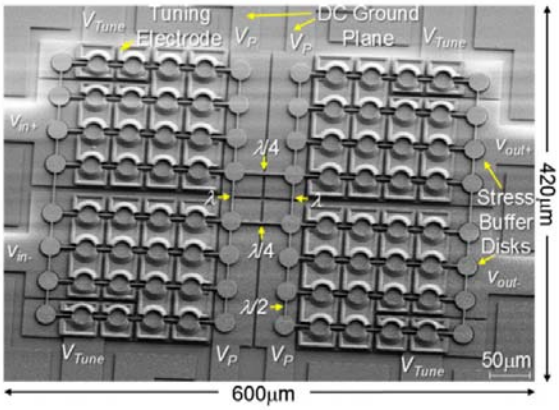

(a) Scanning electron micrograph of the differential second order capacitively transducer VHF channelizing filter

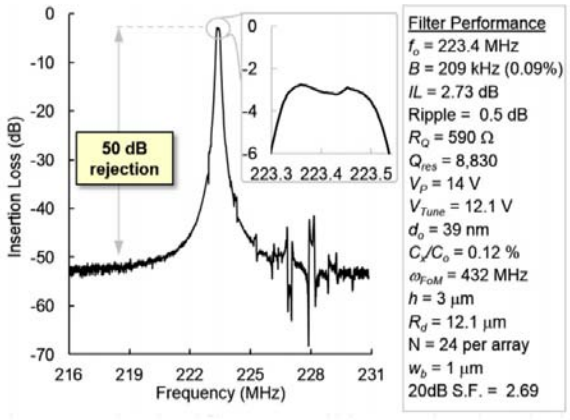

(b) Frequency response for the capacitive-gap transduced filter showing low insertion loss and strong rejection with a narrow fractional bandwidth.

Figure 1.8: A capacitive-gap transduced 0.09% FBW high rejection channel select micromechanical disk filter, from [47].

tuning transducers to correct the passband of the device, which is particularly necessary for small percent bandwidth filters, which have individual resonator manufacturing variations on the order of several hundred ppm which much be corrected.

Although the device achieves unprecedented performance on-chip, it remains to be seen whether capacitive gap transduced filters can be scaled well to higher frequencies far beyond 223 MHz with high yields. Though high performance is possible in principle, a need for reliable manufacturability presents difficulties due to non-idealities related to stress, lithography-based variations, defects, cleanliness, etching, and sacrificial release.

For further review, albeit at lower frequencies, the works of Bannon (9 MHz) [55] and Wang (340 kHz) [56] provide many insights into the design of capacitively transduced micromechanical filters utilizing beam and comb driven resonators respectively, which could find application as IF filters for heterodyne receivers. Such insights include the concept of low velocity coupling for reduced coupling stiffness, design procedures and constraints for filters, high-order filter operation, and manufacturing techniques.

Remarks

In this section, we have reviewed a variety of filter technologies, each having key strengths. SAW filters can achieve very good performance for a wide variety of applications, including both band-selection and channel-selection over a wide variety of frequencies, but they cannot be cofabricated on the chip with other such devices or integrated with transistors. BAW (FBAR) filters have come to be used in band select filters for cell phones and can be integrated

over transistors, but do not possess high enough Q's to achieve narrowband filtering with low insertion loss and cannot be easily fabricated to have multiple frequencies on chip. To allow for multiple frequencies on-chip, AlN contour mode resonators have emerged, offering strong electromechanical coupling, but lower Q's than are desired for truly narrowband applications or for very low insertion loss. Capacitively transduced devices, on the other hand, offer useful advantages over contour mode resonators, including ultra-high-Q, switchability, and tunability, yet they typically suffer from worse electromechanical coupling at high frequencies.

Indeed, what is needed is a resonator technology which combines the strengths of each of these technologies: wide tunability, on/off switchability, high Q, and strong electromechanical coupling–all while maintaining temperature stability, allowing for sufficient power handling, demonstrating sufficient frequency accuracy, and with high manufacturing yields and low cost.

1.4 Outline of Thesis

In this introductory chapter, we have examined how filters play a key role in radio communications. Bringing better filters with strong performance on-chip will allow for improved radios with lower power consumption, lower cost, and smaller size. We aim to introduce new filter technology for radios. In Chapter 2, we will examine in detail all the fundamental operating principles for contour-mode MEMS resonators necessary to understand how our MEMS resonators and filters operate.

Chapter 3 presents the capacitive-piezoelectric radial contour mode disk resonator. Beyond presenting operating principles and a complete model for the device, we include experimental verification of performance optimization techniques which enabled a Q as high as 8,757 at 300 MHz, electromechanical coupling as high as 1.05%, and single disk minimal motional resistance as low as 785 Ω.

Chapter 4 presents disk array resonators which allow for improved motional resistance, power handling, and manufacturing precision for resonance frequency.

Chapter 5 discusses voltage actuation of the top electrode of a capacitive-piezoelectrical transducer. New capabilities including on/off switchability, electromechanical coupling control, and frequency tuning are presented.

Chapter 6 presents a detailed treatment of the fabrication processes used to make the devices of this dissertation.

Chapter 7 discusses capacitive-piezoelectric narrowband filters, including operating principles, automated design techniques, experimental results, and initial demonstrations of switchable and tunable filters using the techniques of Chapter 5.

Chapter 8 concludes this thesis and presents future directions for this research.

Chapter 2

MEMS Resonator Fundamentals

This chapter explains fundamental operating and design principles for micromechanical resonators. High-Q micromechanical resonators enable frequency synthesis and filtering capabilities for wireless communications which greatly outperform LC-tank counterparts, since inductors have low Q's, and are vastly smaller than microwave resonators, since acoustic wavespeeds are more than four orders of magnitude slower than the speed of light. The concepts presented here include lumped element modeling of vibrations, modal analysis, mode shapes, effective mass and stiffness for a mechanical resonator, capacitive and piezoelectric electromechanical transduction, electromechanical circuit modeling, electromechanical coupling, advantages of using multiple transducers, and wave propagation through extensional coupling beams. A solid understanding of these concepts provides insight into the design choices which are presented in later chapters.

2.1 Lumped Element Modeling of Vibrations

The vibratory motion of a solid body, which is the result of a superposition of stress waves traveling within the structure, can be modeled as that of a single degree of freedom (SDF) mass-spring-damper system in many common situations, thus allowing the system behavior to be modeled using discrete elements. Figure 2.1 shows how high-Q micromechanical resonators can be modeled as simple mass spring damper systems. Figure 2.1a presents modal simulations for two different types of micromechanical resonators. On the left, a comb-drive resonator with folded beam supports is shown which vibrates laterally at 10's of kHz, depending on design parameters [57]. On the right, a radial contour mode disk resonator is shown, which vibrates with radial symmetry at frequencies of 100's of MHz, again, depending on design parameters [58]. In these illustrations, arrows are shown which denote the directions for applied force F modal velocity $\dot{u}$. Color denotes normalized modal displacement, ranging from 0 (blue) to 1 (red/orange). Figure 2.1b presents the equivalent resonator lumped element model for either resonator. Although the first structure consists of a relatively rigid portion (mass) and a flexible spring portion (spring), the mass and elasticity

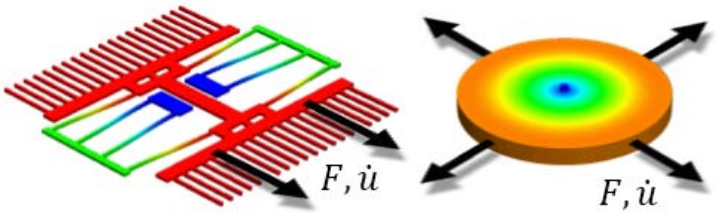

(a) Vibrational mode shapes for two examples of micromechanical resonators. Left: comb-drive resonator with folded-beam supports. Right: radial contour mode disk resonator.

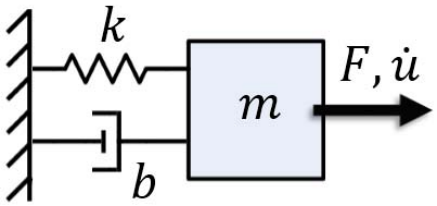

(b) Equivalent resonator lumped element model.

Figure 2.1: A high-Q micromechanical resonator can be modeled as a simple mass spring damper system with a very small damping factor.

(stiffness) are actually distributed throughout the entire structure. For the disk resonator, a distinct spring and mass are even more elusive, since they are more evenly distributed. The calculation methods for the 'effective' mass and stiffness of a resonator, m_r and k_r, are presented in section 2.4 and section 2.5, respectively.

Lumped element (as opposed to distributed) models are useful due to their simplicity, such as when one would like to accurately predict the motion of a mechanical resonator in response to an applied electronic excitation while avoiding the complexity of multi-physics finite element analysis (FEA) techniques. Reducing the complexity of a distributed resonator to a lumped element resonator also allows the use of linear circuit analysis techniques to describe the behavior of a larger system of which a mechanical resonator is just a part. For example, when the mechanical lumped element parameters are known for a micromechanical resonator, it's possible for a resonator, along with its electromechanical transducer(s) and parasitic electrical elements, to be analyzed together using circuit theory so that the electrical impedance of an overall system can be predicted.

Lumped Component Analogues in the Electrical and Mechanical Domains

A lumped element is a discrete, i.e., non-distributed, element that can exchange energy with other such elements. The net power flow exchanged between two lumped elements can be written as the product of a pair of "conjugate power flow" variables called an 'effort' and a 'flow' [59]. Associated with the flow is a generalized 'displacement', where the displacement is the definite integral of the flow with respect to time.

Using these concepts, the mechanical components m, k, and b can be represented as equivalent electrical elements due to a duality between corresponding elements in the mechanical and electrical domains. As voltage and current represent the effort and flow variables in the electrical domain, force and velocity represent the effort and flow variables in the mechanical

Table 2.1: Generalized Lumped Element Parameters and Representations in the Electrical and Mechanical Domains

Generalized Parameter	**Electrical Representation**			**Mech. Representation**		
Effort, $e(t)$	Voltage	v, V	[V]	Force	F	[N]
Flow, $f(t)$	Current	i, I	[C/s]	Velocity	$\dot{u}$	[m/s]
Displcmt., $q(t) = \int_0^t f(\tau)d\tau$	Charge	Q_d	[C]	Displcmt.	u	[m]
Gen. Res., $R_g = e(t)/f(t)$	Resistance	r, R	[Vs/C]	Damping	b	[Ns/m]
Gen. Cap., $C_g = q(t)/e(t)$	Capacitance	c, C	[C/V]	1/Stiffness	$1/k$	[m/N]
Gen. Ind., $L_g = e(t)/\dot{f}(t)$	Inductance	l, L	[Vs^2/C]	Mass	m	[Ns^2/m]

domain. The analogy can be extended further to include mechanical and electrical representations for generalized impedances, including resistance, capacitance, and inductance, as summarized in table 2.1.

There are five types of generalized one-port devices: flow sources, effort sources, resistances, capacitors, and inductances–one for each row of table 2.1, except for displacement. A port is a pair of terminals on a circuit element that must carry the same current through the element, entering the element at one of the terminals and leaving the element at the other. Using generalized lumped elements, one can represent mechanical dashpots, springs, and masses as their respective passive one-port electrical analogues, i.e., resistors, capacitors, and inductors, as follows:

$$r_x = b$$

$$c_x = 1/k$$

$$l_x = m$$

Here the subscript $_x$ denotes a motional variable. A lower case (as opposed to upper case) r, c, or l denotes that the component is a mechanical representation of a resistor, capacitor, or inductor that hasn't been transformed to a fully electrical representation through including the electromechanical transduction factor, η, which is introduced in section 2.6. The corresponding upper case electrical representations are introduced in a latter section.

Principles of Vibratory Motion

In order to predict the vibratory modes of a system, it is first necessary to determine the number of coordinates that specify its state. The number of degrees of freedom for a system, consisting of one or more connected solid bodies, is the minimum number of coordinates required to fully specify the state of the system.

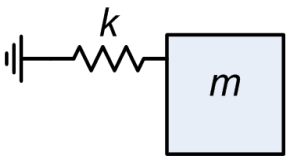

Figure 2.2: A spring-mass system. An undamped resonator

Single-, Multi-, and Infinite-Degree of Freedom (DOF) Systems

To illustrate the concept of degrees of freedom, consider the following examples:

1. For a single particle confined to motion in one dimension (1D), $DOF = 1$.
2. For a two body system with each body confined to motion in 1D, $DOF = 2$.
3. For a single point mass free to move in three dimensions, $DOF = 3$.
4. For a rigid body free to move in three dimensions, $DOF = 5$: three are necessary to specify the location of the origin, and two are needed to specify orientation.
5. For any elastic body, the number of DOFs is technically three times the number of atoms in the body! Thus, an elastic body practically has an infinite number of DOFs and is considered to be a continuous system.
6. A continuous system that is meshed for finite element analysis (FEA) is approximated as a multi-DOF system. For an appropriately fine mesh, modal analysis of the MDF system obtains the same fundamental eigenfrequencies and mode shapes as an infinite DOF system.

Single Degree of Freedom Mass-Spring System

For a rigid (ideal) mass is connected to a massless, linear (ideal) spring, there is a special frequency at which simple harmonic motion occurs. The restoring force due to the spring is directly proportional to displacement, the spring force causes the mass to accelerate towards equilibrium. When the spring force is zero, the inertia of the mass causes it to continue moving past equilibrium. Thus, cyclical motion continues indefinitely in the absence of damping.

In the absence of an external force, the equation of motion for this system is

$$F_{net} = m\frac{\mathrm{d}^2u}{\mathrm{d}t^2} = -ku = 0 \tag{2.1}$$

Solving for the displacement, u,

$$u(t) = A\cos\left(\omega_0 t - \phi\right) \tag{2.2}$$

Where $\omega_0 = \sqrt{k/m}$ is the angular natural frequency of the oscillatory motion and A and ϕ are constants dependent on initial conditions. If the system has nonzero energy, A will be greater than zero and the system will move harmonically.

Equivalently, for a modal frequency to be valid, it must satisfy the following equation:

$$ku - \omega^2 mu = F = 0 \tag{2.3}$$

As will be shown in the following section, a more general form of eq. (2.3) exists for multi-DOF (MDF) systems.

Modal Analysis for multi-DOF Systems

Systems with multiple degrees of freedom can be used to make filters with multi-pole transfer functions. For a general system with $n > 1$ DOF, a system of equations is needed to describe the state of the system. In general, the net forces on particles are dependent on the positions of other particles in the system. Thus, such a system is generally described using a stiffness matrix of size $n \times n$:

$$\mathbf{K} = \begin{bmatrix} k_{11} & k_{12} & \cdots & k_{1n} \\ k_{21} & k_{22} & \cdots & k_{2n} \\ \vdots & \vdots & \ddots & \vdots \\ k_{n1} & k_{n2} & \cdots & k_{nn} \end{bmatrix} \tag{2.4}$$

To perform modal analysis, one assumes harmonic motion occurs, thus acceleration is equal to position times the negative square of angular frequency. The single DOF modal analysis equation eq. (2.3) is modified to accommodate matrices for stiffness $\mathbf{K}$ and mass $\mathbf{M}$, while $\vec{u}$ is a coordinate vector:

$$\mathbf{K}\vec{u} = \omega^2 \mathbf{M}\vec{u} \tag{2.5}$$

Rearranging the terms,

$$\mathbf{M}^{-1}\mathbf{K}\vec{u} = \omega^2 \vec{u} \tag{2.6}$$

Which is reminiscent of the standard form of an eigensystem $\mathbf{A}\vec{x} = \lambda\vec{x}$, for which the eigenvalues (λs) are found by setting the determinant of the matrix $\mathbf{A} - \lambda\mathbf{I}$ equal to zero (here, $\mathbf{I}$ is the identity matrix) and solving for the roots. Similarly, to find the modal frequencies of an MDF mass-spring system, the following characteristic equation is solved:

$$\det\left(\mathbf{M}^{-1}\mathbf{K} - \omega^2\mathbf{I}\right) = 0 \tag{2.7}$$

This equation yields up to n distinct modal frequencies, where n is the number of degrees of freedom. If one or more roots of the characteristic equation occurs more than once, the system has degenerate orthogonal mode shapes at the same modal frequency.

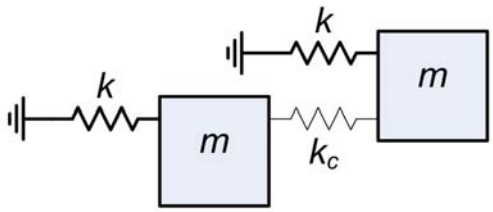

Figure 2.3: Two identical resonators coupled by a spring with stiffness k_c.

Once the eigenvalues (modal frequencies) are known, the eigenvectors (mode shapes) are found by finding the null space of the characteristic equation for each eigenvalue (modal frequency).

$$\left(\mathbf{M^{-1}K} - \omega_i^2\mathbf{I}\right)\vec{u_{\omega_i}} = \mathbf{0} \tag{2.8}$$

To solve for the mode shape vector, $\vec{u_{\omega_i}}$, associated with the i^{th} modal frequency, ω_i, solve eq. (2.8) for $\vec{u_{\omega_i}}$.

Two DOF System Example: Two Identical Spring-Coupled Resonators

Consider the system shown in fig. 2.3, which depicts two identical resonators coupled by a spring with stiffness k_c.

The system of equations describing the forces on the masses is:

$$\underbrace{\begin{bmatrix} k+k_c & -k \\ -k & k+k_c \end{bmatrix}}_{\mathbf{K}} \underbrace{\begin{bmatrix} u_1 \\ u_2 \end{bmatrix}}_{\vec{u}} - \omega^2 \underbrace{\begin{bmatrix} m & 0 \\ 0 & m \end{bmatrix}}_{\mathbf{M}} \underbrace{\begin{bmatrix} u_1 \\ u_2 \end{bmatrix}}_{\vec{u}} = \underbrace{\begin{bmatrix} F_1 \\ F_2 \end{bmatrix}}_{\vec{F}} = \begin{bmatrix} 0 \\ 0 \end{bmatrix} \tag{2.9}$$

The eigenvalues (modal frequencies) and eigenvectors (mode shapes) for this system are:

$$\omega_1 = \sqrt{\frac{k}{m}}, \quad \omega_2 = \sqrt{\frac{k+2k_c}{m}} \tag{2.10}$$

$$u_{\omega_1} = \begin{bmatrix} 1 \\ 1 \end{bmatrix}, \quad u_{\omega_2} = \begin{bmatrix} 1 \\ -1 \end{bmatrix} \tag{2.11}$$

One observes that there are two modes for this system: an in-phase mode at the natural frequency of an uncoupled resonator (where the coupler does not deform) and an out-of-phase mode at a higher frequency. The frequency ratio is given by $\sqrt{1+2k_c/k}$. This example explains intuitively why filter bandwidth is proportional to extensional-mode coupling beam width (for small bandwidths) for mechanically coupled micromechanical resonators, as is discussed in section 7.2.

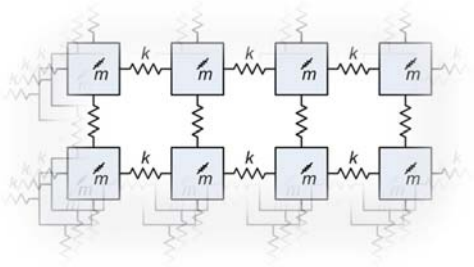

Figure 2.4: A continuous system has nearly an infinite number of DOFs. Atoms making up the material are free to displace in three dimensions.

Modal Analysis for Continuous (Infinite Degree of Freedom) Systems

Practically speaking, there is no such thing as an ideal rigid body, a point mass, or a massless spring. All solid bodies exhibit some elastisticity, and all can be analyzed using modal analysis, despite their continuous composition. Figure 2.4 depicts an illustration of the fundamental internal structure of a solid– the constituent atoms can each be considered to have multiple degrees of freedom. While the notion of describing a system with an infinite numbers of DOF's might seem daunting at first, there are fortunately frequencies (modal frequencies) at which the vibratory motion of any continuous system simplifies to behave like that of a single degree of freedom system.

There are two methods for performing modal analysis on continuous systems. The first method is to use the finite element method (FEM) to divide up the domain over a finite mesh and treat it as an n-degree of freedom system, where n is a finite number. As mesh quality, i.e., the number of nodes, increases, the calculated solution converges toward the true solution. Due to the intense computation involved, finite element modal analysis is most efficiently performed using software packages like COMSOL, ANSYS, or COVENTOR. The second, often preferable method for highly symmetric geometries, is an analytical solution (eigenfunction) which satisfies the partial differential wave equations over the domain of the resonator, subject to boundary conditions. If the mode shapes do not change with time, then separation of variables is equivalent to modal analysis [60].

In section 3.3, an analytical eigenfunction and eigenfrequency are provided for a disk resonator. The result is later shown to match the modal frequency of the measured device to within about 1%, and also matches the eigenfrequency predicted using finite element analysis.

2.2 Single Degree of Freedom Description of Mechanical Resonance

Determining all the lumped element component values for a distributed resonator requires performing an integration over the mode shape of interest and taking into account material parameters, geometry, modal frequency, and internal and external damping factors. As summarized in the three expressions below, these three variables depend on effective mass m_r, angular resonance frequency ω_0, and resonator Q-factor Q, all of which can be determined or estimated using techniques outlined in sections that follow.

$$m = m_r$$
$$k = k_r = \omega_0^2 m$$
$$b = \sqrt{mk}/Q$$

In order to calculate m_r, it is first necessary to understand the concept of a vibrational mode shape.

2.3 Vibrational Mode Shapes

At a specified modal frequency, ω_0, the normalized mode shape for a resonator, $\vec{\Phi}$, is a vector function of reference position $\vec{X}$ in R^3 having a maximum magnitude of 1 at locations of maximum displacement. If a mode shape is known and the displacement of any single point on the resonator is known at resonance, then the displacement is by definition known for every other point on the resonator. The displacement from the original position, $\vec{u}(\vec{X})$, at any original position $\vec{X}$, is less than or equal to the maximum displacement magnitude u_{max}, which only occurs over a limited region. The normalized mode shape is thus defined as:

$$\vec{\Phi}(\vec{X}) = \frac{\vec{u}(\vec{X})}{u_{max}}$$

Over the domain of the resonator, the position of any particle at time t is equal to its original position plus its displacement, $\vec{(u)}$.

$$\vec{x}(\vec{X}, t) = \vec{X} + \vec{u}(\vec{X}, t)$$

For a steady-state modal resonance, a sinusoidal time dependence is assumed at the modal frequency. An example mode shape, the 1st-radial-contour-mode, for a lateral disk resonator is shown in fig. 2.5 in red. This mode shape ideally exhibits no dependence in the z-direction and possesses azimuthal symmetry. Maximum displacement occurs at the outer radial boundary.

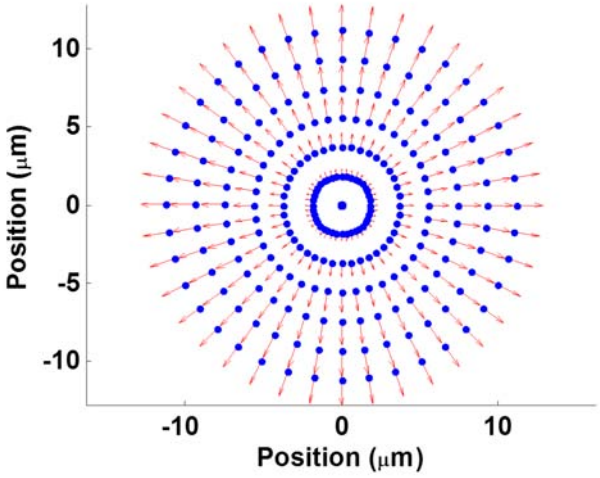

Figure 2.5: An example of a two-dimensional vibrational mode shape for a disk resonator. Each red vector represents displacement from a corresponding reference location shown in blue.

The procedure of determining mode shapes, i.e., eigenfunctions, and corresponding modal frequencies, i.e., eigenfrequencies, for a 1D, 2D, or 3D structure is known as modal analysis. Modal analysis can be performed on an arbitrary structure using the finite element method, through solving partial differential equations governing wave motion over the domain of the resonator, or by simple inspection when rigid bodies and compliant (nearly massless) springs are used. Once the mode shape and modal frequency are known, it is possible for one to calculate the effective dynamic mass for a resonator. The mode shape is used to calculate modal velocity, which in turn is used to calculate kinetic energy for a body as well as effective mass.

Modal Velocity of a Mechanical Resonator

Through knowing the modal frequency and the mode shape of the structure, one knows not only the displacement of every point in the body, but also the velocity over the domain. If this is not immediately evident, first consider that modal displacement is generally expressed as

$$\vec{u}(\vec{X}, t) = \vec{u}(\vec{X}) \sin(\omega_0 t + \phi_0)$$

Where $\vec{X}$ is the reference position, t is time, and ω_0 is the radian modal frequency. Taking the derivative, one finds that the zero-to-peak amplitude of velocity is equal to circular frequency (ω_0) times the magnitude of modal displacement. Scalar magnitudes for velocity and displacement are denoted as quantities without arrows, while arrows denote vector quantities.

$$\vec{\dot{u}}(\vec{X},t) = \omega_0 \vec{u}(\vec{X}) \cos(\omega_0 t + \phi_0)$$

The velocity amplitude at any point on the resonator is then equal to

$$\vec{\dot{u}}(\vec{X}) = \omega_0 \vec{u}(\vec{X})$$

The modal velocity for a vibrating body is useful for calculating its kinetic energy, which is needed to calculate effective mass for a mode shape.

Kinetic Energy of a Mechanical Resonator

The modal kinetic energy of a vibrating body is found by summing up tiny differential pieces of 'mass times one half modal velocity squared' over the domain. Differential mass is given by the density at a location $\rho(\vec{X})$ times a differential volume $dxdydz$. The scalar modal velocity, $\omega_0 u(\vec{X}) \cos(\omega_0 t + \phi_0)$, is a function of position. The full expression for time dependent kinetic energy is thus

$$KE(t) = \frac{1}{2}\left[\frac{1}{2} + \frac{1}{2}\cos(2\omega_0 t + 2\phi_0)\right] \iiint_V \rho(\vec{X})\omega_0^2 u(\vec{X})^2 \, dx\, dy\, dz \tag{2.12}$$

Maximum kinetic energy for the body is achieved when modal velocity is maximum, which occurs when modal displacement is zero.

$$KE_{max} = \frac{1}{2} \iiint_V \rho(\vec{X})\omega_0^2 u(\vec{X})^2 \, dx\, dy\, dz \tag{2.13}$$

2.4 Effective Mass of a Mechanical Resonator

Since different locations on a resonator move at different speeds, it is useful to define a quantity called effective mass, m_r. Effective mass is defined under the assumption that the entire resonator moves at a single reference velocity, $\dot{u}_{ref}$, defined as the modal velocity at a reference position $\vec{X}_{ref}$, so as to achieve the same kinetic energy as the actual resonator. By the definition of kinetic energy,

$$KE_{max} = \frac{1}{2} m_r(\vec{X}_{ref}) \dot{u}_{ref}^2 \tag{2.14}$$

Rearranging terms and simplifying,

$$m_r = \frac{2KE_{max}}{\dot{u}_{ref}^2} = \frac{2 \cdot \frac{1}{2} \iiint_V \rho(\vec{X})\omega_0^2 u(\vec{X})^2 dxdydz}{\omega_0^2 u_{ref}^2} \tag{2.15}$$

$$m_r = \frac{1}{u_{ref}^2} \iiint_V \rho(\vec{X}) u(\vec{X})^2 dxdydz \tag{2.16}$$

Although the choice of $\dot{u}_{ref} = \omega_0 u_{ref}$ is arbitrary, the traditional choice for u_{ref} is the resonator's maximum displacement, u_{max}. However, one might choose a reference position not at a location of max displacement, for example when one wants to estimate the effect of low-velocity mechanical coupling between resonators [61]. When m_r is not explicitly specified as having a reference location of the form $m_r(\vec{X_{ref}})$, it should be assumed that $u_{ref} = u_{max}$.

The choice of u_{ref} affects not only the effective mass, but also effective stiffness, k_r, and the electromechanical transduction factor, η. The same choice of u_{ref} must be used when calculating m_r and η.

Finally, the equivalent mass calculation can simplify to that of an integration over fewer than three variables when the mode shape has no dependence on one or two dimensional variables, for example as occurs with a purely lateral resonator with constant thickness. The location dependence of density ρ is usually constant too, resulting in the following simplified expression for effective mass, where t is the vertical thickness of the resonator.

$$m_r = \frac{\rho t}{u_{max}^2} \iint u(\vec{X})^2 dxdy = \rho t \iint \Phi^2(\vec{X}) dxdy \tag{2.17}$$

2.5 Potential Energy and Effective Stiffness of a Mechanical Resonator

Energy conservation requires that the maximum kinetic energy of the vibrating system KE_{max} equals the maximum potential energy of the system PE_{max}. In a manner analogous to determining the effective mass, an effective stiffness can be defined that assumes the entire resonator displaces the same amount in response to an applied force at the reference location. Intuitively, locations of small modal displacements are effectively stiffer with heavier effective masses than those of large modal displacements. Equating kinetic and potential energies, it is possible to derive an expression for a resonator's effective stiffness, k_r.

$$KE_{max} = \frac{1}{2} m_r \dot{u}_{ref}^2 = \frac{1}{2} k_r u_{ref}^2 = PE_{max} \tag{2.18}$$

Without the need to calculate and integrate strain energy density over the domain of the resonator, the effective stiffness k_r is found by multiplying effective mass by ω_0^2.

$$k_r = \omega_0^2 m_r \tag{2.19}$$

In summary, r_x, c_x and l_x are now known. From this point, electrical circuit analysis can be performed on one-port (two-terminal) mechanical components in tandem with electrical components, provided there exists one or more electromechanical transducers to translate between energy domains. In the following section, an explanation for representing an electromechanical transducer as a two-port transformer is provided.

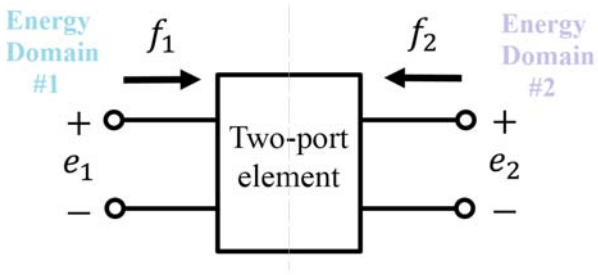

Figure 2.6: A general two port model for a transducer, where e's and f's represent efforts and flows in two different energy domains, #1 and #2.

2.6 Electromechanical Transduction

Electromechanical transduction explains how electrical signals generate, and are generated by, changes in spacing between adjacent planes of atoms in a material. A *transducer* is a term for any device that converts a signal in one energy domain to another. A transducer can function either as a sensor or an actuator. A *sensor* accepts a parameter in one energy form, e.g., pressure, and reports the value in another form, e.g., voltage. An *actuator* accepts energy, e.g., electrical, and creates action or movement, e.g., the motion of a diaphragm of a loudspeaker. Often, a transducer performs both functions simultaneously, e.g., in an oscillator's one-port quartz resonator. Whether an application calls for sensing, actuation, or both, a transducer is an essential element in any MEMS device. For RF MEMS applications, electromechanical transducers are most often implemented through either piezoelectric or DC-biased capacitive gap transduction.

Figure 2.6 presents a general two-port circuit model for a transducer, indicating that at each port there is an effort (e), e.g., a voltage or a force, and a flow (f), e.g., a current or a velocity. The product of effort and flow at a port is equal to the power entering that port. For any transducer, the power entering one port equals the power leaving the other port:

$$P_{net} = e_1(t)f_1(t) + e_2(t)f_2(t) = 0 \tag{2.20}$$

Since no power is dissipated in a transducer, there are two sets of two-port parameters that satisfy eq. (2.20). A transducer can function either by having a fixed scale factor between e_1 and e_2 *or* by having a fixed scale factor between e_1 and f_2. The former type of transducer, referred to as a *transformer*, is more relevant to our discussion of RF MEMS devices than is the latter type of transducer, known as a *gyrator*. Gyrators are useful, for example, in modeling the behavior of a $\lambda/4$-length mechanical coupler for a filter (see section 2.10). One can also model an inductor using a gyrator, through cross-linking efforts to flows between two energy domains, i.e., current is proportional to magnetomotive force, while voltage is proportional to the time derivative of magnetic flux [59].

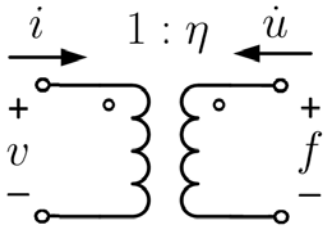

Figure 2.7: A circuit symbol diagram for a transformer representing an electromechanical transducer.

Electromechanical Transformers

Figure 2.7 depicts a typical model for an RF MEMS electromechanical transducer: a two port ideal transformer having the two port parameters of eq. (2.21). Here, electrical variables current and voltage act on one port of the transformer, while mechanical variables force and velocity act on the other port. The factor η is referred to as the *transformer factor* or *transduction factor* for the transformer. Additionally, η is sometimes called a *turns ratio*, but since an electromechanical transducer does not have a turns ratio like an electrical transformer, use of the term may be avoided.

$$\begin{bmatrix} f \\ \dot{u} \end{bmatrix} = \begin{bmatrix} \eta & 0 \\ 0 & -1/\eta \end{bmatrix} \begin{bmatrix} v \\ i \end{bmatrix} \tag{2.21}$$

Through examining eq. (2.21), one can see that η has equivalent units of either [N/V] or [C/m]. Although η has these units, when using a circuit simulator, it is acceptable to express η as a unitless factor, as it is for a standard transformer, so that mechanical variables can be expressed in the standard units of their electrical counterparts.

Performing a dimensional analysis, one sees that the units relating the input and output variables are consistent and that power is conserved. No power is ever dissipated in the ideal transformer. Thus, if either side acts as a power source, the other side acts as a power sink for the same amount. As an example, consider an actuator for which input electrical power is given by $P_{in} = v_{in} i_{in}$. The mechanical side of the transformer will act as a power source for which $P_{out} = -f_{out} \dot{u}_{out}$. Through eq. (2.21), one can readily show that $P_{in} = P_{out}$.

Equivalent Physical Interpretations of η

As summarized in table 2.2, η has three distinct yet equivalent physical meanings which are tied to the electromechanical transformations of the three types of conjugate power variables: efforts, flows and displacements. Dimensional analysis checks are also included to verify equivalent units for η for each case.

Understanding all three equivalent explanations for η is useful for determining the most straightforward manner to calculate η for each type of transduction.

Table 2.2: Equivalent physical interpretations of the electromechanical transformer factor, η

Transformed Parameter	Physical Meaning	Dimensional Analysis
Effort, $e(t)$	Modal force per unit voltage	$\{\eta\} = [\text{N}]/[\text{Nm/C}] = [\text{C/m}]$
Flow, $f(t)$	Electrical current per unit modal velocity	$\{\eta\} = [\text{C/s}]/[\text{m/s}] = [\text{C/m}]$
Displacement, $q(t)$	Displaced charge per unit modal displacement	$\{\eta\} = [\text{C/m}]$

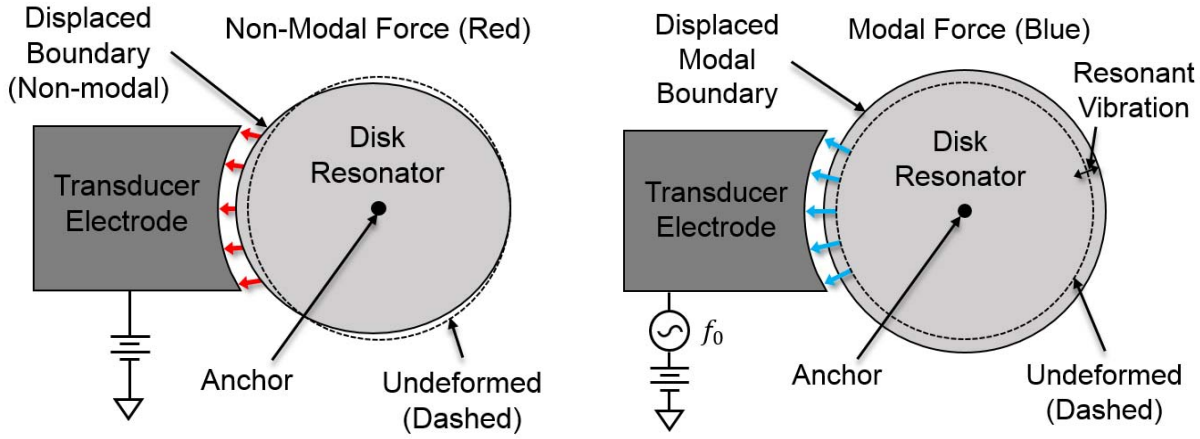

(a) Deformation of a disk resonator due to a non-modal force. Here, the shape of the transduction electrode determines the disk's deformation. Modal displacement is not assumed.

(b) Deformation of a disk resonator due to a modal force. Modal deformation is assumed due to an excitation at the modal frequency f_0. Modal force is used to calculate η.

Figure 2.8: Comparison of non-modal force and modal force. Modal vibration is assumed to calculate η for an electromechanical resonator.

Modal Force: Calculating η For a Vibrational Mode

Fundamental to understanding how to calculate η for a resonator is an awareness of the difference between non-modal and modal forces (and displacements). A modal force occurs at the modal frequency and assumes modal displacement; a non-modal force does neither. To illustrate, fig. 2.8 presents a comparison of a disk resonator under influence of (a) a non-modal force and (b) a modal force.

Figure 2.8a shows that applying a non-modal force through an arbitrary transducer geometry generally generates a static structural displacement field that may not match a desired vibrational mode shape, e.g., here, a radial contour mode. Likewise, again with a general transducer geometry, an impulsive excitation (containing energy at all frequencies)

from the transducer electrode will incite wave motion in the resonator such that displacement at any reference location as a function of time, i.e., the impulse response, will generally have some frequency content outside of, and not solely at, the desired modal frequency. An arbitrary electrode geometry thus can excite multiple modes.

Now, considering only excitations at the modal frequency, c.f. fig. 2.8b, numerous excitation cycles are generally, but not always, required for the wave motion originating from the transducer electrode(s) at the modal frequency to result in a displacement profile that resembles the mode shape. When an excitation's frequency matches the desired modal frequency, and when a resonator's Q is large, the desired mode shape will grow over the start up time, eventually dwarfing transient displacements at other frequencies. Once in the sinusoidal steady state, the assumption of a pure mode shape becomes valid and is thus used to calculate the electromechanical transformer factor η for the mode of interest. The resultant voltage v_x, current i_x, or displaced charge Q_d from the modal displacement or modal velocity profile can then be used to calculate η, according to the following equivalent expressions:

$$\eta = \frac{Q_d}{u_{ref}} = \frac{i_x}{\dot{u}_{ref}} = \frac{F_{modal}}{v_x} \tag{2.22}$$

Depicted in fig. 2.8b using blue arrows, modal force is an areal sum of the stress that is generated, or acts, over a transduction region. One can alternatively, for the purpose of lumped element modeling, consider modal force as existing at a single reference point, $\vec{X}_{ref}$. Through modal vibration, a resonator acts as a single degree of freedom system. The modal force having magnitude F_{modal} causes a displacement magnitude u_{ref} at the reference location. At resonance, deformation of the whole structure is known if the displacement of the reference point is known. At resonance, the familiar Hooke relation for resonator dynamic stiffness $k_r = 1/c_x$ applies, but also must account for displacement amplification (multiplication by Q) and a 90° phase shift, both due to resonance:

$$F_{modal} = \frac{jk_r u_{ref}}{Q} \tag{2.23}$$

η for a Capacitively Transduced Resonator

The expression for η for a polarized capacitive-gap transduced resonator is a function of how the stored energy of a capacitive transducer changes due to gap modulation through a resonator's modal displacement.

Starting from fundamental principles, the energy stored on a capacitor is equal to the work W required to displace a total amount of charge Q_d across a capacitor having capacitance C:

$$W = \int_0^{\Delta V} Q_d \, \mathrm{d}V = \int_0^{\Delta V} CV \, \mathrm{d}V = \frac{1}{2} C \Delta V^2 \tag{2.24}$$

If the capacitor voltage ΔV is held constant and the capacitive gap changes due to modal displacement u_{ref}, the stored energy of the capacitor changes. For a system where the gap is expressed as a function of resonator displacement at the reference location, u_{ref}, by taking the derivative of the stored energy with respect to u_{ref}, the attractive force on a capacitive actuator becomes apparent:

$$F = \frac{\mathrm{d}W}{\mathrm{d}u_{ref}} = \frac{1}{2}\frac{\mathrm{d}C}{\mathrm{d}u_{ref}}\Delta V^2 \tag{2.25}$$

When ΔV is set as the sum of a polarizing voltage V_p and an ac voltage $v_x \sin \omega t$, force terms arise at DC, ω, and 2ω:

$$F(t) = \frac{1}{2}\frac{\mathrm{d}C}{\mathrm{d}u_{ref}}\left[V_p^2 + 2V_p v_x \sin \omega t + \frac{1}{2}v_x\left(1 - \cos 2\omega t\right)\right] \tag{2.26}$$

Thus, considering only the term at ω,

$$F_{modal} = \frac{\mathrm{d}C}{\mathrm{d}u_{ref}}V_p v_x \tag{2.27}$$

η for a capacitively transduced resonator can then be expressed as a ratio of efforts:

$$\eta = \frac{F_{modal}}{v_x} = V_p\frac{\mathrm{d}C}{\mathrm{d}u_{ref}} \tag{2.28}$$

The ratio of displacements definition for η, in terms of induced charge, is:

$$\eta = \frac{\mathrm{d}C}{\mathrm{d}u_{ref}} = \frac{\mathrm{d}Q_d}{\mathrm{d}u_{ref}} \tag{2.29}$$

The ratio of flows definition, useful for calculating output current due to modal velocity, is:

$$\eta = \frac{\dfrac{\mathrm{d}Q_d}{\mathrm{d}t}}{\dfrac{\mathrm{d}u_{ref}}{\mathrm{d}t}} = \frac{i_x}{\dot{u}_{ref}} \tag{2.30}$$

For a capacitive resonator, electromechanical transduction manifests itself solely on resonator surfaces that form transducing capacitive gaps with interfacing electrodes. On the other hand, for a piezoelectric resonator, transduction occurs throughout the body of the resonator, not just on surfaces. For this reason, piezoelectric transduction often is stronger than capacitive transduction, particularly for stiff structures at higher frequencies. The method for calculating η for a piezoelectric resonator is explained in the following section.

η for a Piezoelectrically Transduced Resonator

For a piezoelectric resonator, η is most easily calculated through integrating charge density over electrode area given a unit amount of modal displacement. Since displacement at every point on the resonator is fully specified due to the mode shape, strain is also specified, and in turn, induced area charge density is specified via the direct piezoelectric effect. The strain at any point on the resonator is equal to the spatial derivative of displacement.

$$\epsilon_x = \frac{\partial u_x}{\partial x} \tag{2.31}$$

$$\epsilon_y = \frac{\partial u_y}{\partial y} \tag{2.32}$$

For a c-axis aligned piezoelectric material such as sputtered AlN, perpendicular lateral strains ϵ_x and ϵ_x sum together to create a z-axis (c-axis) strain ϵ_z through the poisson effect that gives rise to an induced charge density. The e_{31} coefficient captures this, as it is the area charge density developed for a unit amount of net lateral strain. η can thus be expressed as follows, where Q_d represents induced (displaced) electrode charge, D_z is the z-directed electric displacement field, A is the region over which transduction electrodes exist for the resonator, and $\nabla_{xy}\cdot$ represents the mathematical divergence operator in the xy-plane:

$$\eta = \frac{Q_d}{u_{ref}} = \frac{\iint_A D_z \,\mathrm{d}x\mathrm{d}y}{u_{ref}} = \frac{e_{31}}{u_{ref}} \iint_A \left(\frac{\partial u_x}{\partial x} + \frac{\partial u_y}{\partial y} \right) \mathrm{d}x\mathrm{d}y = \frac{e_{31}}{u_{ref}} \iint_A (\nabla \cdot \vec{u}) \,\mathrm{d}x\mathrm{d}y \tag{2.33}$$

In cylindrical coordinates, this equates to:

$$\eta = \frac{e_{31}}{u_{ref}} \iint_A \left(\frac{u_r}{r} + \frac{\partial u_r}{\partial r} + \frac{1}{r}\frac{\partial u_\theta}{\partial \theta} \right) dxdy \tag{2.34}$$

The procedure for calculating η involves integrating the divergence of the normalized mode shape over the electroded area and multiplying by the piezoelectric coefficient $e_{31} = 0.7\mathrm{Cm}^{-2}$. Note that regions of negative and positive divergence should have electrodes of opposite polarities to avoid net charge cancellation. Also, if ϵ_x and ϵ_y are equal and opposite at a location, ϵ_z will be zero at that location.

η for a Capacitive-Piezoelectrically Transduced Resonator

The same method for calculating η for a piezoelectric resonator with contacting electrodes is used to calculate that for a capacitive-piezoelectric resonator. To further improve accuracy, one may wish to introduce a correction factor for η to account for deviations due to fringing fields due to electrode separation, but such a factor can usually be neglected, especially for small gaps. The current simulation method seems satisfactory, accurately predicting the

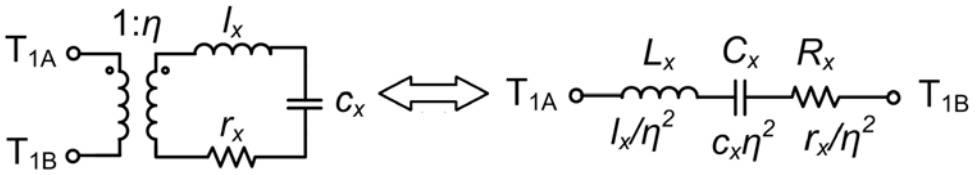

Figure 2.9: Equivalent single-transducer resonator circuits.

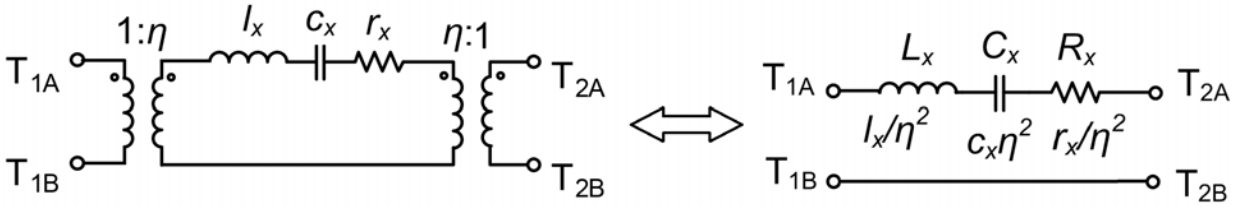

Figure 2.10: Equivalent two-transducer resonator circuits.

transduction for capacitive piezoelectric resonators to within a smaller margin of error than that which exists for other quantities, such as e_{31}.

A different factor, α, is used to account for the reduced coupling due to the introduced capacitive gaps, as will be discussed in a latter section.

Beyond knowing how electromechanical transducers operate and how η can be computed for different types of transduction, it is also useful to examine how the effects of electromechanical transducers can be absorbed into mechanical lumped elements in order to create simpler, fully electrical, equivalent circuits.

Equivalent Electrical Components via Transducer Absorption

As shown in fig. 2.9 and fig. 2.10, it is possible to combine one or two transducers with mechanical resonator lumped elements r_x, c_x, and l_x to translate to the equivalent electrical parameters R_x, C_x, and L_x, for each of which an uppercase letter denotes that the effect of the transducer has been integrated into the value. Here, the subscript $_x$ denotes a motional variable. Note that the circuit of fig. 2.10 is only valid when the two transducers have equal transformer coefficients.

2.7 Butterworth-Van Dyke (BVD) Equivalent Circuit Model

The Butterworth-Van Dyke (BVD) circuit is the classical lumped element circuit model for an electrically transduced mechanical resonator. The BVD model was first used to describe the electrical behavior of quartz crystal resonators. Later, the model was used

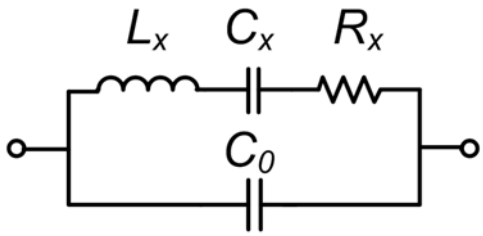

Figure 2.11: Butterworth-Van Dyke (BVD) circuit.

to model AlN resonators, such as Surface Acoustic Wave (SAW) devices and thin Film Bulk Acoustic Resonators (FBARs). It can be used for one-port capacitively transduced resonators. The model is also applicable for capacitive-piezoelectric devices, albeit with some modifications to the component values.

In fig. 2.11 below, the BVD circuit is shown, the upper branch of which is the acoustic path, consisting of the familiar L_x, C_x, and R_x which represent mass, stiffness, and damping in the resonator, respectively, and which take into account the electromechanical transduction factor, η. The lower branch is the electrical path, a capacitance between the input and output electrodes across the piezoelectric (dielectric) material.

The interplay of the shunt capacitance and the series LCR gives rise to two resonance frequencies. The first is a series resonance f_s exhibiting a minimal impedance. The second is a parallel resonance f_p exhibiting a maximal impedance.

Series and Parallel Resonance Frequencies of the BVD Circuit

The impedance in terms of complex frequency s for the equivalent circuit is given by:

$$Z(s) = \frac{R_x + \frac{1}{sC_x} + sL_x}{1 + sR_xC_0 + \frac{C_0}{C_x} + s^2L_xC_0} \tag{2.35}$$

Substituting $j\omega$ for s, assuming sinusoidal steady state operation, one obtains

$$Z(j\omega) = \frac{R_x + \frac{1}{j\omega C_x} + j\omega L_x}{1 + \frac{C_0}{C_x} - \omega^2 L_xC_0 + j\omega R_xC_0} \tag{2.36}$$

Series resonance occurs when the impedance magnitude of the numerator is minimized:

$$\frac{1}{j\omega C_x} + j\omega L_x = 0 \tag{2.37}$$

$$\omega_s = \sqrt{\frac{1}{L_xC_x}} \tag{2.38}$$

$$f_s = \frac{1}{2\pi}\sqrt{\frac{1}{L_xC_x}} \tag{2.39}$$

Parallel resonance occurs when the impedance magnitude of the denominator is minimized:

$$1 + \frac{C_0}{C_x} - \omega^2 L_x C_0 = 0 \tag{2.40}$$

$$\omega_p = \sqrt{\frac{1 + \frac{C_x}{C_0}}{L_x C_x}} = \omega_s \sqrt{1 + \frac{C_x}{C_0}} \tag{2.41}$$

$$f_p = f_s \sqrt{1 + \frac{C_x}{C_0}} \tag{2.42}$$

An oscillator (frequency generator) circuit can be created using the crystal as a frequency control element by utilizing either the series or parallel resonance frequency of the crystal, depending on whether the sustaining amplifier selects a maximum admittance or a maximum impedance. For example, a resonator with a very low series resonance impedance such as an FBAR, an oscillator circuit must utilize the parallel resonance so that the series resonance Q-factor is not heavily loaded by the input impedances of the amplifier circuitry.

The series and parallel resonance frequencies can be used to calculate an important BVD circuit model parameter, the electromechanical coupling coefficient, k_{eff}^2.

2.8 Electromechanical Coupling Coefficient, $k_{eff}^2 = C_x/(C_x + C_0)$

The electromechanical coupling coefficient (EMCC, expressed as k_{eff}) for a BVD resonator is defined as follows: the square of the EMCC, k^2, is the ratio of mechanical energy stored in the volume of the resonator body and capable of conversion to the total electrical energy supplied to the body [62]. Due to the reciprocal nature of electromechanical transduction, the definition is also valid when the words *electrical* and *mechanical* are transposed. To determine the EMCC for a particular mode, one can assume that a sinusoidal voltage of amplitude V is applied across the terminals of the resonator at the modal frequency, as shown in fig. 2.12.

The mechanical and electrical energies of the body U_m and U_e can be expressed as:

$$U_m = \frac{1}{2} C_x V^2 = \frac{1}{2} c_x \eta^2 V^2 = \frac{1}{2} \frac{1}{k_r} F_{modal}^2 = \frac{1}{2} k_r u_{ref}^2 \tag{2.43}$$

$$U_e = \frac{1}{2} C_0 V^2 \tag{2.44}$$

Thus,

$$k_{eff}^2 = \frac{U_m}{U_e + U_m} = \frac{\frac{1}{2} C_x V^2}{\frac{1}{2} C_0 V^2 + \frac{1}{2} C_x V^2} = \frac{C_x}{C_0 + C_x} \approx \frac{C_x}{C_0} \tag{2.45}$$

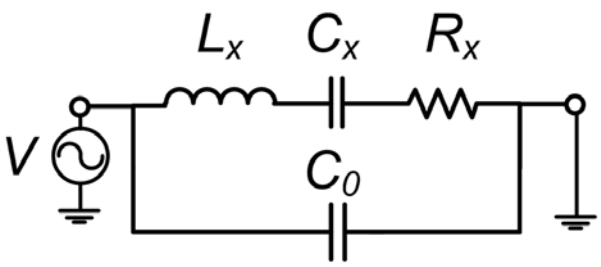

Figure 2.12: Butterworth-Van Dyke (BVD) circuit.

Since f_p can be expressed as a function of f_s and C_x/C_0 as defined in eq. (2.42), the ratio of capacitances and thus the EMCC can also be expressed as a function of the parallel and series resonance frequencies. The EMCC can therefore be experimentally determined via measurement of a resonator's frequency characteristic as follows:

$$\frac{k_{eff}^2}{1-k_{eff}^2} = \frac{\frac{C_x}{C_0+C_x}}{1-\frac{C_x}{C_0+C_x}} = \frac{C_x}{C_0} = \frac{f_p^2 - f_s^2}{f_s^2} \tag{2.46}$$

The C_x/C_0 of a transducer port is an important parameter which sets an upper limit on the achievable bandwidth for filters–the maximum fractional bandwidth an electromechanical bandpass filter can transmit without added insertion loss is approximately equal to $k_{eff}^2/2$. Matching inductors can be used to form one or more L-networks to broaden the bandwidth beyond this limit by resonating out the shunt capacitance, if needed.

2.9 Multi-Transducer Resonant Systems

For many resonant systems, it is useful to employ multiple electromechanical transducers each serving a different purpose. For example, three common transducer functions for RF MEMS include *drive*, *sense*, and *tune*. Since available area for placing transducer electrodes is limited for a given structure, it might seem desirable to use a single transducer to simultaneously excite a mechanical structure, sense its motion, and tune its frequency via a control voltage. Although possible in principle for a limited set of applications, it is often not desirable or possible in practice to combine transducer functions. Additionally, separating transducers can provide new benefits.

Frequency Tuning Without Affecting Motional Impedance

For a stable oscillator or filter system, motional impedance R_x should stay constant when resonance frequency is tuned. Single transducer frequency tuning requires placing either a control bias voltage or an external capacitance in the input/output (I/O) signal path. For a capacitively-transduced resonator, frequency tuning works by changing the polarizing voltage

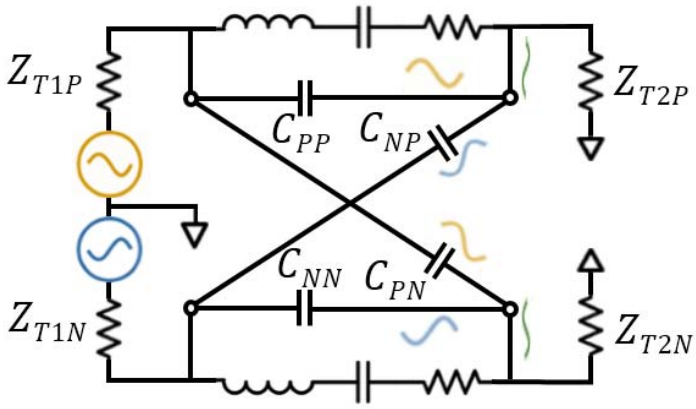

Figure 2.13: A schematic of a simplified fully differential filter.

V_p of the transducer and thus changing its electrical stiffness, while for a piezoelectrically-transduced resonator, a series (or parallel) capacitance added to a transducer tunes either its series (or parallel) resonance frequency. In either case, these tuning elements affect the I/O transduction strength and motional impedance R_x of a resonator. On the other hand, dedicated tuning transducers, i.e., those not in the I/O path, offer independent control knobs for resonance frequency that avoid affecting R_x, albeit at the expense of some I/O transduction strength. For example, this method is used to obtain an accurate 32.768 kHz clock frequency for the resonator of [53].

Two-Port Capacitive Feedthrough Reduction Via I/O Separation

A two-port resonant system can be constructed using either one or two I/O transducers. A single transducer two-port resonator has one terminal of each of its ports tied to the same node, e.g., ground, while the remaining two terminals of the two ports connect to the two terminals of the transducer. This device has relatively strong transduction but relatively poor capacitive isolation between input and output.

A two transducer two-port resonant system utilizes a dedicated transducer at each port. This system has the advantage of potentially very good capacitive feedthrough isolation between input and output. For a bandpass filter, minimizing capacitance between input and output is essential for realizing high levels of stop band rejection. If the distance between the transducers is maximized and appropriate ground shielding is placed between the two transducers, this unwanted capacitance can be fully minimized.

Differential Operation for Further Capacitive Feedthrough Reduction

In addition to using separate I/O transducers for a filter, differential operation enables significant feedthrough cancellation. A diagram illustrating how differential signals are helpful for improving stopband rejection is included in fig. 2.13. Here, the feedthrough capacitances

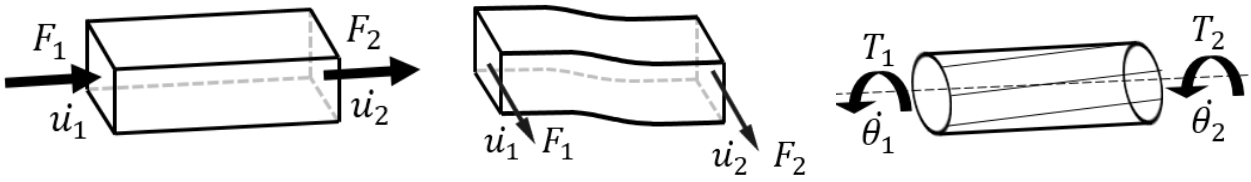

(a) Extensional. (b) Flexural. (c) Torsional.

Figure 2.14: Three types of mechanical coupling beams.

C_{pp} and C_{nn} act to transmit their electrical input signals directly to their respective outputs. Differential signaling is useful to the degree that the cross feedthrough capacitances are equal to each other–the signals transmitted through the cross feedthrough capacitances C_{np} and C_{pn} destructively interfere with the direct feedthrough signals thus reducing net feedthrough at each output.

For inputted differential signals, effective feedthrough capacitance becomes:

$$C_{FT,diff} = C_{pp} - C_{pn} = C_{nn} - C_{np} \tag{2.47}$$

For example, if $C_{pn} = 0.9C_{pp}$, then feedthrough capacitance is reduced by 90% (or 20 dB) through differential operation. Differential operation was used in the VHF capacitively-transduced filters of [48] and [47] to improve stopband rejection by about 30 dB. Comparable gains could be expected for piezoelectric filters using this technique at the cost of increased system complexity.

2.10 Coupling Beams

Mechanical coupling elements to connect larger vibrating bodies together can include extensional, flexural and torsional beams, as are illustrated in fig. 2.14. Mechanical couplers transmit forces and velocities between their connection points and thus are useful for enforcing various boundary conditions on vibrating systems. The following analysis assumes that the lengths of the beams are on the same order as the extensional, flexural, or torsional wavelengths in the material, thus necessitating the use of transmission line theory. Our analysis focuses on extensional coupling beams, for which propagation velocity and force are in the same direction. Extensional coupling beams will later be shown as being useful for coupling radial contour mode disk resonators together to create disk arrays.

2-Port Models for Extensional Coupling Beams

Extensional coupling beams, for which wavelength is decoupled from beam height and beam width and for which displacements run parallel to wave propagation direction, are simpler to model than torsional or flexural coupling beams. Contour mode resonators can easily

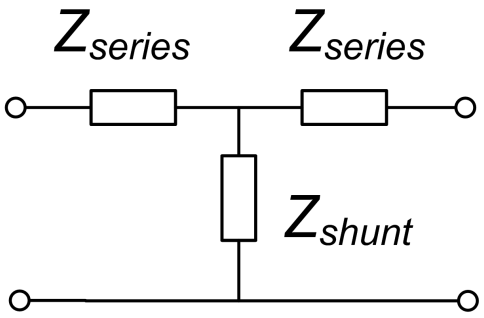

Figure 2.15: Two-Port impedance T-network representation for an extensional coupling beam.

be coupled together using extensional couplers, since displacement at coupler attachment points is purely in the radial direction.

To model a coupler, a transmission line model can be used. The behavior of the transmission line, assumed to be lossless, can be described using a 2-port model, which can be most conveniently be expressed as an ABCD matrix. The ABCD 2-port parameters for an extensional coupler are given by [63]:

$$\begin{bmatrix} F_1 \\ \dot{x}_1 \end{bmatrix} = \begin{bmatrix} A & B \\ C & D \end{bmatrix} \begin{bmatrix} F_2 \\ \dot{x}_2 \end{bmatrix} = \begin{bmatrix} \cos \alpha l_c & \frac{j \sin \alpha l_c}{Z_0} \\ j Z_0 \sin \alpha l_c & \cos \alpha l_c \end{bmatrix} \begin{bmatrix} F_2 \\ \dot{x}_2 \end{bmatrix} \tag{2.48}$$

Where l_c is the length of the coupler and α is the wave number, given by

$$\alpha = \frac{2\pi}{\lambda} = \frac{2\pi f}{v_a} = \frac{2\pi f}{\sqrt{E/\rho}} \tag{2.49}$$

In eq. (2.49), λ is the extensional wavelength in the coupling beam, f is the frequency of operation, v_a is the acoustic velocity, and E and ρ are the Young's modulus and density of the material, respectively. In eq. (2.48), Z_0 is the characteristic mobility, defined in eq. (2.50)

$$Z_0 = \frac{1}{h_c w_c \sqrt{E\rho}} \tag{2.50}$$

In eq. (2.50), h_c and w_c represent the height and width of the coupling beam's cross section respectively, assuming a rectangular cross section. Using a conversion from ABCD parameters to an impedance network, the coupling beam can be modeled by a T-network of symmetric impedances [64], as is shown in fig. 2.15 since $B = (AD - 1)/C$.

$$Z_{series} = \frac{A - 1}{C} = \frac{D - 1}{C} \tag{2.51}$$

$$Z_{shunt} = \frac{1}{C} \tag{2.52}$$

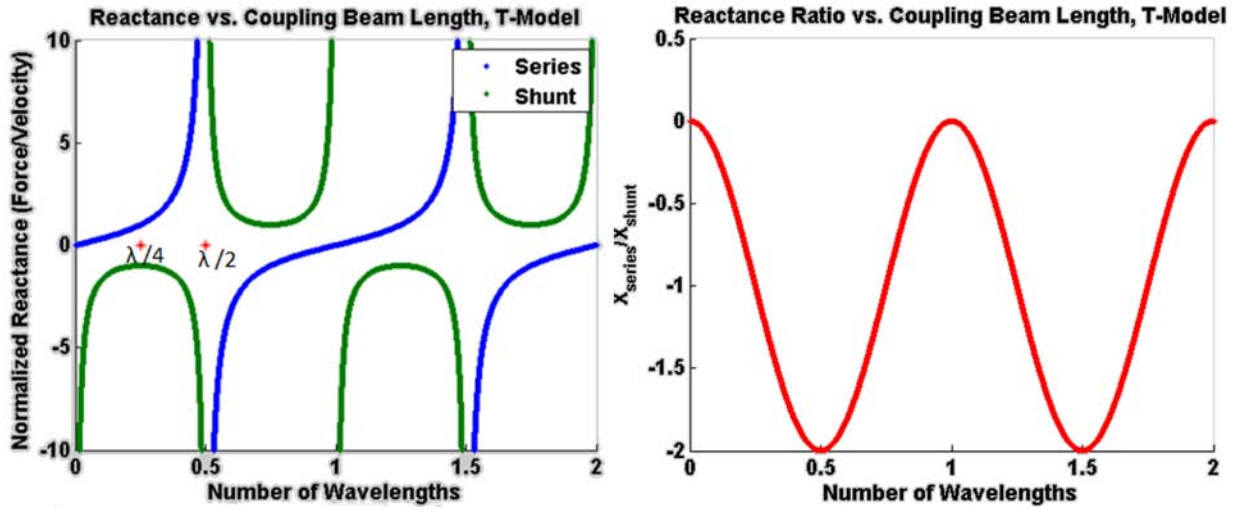

Figure 2.16: Normalized series and shunt impedance magnitudes for the T-network extensional coupling beam model as a function of beam length.

One finds that for the extensional coupling beam model of fig. 2.15, the impedances Z_{series} and Z_{shunt} are given by:

$$Z_{series} = \frac{\cos(\alpha l_c) - 1}{jZ_0 \sin(\alpha l_c)} = \frac{j \tan\left(\frac{\alpha l_c}{2}\right)}{Z_0} = \frac{j \tan\left(\frac{\pi l_c}{\lambda_a}\right)}{Z_0} = \frac{j \tan\left(\frac{\pi l_c f}{\sqrt{E/\rho}}\right)}{Z_0} \tag{2.53}$$

$$Z_{shunt} = \frac{1}{jZ_0 \sin \alpha l_c} = \frac{1}{jZ_0 \sin\left(\frac{2\pi l_c}{\lambda_a}\right)} = \frac{1}{jZ_0 \sin\left(\frac{2\pi l_c f}{\sqrt{E/\rho}}\right)} \tag{2.54}$$

Writing out these expressions in terms of fundamental variables,

$$Z_{series} = jh_c w_c \sqrt{E\rho} \tan\left(\frac{\pi l_c f}{\sqrt{E/\rho}}\right) \tag{2.55}$$

$$Z_{shunt} = -jh_c w_c \sqrt{E\rho} \csc\left(\frac{2\pi l_c f}{\sqrt{E/\rho}}\right) \tag{2.56}$$

To illustrate how the relative magnitudes of the series and shunt impedances of fig. 2.15 change with respect to beam length, fig. 2.16 presents plots of the normalized series and shunt reactances of the T-model for the coupling beam with respect to wave number. The ratio of the impedances is also plotted to show the important ratio values of 0, -1, and -2, respectively, that correspond to special lengths of couplers.

Using equation-defined one-port impedance elements allows for general coupling beam modeling that works over a broad range of frequencies and beam lengths. Using an equation-based ABCD matrix model for a coupling beam is an equally valid approach, in principle,

though it was found that simulations run in *Advanced Design System 2009* (ADS2009) using the T-network model worked with less difficulty.

Special lengths of mechanical couplers

At a frequency of interest, just like with any transmission line, one can create simplified equivalent two-port circuit models for coupling beams that have special lengths relative to the acoustic wavelength. Due to the periodicity of fig. 2.16, any special beam length condition that is satisfied for a given beam length will also be satisfied when one or more acoustic wavelengths is added its length.

$l_{beam} = n\lambda, n \in \mathbb{N}$

If the length of a coupling beam is either neglible, i.e., $l_{beam} << \lambda/10$, or is a positive multiple of one wavelength, then there are no significant phase or magnitude differences between the sinusoidal forces and velocities acting on opposite boundaries of the coupling beam. The ABCD matrix of eq. (2.48) simplifies to that of eq. (2.57):

$$\begin{bmatrix} F_1 \\ \dot{x}_1 \end{bmatrix} \approx \begin{bmatrix} 1 & 0 \\ 0 & 1 \end{bmatrix} \begin{bmatrix} F_2 \\ \dot{x}_2 \end{bmatrix} \tag{2.57}$$

The resulting equivalent two-port circuit model for a very short coupling beam is included in fig. 2.17. The two port network becomes a short-circuited through connection.

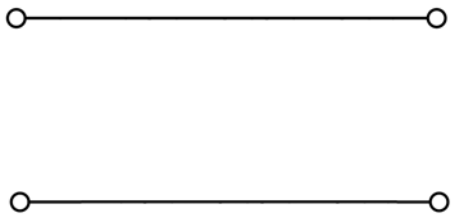

Figure 2.17: Equivalent two-port circuit model for a coupling beam of length $l_{beam} = n\lambda, n \in \mathbb{N}$

Couplers that are a whole number of wavelengths long have equal displacements and forces present at either side and are useful for making differential mechanical circuits having resonators that vibrate out of phase.

$l_{beam} = \frac{\lambda}{4} + n\lambda, n \in \mathbb{N}$

If the length of a coupling beam is one quarter-wavelength, the coupling beam can be used for coupling matched resonators, i.e., those having identical resonant frequencies, together to make a narrowband filter. Conveniently, the characteristic mobility Z_0, and thus width

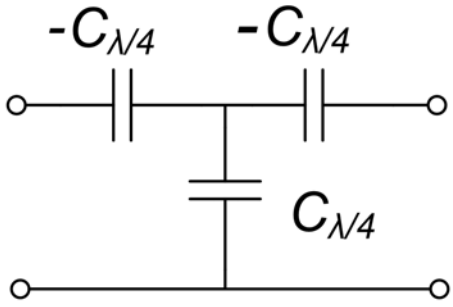

Figure 2.18: Equivalent two-port circuit model for a coupling beam of length $l_{beam} = \frac{\lambda}{4} + n\lambda, n \in \mathbb{N}$

of the coupling beam w_c, determines the coupler's stiffness. Furthermore, using $\lambda/4$-length coupling beams avoids unwanted shifts in modal frequencies in multi-resonator filters while still allowing resonator-to-resonator coupling to achieve mode splitting.

The ABCD matrix for the $\lambda/4$ coupler simplifies to that of eq. (2.58):

$$\begin{bmatrix} F_1 \\ \dot{x}_1 \end{bmatrix} = \begin{bmatrix} 0 & \frac{j}{Z_0} \\ jZ_0 & 0 \end{bmatrix} \begin{bmatrix} F_2 \\ \dot{x}_2 \end{bmatrix} = \begin{bmatrix} 0 & \left(sC_{\lambda/4}\right)^{-1} \\ sC_{\lambda/4} & 0 \end{bmatrix} \begin{bmatrix} F_2 \\ \dot{x}_2 \end{bmatrix} \tag{2.58}$$

Interestingly, this two-port network has the same two-port parameters as a gyrator, one of the two types of transducers (the other being a transformer) discussed in ****. As shown in fig. 2.18, the $\lambda/4$-length coupler can be modeled as a T-network of capacitors. Here, the value of $C_\lambda/4$ is given by eq. (2.59):

$$C_{\lambda/4} = \frac{Z_0}{\omega} = \frac{1}{2\pi f h_c w_c \sqrt{E\rho}} \tag{2.59}$$

Just like for any gyrator, looking into one port of a $\lambda/4$-length coupler has the interesting property of presenting an inverted version of impedance of the load on the other side, which has implications for the input impedances and transfer functions for multi-resonator filters, as will be discussed in a latter section. The input impedance of the combined two-port network shown in fig. 2.19 of a $\lambda/4$-length coupler and a load impedance, Z_L, is given by:

$$Z_{in} = -\frac{1}{s^2 C_{\lambda/4}^2 Z_L} \tag{2.60}$$

This relation simplifies the input impedance calculation of cascaded $\lambda/4$-coupled resonators.

$l_{beam} = \frac{\lambda}{2} + n\lambda, n \in \mathbb{N}$

If the length of the mechanical coupler $l_{beam} = \frac{\lambda}{2}$, the forces and velocities at the opposite ends of the coupler are equal in magnitude and opposite in phase. Half-wavelength

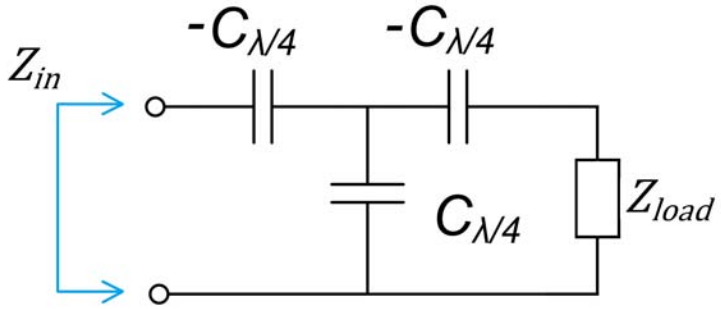

Figure 2.19: Equivalent impedance seen at the opposite side of a $\lambda/4$ coupling beam.

couplers are useful for building arrays of fundamental resonators vibrating in phase as a single composite resonator. The ABCD matrix for the $\lambda/2$-length coupler simplifies to that of eq. (2.61):

$$\begin{bmatrix} F_1 \\ \dot{x}_1 \end{bmatrix} = \begin{bmatrix} -1 & 0 \\ 0 & -1 \end{bmatrix} \begin{bmatrix} F_2 \\ \dot{x}_2 \end{bmatrix} \tag{2.61}$$

It's possible to again use the T-network capacitor model as shown in fig. 2.20, however, the capacitor values must become vanishingly small. As $l_{beam} \to \frac{\lambda}{2}, C_{\lambda/2} \to 0$.

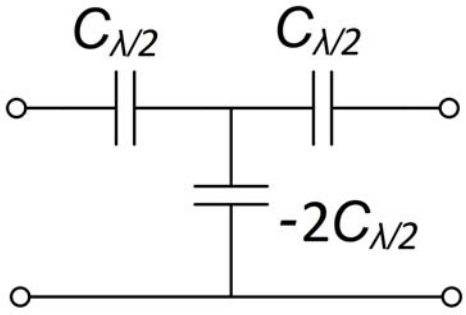

Figure 2.20: Equivalent two-port circuit model for a coupling beam of length $l_{beam} < \frac{\lambda}{2} + n\lambda, n \in \mathbb{N}$

For simulation purposes, the value chosen for $C_{\lambda/2}$ is valid as long is it is several orders of magnitude smaller than the capacitances of the resonators that are being coupled.

$l_{beam} = \frac{3\lambda}{4} + n\lambda, n \in \mathbb{N}$

Lastly, if the length of a coupling beam is three quarters of one wavelength, the coupling beam essentially behaves the same as a $\lambda/4$-length coupler, but the polarities on all of the capacitances change. In other words, the capacitors of fig. 2.18 are changed according to the following substitution:

$$C_{3\lambda/4} = -C_{\lambda/4} \tag{2.62}$$

The input impedance result of eq. (2.60) is unchanged when substituting $l_{beam} = 3\lambda/4$ for $l_{beam} = \lambda/4$.

Chapter 3

AlN Contour Mode Disk Resonators with Unattached Electrodes

To reduce the power consumption and improve the sensitivity of ultra low power wireless sensor networks, an RF MEMS resonator technology possessing very high Q, strong electromechanical coupling C_x/C_0 and low motional resistance R_x is of great interest for frequency synthesizer and RF filter components. It is also highly desirable to allow for multiple operating frequencies on the same chip. The resonance frequencies of "contour mode" resonators are set by lateral dimensions– thus they have CAD-definable resonance frequencies. A MEMS technology possessing all of these favorable properties may enable transformative improvements in low power integration for wireless transceivers.

In this chapter, we report our work to improve the performance of contour mode resonators made from AlN by spacing the electrodes from the device. First, we introduce capacitive-piezoelectric transduction as a means to improve the Q's of piezoelectric contour mode resonators. In particular, we focus on the optimization and modeling of radial contour mode disks utilizing capacitive-piezoelectric transduction. With an optimizing single disk resonator, multiple single disk devices may then be electrically connected in parallel and mechanically coupled to vibrate synchronously. Such disk arrays offer reduced motional resistance, increased power handling, and improved manufacturing precision for frequency.

3.1 Introduction to Capacitive-Piezoelectric Transduction

Capacitive-piezoelectric electromechanical transduction is a hybrid of two transduction mechanisms. To provide background on how it works, it is useful to review the two transduction mechanisms for micromechanical resonators on which it is based.

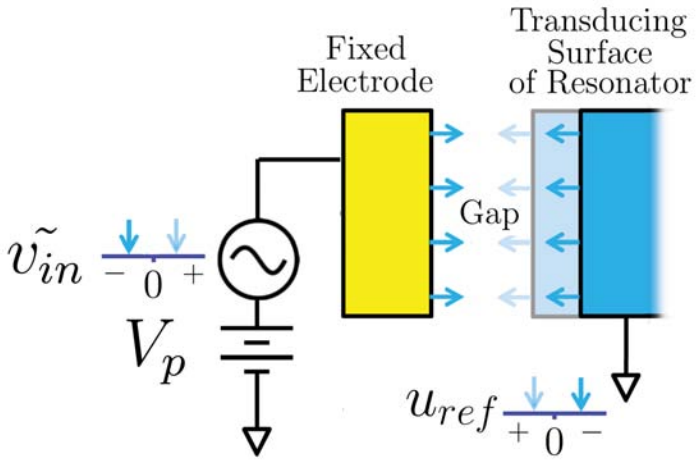

Figure 3.1: A conceptual diagram of capacitive transduction. An oscillating voltage drop across a capacitor has an associated time harmonic surface force on the transducing surface of a resonator.

Two Common Methods for MEMS Transduction

Electromechanical transduction of MEMS resonators provides a means for both exciting and detecting mechanical motion (or deformation) electrically. Capacitive and piezoelectric transduction methods, two common ways to provide electromechanical coupling, are compared to describe the advantages and shortcomings of each technology.

Capacitive Transduction

Included in fig. 3.1 is an illustration of a micro-mechanical resonator utilizing biased capacitive-gap transduction, here referred to simply as *capacitive* transduction, where a DC polarizing voltage, V_p, is superimposed with an AC input voltage, $\tilde{v_{in}}$, to generate an AC modal force $\tilde{F}$ having the same frequency as the excitation $\tilde{v_{in}}$ and having the following magnitude:

$$\tilde{F} = V_p \tilde{v_{in}} \frac{\mathrm{d}C}{\mathrm{d}u_{ref}} \tag{3.1}$$

In eq. (3.1), $\frac{\mathrm{d}C}{\mathrm{d}u_{ref}}$ represents the spatial derivative of transducer capacitance C with respect to modal displacement of a reference point u_{ref}. Note that v_{in} and u_{ref} are drawn as being in phase, which is applicable to frequencies far below resonance. At resonance, v_{in} is instead in phase with modal velocity $\dot{u}_{ref}$.

Capacitively transduced micromechanical resonators can achieve very high quality factors (Q's) ranging from 10k to 100k+ at frequencies ranging from several kHz to several GHz. Such high Q's are attributable to several factors as discussed in Chapter 1. In particular,

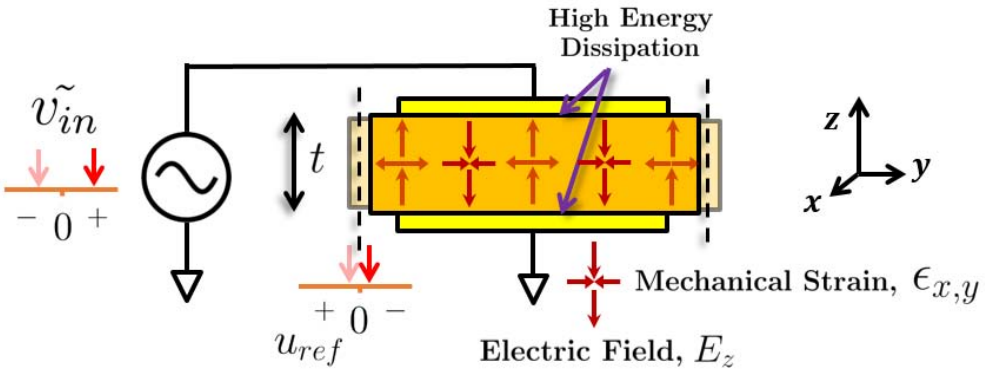

Figure 3.2: A conceptual diagram of piezoelectric transduction. Electric field due to voltage across an electrode pair surrounding a piezoelectric material has an associated strain throughout the body of the material.

we highlight two key factors for attaining high Q: (a) the separation of electrodes from the device and (b) the use of high-Q materials.

Though high Q's are achieved by capacitive devices, their electromechanical coupling coefficients, k_{eff}^2's are usually too small at very high frequencies to permit their use in practical applications. The motional impedances (R_x's) of capacitively transduced resonators are generally larger than desired. Typical R_x values for capacitively transduced MEMS resonators range from 1kΩ to several MΩ.

Although efforts to improve $\frac{C_x}{C_0}$ fand R_x have had various degrees of success, coupling can most easily be greatly improved through the use of piezoelectric transduction and material, but at the cost of reduced Q's.

Piezoelectric Transduction

Included in fig. 3.2 is an illustration of a piezoelectric transducer. A piezoelectric transducer consists of an electrode pair that electrically interacts with a structure made of piezoelectric material, such as quartz (crystalline SiO_2), ZnO, $LiNbO_3$, $Pb[Zr_xTi_{1-x}]O_3$, or AlN. Piezoelectricity is a material property existing for some crystal structures that essentially manifests itself as a constant of proportionality between strain and electric field. For a laterally vibrating resonator, the transverse (x,y) strain generated by a vertically oriented AC excitation voltage, $\tilde{v_{in}}$, across a piezoelectric film of thickness t and having a piezoelectric coefficient of e_{31} has the following magnitude:

$$\tilde{\epsilon_{x,y}} = \frac{\tilde{v_{in}} e_{31}}{t} \tag{3.2}$$

Most piezoelectric resonators have their electrodes directly attached to the piezoelectric material for maximum coupling and ease of fabrication. It is notable that the piezoelectric's attached electrodes are generally made from metal materials which are inherently lossier than

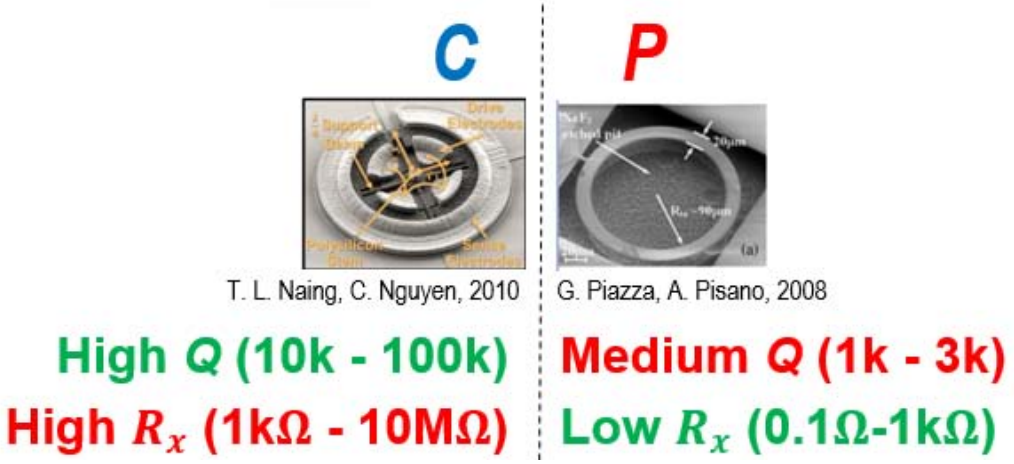

Figure 3.3: Comparative performance summary of capacitively- and piezoelectrically- transduced micromechanical resonators at 100 MHz to 3 GHz. High Q and low R_x are desired.

the piezoelectric material itself. Metals typically generate excessive losses via thermo-elastic damping (TED) and Akhiezer damping, and thus exhibit low Q's. Thus, an electroded structure can have a lower Q-factor than its electrodeless counterpart, due to energy sharing alone, with a metal structure. Other theory suggests that friction at the interface between the metal and piezoelectric films results is to blame for significant energy loss and leads to degraded Q-factors. Regardless of the true culprit, electrodeless AlN resonators have been shown to achieve higher Q's than electroded AlN resonators [65]. The Q's of piezoelectric VHF and UHF resonators are typically limited to several thousand.

Comparitive Summary

To compare the performance of capacitively- and piezoelectrically- transduced micromechanical resonators, fig. 3.3 summarizes the strengths and weaknesses of each technology over frequencies ranging from 100 MHz to 3 GHz and includes SEMs of representative devices. Since both high Q and strong electromechanical coupling (high C_x/C_0 and low R_x) are desired, designers are not fully satisfied with either technology.

Piezoelectric Resonators with Non-Contacting Electrodes

By separating the electrodes from a piezoelectric device, one can combine the strengths of both capacitive and piezoelectric technologies. Figure 3.4 succinctly illustrates "capacitively-piezoelectric" transduction, whereby detaching the transduction electrodes of a piezoelectric resonator and spacing them in close proximity allows for higher Q's while maintaining low R_x. At any non-zero spacing distance, the effect of higher Q is attained, due to the elimination of both electrode interface losses and acoustic damping of the electrodes. Additionally, the electrodes of a capacitive piezo resonator can be thickened to reduce series resistance compared to

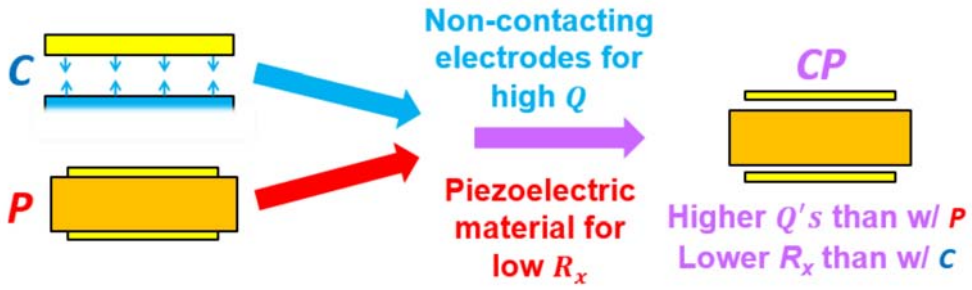

Figure 3.4: A conceptual diagram of capacitive-piezoelectric transduction.

an attached electrode counterpart without any performance penalties, further increasing Q. What's more, electromechanical coupling can in fact be higher for such devices if the gaps are small enough, due to the absence of any unwanted vibration in non-transducing electrodes. For non-negligible gap sizes, however, there is a reduction in electromechanical coupling. For applications such as narrowband filtering, the ability to tradeoff electromechanical coupling for higher Q is desirable. In any case, capacitive-piezoelectric technology should allow for higher $Q \cdot k_{eff}^2$ figures of merit than comparable attached electrode counterparts.

Previous Work

The first known demonstration of a piezoelectric resonator with detached, closely spaced electrodes was made by R. Besson in 1977 [66] in Besançon, France. In the paper, 5 MHz electrodeless hemispherical quartz resonators, called "B.V.A." resonators, were demonstrated having Q's of 3 million and aging stabilities of ≈8 ppb per day. As predicted, the detached electrodes were shown to offer exceptional performance in quartz.

More recently at UC Berkeley, Hung and Nguyen fabricated electrodeless piezoelectric resonators, called "capacitive-piezoelectric" resonators due to the introduced capacitive gaps, with much higher frequencies on-chip using AlN as the piezoelectric material. For example, in 2010, a 1.2 GHz ring resonator with a Q of 3.1k and a motional resistnace of 889Ω was demonstrated [67]. Calculations give a k_{eff}^2 value of 0.3% for this resonator [68]. A second device by Hung was demonstrated with a much higher Q of 12,000 using a wine-glass mode shape, albeit at a lower frequency of 50 MHz [69]. Nonetheless, this high Q value proved the efficacy of capacitive-piezoelectric transduction for achieving high-Q. Lastly, in 2013, Yen and Nguyen demonstrated the first capacitive-piezo Lamb Wave Resonator (LWR) at 1 GHz with an improved UHF Q of 5,000 [70], further cementing the idea that capacitive-piezo transduction offers strong benefits by exceeding the Q's of FBARs.

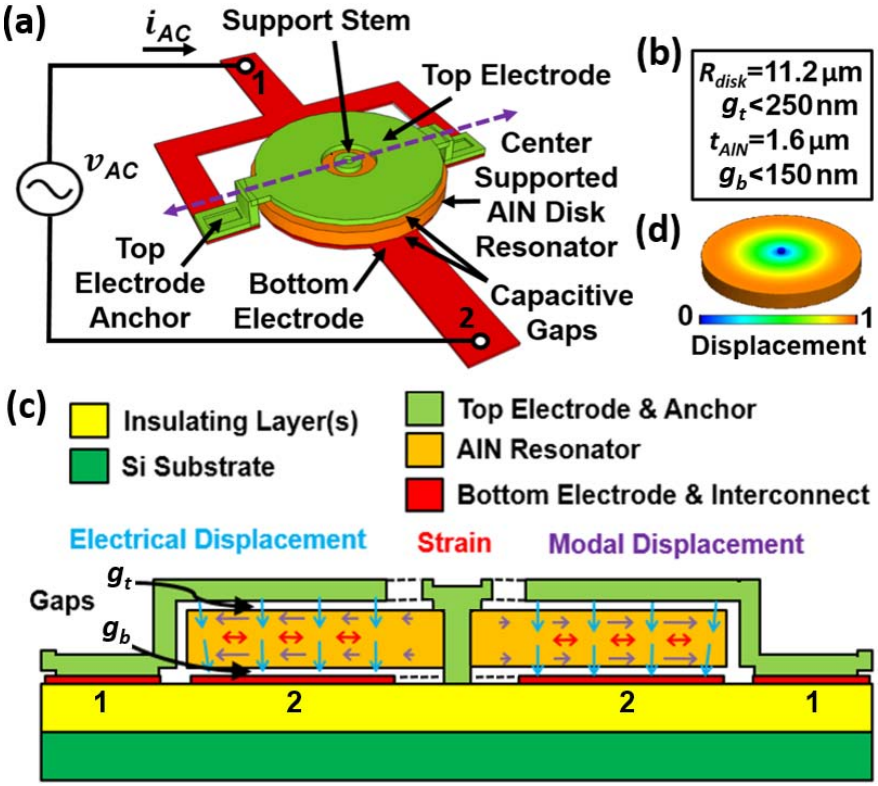

Figure 3.5: (a) Illustration of a capacitive-piezoelectric radial contour mode unit disk resonator and its essential parts. (b) Typical dimensions for a 300 MHz device. (c) Device cross section. (d) First radial contour mode shape.

3.2 Capacitive-Piezoelectric Radial Contour Mode Disk Resonators

First introduced in [71], the radial contour mode AlN capacitive piezoelectric disk resonator has a central role in this thesis project. Capacitive-piezo disk resonators possess several desirable properties: high Q, disk radius dependent resonance frequency, spurious mode suppression, amenability to size scaling through arraying, and additional capabilities enabled by voltage controlled electrode actuation as will be discussed in Ch. 4.

Figure 3.5 presents the structure and operating principles for a capacitive-piezo disk resonator via (a) a perspective view illustration of a radial contour mode disk resonator and its essential parts; (b) a list of typical dimensions for a 300 MHz disk; (c) a device cross section; and (d) the disk's mode shape of radial displacement. At the core of the device is a centrally-supported piezoelectric disk made from aluminum nitride. The capacitive-piezoelectric transducer utilizes capacitive gaps g_b and g_t below and atop the piezoelectric resonator, as shown in the cross section of fig. 3.5(c). Through detaching the conductive electrodes from the resonator and spacing them in very close proximity, one avoids undue

vibration in the electrodes and frictional energy dissipation at the AlN-electrode interface, resulting in potentially higher Q than in an attached electrode device. The piezoelectric effect provides coupling between vertical electric field and lateral mechanical strain. Thus, when a voltage is applied, the device displaces radially. The top electrode layer connects to the bottom interconnect layer through a supporting structure around the disk which is enabled through the use of a conformal deposition of the top electrode material. Here, CVD doped polysilicon is used, but a CVD metal film might be utilized in future renditions for improved electrical conductivity and lower deposition temperature. During operation, an electric field due to an ac voltage applied across top and bottom electrodes induces strain in the piezoelectric disk, which, for an electrical signal at the resonator's natural frequency of vibration, excites the device into resonance.

3.3 Radial Contour Mode Eigenfrequency and Mode Shape

As an alternative to using finite element analysis, to compute the modal frequency for a radial mode disk resonator, one can more simply calculate solutions of a frequency equation as described in [72]. To calculate the first radial contour modal frequency, one seeks to find the smallest value of f satisfying eq. (3.3). Higher order radial contour modes correspond to larger values of f that also satisfy eq. (3.3).

$$\mathfrak{J}_0\left(\frac{\zeta}{\xi}(f)\right) = \frac{\zeta}{\xi}(f)\frac{J_0(\frac{\zeta}{\xi}(f))}{J_1(\frac{\zeta}{\xi}(f))} = 1-\nu \tag{3.3}$$

Here, $\mathfrak{J}_0(x)$ is a modified bessel quotient of the 0^{th} order, as defined in [72]. $J_n(x)$ represents a Bessel function of the first kind of order n. The function $\frac{\zeta}{\xi}(f)$ is defined as:

$$\frac{\zeta}{\xi}(f) = 2\pi f R\sqrt{\frac{\rho(1-\nu^2)}{E}} \tag{3.4}$$

By solving the equation using Young's modulus $E = 345\,\mathrm{GPa}$, Poisson's ratio $\nu = 0.22$, mass density $\rho = 3,260\,\mathrm{kg/m^2}$, and disk radius $R = 11.18\,\mu\mathrm{m}$, the first natural frequency of the resonator is calculated to be 299.97 MHz. For AlN disk resonators of different radii, the modal frequency of interest as a function of radius R is given by:

$$f_0(R) = \frac{11.18\,\mu\mathrm{m}}{R\cdot(300.0\,\mathrm{MHz})} \tag{3.5}$$

Here, just like for all contour mode resonators, the resonance frequency does not depend on the AlN's thickness, but rather depends purely on lateral dimensions, thus eliminating film thickness nonuniformity over a wafer as a source of manufactured frequency error.

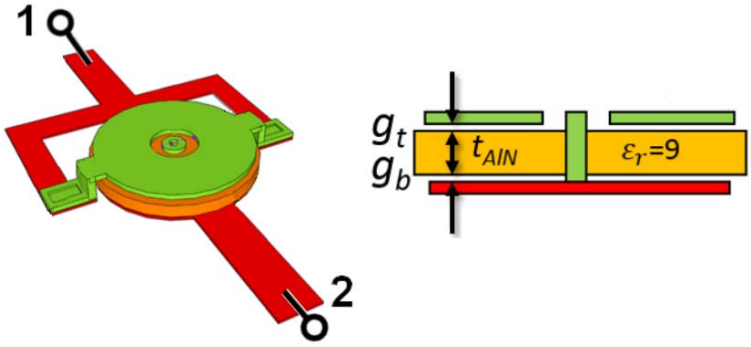

Figure 3.6: A capacitive piezoelectric disk resonator and its cross section, with capacitive gaps g_t and g_b highlighted.

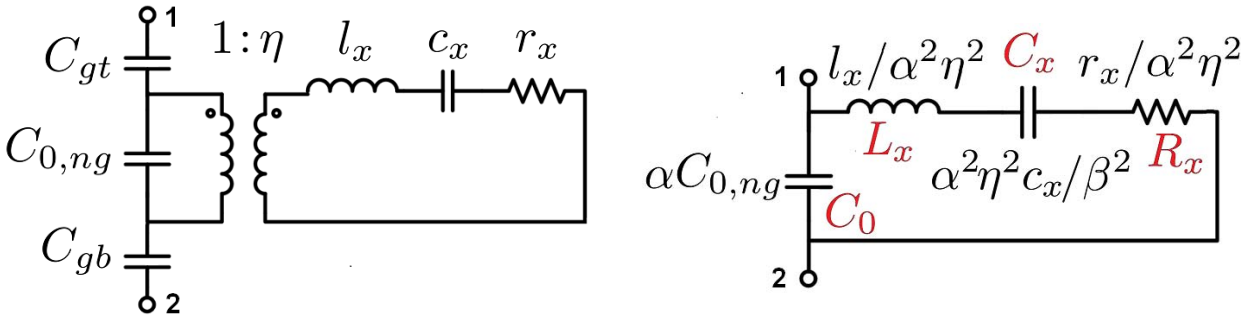

(a) Electromechanical circuit for a capacitive-piezo resonator

(b) Equivalent Butterworth Van Dyke (BVD) circuit

Figure 3.7: Equivalent models for a capacitive-piezo resonator.

The mode shape for the radial contour mode has no tangential component, and consists purely of radial displacement, $u_R(r)$. Up to a constant of proportionality, A, the mode shape as a function of position (r, θ) in polar coordinates is given by:

$$\vec{u}(r,\theta) = u_r(r)\hat{r} = AJ_1\left(2\pi f r\sqrt{\frac{\rho(1-\nu^2)}{E}}\right)\hat{r} \tag{3.6}$$

Where $\hat{r}$ is a unit vector in the radial direction.

3.4 Disk Resonator Circuit Model

A capacitive piezo resonator, such as the device illustrated in fig. 3.6 alongside its cross section, may be modeled using a two terminal equivalent circuit.

Figure 4.8 presents two equivalent circuit models for a capacitive-piezo resonator. These are general capacitive-piezo circuit models which are not exclusively applicable to disk resonators. First, in fig. 3.7a, sandwiched between the two gap capacitors, C_{gt} and C_{gb}, is an

electromechanical representation of an AlN resonator, consisting of resonator capacitance $C_{0,ng}$ ($_{ng}$ denotes "no gaps"); an electromechanical transformer with transduction factor η; and mass, inverse stiffness, and damping elements l_x, c_x, and r_x, respectively. The circuit of fig. 3.7a is behaviorally equivalent to the simpler circuit of fig. 3.7b having Butterworth Van Dyke (BVD) circuit component values, C_0, L_x, C_x, and R_x. To account for the changes introduced by capacitive gaps, two factors α and β are introduced to modify the component values; α is the factor by which capacitive voltage division affects coupling into the resonator while β is a resonance frequency shift factor.

Electromechanical Model Component Values

We first present expressions for the components of fig. 3.7a. The electrical capacitance $C_{0,ng}$ between the top and bottom surfaces of the piezoelectric is given by:

$$C_{0,ng} = \frac{A_e \varepsilon_0 \varepsilon_{r,AlN}}{t_{AlN}} \tag{3.7}$$

A_e in eq. (3.7) represents the parallel plate area of one of the electrodes forming a transducer around the resonator. It may be desirable for A_e to act as an effective area, slightly greater than the nominal area, to account for fringing fields. The electrical permittivity of the AlN film is the product of the free space permittivity $\varepsilon_0 = 8.85 \times 10^{-12}$F/m and the z-directed relative permittivity of AlN, $\varepsilon_{r,AlN} = 9$. Piezoelectric film thickness is represented by t_{AlN}.

As fig. 3.7a shows, in series with the core piezoelectric resonator are two capacitors, denoted as C_{gt} and C_{gb}, atop and below the resonator, respectively. These capacitances depend on the top and bottom gap sizes, g_t and g_b, and combine to form a single equivalent series capacitor C_g:

$$C_{gt} = \frac{A_e \epsilon_0}{g_t}; \quad C_{gb} = \frac{A_e \epsilon_0}{g_b}; \quad C_g = \frac{A_e \epsilon_0}{g_t + g_b} \tag{3.8}$$

The values for the three core mechanical components of the circuit model, l_x, c_x, and r_x, are determined by resonator geometry. Effective mass is calculated as a volume integration of density ρ normalized by the square of the magnitude of the normalized mode shape vector, which is expressed as $\Phi(r) = u_r(r)/u_r(R)$ for a radial contour mode disk. Here, $u_r(r)$, as defined in eq. (3.6), represents radial displacement magnitude as a function of radial distance from the disk's center, r. Displacement is maximum at the resonator's boundary for this mode shape, thus $u_r(R)$ is the max displacement used for normalization. For a disk resonator of radius R with a circularly symmetric mode shape, this volume integration may be most simply expressed as[1]:

[1]For non-circular or non-radially symmetric mode shapes, a more general expression for effective mass as a function of position $\vec{X}$ is:

$$l_x = m_r = \iiint \frac{\rho}{\|\vec{\Phi}(\vec{X})\|^2} \, \mathrm{d}x \, \mathrm{d}y \, \mathrm{d}z \tag{3.9}$$

$$l_x = m_r = 2\pi\rho t_{AlN} \int_0^R \frac{r}{\Phi(r)^2}\,\mathrm{d}r; \quad \Phi(r) = \frac{u_r(r)}{u_r(R)} \tag{3.10}$$

A resonator's compliance $c_x = 1/k_r$ may be defined in terms of angular resonance frequency $\omega_0 = 2\pi f_0$:

$$c_x = \frac{1}{k_r} = \frac{1}{\omega_0^2 m_r} \tag{3.11}$$

The following expression is used for the damping r_x, where Q is the quality factor of the resonator, typically an empirically determined value:

$$r_x = \frac{\omega_0 m_r}{Q} = \frac{\sqrt{k_r m_r}}{Q} \tag{3.12}$$

Electromechanical transformer factor, η

The expression for the piezoelectric electromechanical transformer factor, η, assumes modal vibration. Here, η takes on three equivalent meanings. First, η is the modal force developed per unit input voltage across the piezoelectric resonator. Modal force is defined as the product of the modal stiffness k_r and maximum modal displacement magnitude, $u_r(R)$. Secondly, η is the ratio of electrical current to unit modal velocity in the transducer. Finally, η is also equal to the ratio of displaced charge per unit modal displacement. Each of these equivalent meanings carries units of [C/m]. To develop an expression for η for a contour mode piezoelectric resonator, it is most straightforward to integrate the charge density developed over electrode area given a unit amount of modal displacement, which is proportional to the divergence of the mode shape. Since displacement at every point on the resonator is fully specified due to the mode shape, strain is also specified, and in turn, induced charge density is specified via the direct piezoelectric effect. The lateral strain at any point on the resonator in a given lateral direction is equal to the spatial derivative of displacement u.

$$\epsilon_x = \frac{\partial u_x}{\partial x}; \quad \epsilon_y = \frac{\partial u_y}{\partial y} \tag{3.13}$$

It has been shown that for a class 6mm crystal dielectric piezoelectric material such as AlN, perpendicular lateral strains ϵ_x and ϵ_y sum together, in a laterally isotropic manner, to create a z-axis oriented induced charge density [73]. The e_{31} coefficient, $e_{31} = 0.7$ Cm^{-2}, captures this, as it represents the areal charge density developed for a unit amount of net lateral strain. η can thus be expressed as follows, using a polar coordinate system, where Q_d represents induced (displaced) electrode charge, $D_z(r,\theta)$ is the z-directed electric displacement field, A_e is the region over which transduction electrodes exist for the resonator, and $\nabla\cdot$ represents the mathematical divergence operator in the xy-plane:

$$\eta = \frac{Q_d}{u_r(R)} = \frac{\iint_{A_e} D_z(r,\theta)\mathrm{d}A}{u_r(R)} = e_{31} \iint_{A_e} \frac{\nabla\cdot\vec{u}(r,\theta)}{u_r(R)}\mathrm{d}A \tag{3.14}$$

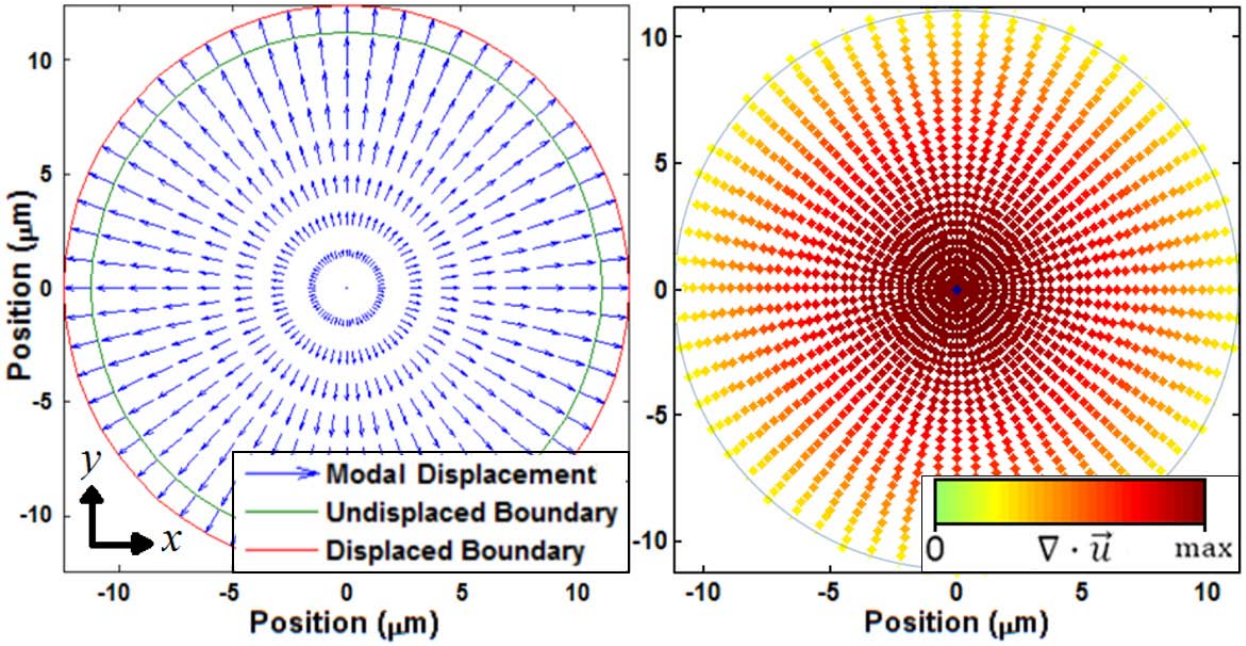

Figure 3.8: Left: Simulated 1st radial contour mode shape $\vec{u}(r,\theta)$ of an 11.2-μm-radius AlN disk at an eigenfrequency of 300 MHz. Right: Divergence of the mode shape $\nabla \cdot \vec{u}(r,\theta)$, of which an area integration over the domain of electrode coverage is performed to obtain η.

Since $\nabla \cdot \vec{\Phi}(r)$ has no θ dependence, the expression for η in cylindrical coordinates simplifies to:

$$\eta = e_{31} \iint_{A_e} \left(\frac{\Phi(r)}{r} + \frac{\partial \Phi(r)}{\partial r} \right) r \mathrm{d}r\mathrm{d}\theta \tag{3.15}$$

As the divergence is positive everywhere within the first radial contour mode shape, it is not necessary to use multiple electrodes of opposite polarities to avoid net charge cancellation.

Using the mode shape of eq. (3.6), one may plot the lateral divergence of the modal displacement $\nabla \cdot \vec{u}$, which gauges the amount of local strain in the x and y directions. The divergence of the modal displacement describes how much localized transduction strength per unit area is available as a function of position on the resonator. The radial contour mode shape is plotted in fig. 3.8 alongside a color map plot of the divergence. The divergence of the modal displacement as a function of position, the e_{31} piezoelectric constant, and the electrode coverage directly determine the electromechanical transformer factor η of eq. (3.14). As fig. 3.8 shows, the center of the disk resonator is the most important transduction region per unit area for the first radial contour mode. To maximize η, and hence maximize C_x/C_0 and minimize R_x, electrode coverage should extend over as much of the resonator as possible.

BVD Model Component Values

To derive the capacitive-piezoelectric resonator's equivalent Butterworth Van-Dyke (BVD) circuit shown in fig. 3.7b, the impedance of a BVD circuit is equated to that of a gapless BVD circuit with an added series capacitance C_g (see eq. (3.8)). Through solving five equations for four unknowns [2], the BVD lumped components C_0, C_x, R_x, and L_x are found in terms of C_g, $R_{x,ng}$, $C_{0,ng}$, $C_{x,ng}$, and $L_{x,ng}$, where the subscript $_{ng}$ is appended to denote component values for a resonator with no gaps. As fig. 3.7b implies, the effect of C_g on the rest of the circuit can be accounted for through the use of two parameters, α and β:

$$\alpha = \frac{V_{AlN}}{V_{in}} = \frac{C_g}{C_g + C_{0,ng}} = \frac{t_{AlN}}{t_{AlN} + \epsilon_{r,AlN}(g_b + g_t)} \tag{3.16}$$

$$\beta = \sqrt{\frac{C_g + C_{0,ng} + c_x\eta^2}{C_g + C_{0,ng}}} = \sqrt{1 + \frac{C_{x,ng}}{C_g + C_{0,ng}}} \tag{3.17}$$

In terms of α, β, η, r_x, c_x, and l_x, the equivalent BVD parameters are as follows:

$$C_0 = \alpha C_{0,ng} \tag{3.18}$$

$$R_x = \frac{R_{x,ng}}{\alpha^2} = \frac{r_x}{\alpha^2\eta^2} \tag{3.19}$$

$$L_x = \frac{L_{x,ng}}{\alpha^2} = \frac{l_x}{\alpha^2\eta^2} \tag{3.20}$$

$$C_x = \frac{\alpha^2 C_{x,ng}}{\beta^2} = \frac{\alpha^2\eta^2 c_x}{\beta^2} \tag{3.21}$$

It is desirable to reduce motional resistance R_x and to maximize the electromechanical coupling factor C_x/C_0. To do so, α and η must be maximized.

Capacitive-Piezo Voltage Coupling Efficiency, α

In eq. (5.3), α is a factor ranging from 0 to 1 that gauges how effectively a voltage present across the electrodes is coupled into the piezoelectric resonator due to capacitive division. Figure 3.9 presents a plot of α vs. total gap size, i.e. g_b+g_t, for a 1.6-μm-thick AlN resonator. As a useful reference point, $\alpha \approx 0.43$ for a resonator using a chosen AlN thickness t_{AlN} of 1,600 nm with 120 nm top and bottom gap sizes.

Notably, AlN is a suitable material among piezoelectrics for capacitive-piezoelectric transduction, since its α factor is relatively large compared to that of other materials due to its relatively small relative permittivity ϵ_r of 9.1. For example, lead zirconate titanate (PZT) has a dielectric constant on the order of 1,000. For such a strong piezoelectric, α would equal only .016 even for an aggressive g_{total} of 100 nm, thus degrading motional resistance by a factor of 3900× compared to an attached electrode device.

[2] Equate the impedances of the circuits of fig. 3.7a and fig. 3.7b as a function of s and cross multiply. Obtain 5 equations by equating coefficients of $s^n, -1 \leq n \leq 3$, on the left- and right-hand sides. Solve for C_0, C_x, R_x, and L_x as a function of C_g, $R_{x,ng}$, $C_{x,ng}$, $L_{x,ng}$, and $C_{0,ng}$.

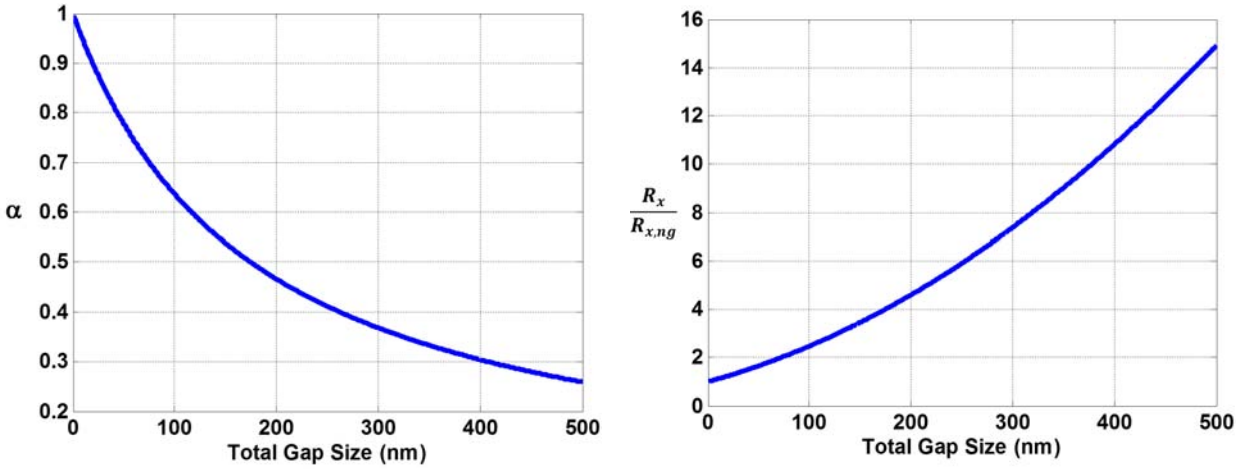

(a) α vs. total gap size

(b) Normalized R_x vs total gap size

Figure 3.9: α and $R_x/R_{x,ng}$ vs. $g_{total} = g_b + g_t$, for a 1,600-nm thick AlN resonator

Capacitive-Piezo Resonance Frequency Tuning Factor, β

In the motional capacitor of fig. 3.7b, β of eq. (5.4) and eq. (3.21) is the factor by which series resonance frequency f_s, i.e., the frequency of minimum impedance, is tuned in a capacitive piezo resonator. β ranges from 1 to $\sqrt{1+\frac{C_{x,ng}}{C_{0,ng}}}$ as a function of gap size. Solving the BVD circuit for the frequency of minimum impedance, f_s of a capacitive-piezo resonator is found as:

$$f_s = \frac{1}{2\pi}\sqrt{\frac{1}{L_x C_x}} = \frac{1}{2\pi}\sqrt{\frac{\beta^2}{L_{x,ng} C_{x,ng}}} = f_{s,ng}\beta \tag{3.22}$$

Thus with a gap, f_s takes on an intermediate value between $f_{s,ng}$ and $f_{p,ng}$. Series resonance frequency is positively correlated with gap size in a capacitive-piezo resonator, and has been shown to be tunable via voltage controlled electrode pull down by at least 1,500 ppm [74]. Parallel resonance frequency f_p, the frequency of maximum impedance, is found as:

$$f_p = f_s\sqrt{1+\frac{C_x}{C_0}} = f_{s,ng}\sqrt{1+\frac{C_{x,ng}}{C_{0,ng}}} = f_{p,ng} \tag{3.23}$$

As eq. (3.23) shows, the parallel resonance frequency does not change as a function of capacitive gap size.

Electromechanical Coupling

The electromechanical coupling, $k^2_{eff} = \frac{C_x}{C_0+C_x} \approx \frac{C_x}{C_0}$ of this circuit, a performance metric gauging both maximum fractional resonator tuning range and fractional filter bandwidth,

derives from the relationship between f_p and f_s as follows:

$$f_p = f_s\sqrt{1+\frac{C_x}{C_0}} \rightarrow \frac{C_x}{C_0+C_x} = \frac{f_p^2 - f_s^2}{f_p^2} = k_{eff}^2 \tag{3.24}$$

To first order, introducing capacitive gaps degrades k_{eff}^2 in the following manner:

$$k_{eff}^2 = k_{eff,ng}^2\alpha \tag{3.25}$$

3.5 MATLAB Computation of Resonator Parameters

Computer techniques were used to simulate the performance of capacitive piezo disk resonators. A capacitive piezoelectric radial contour mode capacitive piezo resonator simulator was implemented in MATLAB to do the following: (1) aid in the design of more complex systems such as arrays and filters; (2) verify the capacitive-piezo circuit model by matching to experimental data; (3) estimate dependencies of resonator performance metrics on design parameters; and (4) allow for quick computations. Starting from the following design parameters, it is possible to compute all the parameters of our circuit model.

- Material: AlN [E=345GPa, ρ=3260 kg/m^3, ν=0.22, e_{31}=0.7 C/m^2]
- $R_{disk} = 11.18\mu$m
- $Q = 8000$
- $t_{AlN} = 1.6\mu$m
- $g_{bottom} = g_{top} = 150$ nm
- Electrode coverage between $r_{min} = 3.0\mu$m and $r_{max} = 10.9\mu$m

The MATLAB simulator is used to calculate and predict such resonator quantities as r_x, c_x, l_x, η, R_x, C_x, L_x, C_0, C_g, α, β, k_{eff}^2, f_s, and f_p. Additionally, it can be used to plot simulated S_{21}, admittance, and impedance as a function of frequency; the mode shape; the divergence of the mode shape; the effect of gap reduction on resonance frequency, i.e., frequency tuning; and electrode pull-down as a function of voltage. The simulator accommodates arbitrary electrode coverage schemes.

The first steps in simulating this resonator are to compute the modal frequency and find the mode shape as a function of position. To do this for a radial mode disk resonator, one can implement a script to perform the necessary numerical calculations as described in [72], [75], and section 3.3. Note that Onoe uses the variables p, σ, and a to represent angular frequency, Poisson's ratio, and disk radius respectively, for which this thesis instead uses ω, ν, and R, respectively.

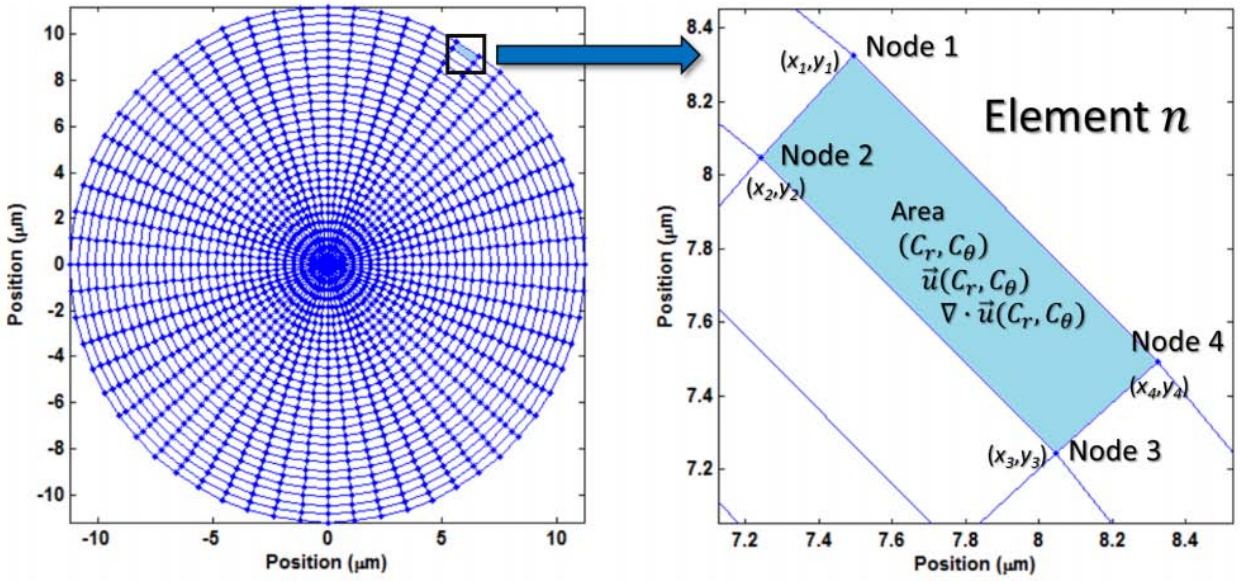

Figure 3.10: Disk resonator mesh for performing numerical integrations, $[N_r \times N_\theta] = [30 \times 60]$.

Radial Contour Mode Eigenfrequency Calculation

To find the modal frequencies, one must numerically solve eq. (3.3) for valid values of natural frequency f, where disk radius R, density ρ, Young's modulus E, and Poisson's ratio ν are specified. To calculate the first radial contour modal frequency, one seeks to find the first (smallest) value of f satisfying eq. (3.3). Higher order radial contour modes correspond to larger values of f that also satisfy eq. (3.3). Running the simulation, using $E = 345\,\text{GPa}$, $\nu = 0.22$, $\rho = 3,260\,\text{kg/m}^2$, and $R = 11.18\,\mu\text{m}$, the first natural frequency of the resonator is calculated to be 299.97 MHz.

1st Radial Contour Mode Shape Function Definition

Next, the mode shape as a function of position is found. The mode shape is given by eq. (3.6) and is plotted in fig. 3.8. To obtain a normalized mode shape which ranges in magnitude from 0 to 1, A is calibrated so that $u_r(R)$ equals 1.

Meshing of the Domain for Numerical Integrations

It is useful to set up a mesh over the domain to aid numerical integrations. To do this, the domain is broken up into a finite number of area elements, each of which is associated with four nodes defining the corners of the element. A connectivity matrix attaches to each element its associated four node numbers, while a second data structure keeps track of nodal coordinates for each node number. For each element, the centroid (C_R, C_{theta}) and area can be quickly calculated from the nodal coordinates. An example mesh is included in fig. 3.10,

where the domain is broken up into 1,800 elements. Included to the right of the mesh illustration in the same figure is a zoomed-in diagram of a single finite element to show its four nodes and to emphasize that element area, modal displacement and divergence are to be computed. An area integral approach is used, even though the radial contour mode has azimuthal symmetry, to also enable the simulation of compound radial modes such as the "wineglass" mode.

As shown in fig. 3.10, each element of the mesh consists of four sets of nodal coordinates, useful for calculating an element's centroid and differential area. Additionally, for each element, modal displacement $\vec{u}$ (as defined in eq. (3.6)) and divergence of $\vec{u}$ (as defined in eq. (3.26), assuming purely radial displacement) are calculated.

$$\nabla \cdot \vec{u_r}(r,\theta) = \frac{u_r}{r} + \frac{\partial u_r}{\partial r} \tag{3.26}$$

The derivative of eq. (3.26) is calculated numerically using a small value (e.g. 1nm) for δr.

$$\left.\frac{\partial u_r}{\partial r}\right|_{(r,\theta)} = \lim_{\delta r \to 0} \frac{u_r(r+\delta r,\theta) - u_r(r,\theta)}{\delta r} \tag{3.27}$$

Effective Mass Calculation

Effective mass is calculated by evaluating an equivalent area integral expression of eq. (3.10), where differential mass is normalized by displacement squared. The simulator uses the mesh defined in section 3.5 for sums over area. A sum is generated through iterating through all elements and dividing differential area by normalized displacement squared. The sum is then multiplied by film thickness and density to get m_r=l_x.

Electromechanical Transformer Coefficient Calculation

Calculating η requires integrating the divergence of the mode shape over the electroded area of the resonator. The divergence is a measure of how much the mode shape is spreading out at a location– stronger divergence leads to stronger transduction per unit area. A color plot of divergence (a scalar) as a function of position is included in fig. 3.11a. Since non-electroded area does not contribute to transduction, electroded area is distinguished from non-electroded area in the plot through the use of small x's. The uncoupled center of the disk is shown using small dots; this region is not summed over in computing η. For the radial contour mode disk, divergence is positive everywhere and strongest in the center. Thus, not capturing electrode area at the center area of the disk significantly reduces coupling.

Similarly to how effective mass is calculated, a sum is generated through iterating through all elements. Divergence of the mode shape times differential area is summed, but only for the electroded region(s). The sum is multiplied by e_{31} and normalized by u_{max} to get

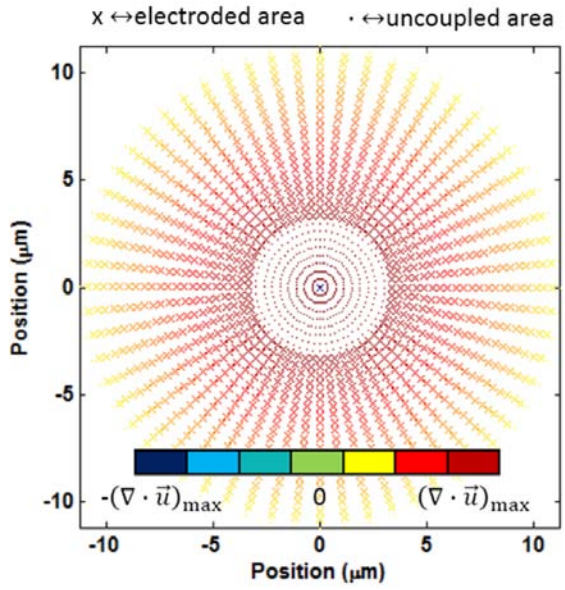

(a) Colored divergence of the mode shape plot for a radial contour mode disk resonator as a function of x and y.

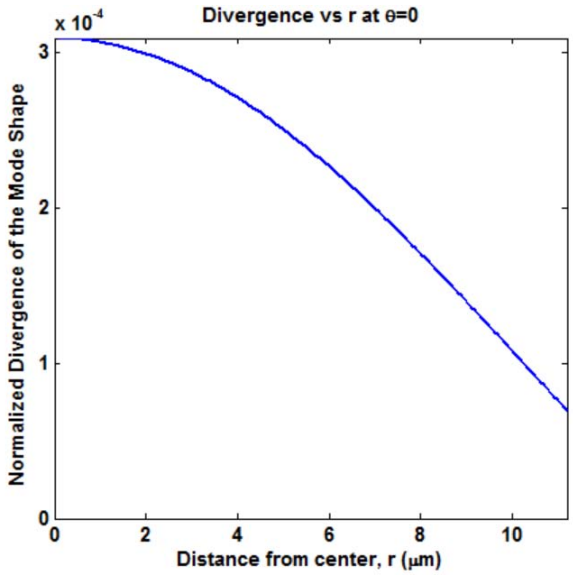

(b) Divergence of the mode shape vs. radius r for $\theta = 0$.

Figure 3.11: Plots of the divergence of the mode shape for a radial contour mode disk resonator. The strongest transduction occurs at the disk's center.

η. This simulation method offers the ability to predict η for different electrode coverage configurations, e.g., for $3.0\mu m \leq r \leq 10.9\mu m$.

Resonator Impedance and Admittance

Once the resonator parameters are known, impedance and admittance plots such as those included in fig. 3.12 can be generated. Such plots are useful for oscillator design, for example in determining the frequency of oscillation for an amplifier circuit with a complex input impedance.

Simulated S_{21} Response

To simulate the transmission in a two-port S_{21} of the device, at each frequency the following transformation is applied:

$$S_{21}(f) = 20\log_{10}\left[\frac{2Z_0}{2Z_0 + Z_r(f)}\right] \tag{3.28}$$

The resulting transmission plot is very similar to the admittance plot when impedances are large compared to $2Z_0$. However, for motional resistances smaller than $10 \cdot 2Z_0$, significant

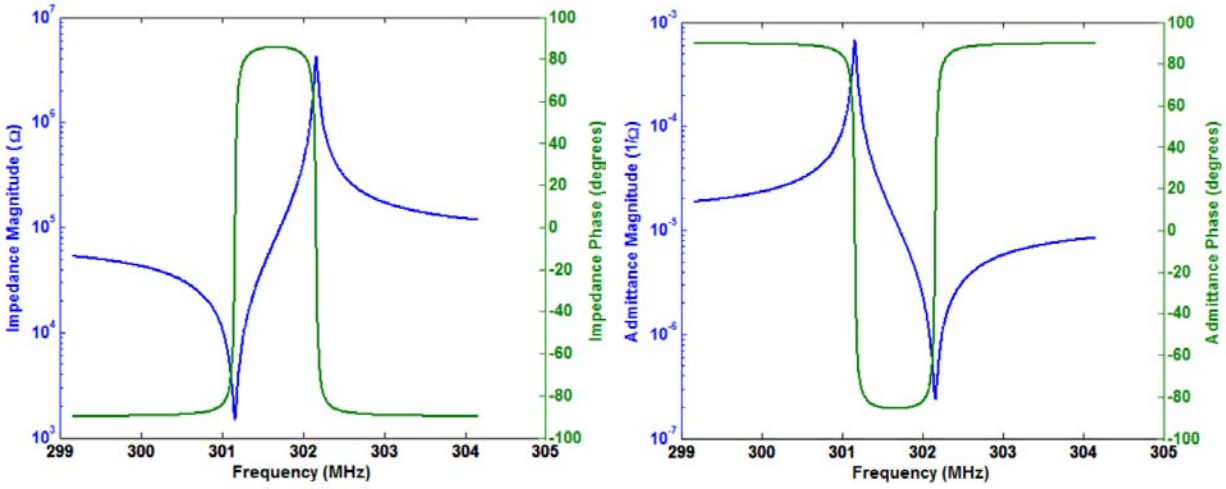

(a) Impedance vs. Frequency.

(b) Admittance vs. Frequency

Figure 3.12: Simulated plots of impedance and admittance vs. frequency for the 11.2 μm-radius AlN capacitive-piezo disk resonator. Magnitude is shown in blue, phase in green.

Q loading of the series resonance occurs. This creates (a) a widening of the magnitude peak as it approaches 0 dB and (b) a reduced slope in the phase transition.

3.6 Two-Port Characterization Method for Capacitive-Piezoelectric Resonators

The goal of our resonator characterization method is to accurately extract parameter values from measured data, including unloaded Q, unloaded motional resistance R_x, and electromechanical coupling $k_{eff}^2 = C_x/C_0$.

Measurement Setup

A Desert Cryogenics Lakeshore probe station is used to provide a vacuum environment (of $\approx 10^{-5}$ Torr) in which to characterize resonators. Reducing air damping is helpful for maximizing Q's of resonators with extremely small amounts of damping and particularly for ones operating at lower frequencies. However, vacuum operation is not as essential for our stiffer capacitive-piezo devices at UHF which have moderate amounts of intrinsic damping. At 300 MHz, vacuum increases Q's by about 10%.

Ground-Signal-Ground (GSG) probes are used to provide a 50Ω characteristic impedance transmission line all the way to the device under test. To move the measurement plane to the ends of the probes, i.e., eliminate any attenuation losses and phase shifts that the cables introduce, a full two port calibration is performed using a CS-5 calibration substrate. An

Agilent E5071B network analyzer is used to collect data. To collect and archive measurement data and perform analysis, MATLAB interfaces with the network analyzer via a GPIB link. Images of the GSG probes, the probe station, and network analyzer are included in fig. 3.13.

Rationale for Using Two Ports

To characterize capacitive piezoelectric resonators with impedances significantly larger than 100 Ω, a two-port transmission (S_{21}) measurement is performed, rather than a one-port S_{11} measurement. The reason for this is that a small parasitic capacitance can introduce significant error into a one port measurement when the device under test (DUT) has an impedance significantly larger than the port's characteristic impedance Z_0, whereas a two-port measurement still captures the proper impedance even when the same parasitic capacitance is shunted to ground. On the other hand, a one-port measurement is preferred for characterization of smaller impedances.

Parameter Extraction

Assuming that the resonator is represented by a two port network consisting of an impedance Z_r connecting ports 1 and 2, the measured transmission scattering parameter characteristic is dependant on the measured (loaded) resonator impedance Z_r' as follows:

$$S_{21}(f) = \frac{2Z_0}{2Z_0 + Z_r'(f)} \tag{3.29}$$

At series resonance (f_s), one can assume that the reactive impedances from C_x and L_x cancel out, leaving only the loaded motional resistance R_{xL}. The decibel expression for S_{21} at resonance is thus:

$$S_{21,dB}\big|_{f=f_s} = 20\log_{10}\left|\frac{2Z_0}{2Z_0 + R_{xL}}\right| \tag{3.30}$$

Loaded motional resistance can be calculated from the transmission peak height:

$$R_{xL} = 2Z_0\left(10^{-\left(S_{21,dB}\big|_{f=f_s}\right)/20} - 1\right) \tag{3.31}$$

Here, measured motional resistance R_{xL} is loaded by the input and output terminating impedances which degrade resonator Q. The loaded Q-factor Q_L is measured by dividing resonance frequency f_s by the 3dB bandwidth of the series resonance off of the frequency characteristic Δf_{3dB}.

$$Q_L = f_s/\Delta f_{3dB} \tag{3.32}$$

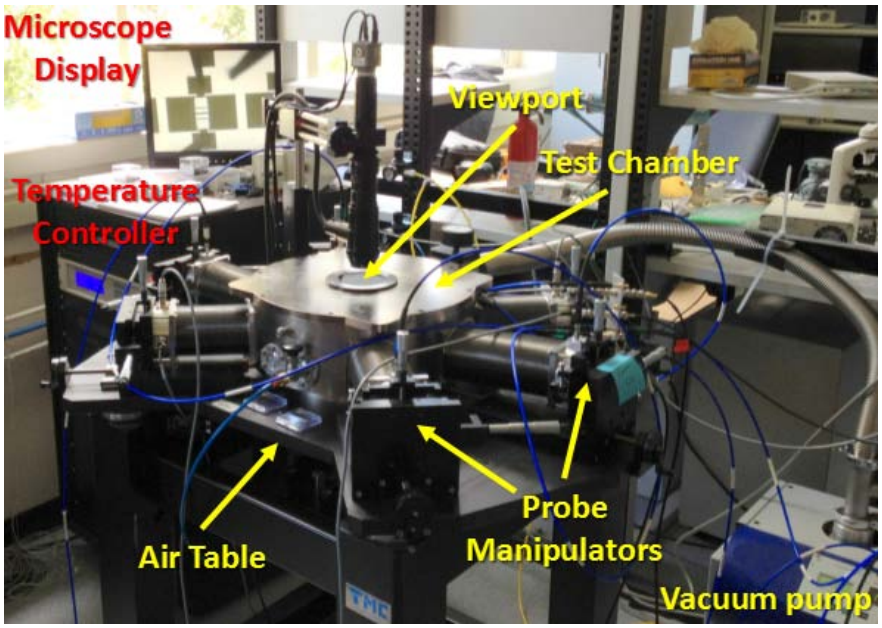

(a) Desert Cryogenics Lakeshore probe station.

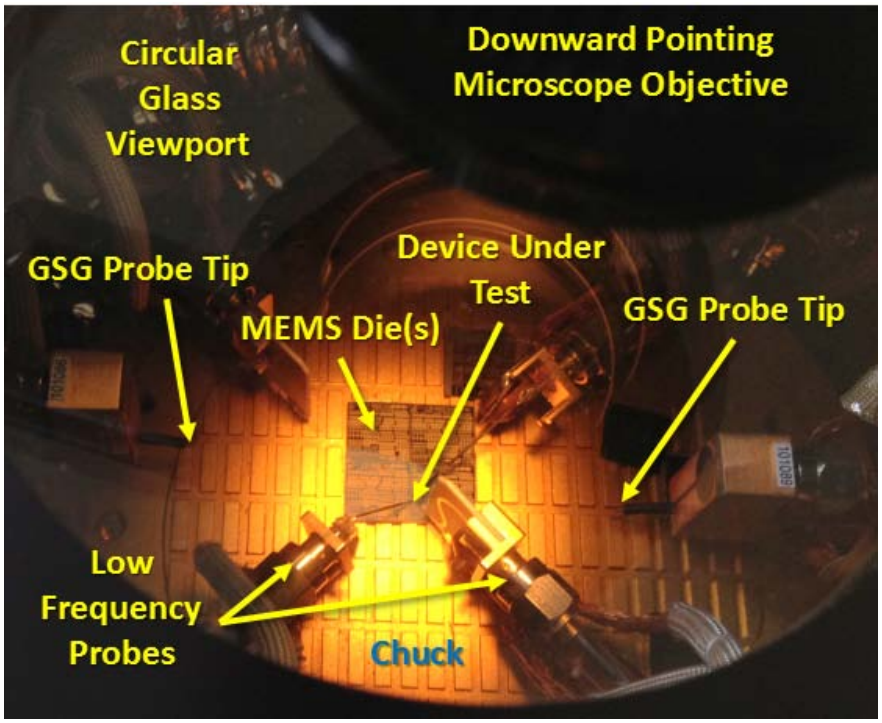

(b) View of a MEMS die with probes in place as seen through probe station's view port. The GSG probes, shown disengaged in this image, are used to characterize the capacitive-piezo resonators in this project. Low frequency probes are sometimes used for biasing.

Figure 3.13: Images of resonator characterization setup.

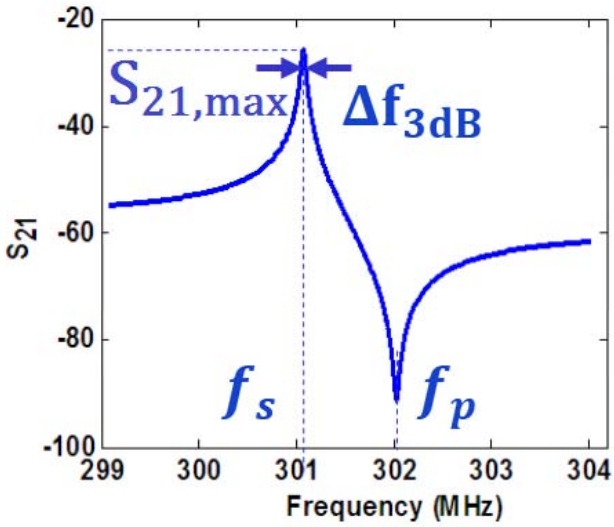

Figure 3.14: A two-port S_{21} magnitude measurement is used to extract Q, R_x, C_0, and k^2_{eff} for a capacitive piezo resonator.

Unloaded Q and R_x

The loading effect from the 50 Ω measurement ports is accounted for in the extraction of resonator Q and R_x.

$$Q = Q_L(1 + 2Z_0/R_{xL}) \tag{3.33}$$

$$R_x = \frac{R_{xL}Q_L}{Q} = \frac{R_{xL}}{1 + 2Z_0/R_{xL}} \tag{3.34}$$

For example, if a resonator with a Q of 10,000 and an R_x of 1000 Ω were measured using S_{21}, the network analyzer would give a loaded Q measurement of 9090 and one would measure a loaded motional resistance of 1,100 Ω based on the peak height. Using this correction method, the proper values are extracted.

k^2_{eff} Extraction

Electromechanical coupling $k^2_{eff} = C_x/C_0 = (f_p^2 - f_s^2)/f_p^2$ is measured according to the spacing of the series and parallel resonance frequencies, f_s and f_p, which are the frequencies at which maximum and minimum transmission occur in the measured S_{21} plot, respectively.

C_0 Extraction

The feedthrough capacitance C_0 is estimated using the off-resonance feedthrough level of S_{21}. For high frequencies and small capacitances, the following simple expression for the capacitance holds[3]:

[3]The expression for S_{21} is $\frac{2Z_0}{2Z_0+1/(j\omega C_0)}$

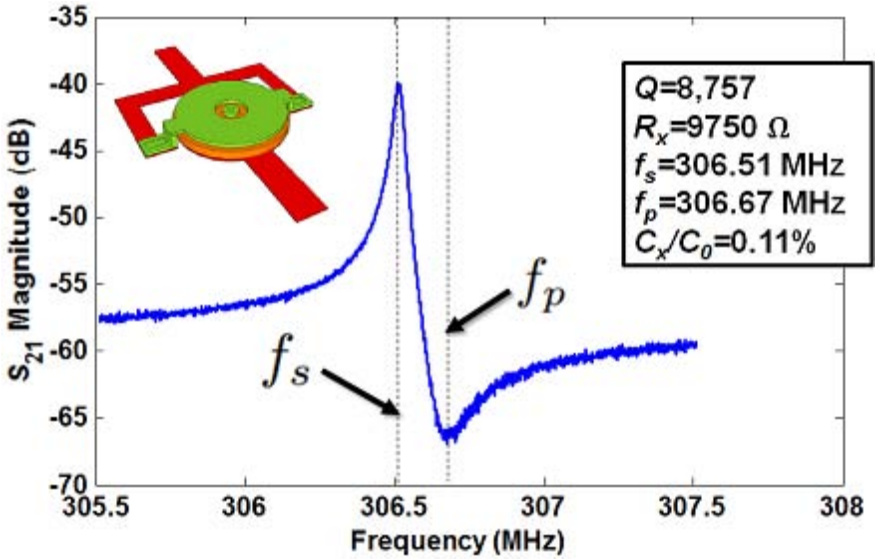

Figure 3.15: Frequency characteristic of a 300 MHz capacitive piezoelectric unit disk resonator with a 1.2 μm diameter stem and a Q of 8,757.

$$C_0 = \frac{10^{S_{21,dB}/20}}{2Z_0(2\pi f)} \tag{3.35}$$

3.7 Capacitive-Piezo Disk Resonator Performance Optimization

Several batches of capacitive-piezoelectric resonators were fabricated to overcome fabrication obstacles, experiment with new designs, and improve Q, k^2_{eff}, R_x, frequency accuracy, and yield. In each iteration, lessons were learned that enabled improvements in subsequent runs. This section presents design and fabrication process optimizations that were implemented alongside the best results achieved to date.

Anchor Loss Minimized 300 MHz AlN Capacitive-Piezo Disk Resonator with Q=8.8k

Figure 3.15 presents an illustration of a 300 MHz 11.2-μm-radius capacitive piezo disk resonator alongside a frequency characteristic for one such device, with a 1.2 μm wide anchor, which exhibits a record high Q factor of 8,757 at 300 MHz for AlN. In this device, conservatively-sized ≈200 nm gaps above and below the resonator are used to ensure proper operation and to aid proper clearing of the gaps. The AlN is 1.6 μm thick. Molybdenum and polysilicon are used for the bottom and top electrode materials, respectively. Here, the

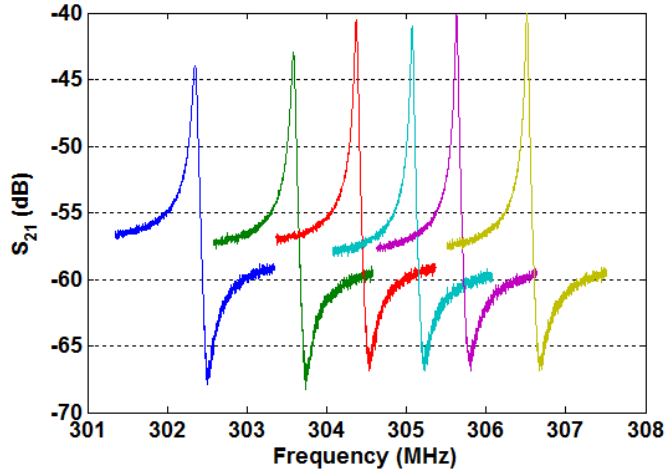

(a) Frequency characteristics for capacitive piezo disk resonators having various stem sizes.

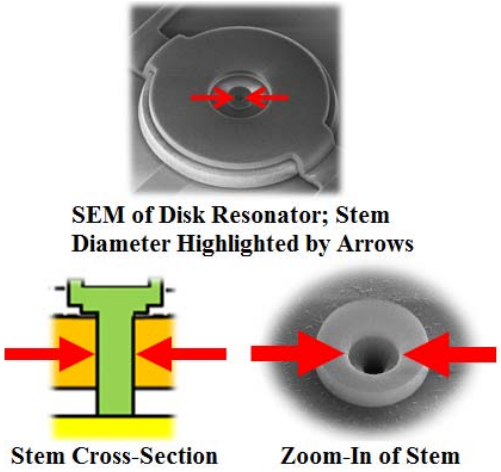

(b) Illustrations of the disk resonator and its center-supporting anchor stem.

S. D.	2.2μm	2.0μm	1.8μm	1.6μm	1.4μm	1.2μm
Color	●	●	●	●	●	●
Q	4,743	5,924	7,609	8,416	8,431	8,757

(c) Unloaded Q Measurements and associated stem diameters (S.D.'s) for the measurements of fig. 3.16a.

Figure 3.16: Measurement results demonstrating improved Q's through stem diameter and anchor loss minimization on 300 MHz capacitive-piezo disk resonators.

demonstrated electromechanical coupling is weak. This is not only because of the relatively large gaps used, but due to relatively poor c-axis crystallinity in the sputtered AlN film as gauged by the X-ray diffraction measured rocking curve full-width half-max (FWHM) value exceeding 2.0° on this particular run.

Figure 3.16 presents the measurement data of the highest Q measured on a 300 MHz AlN disk resonator, alongside additional measurements of adjacent disk resonators having incrementally larger stem diameters [71]. This experiment shows that anchor size plays a key role in maximizing Q. The data also suggest that as stem diameter is shrunk below a certain value, below about 1.5 μm, Q improvements from reducing the stem size begin to diminish, at which point Q_{anchor} is likely greater than ≈50,000 and thus not a dominant limiter of overall Q as compared to other active dissipation mechanisms, which could include Akheizer (phonon-phonon) damping and thermoelastic damping (TED) [76].

That achievable stem sizes are smaller than the smallest needed to achieve Q >8,000 at 300 MHz bodes well for the design of higher frequency disks with similarly high Q, for which proportionately smaller anchors are needed to properly scale down the device. However, the fabrication challenge of making smaller anchors in the presence of 1 to 3 μm of topography

makes scaling down to frequencies beyond 1 GHz difficult when using the first radial contour mode resonance. Modifying the fabrication process to eliminate the need for thick photoresist should enable further stem size scaling. One way to accomplish this would be to add a thick oxide deposition step after AlN etching followed by CMP to attain a flat surface.

Figure 3.16a shows also that resonance frequency depends on stem diameter, which here refers to the diameter of a circular opening at the center of the AlN disk. To understand why, consider that the mode shape of the device has a node at its center, so the effective mass contribution of the center stem is insignificant. However, since the stem is made of polysilicon, which has a lower Young's modulus of 150 MPa than the 345 MPa of AlN, and is partially hollow [77] for large stem diameters, reducing stem size increases the rigidity of the center of the resonator, causing a fractional stiffness increase δ. Resultant resonance frequency shifts from stem size modification may be quantified in the following manner:

$$\Delta f_0 = \frac{1}{2\pi}\sqrt{\frac{[k_r(1+\delta)]}{[m_r(1+(\approx 0))]}} - f_0 \approx f_0\frac{\delta}{2} \tag{3.36}$$

Here, a fractional increase δ to stiffness k_r causes f_0 to increase while effective mass m_r stays relatively unchanged. Decreasing stem size from 2.2 μm to 1.2 μm increased effective stiffness by 2.8%, hence effected a frequency shift Δf_0 of +1.4%.

Remark

The significance of this high Q measurement is that it represents over a 4× increase in Q compared to typical AlN contour mode resonators with attached electrodes at UHF, which typically achieve Q's of 2,000 or less [33] [78] [79], validating the efficacy of the electrodeless approach.

C_x/C_0 Optimization Through Gap Minimization, Film Quality Improvement, and Increased Electrode Coverage

The demonstrated electromechanical coupling of the device of fig. 3.15 is weaker than is attainable with smaller gaps and better AlN film quality. The c-axis crystalline orientation of the sputtered AlN film on the wafer, as gauged by the full-width half-max (FWHM) value of an X-ray diffractometer's rocking curve measurement, strongly affects the piezoelectric coefficient of the film. The FWHM of the AlN film used to make the devices of fig. 3.15 is 2.3°, but smaller values are more desirable. After fabricating the first wafer, it became evident that better FWHM's, measured as low as 1.2°, were achievable through heating the wafer during AlN deposition and by depositing five to ten dummy films after any target or shielding changes to properly condition the sputtering tool before use. Reducing the FWHM of the AlN subsequently yielded an estimated 2.3× improvement in e_{31}, determined via curve-fitting.

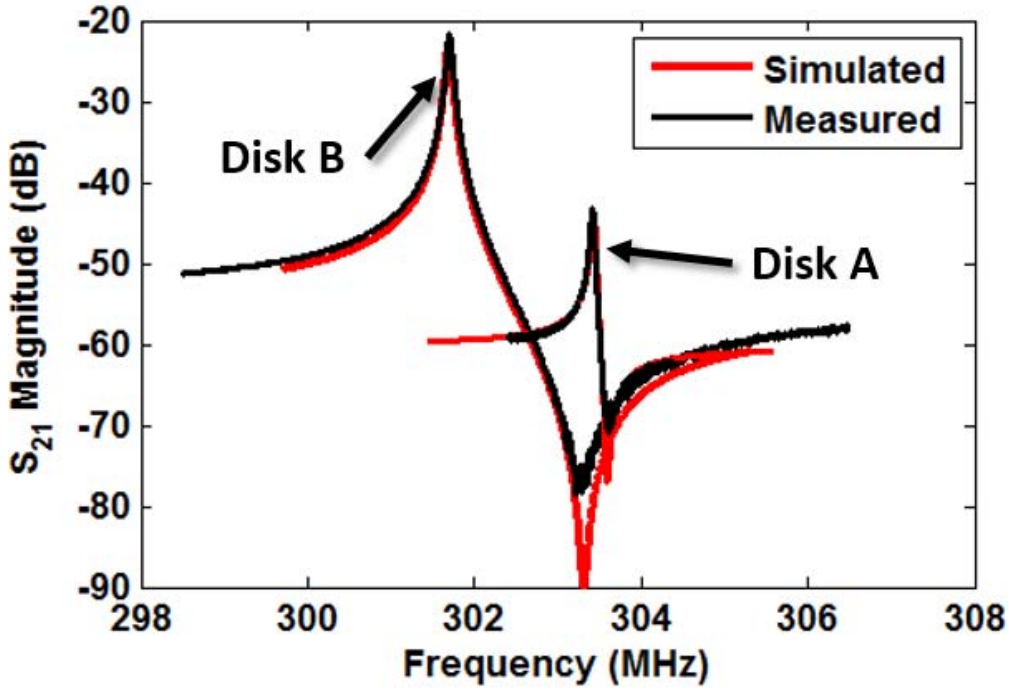

Figure 3.17: Measurements of a weakly coupled 300 MHz unit disk resonator (Disk A) and a strongly coupled one (Disk B).

To illustrate the methodology used to back calculate e_{31}, fig. 3.17 presents a comparison between frequency characteristics obtained from Disk A, a single disk from the same fabrication run that produced the device of fig. 3.15 (Run A) and, Disk B, one from a subsequent improved run (Run B) using AlN with a FWHM of 1.62° and reduced nominal total gap spacing $g_t + g_b$ of 240 nm, down from 400 nm. Hence, Disk B exhibits vastly stronger electromechanical coupling, as evidenced by the reduced insertion loss (distance between peak height and 0 dB) at series resonance and increased separation of f_s and f_p.

Superimposed upon the measured frequency characteristics of fig. 3.17 are simulation curves for Disks A and B. Here, the model presented in section 3.4 is used with the simulation input parameters presented in table 3.1 and AlN material parameters for ρ, E, ν and ε_r of 3260 kg/m^3, 345 GPa, 0.22, and 9.0, respectively, to generate the simulated plots.

$R_{el,min}$ and $R_{el,max}$ of table 3.1 refer to the minimum and maximum radii of electrode coverage to determine η. To obtain a better fit, the effective electrode coverage boundaries were expanded by 0.5 μm beyond the physical electrode boundaries to account for fringing electric field lines. Disk B has 1 μm of added radial electrode coverage at the disk's center over Disk A to further increase η and C_x/C_0, and hence reduce R_x. All told, as table 3.1 shows, Disk B has an R_x that is 15× lower than that of Disk A. Table 3.1 also presents measured and simulated parameters for Disks A and B, demonstrating good matching for both devices, to provide a complete circuit model for the device and confirm the efficacy of the modeling methods.

Table 3.1: Comparison of Simulated and Measured Model Parameters for Capacitive Piezoelectric Disk Resonator Devices A and B of fig. 3.17.

Sim. Input Parameter	**Nominal (Disk A)**	**Corrected (Disk A)**	**Nominal (Disk B)**	**Corrected (Disk B)**
R_{disk}	11.18 μm	11.065 μm	11.18 μm	11.175 μm
$R_{el,min}$	3.5 μm	3.0 μm	2.5 μm	2.0 μm
$R_{el,max}$	10.4 μm	10.9 μm	10.9 μm	11.175 μm
e_{31}	0.7 C/m	0.3 C/m	0.7 C/m	0.7 C/m
$g_t + g_b$	400 nm	400 nm	238 nm	200 nm
t_{AlN}	1.65 μm	1.65 μm	1.75 μm	1.75 μm
Model Parameter	**Measured (Disk A)**	**Simulated (Disk A)**	**Measured (Disk B)**	**Simulated (Disk B)**
Empirical Q	6,429	6,429	4,730	4,730
R_x	15,586 Ω	15,423 Ω	1,017 Ω	1,223 Ω
$(f_p^2\text{-}f_s^2)/f_p^2$	0.12%	0.10%	1.05%	1.07%
C_0	4.9 fF	5.08 fF	9.0 fF	8.43 fF
η [C/m]	–	1.73e-5	–	4.73e-5
C_x	–	5.27 aF	–	90.66 aF
L_x	–	52.1 mH	–	3.07 mH
r_x [kg/s]	–	4.527e-7	–	6.66e-7
c_x [s^2/kg]	–	1.784e-7	–	1.682e-7
l_x [kg]	–	1.545e-12	–	1.670e-12
α	–	0.31	–	0.493
β-1	–	1133 ppm	–	5577 ppm

2nd Radial Contour Mode of Device B

Figure 3.18 presents a measured wideband frequency characteristic for Device B to highlight the disk resonator's clean wideband frequency response. Due to the radial symmetry of the device, only one other mode mechanical mode is excited in the range from 0 to 1000 MHz, at 780 MHz, corresponding to the second radial contour resonance at a frequency 2.6× higher than that of the fundamental mode resonance. The second mode of Device B exhibits a Q of 2,900 and a C_x/C_0 of 0.15%.

Electrode Coverage Maximization

Assuming film quality is optimized and the gaps are as small as possible, it is still possible to improve electromechanical coupling through the use of an alternative electrode anchoring method that allows for maximum electrode coverage. Figure 3.19 presents a comparison

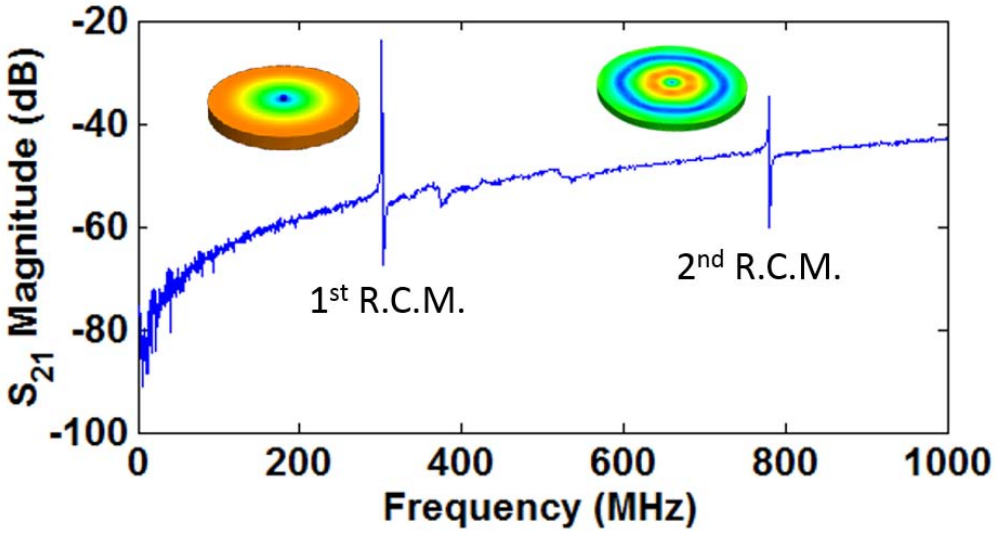

Figure 3.18: Wideband frequency response for Device B up to 1 GHz containing the first and second radial contour modes.

of two designs for capacitive piezo disk resonators: one utilizes a previously demonstrated bottom electrode support while the other sports an improved top electrode support. Plots are included of the divergence of the mode shape, for which electroded regions are denoted by x's and non-electroded regions are denoted by ·'s, and for which dark red indicates maximum divergence. As fig. 3.19a shows, since the center stem visible in the cross section must be electrically isolated from the top electrode, there is a ring shaped opening separating them by design. Thus, the top electrode, and hence transduction area [4], only covers the disk at positions greater than 3.0 μm from the center. A top-supported design, which uses the anchor lithography step to etch a small circular opening, allows for full top electrode coverage, thus maximizing transduction strength. This is particularly valuable because the center of the disk offers the strongest contribution to transduction per unit area. As shown in the figure, the 29% increase in C_x/C_0 allows for a large reduction in motional resistance, R_x.

To test this design improvement, Figure 3.20 presents a frequency response for a strongly coupled disk resonator with a k^2_{eff} of 0.94%, confirming the efficacy of a top-electrode support structure somewhat in that the coupling is quite good; however, this coupling is puzzingly slightly lower than, although similar to, that of device B of table 3.1. At least two explanations can possibly account for this discrepancy. First, it is possible that a different stress configuration in the electrode due to the top supported design resulted in an increase in total average gap spacing resulting in a reduction in coupling. A more likely alternative, as indicated by the need for a 200 nm simulated gap on Disk B instead of the nominal 238 nm value, is that the donut design performed better than expected due to a reduced gap due to a different stress profile on the 300 nm thick film. Secondly, fringing fields in the "donut"

[4] as determined by top-to-bottom electrode overlap

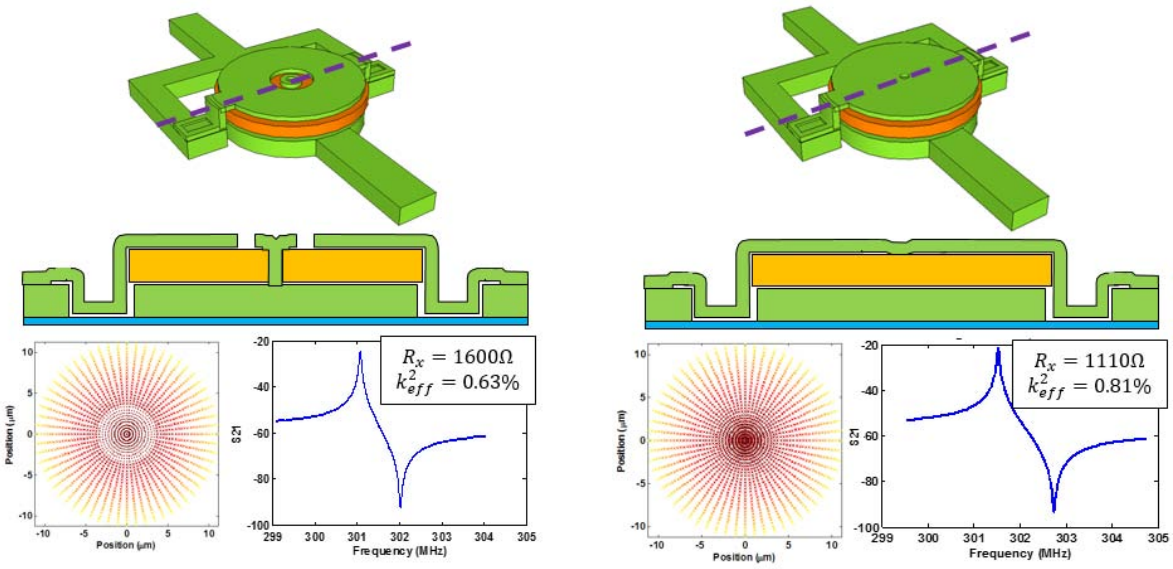

(a) Bottom electrode connected center stem support design. There is an uncoupled region at the disk's center (r≤3.0μm).

(b) Top electrode connected center stem support design. Top electrode coverage extends over the entire disk area.

Figure 3.19: Simulated improved electromechanical coupling for a top supported capacitive piezo resonator.

design are perhaps coupling into the center of the resonator more than previously thought, particularly for a small enough hole in the electrode. An electrostatic capacitance simulation could confirm this hypothesis. Additionally, needing to expand the electrode boundaries in table 3.1 for both donut designs to match experiment supports this hypothesis.

Regardless of whether the full electrode coverage offers the highest coupling in practice– it certainly shouldn't reduce coupling with equal gaps– the top-supported full-coverage design is needed for higher frequency disk designs for which the margin between the center stem and the beginning of the top electrode would cover a very large portion of the disk, and for which the donut design becomes impractical due to lithographic constraints.

Minimization of Capacitive-Piezo Disk Resonator R_x

As the needed termination resistance for a filter scales proportionately with the R_x seen by its input and output transducers, minimizing the R_x of a single disk resonator is essential for enabling filters with reasonably low termination resistances between 50 and 500 Ω. Similarly, for an oscillator, the required amplifier gain scales with R_x, thus R_x should be minimized to reduce power consumption. Fortunately, efforts to increase C_x/C_0 typically will also reduce R_x, as both variables depend on the electromechanical transformer factor η and the capacitive piezo voltage reduction coefficient α, which are both maximized by design.

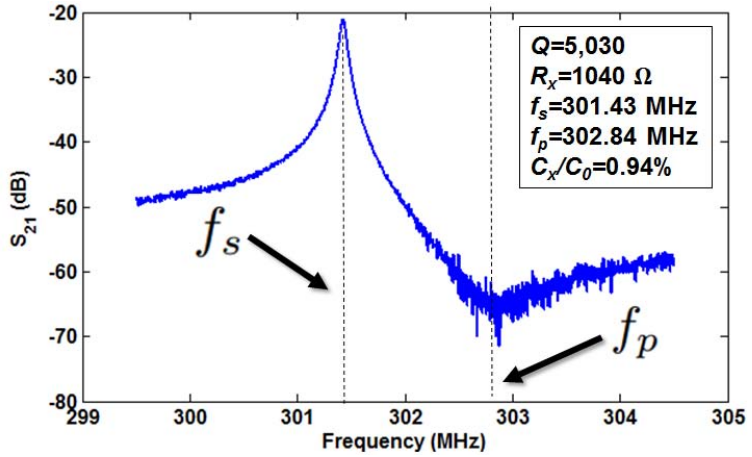

Figure 3.20: Frequency characteristic for a resonator with a large $k^2_{eff} = C_x/C_0$ value utilizing the top support anchor design of fig. 3.19b.

Although R_x and C_x/C_0 are strongly related, R_x can still be scaled down while holding C_x/C_0 constant by increasing the area of the resonator. However, this is not possible on a unit disk resonator, but it can be done through the use of coupled disk arrays, for which R_x scales inversely to the number of disks in the array, just like resistors in parallel. Array resonators are discussed in chapter 4. Nonetheless, for arrays to have low R_x, it is desirable to optimize the R_x of a solitary disk resonator.

Smallest Measured Single Disk R_x

Figure 3.21 presents the frequency characteristic for the resonator exhibiting the lowest measured single disk R_x of 785 Ω, assuming two 50 Ω loading impedances. For this device, resistance has been lowered somewhat through the use of an electrostatic bias of 34V which reduced the gap size, and hence reduced R_x from its no bias value of 938 Ω. If this same disk were to instead have an unloaded Q of 8,757 like the device of fig. 3.15, the R_x of the single disk would be 410 Ω. Thus, filters making use of 50-500 Ω terminating resistances should be readily achievable after further development.

Estimation of Trace Resistance R_p Loading of Q

Although the loading effect of the network analyzer ports has been accounted for in the calculation of R_x and Q, the loading of additional parasitic series resistance so far has not. To estimate the parasitic resistance R_p, it's possible to look at how loaded Q (Q') and loaded R_x (R'_x) change with bias voltage. If one assumes that unloaded resonator Q should remain constant as R'_x changes due to V_{bias}, then one can more accurately estimate the total loading resistance, $R_l = 2Z_0 + R_p$. Table 3.2 presents a data set consisting of loaded Q and R_x values as a function of V_{bias} along with two sets of unloaded values: one

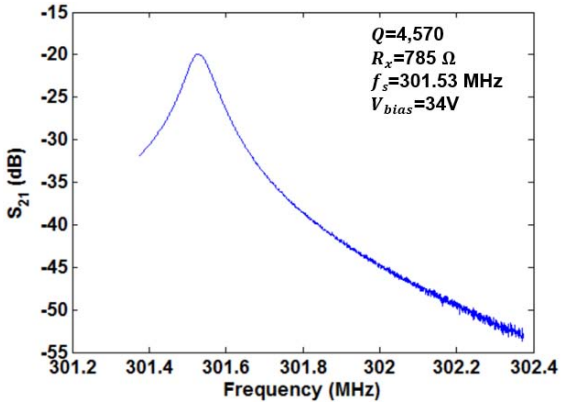

Figure 3.21: Frequency response for a single resonator with the lowest measured R_x of 785 Ω.

Table 3.2: Loaded and Unloaded Q and R_x values as a function of V_{bias} .

V_{bias}	Q'	R'_x	Q_{100}	$R_{x,100}$	Q_{200}	$R_{x,200}$
20V	4,236	1,034 Ω	4,690	934 Ω	5,252	834 Ω
25V	4,235	1,000 Ω	4,706	900 Ω	5,294	800 Ω
30V	4,197	947 Ω	4,692	847 Ω	5,321	747 Ω
34V	4,054	885 Ω	4,570	785 Ω	5,238	685 Ω

set for assuming $R_p = 0\Omega$ and one set assuming $R_p = 100\Omega$. Thus, R_l is set at 100 Ω and 200 Ω, respectively. Looking at the data, the proper value of R_p is about 30 Ω, lying within the 0-100 Ω range presented. If unloaded Q were to increase dramatically with R'_x, then R_p would be overestimated. Similarly, a decreasing Q that is not due to electrode contact would imply R_p is underestimated. A finer measurement with more data points would likely yield an even more accurate estimate of R_p.

If parasitic resistance is significant, then efforts should be taken to increase the conductivity of the electrodes to avoid unwanted dissipation. Fortunately, capacitive-piezo transducers have the advantage of allowing for arbitrarily thick electrodes. Thus, in future renditions, parasitic resistive loading could be further minimized.

Remarks

In this section on optimizing a unit capacitive-piezo disk resonator, we have reported efforts to improve the performance of the unit disk resonator with regard to Q, k^2_{eff}, and R_x for a design frequency of 300 MHz. To review, a Q of 8,757 was achieved due to very good cleanliness and a very narrow anchor diameter of 1.2 μm. A k^2_{eff} mark of 1.05% was achieved. As will be detailed in Chapter 5, the technology allows up to a 2.2% theoretical maximum with negligible gap sizes (when α approaches 1). An R_x of 785 Ω was achieved

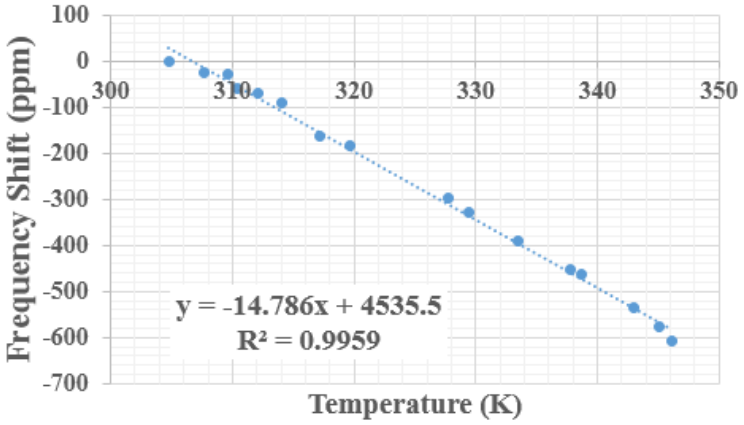

Figure 3.22: Measured fractional frequency shift in resonance frequency vs. chuck temperature for a 300 MHz capacitive-piezo disk resonator.

with a Q of 4,570– with a higher Q of 8,757, a single disk with a resistance of 410 Ω is perhaps within reach.

3.8 Temperature Coefficient of Frequency

Fractional shifts in resonance frequency due to temperature are problematic for oscillator applications which typically demand very high frequency accuracy, e.g., of ±50 ppm over a typical operating range. Narrowband filters also require minimal frequency shifts due to temperature. If the resonance frequency has a predictable dependence on temperature, the unwanted variations can be eliminated through passive or active compensation techniques. For example, a judicious amount of silicon dioxide in the film stack can zero out the linear temperature coefficient of the resonator [80]. Alternatively, one may choose to sense the temperature and apply a control signal based on a lookup table to compensate the resonator.

To measure the temperature coefficient of frequency of our device, the chuck heater was powered on in the vacuum cryogenic probe station. As the sample's temperature rose, chuck temperatures were sensed and recorded on 16 occassions via GPIB. The corresponding resonance frequencies were obtained at the same time using the network analyzer. Figure 3.22 presents a plot of the data points for fractional frequency shift vs temperature in K along with a linear trend line. The regression indicates that the device has a temperature coefficient of frequency of -14.8 ppm/K, with an R^2 value of 0.9959. This measurement can provide insight into how much compensation should be used on future devices to obtain a flat temperature dependency. For even better accuracy, it will be necessary to address the second order dependence, too.

Chapter 4

Capacitive-Piezo Disk Array Resonators

High Q and strong electromechanical coupling represent only two of the necessary conditions for use in a high performance oscillator or filter. A resonator must also have the proper motional resistance to meet system demands. R_x, hence, must be scalable in size while maintaining constant resonance frequency.

In this section, we report various aspects of the design and experimental performance of radial contour mode disk resonator arrays utilizing capacitive piezoelectric transduction, pursuant towards realizing an RF MEMS technology with high Q, strong C_x/C_0, and low R_x. Various elements of array design are examined and we report measurements of array resonators utilizing both one and two transducers. Benefits of improved power handling, improved manufacturing precision of resonance frequency, and improved capacitive feedthrough suppression are highlighted to encourage deploying capacitive piezoelectric disk array resonators for frequency control applications.

4.1 Area Scaling of Piezoelectric Microresonators

The manner in which the R_x of a piezoelectric or capacitive-piezoelectric resonator may be scaled to meet a system's demand depends on resonator geometry. To reduce R_x in a bulk acoustic wave resonator, for which the modal frequency is dependent only on thickness, one may increase transduction area through increasing both lateral dimensions–the shape of the resonator does not influence the primary resonance mode [26]. For contour mode resonators, which are advantageous in allowing for multiple frequencies on the same chip, resonance frequencies depend on certain lateral dimensions, so area may be scaled only in a manner that does not affect these critical dimensions. For example, for a resonator with interdigitated electrodes, the number of electrodes may be increased or the electrodes may be lengthened to change R_x. However, for a contour mode resonator for which resonant frequency depends on all lateral dimensions, such as for a circular geometry with a fixed

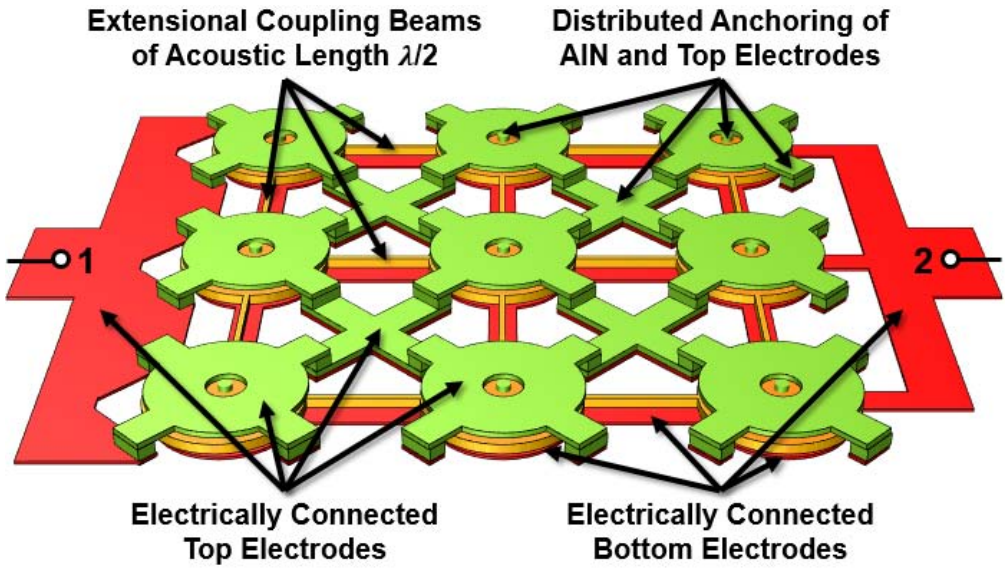

Figure 4.1: Illustration of a 300 MHz radial contour mode disk array comprised of nine unit resonators wired in parallel, mechanically coupled via extensional mode coupling beams of length $\lambda/2$.

radius, it becomes necessary to mechanically couple multiple single disks together, forming an array which reduces R_x by a discrete factor equal to the number of constituent unit resonators. An illustration of one embodiment of such an array is presented in fig. 4.1, in which coupling beams enforce synchronous vibration and the electrodes of the unit resonators are wired in parallel.

4.2 Disk Array Structure and Operation

The device of fig. 3.5 may be used as a fundamental element in a properly connected ensemble of many resonators. For example, fig. 4.1 presents an illustration of one embodiment of a mechanically coupled array of nine unit disk resonators. To enforce in-phase vibration of the constituent resonators of the array, extensional mode coupling beams of length $\lambda/2$ are used, forming mechanical connections between adjacent disks in a manner similar to the capacitively-transduced disk arrays of [48]. The rationale of the chosen $\lambda/2$ length is to form a standing wave pattern in the beam, with a node at the center of the beam and antinodes at the attachment points to the resonators on either side, as shown in the array mode shape illustration of fig. 4.2. The coupling beams ideally do not load the operating frequency of the resonator because they present a near-zero acoustic impedance to the disk at the attachment points at the design frequency. The top electrodes of each disk are electrically connected together through the routing of the interconnect, as are the bottom electrodes. Thus, the disk resonators are electrically connected in parallel. The length of each coupling beam is

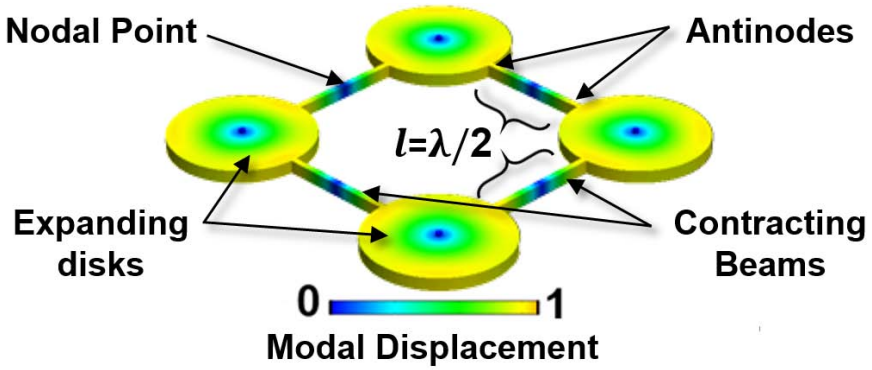

Figure 4.2: Modal displacement illustration for a radial contour mode array in a positive half cycle of vibration.

given by[1]:

$$\lambda/2 = \frac{v_a}{2f} = \frac{1}{2f}\sqrt{\frac{E}{\rho}} \tag{4.1}$$

Where f is the operating frequency, v_a is the acoustic velocity in the material (10,260 m/s in AlN), E represents Young's modulus, and ρ represents density. For a 300 MHz resonator, coupling beams in AlN are designed to be 17.1 µm long.

4.3 Distributed Anchoring as a Solution for Area Scaling of Capacitive Piezo Resonators While Avoiding Electrode Contact

Even though arraying is the only feasible method for scaling the R_x of disk resonators, arraying also provides one of the only viable paths towards realizing capacitive-piezoelectric transducers with extremely small gaps and large surface areas. For capacitive piezoelectric resonators, avoiding contact between the device and its electrodes is key for realizing high Q and the proper mode shape. Unfortunately, if significant bending moments due to residual stress exist in the structure or its electrodes, electrode contact can occur, particularly for structures with large distances between anchoring points and/or small capacitive gaps. For example, the capacitive-piezo lamb wave resonator demonstrated in [70] utilized large 250 nm capacitive gaps above and below the resonator due to the resonator's large size and the AlN film's propensity for bending after release. Preferably, a designer would not have to sacrifice gap spacing to increase the size of the device. The use of an array of smaller radial contour mode unit disk resonators reduces stress concerns inherent to large capacitive-piezo

[1]A more in depth discussion of coupling beams is included in section 2.10

transducers since the resonators and their electrodes are each locally anchored, preventing large displacements. The use of thick poly-Si further ensures minimal stress related bending in the top electrode. Distributed anchoring within the body of the AlN array is very useful, since vertical displacements due to vertical bending moments in a film follow a square law.

4.4 Single Transducer Disk Arrays

A single transducer disk array, such as the device depicted in fig. 4.1, is most effective when used as a component in a larger system such as a multi-pole filter or a single-pole resonator with two transducers. Before examining more advanced disk array systems, we focus on arrays with a single transducer to examine and improve their performance. In this section, we report SEM's of fabricated arrays, describe the circuit model for a disk array employing a single transducer, and report measurements of such devices to confirm high Q operation, R_x scaling, and a large number of disks. We also examine manufacturing precision.

Capacitive-piezo disk resonators from two fabrication sequences, Runs A and B, are presented in this section. Several single disk devices from Run A are also published in [71]. The two fabrication sequences differ in three primary ways: first, the interconnect material was changed from 150 nm thick molybdenum (Mo) in Run A to 2 μm thick polysilicon (poly-Si) in Run B; secondly, gap sizes were reduced in Run B to achieve better coupling; and third, the crystalline alignment of the AlN was improved in Run B, also to achieve better coupling.

Disk Array SEM's and Fabrication Remarks

Figure 4.3 presents SEMs of nanofabricated capacitive piezoelectric disk arrays from Runs A and B. Run A utilizes 150 nm thick molybdenum interconnect, while Run B uses 2 μm thick poly-Si interconnect. Smaller gaps and improved AlN crystallinity contribute to better electromechanical coupling in Run B's devices.

As is evident in fig. 4.3b, the arrays from Run B are affected by several fabrication related complications. The poly-Si film forming the top electrode is rough in texture and only half as thick as the targeted 600 nm deposition thickness, while that of Run A is smooth and has the proper thickness. The interconnect of Run B is over etched. Most problematically, there are thin stringers, 10's of nm wide, hanging below the edges of the AlN structure, which attach to the bottom electrode in regions of overlap. After release, these formations could not be removed using a post-etch residue remover (EKC-270$^{\text{TM}}$), annealing, nor a strong O_2 plasma. The stringers are suspected of lowering Q's and affecting the operation of coupling beams from Run B due to undesired shear coupling to the substrate at the bottoms of the beams. The shown coupling beams are 0.8 μm wide as drawn in layout, while beams drawn as narrow as 400 nm were successfully defined and etched using our process.

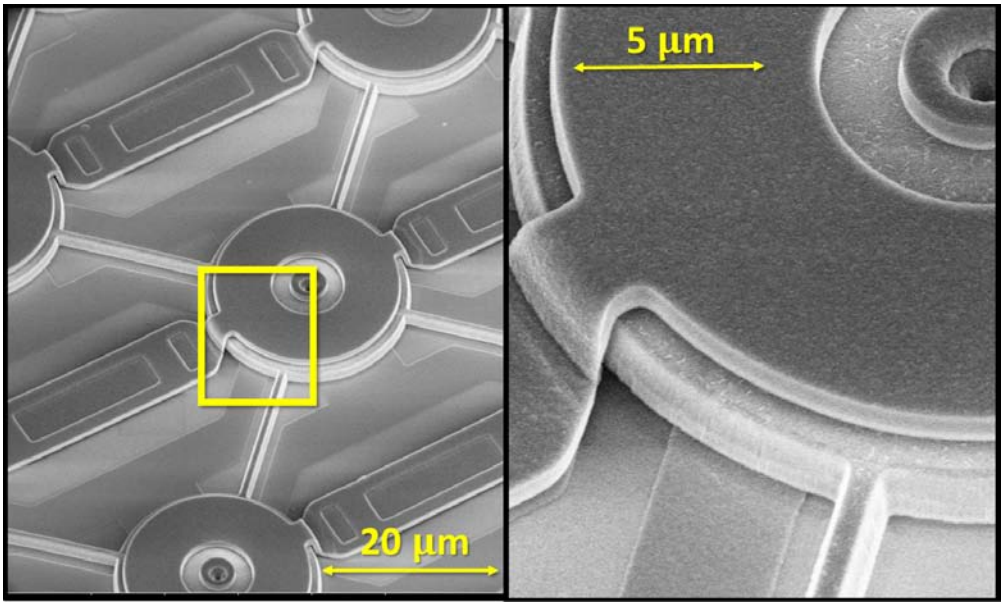

(a) 300 MHz disk array from Run A, utilizing electrode routing which does not pass under the coupling beams.

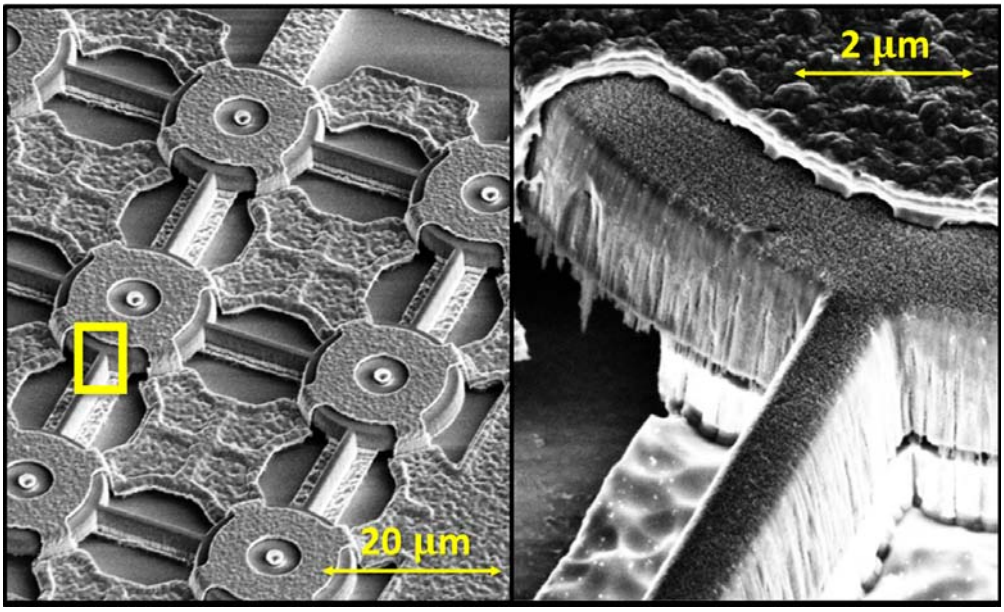

(b) 433 MHz disk array from Run B, utilizing electrode routing under the coupling beams.

Figure 4.3: SEM's of capacitive piezoelectric disk arrays from Runs A and B. Left: Wide view images. Right: Higher magnification images of edge of disks with view of gaps, electrodes, and coupling beams.

The two devices shown are distinct from each other not only in their fabrication process, but also in their electrode routing and central stem sizes. The electrode routing for the array of fig. 4.3a avoids placing electrodes under coupling beams for better reliability, while the design shown in fig. 4.3b includes bottom electrode interconnect routed under coupling beams to minimize parasitic resistance between electrodes, thus reducing Q loading. The rigidity of the top electrode is also improved through the use of four anchoring points instead of two. The layout defined stem dimensions in lithography layers 2, 3, and 4 were reduced in Run B to reduce the footprint of the stem anchor to allow more electrode coverage. However, for reliability, the stem lithography layout of layers 2, 3, and 4 of Run A should allow for a radial margin of 500 nm between subsequent layers–significantly reducing this margin in Run B led to some failed devices due to reduced lithographic resolution when using 3.5 μm thick resist for layers 3 and 4.

BVD Circuit Model for Single Transducer Disk Arrays

When the single transducer array in fig. 4.1 is formed through the in-phase coupling of multiple unit resonators, the BVD model for the unit resonator of fig. 3.7b may still be used by modifying the BVD component values to account for the increased size of the device. If n_d refers to the number of disks comprising the array, and the subscript $_{,s}$ denotes a single disk's component value, then the BVD model component values will be modified in forming an array by the n_d factor as follows:

$$R_x = \frac{\sqrt{(k_{r,s}n_d)(m_{r,s}n_d)}}{Q(\eta_s n_d)^2} = \frac{R_{x,s}}{n_d} \tag{4.2}$$

$$L_x = \frac{m_{r,s}n_d}{(\eta_s n_d)^2} = \frac{L_{x,s}}{n_d} \tag{4.3}$$

$$C_x = \frac{(\eta_s n_d)^2}{k_{r,s}n_d} = n_d C_{x,s} \tag{4.4}$$

$$C_0 = n_d C_{0,s} \tag{4.5}$$

If a designer wishes to account for the effects of coupling beams, here assumed to be thin, effective mass and stiffness may be increased by the same small amount, on the order of 5%, depending proportionately on the widths of the beams. Such a modification does not affect resonance frequency to first order approximation.

Measured Performance of Arrays

To demonstrate the parallel impedance scaling predicted by the single transducer array BVD model, fig. 4.4 compares measured frequency characteristics for a single disk resonator and a four disk array resonator. The four disk array exhibits the same vibrational mode shape shown in fig. 4.2. The two resonators each have a Q of about 6.5k, stem diameters of

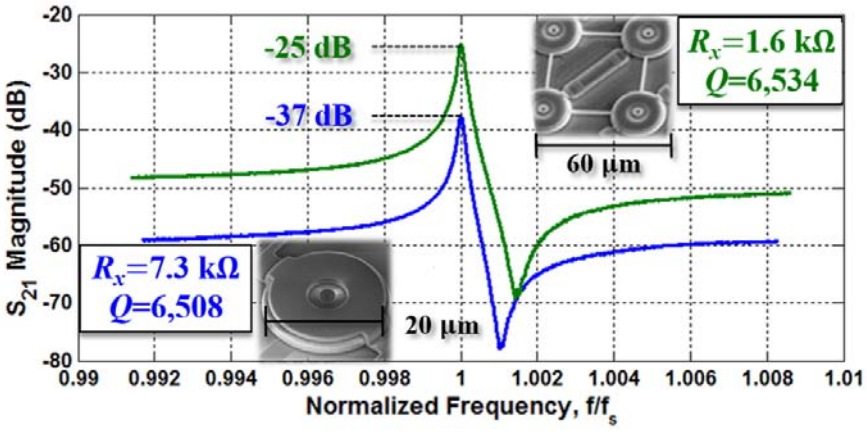

Figure 4.4: Frequency characteristic of a 300 MHz single transducer 4-disk array (green) alongside that for a single disk resonator (blue), both from Run A.

Table 4.1: Selected Measurements of Capacitive Piezoelectric Unit and Disk Array Resonators from Runs A and B.

Device (Run/#)	n_d	f_s	Q	C_x/C_0	R_x
A1	4	289.33 MHz	6534	0.28%	1611 Ω
A2	9	301.56 MHz	4372	0.25%	665 Ω
A3	9	300.53 MHz	4872	0.18%	783 Ω
A4	16	301.64 MHz	2954	0.27%	433 Ω
A5	25	301.48 MHz	3713	0.09%	1191 Ω
A6	25	301.38 MHz	1563	0.28%	418 Ω
B1	4	308.83 MHz	1587	1.15%	555 Ω
B2	9	301.59 MHz	542	1.26%	725 Ω
B3	16	301.50 MHz	765	1.26%	225 Ω
B4	4	431.01 MHz	3228	0.73%	720 Ω
B5	1	585.87 MHz	4768	0.55%	2271 Ω
B6	16	589.95 MHz	1189	0.59%	662 Ω

1.8 µm, and come from the same die from Run A. The array has an R_x that is nominally about 4× smaller than that of the unit resonator. In reality, the array's R_x is 4.5× smaller, as there is significant local and die-to-die variation in observed C_x/C_0 among devices from Run A due to one or more of the following: CMP determined gap size, corrosion of electrodes, or location dependent AlN film quality. The feedthrough capacitance level of the array, determined by C_0, is increased over that of the single disk resonator again by about 4× (12 dB).

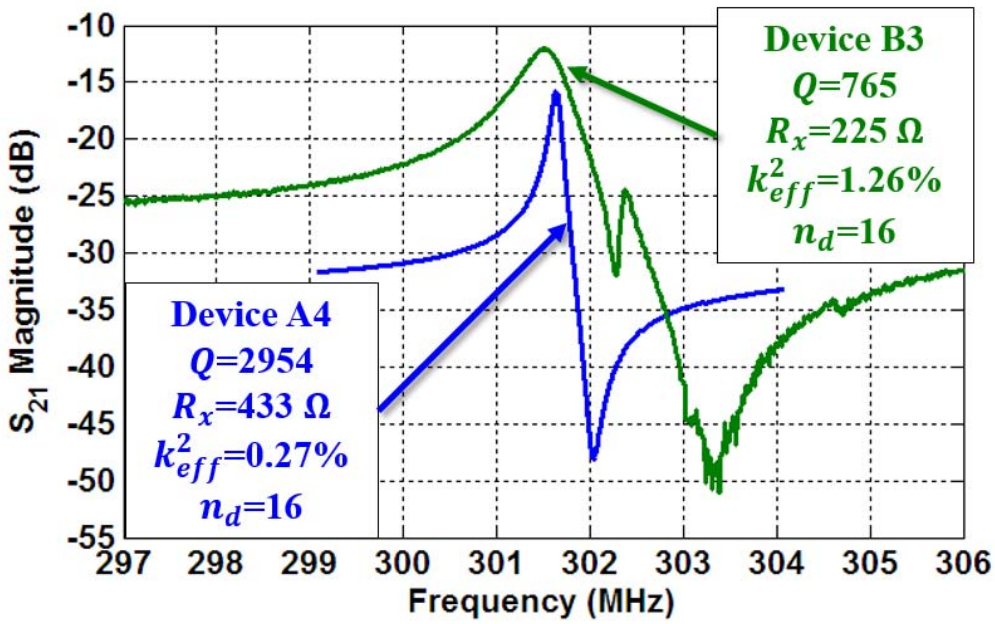

Figure 4.5: Comparison of frequency characteristics for two 4×4 disk arrays: A4 and B3.

For more examples of disk array measurements, table 4.1 presents measurement data of our best performing capacitive-piezo disk resonators from runs A and B with various numbers of disks (n_d) to highlight best to date observed Q's, R_x's, and C_x/C_0's for various array sizes at design frequencies of 300, 433, and 600 MHz.

Device A1, reproduced from fig. 4.4, posts the best observed Q of 6,534 of any non-unit resonator in this study. Devices A2 through A6 demonstrate that AlN arrays of 9, 16, or even 25 devices can function with Q's of 3,000 or more with linearly reduced R_x's, and increased power handling due to the commensurate increase in size, compared to unit disk resonators. Device A5, an array with 25 disk resonators, was damaged, as several of its top electrodes became detached, so it had reduced coupling, yet still posted a good Q of 3,713 considering the size of the array.

The arrays from Run B, in contrast, attain very strong electromechanical coupling exceeding 1.0%. For example, Device B3, an array of 16 disks, has a measured C_x/C_0 of 1.26% and posts the lowest measured R_x of any capacitive-piezoelectric AlN resonator to date at 225 Ω, despite a Q of only 765. Generally, Run A's arrays boast high Q's while Run B's arrays boast high k^2_{eff}. Figure 4.6 presents a comparison of frequency characteristics for 4×4 arrays taken from Runs A and B. An array which combines the high Q, clean frequency response of A4 with the strong coupling and low R_x of B3 is desired. For reference, the layout illustrations for the two arrays, which differ primarily in their electrode routing, are included in fig. 4.6a and fig. 4.6b. Here, red represents interconnect, orange represents AlN, and green represents the top electrode. A fourth layer is present in some regions of green and red overlap to connect the two layers, but is difficult to view among overlapping layers.

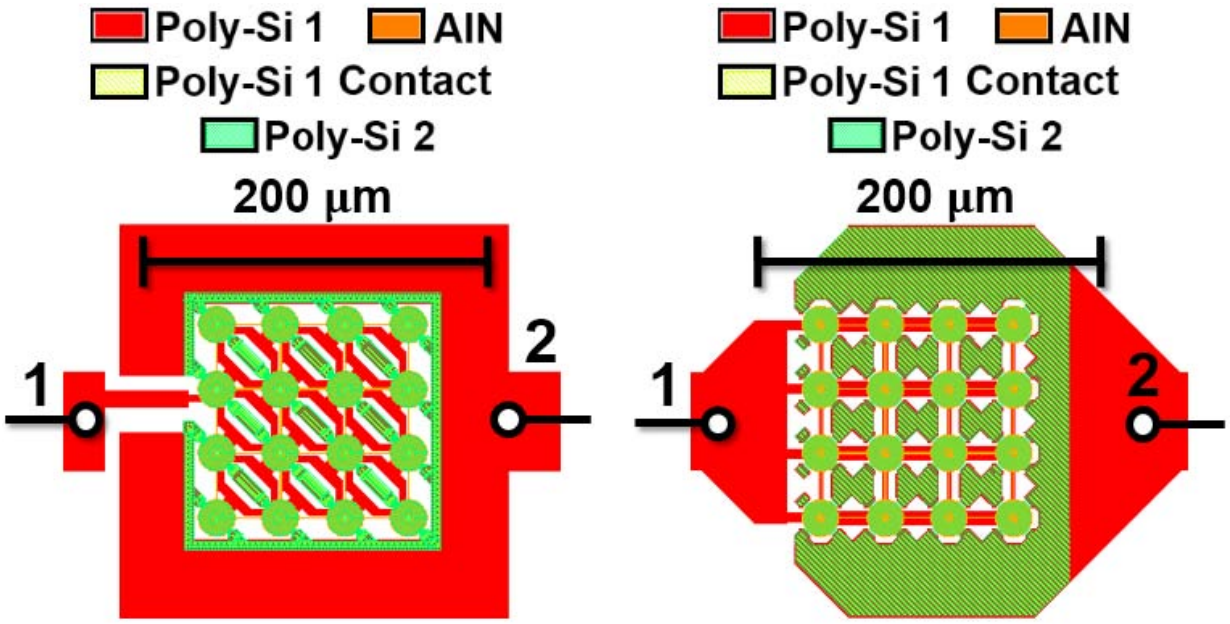

(a) Layout overview for A4.

(b) Layout overview for B3.

Figure 4.6: Layout views of 4×4 disk arrays: Devices A3 from Run A and B4 from Run B.

The non-ideal frequency characteristic and reduced Q of B3 of fig. 4.6 are probably due to fabrication related changes, not layout modifications, although electrode routing under the coupling beams may affect performance.

The observed Q's of arrays at 300 MHz are lower than expected in Run B. For example, twelve adjacent four-disk 300 MHz arrays not included in table 4.1 had Q's ranging from 512 to 1,340. Interestingly, disk arrays at higher frequencies posted higher Q's. For example, device B4, a 4 disk array at 431 MHz, posted a Q of 3,228, indicating that smaller size disks were less lossy, and further, that strain gradient bending of AlN is likely causing electrode contact in 300 MHz arrays. As 300 MHz unit resonators were seemingly not affected, arrays evidently have larger maximum vertical displacements due to stress related bending than do unit resonators. Vertical displacements due to AlN film curvature must be minimized through film quality improvement to achieve high aspect ratio gaps with large values of R_{disk}/g_t. One clever design approach to work around this issue is to utilize additional stress relieving "buffer" disks outside of the transducing region so that transducing resonators do not bend significantly [47] [48].

At the higher end of the frequency spectrum investigated in this study, unit resonator B5, with a design frequency of 600 MHz, posts a Q of 4,768 and C_x/C_0 of 0.55%. An array of sixteen disks at 600 MHz had a lower Q of 1189 but was useful for reducing R_x down to 662 Ω.

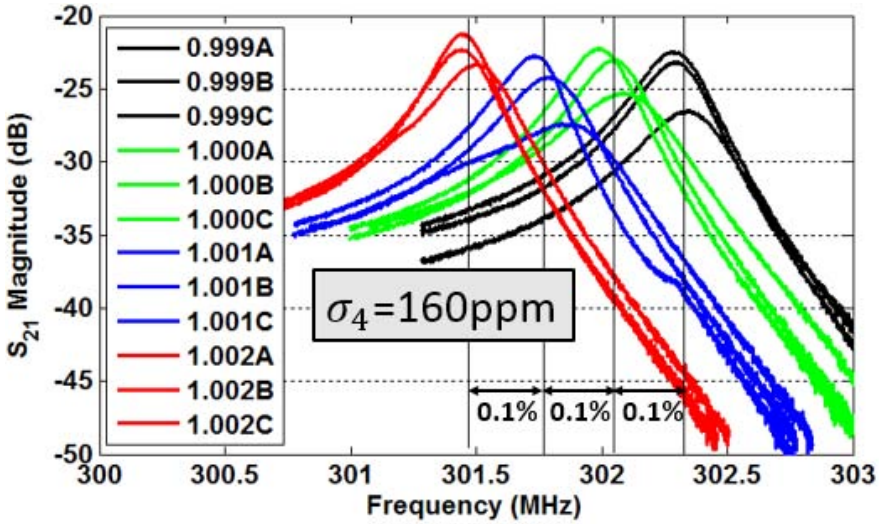

(a) Frequency characteristics for twelve 2×2 disk capacitive-piezoelectric resonator arrays from Run B, evenly divided among four distinct device magnifications shown in the legend. The four design frequencies are spaced 1,000 ppm apart.

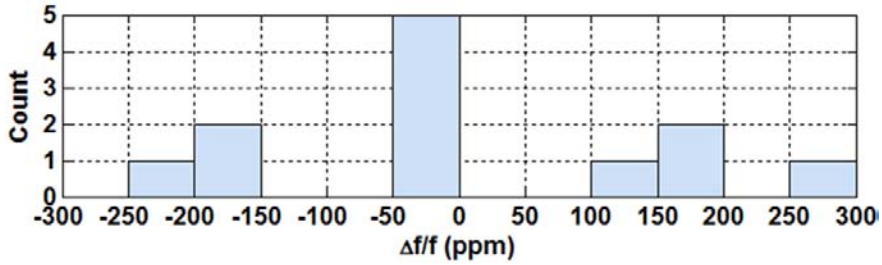

(b) Histogram of frequency shifts from target frequency in parts per million.

Figure 4.7: Manufacturing precision study for capacitive-piezoelectric 300 MHz four-disk arrays.

Manufacturing Precision

To gauge the manufacturing precision of AlN 300 MHz disk array resonators, fig. 4.7 presents a plot of twelve overlaid 2×2 disk array resonator frequency responses from a single die from Run B. Sets of three arrays each, sized using four distinct magnification factors of 0.999, 1.000, 1.001, and 1.002, were manufactured to effect small 1,000 ppm shifts in resonance frequency, as would be needed for fine frequency selection and synthesis. As denoted in the legend, these four magnification factors are distinguishable by line color. The four vertical lines in the plot represent 1,000 ppm spacings, corresponding to target frequencies for the four different sizes about the mean measured resonance frequency. Based on the average difference between measured and expected frequencies, the standard deviation representing manufacturing precision of series resonance frequency for 2×2 disk arrays, σ_4, at 300 MHz is calculated to be 160 ppm. A histogram showing the counts for different

frequency deviations is included below the frequency characteristics in fig. 4.7.

It has been experimentally shown in a previous study of capacitively-transduced disk resonator arrays that device-to-device resonance frequency variation decreases as n_d increases [81]. The expected standard deviation describing the manufacturing precision for resonance frequency of an array with n_d disks, σ_{n_d}, in terms of the standard deviation for resonance frequency of a single disk, σ_1, is:

$$\sigma_{n_d} = \frac{\sigma_1}{\sqrt{n_d}} \tag{4.6}$$

Increasing the number of unit resonators per array beyond n_d=4 is expected to improve manufacturing precision of capacitive-piezo disk arrays. Sources of manufacturing precision variance in these devices could include one or more of the following: photoresist and photo mask line edge roughness, photoresist contamination, or localized plasma loading in the etcher.

Remarks

The benefits of using array resonators include R_x reduction, power handling improvement, and improved manufacturing precision of frequency accuracy. However, table 4.1 indicates that as array size increases, Q decreases. If high Q cannot be maintained as n_d scales, then the benefit of increasing n_d is diminished. However, n_d and Q need not be negatively correlated, and we predict that the high Q's achieved on unit disk resonators, e.g., 8,757 at 300 MHz, should be achievable in array form too. Expected Q as a function of array size should remain constant when the energy dissipated per cycle per disk stays constant, which one expects from an ideal array, notwithstanding possible increased average interconnect loading from longer trace resistance to the transducer terminals. However, capacitive-piezo transducers have the ability to completely eliminate interconnect loading: one can make electrode films very thick without affecting coupling or the mode shape, a marked advantage over attached-electrode piezoelectric resonators.

Besides interconnect loading, a second form of Q degradation in an array, a likely culprit in our devices, is the presence of just one or more lower Q disks, possibly due to one or more of the following: residual liquid in a gap, stiction, handling damage, electrode corrosion, stem detachment, electrode-disk contact, contamination, or lithography defects. Without attaining near perfect yield, which is difficult in a university setting, the probability of having one or more lower Q disks in the array increases with n_d. If observed problems were eliminated, the observed Q's of large arrays would be higher and have less variance.

4.5 Two-Transducer Disk Arrays

Single transducer disk arrays are most useful as a functional element in a larger system, mainly since the large direct feedthrough path in a single transducer array presents an

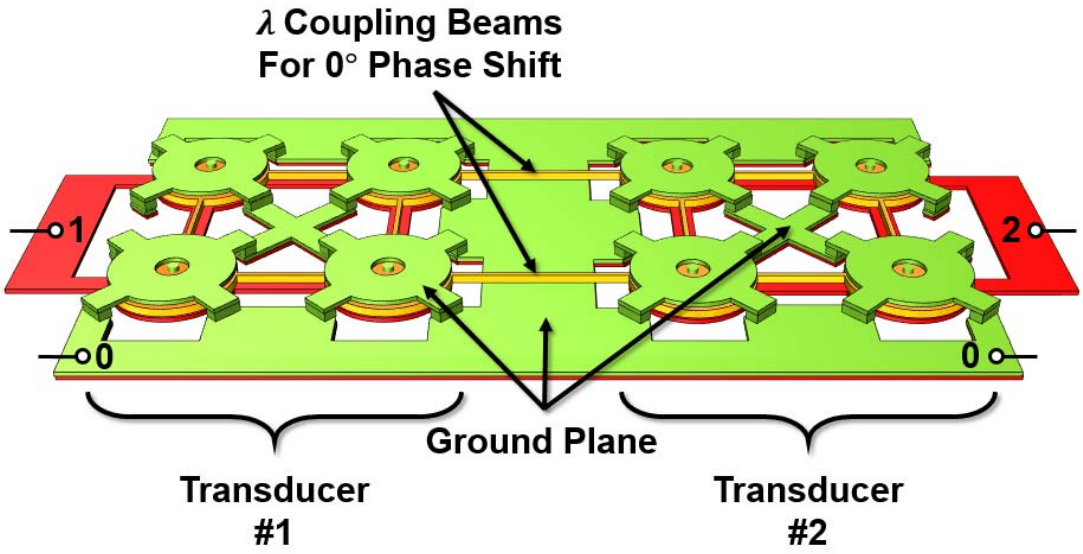

(a) Illustration of a two-transducer disk array for an oscillator.

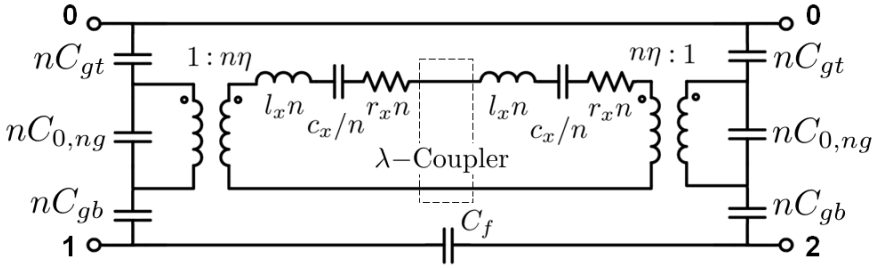

(b) Electromechanical circuit model for a λ-coupled two-transducer capacitive-piezoelectric disk array with n disks per transducer.

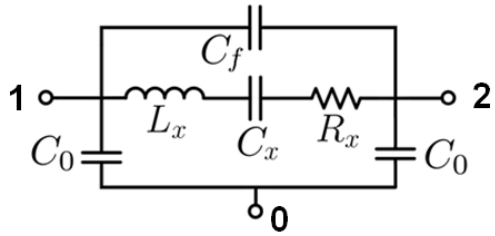

(c) Equivalent simplified circuit.

Figure 4.8: Illustration and equivalent circuit models for a capacitive-piezoelectric disk array resonator with two transducers.

unwanted large capacitance. Capacitive feedthrough between input and output terminals in a resonator determines stop band rejection in a filter application and affects minimum power consumption in an oscillator application [82], hence should be minimized. An effective technique for reducing this unwanted capacitance is to use two separate transducers instead of one, preferably with an electrically isolating ground plane separating them, with only thin mechanical couplers linking the two separately transduced arrays together. Figure 4.8a presents an illustration of one example of such a device, in a 2×2×2-disk configuration, tailored for an oscillator application needing a 0° phase shift at resonance by the use of coupling beams of acoustic length λ to link two single transducer arrays together. The equivalent circuit for the device is shown in fig. 4.8b, with the two port network representing the coupling element(s) outlined in the circuit's center. As for all transmission lines, the equivalent two-port network for a coupling beam of length λ is a thru connection, in which corresponding terminals in the two ports are connected as is drawn. In this circuit drawing, n refers to the number of disks in a single transducer to emphasize the scaling of the unit resonator component values–l_x, c_x, r_x, η, C_{gt}, $C_{0,ng}$, and C_{bt}–for which subscripts denoting single disk values have been omitted for brevity. The device can be shown to have the simplified equivalent circuit of fig. 4.8c, where the equivalent component values are calculated in the same manner as in section 3.4. At resonance, L_x and C_x effectively cancel each other out, thus the phase shift between terminals 1 and 2 is nearly 0°, as C_f is very small.

To demonstrate, fig. 4.9 presents the frequency characteristic for a two-transducer array to highlight greatly reduced feedthrough capacitance as estimated from the S_{21} magnitude away from resonance. Despite having 18 disk resonators, the device exhibits a mere 1.7 fF of estimated feedthrough capacitance based on the S_{21} magnitude floor of -70 dB at 300 MHz in a 50 Ω system. As a comparison, the 16-disk array fig. 4.5 has an estimated C_f of 121 fF based on a much higher S_{21} floor of -33 dB. The R_x for this device is expected to be (9+9)/(9×9)=2/9 times less that of a unit resonator. Due to a reduced Q however, presumably due to disk-electrode contact and stringers, the R_x value observed is similar to that of Disk B from section 3.7, albeit with reduced feedthrough and better power handling capacity. What is remarkable about fig. 4.9 is how it shows that mechanically coupled AlN filters, such as those first demonstrated in attached-electrode contour mode AlN at 100 MHz in [79], can simultaneously achieve a strong resonant response with strong stopband rejection at UHF, even with a single-ended design. Differential operation, as used to make AlN contour mode filters in [36], would offer even lower effective feedthrough, due to destructive interference between opposing capacitive feedthrough paths.

By changing the λ-coupler in fig. 4.8b to a $\lambda/4$-length coupler, which functions as an impedance inverter and which may be modeled as a symmetric capacitive T-network [63], a multi-pole filter may be implemented with steeper rolloff between the passband and stopband than a single pole resonator. Furthermore, filter bandwidth is determined by the width of the mechanical coupler(s), which paves the way for a highly customizable filter technology, offering high Q alongside the potential for multiple frequencies and multiple bandwidths on the same chip. Due to the higher Q's afforded by capacitive-piezoelectric transduction, and now low R_x afforded through AlN disk arrays, capacitive-piezoelectric narrowband filters

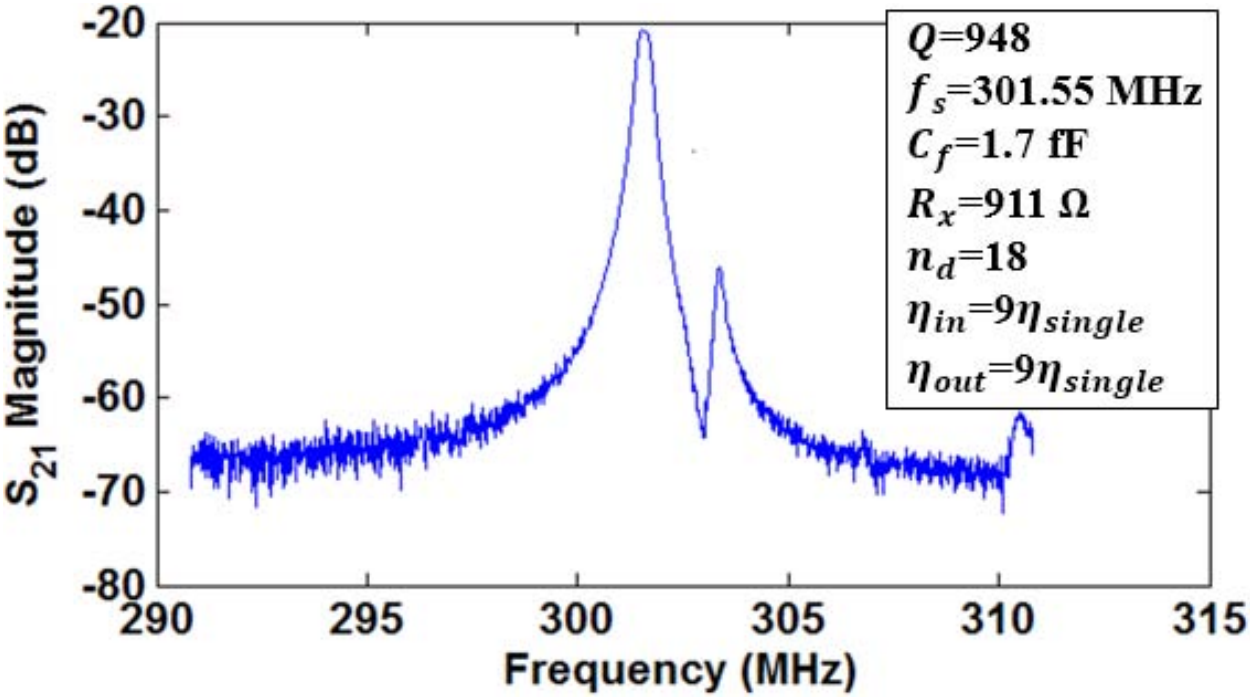

Figure 4.9: Frequency characteristic for a strongly coupled 300 MHz $2\times3\times3$ array resonator with greatly reduced feedthrough capacitance utilizing two transducers. The device was fabricated in Run B.

with bandwidths in the range of 0.1%-0.5% and insertion losses less than 3 dB should be possible, potentially with terminations of just 50 Ω.

4.6 Conclusions

In this chapter, we have highlighted the capabilities of capacitive-piezoelectric disk array resonator technology. Although further improvements in fabrication techniques are needed to simultaneously attain the high Q of Run A and the small gaps and strong coupling of Run B, the performance marks attained so far are promising. The capacitive-piezo disk array resonator thus seems well suited for competitive low power oscillator and narrowband filter applications at frequencies ranging from about 100 to 1000 MHz or beyond, as no other resonator, among SAW, FBAR, contour mode AlN, and capacitively transduced technologies, simultaneously offers higher Q, stronger C_x/C_0, and multi-frequency capability on the same chip. Capacitive-piezo transducers also offer integrated on/off switching [71] and frequency tuning [74] capabilities via gap actuation as will be discussed in the following chapter. To apply these techniques and build upon previous work, future research efforts should aim towards realizing switchable filters and tunable oscillators using capacitive-piezoelectric disk array technology.

Chapter 5

Top Electrode Actuation for Switching, Frequency Tuning, and C_x/C_0 Control

In this chapter, we examine the capabilities offered by voltage-controlled top electrode actuation of a capacitive-piezoelectric transducer. Although Q improvement alone is a compelling reason to separate the transducing electrodes from the body of a piezoelectric resonator, each of the following system-level needs may also be met by actuating the top electrode of a capacitive-piezoelectric transducer. First, effective frequency control of oscillators and narrowband filters is needed to eliminate unwanted manufacturing or temperature induced frequency shifts. Secondly, for a reconfigurable RF front end, intrinsic on/off switchability for resonators would allow for the selection of an operating frequency among several discrete choices without costly external series switches. Lastly, the ability to tune the coupling or Q of a resonator can potentially allow for increased dynamic range in a receiver.

In this chapter, we highlight the following four capabilities of capacitive-piezoelectric disk resonators which aim to enhance performance and provide new integrated functions for piezoelectric oscillators and filters. First, we report an electrode collapse based switching capability, for which a strong pull-down force quenches the modal vibration of a capacitive-piezo resonator. Secondly, it is possible to tune a resonator's Q to an intermediate value using the aforementioned technique, thus allowing voltage control of the amount of damping. Third, and perhaps most importantly, through tuning the gap, it is possible to tune the resonance frequency of capacitive-piezoelectric resonators, thus providing a critically needed method for compensating for unwanted frequency shifts. Lastly, it is possible to improve the coupling of these resonators through voltage controlled gap reduction, which allows one to operate with a smaller gap than initially manufactured.

By providing the necessary Q, R_x, C_x/C_0, and now, an additional integrated mechanism for providing frequency control, self-switching, and variable coupling, capacitive-piezo resonators with actuated transducing electrodes provide an attractive means for making MEMS oscillators and filters for radios meeting the needs of tomorrow's ultra-low-power

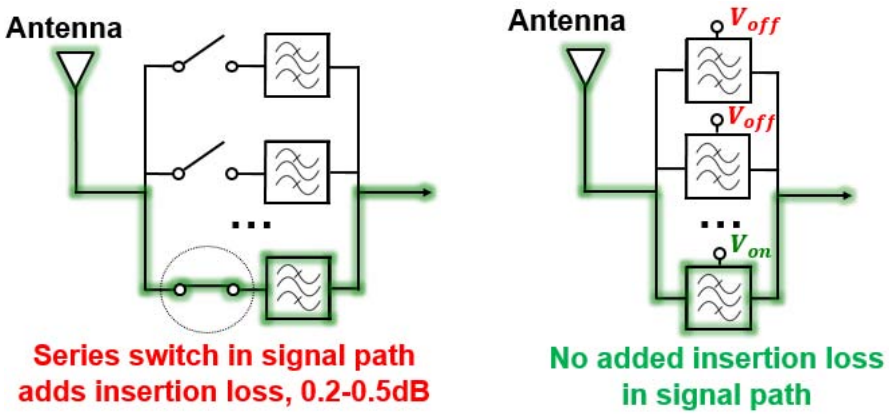

(a) Externally switched.

(b) Self-switched.

Figure 5.1: Comparison of externally- and self-switched parallel resonant filter banks.

wireless sensor networks.

5.1 Integrated Switching for Capacitive-Piezoelectric Disk Resonators

A parallel filter bank may be used in an RF front end to select among multiple operating frequencies in a spectrum constrained environment. Using a filter bank in a receiver is one way to realize (a) multi-band reconfigurable radio, which switches between different communications standards (bands), or (b) RF channel selection, which substitutes a traditional single low-Q band select filter with many switchable high-Q narrowband filters (or a single tunable one) to attenuate in-band interferers, potentially allowing for reduced power consumption.

Figure 5.1 presents two simplified architectures for implementing a switched bank of filters. External switching, as shown in fig. 5.1a, provides low off state capacitance but requires series switches in the signal path which add insertion loss, increase fabrication cost, and occupy considerable chip area. On the other hand, a self-switched architecture is preferred, assuming parasitics can be mitigated with inductors, as it dispenses with the need for external switches.

Capacitively transduced MEMS resonators can be self-switched [54], enabling the architecture of fig. 5.1b, since the application of a polarizing DC voltage (V_p) determines whether the capacitive resonator is on or off. Although traditional piezoelectric transducers with attached electrodes cannot be self-switched, researchers seek integrated alternatives to external switches for piezoelectric resonators. For example, the work of [83] seeks to integrate phase-change-material-based switches with piezoelectric resonators. The switch can be turned on, i.e., made crystalline and conductive, or turned off, i.e., made amorphous and insulating,

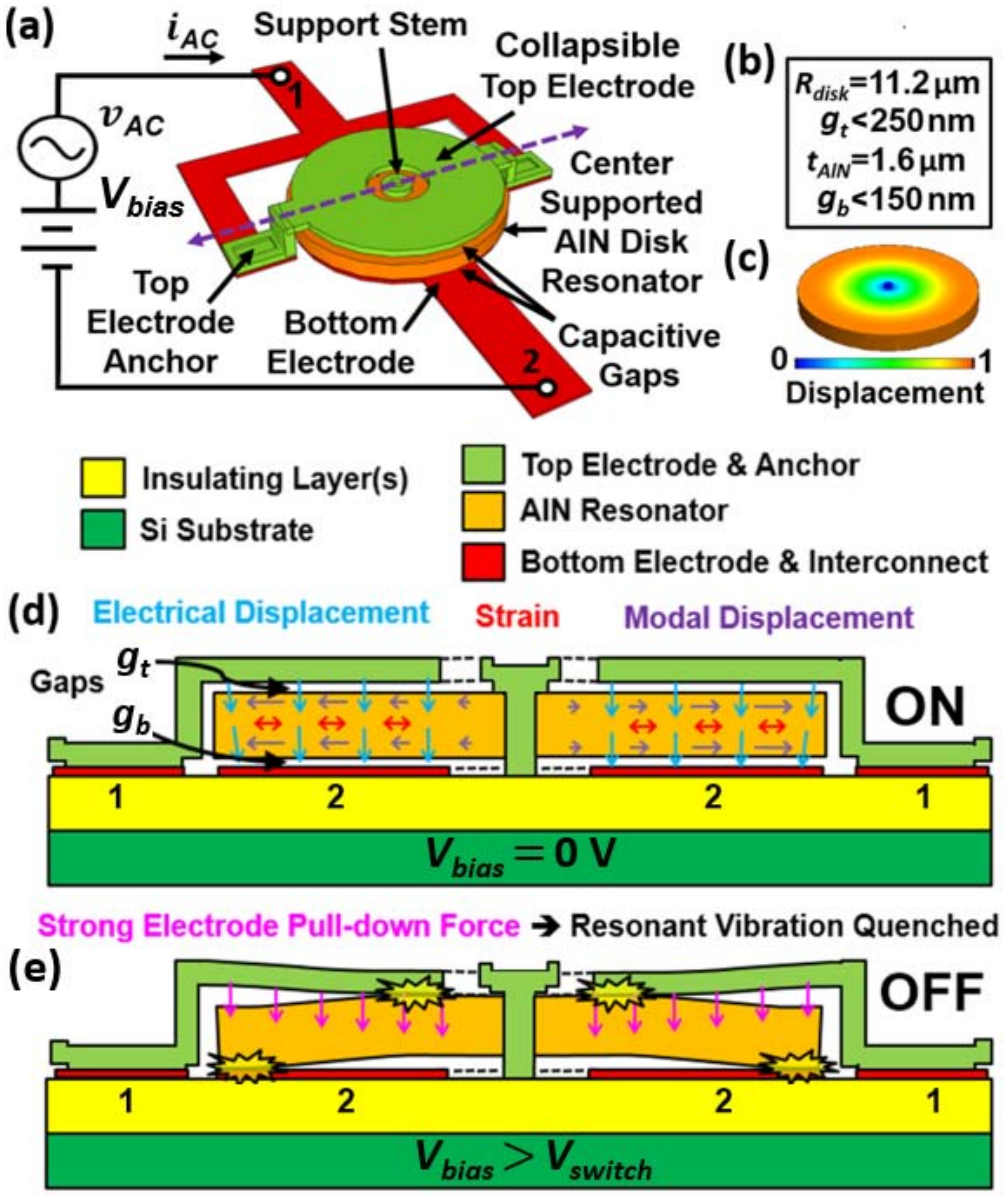

Figure 5.2: (a) Perspective view illustration of the on/off switchable 300 MHz capacitive-piezo resonator demonstrated in this work. (b) Key dimensions. (c) Radial contour mode shape. (d) On state. (e) Off state.

through the mere application of voltage pulses. This approach so far permits only a minimal number of cycles however, which may prove difficult to overcome. A preferred approach may be to implement gap actuated switching using capacitive-piezoelectric transducers, to allow for voltage-controlled self-switching, as will be shown, while allowing for higher Q's at the same time.

Structure and Operation of Switchable Capacitive-Piezo Resonators

Figure 5.2 presents a series of illustrations depicting the structure and operation of a 300 MHz on/off switchable capacitive-piezo radial contour mode disk resonator utilizing a resonance quenching mechanism. As the perspective view illustration and schematic of fig. 5.2(a) shows, the structure consists of a centrally supported piezoelectric disk, made of AlN, disposed between circular top and bottom electrodes separated from the disk by small capacitive gaps, g_t and g_b. A harmonic excitation v_{ac} acts on the capacitive-piezoelectric transducer between terminals 1 and 2, which at the device's natural frequency of vibration, excites the device into resonance. Superimposed on v_{ac} is a bias voltage V_{bias} which serves to control electrode actuation. Device dimensions are included in fig. 5.2(b), including the disk resonator's radius R_{disk}; the top and bottom capacitive gap sizes g_t and g_b, respectively; and the thickness of the aluminum nitride film, t_{AlN}. In this work, 600 nm of polysilicon is used for the top electrode, while the bottom electrode is made of 150 nm of molybdenum. Silicon dioxide is used as a sacrificial layer. The lateral displacement shape for the 1st radial contour mode is shown in fig. 5.2(c).

The cross sectional illustrations of fig. 5.2(d) and fig. 5.2(e) illustrate the device in its on and off states. The key to on/off switching of this device is the structure of its capacitive-piezoelectric transducer, which provides a suspended electrode atop the suspended AlN resonator that can be pulled electrostatically towards the substrate, pinning the combined resonator-electrode structure to the substrate, thereby opening new conduits for energy loss that compromise signal transmission. To shut the device off, one merely raises V_{bias} until it exceeds the critical switching voltage (V_{switch}) between the top and bottom electrodes until the electrostatic force acting downward on the top electrode is large enough to pull the top plate down, taking with it the AlN resonator structure so that both end up pinned to the substrate. With top and bottom electrodes abutted against, but not attached, to the AlN structure, frictional loss becomes quite large. In addition, direct contact of the resonator with the substrate, without the Bragg reflectors used by solidly-mounted resonators (SMRs) [25], also steals considerable energy. All told, the energy loss inflicted by voltage-induced collapse is large enough to completely remove the resonant peak. Of course, the real magic of such a device is the ability to turn on again. Upon removal of the switching voltage, the top plate springs back up, resuming normal operation.

Measurement Setup (Single Transducer)

To test the operation of a single switchable capacitive-piezo disk resonator having just two terminals, we use a network analyzer in conjunction with a voltage source to supply the needed switching voltage. Figure 5.3 presents a schematic of the test setup used, where a DC switching voltage V_{bias} is added to an RF input signal using a bias tee. On-state operation of the switchable resonator entails measuring the magnitude of the two-port scattering parameter for transmission (S_{21}) while the DC switch-control voltage V_{bias} is turned off. Here,

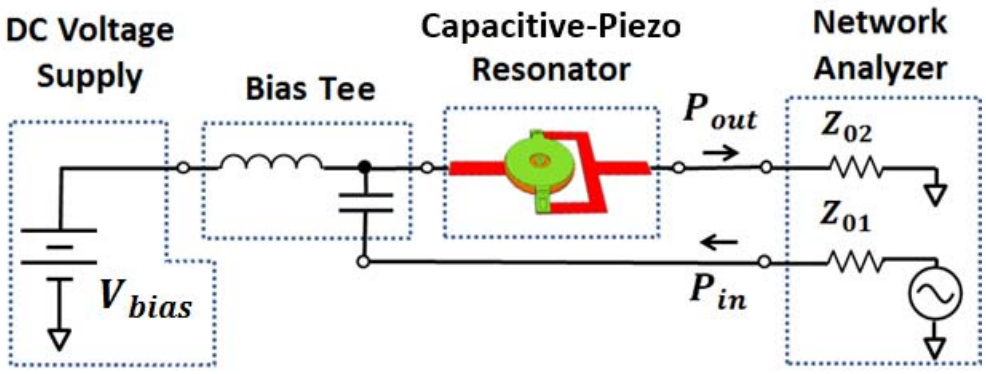

Figure 5.3: Measurement setup used to test switchable capacitive-piezo resonators possessing a single transducer.

a two-port transmission measurement is used for accurate impedance characterization due to the large R_x of the device. To characterize the disk's on/off switchability, S_{21} magnitude measurements are made in between repeated transitions between the on and off states of $V_{bias} = 0$ V and $V_{bias} > V_{switch}$, respectively, to verify extinguished resonance and the return of the resonant peak.

Switchability Demo Using a High Stiffness Electrode

To demonstrate the efficacy of the described switching method, fig. 5.4 presents three superposed S_{21} measurements made before, while, and after applying the needed turn-off voltage on a capacitive-piezo disk resonator. Also included in fig. 5.4 are illustrated device cross sections corresponding to the three measurements and an SEM of the tested device. The measurements made before and after turning the device off are overlapping, indicating a proper return to the on state. This measurement was manually cycled 20 times with no failure or initial frequency or Q changes over the duration of the experiment. Only when the voltage was increased to 250 V, representing a 30% increase in force, did the device become permanently damaged.

Due to its 600 nm thickness and fixed-fixed anchoring just beyond the boundaries of the disk, the top electrode for the device of fig. 5.4 has a very high stiffness, hence is effective for transitioning back to the on state. As V_{bias} is increased past the transition voltage V_{switch}, the device experiences instantaneous electrode collapse due to buckling, and a resultant dramatic rise in the amount of damping. Here, the needed pull-down voltage of 220 V is high, but not dissimilar from voltages normally needed to actuate RF MEMS switches. The good news is smaller gaps, a thinner top electrode layer, or even an added top electrode suspension can make V_{switch} much smaller.

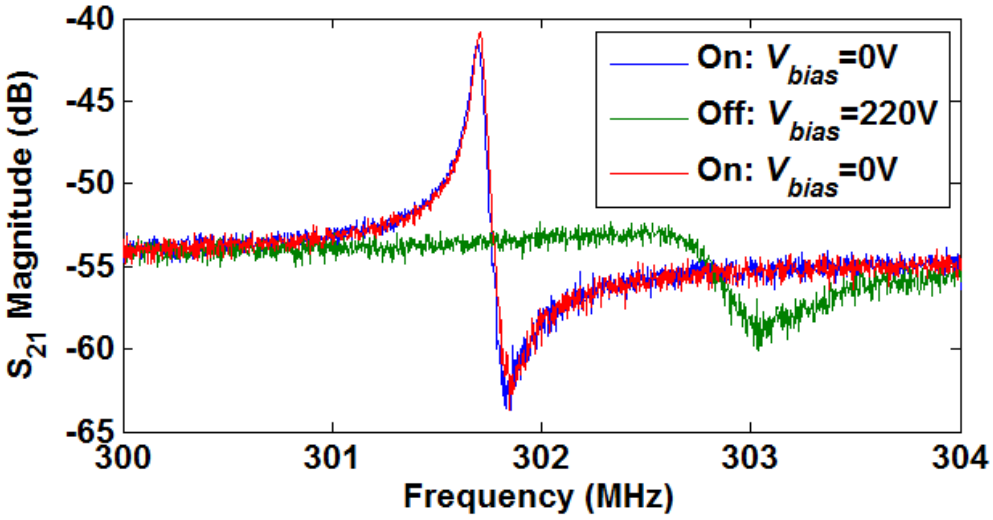

(a) Device measurements in the On and Off states.

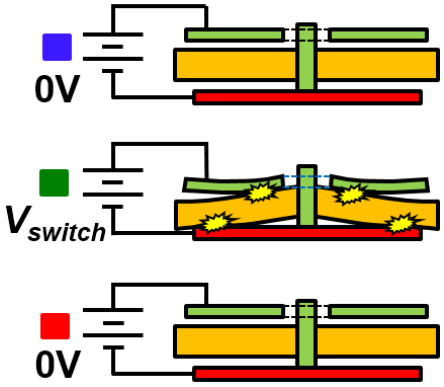

(b) Device cross sections in the On, Off, and Back-On states.

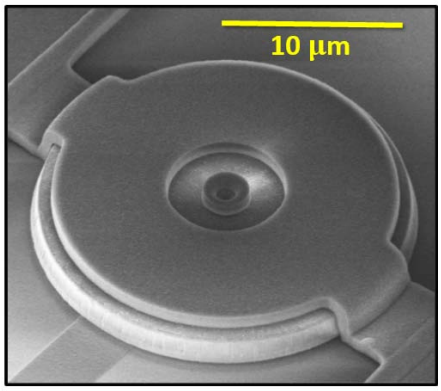

(c) Scanning electron micrograph.

Figure 5.4: Demonstration of switching capability. The resonator is ON when no switching voltage is applied. Next, a DC voltage of 220V is applied, causing the top electrode to collapse, effectively turning the device OFF. When the switching bias is removed, the resonator turns back ON, with no degradation in performance.

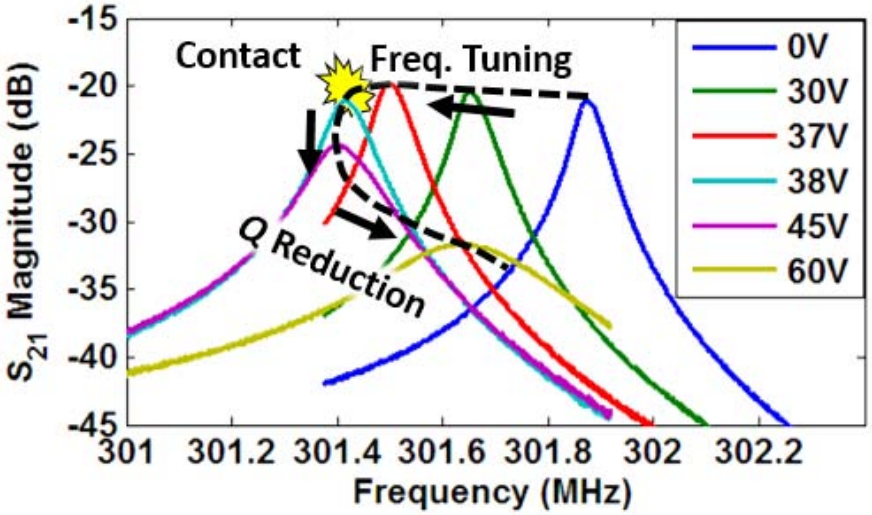

Figure 5.5: Frequency characteristics at various values of V_{bias} for a switchable capacitive-piezo disk resonator with a compliant top electrode. For voltages below 38 V, electrode pulldown induced gap reduction causes a frequency shift. Contact between the actuated top electrode and AlN resonator occurs at 38V, beyond which Q drops as downforce increases.

Switchability Demo Using a Low Stiffness Electrode

To reduce V_{switch}, the top electrode's stiffness may be made more compliant, through a cubic dependency, by reducing the thickness of the top electrode. A second method to reduce V_{switch} is to reduce the gap size g_t over which the top electrode actuates. To demonstrate these effects, we present a second switchable disk resonator from a subsequent fabrication run. This device utilizes the same layout design but is modified to have stronger electromechanical coupling and to actuate using lower voltages. The top electrode's thickness was reduced from 600 nm to 300 nm, the disk-to-top-electrode gap spacing (g_t) was reduced from 250 nm to 120 nm, and the AlN's piezoelectric e_{31} coefficient was also increased, as gauged by a reduction of the full-width half maximum rocking curve measurement by an X-ray diffractometer, from 2.3° to 1.6°. The bottom electrode material was changed to n-doped polysilicon so as to use the same material as the top electrode, while thickness was increased to 2.0 μm to attain a reasonably low sheet resistance of 5 Ω/□.

Six measurements are presented in fig. 5.5, each of which corresponds to a different value of V_{bias}. Starting out, varying V_{bias} between 0 and 37 V yields a series capacitance dependent resonance frequency shift, the mechanism for which is described in section 5.2. Once V_{bias} reaches 38 V, weak electrode contact occurs, which lowers Q by a marginal amount. As the pulldown voltage is further increased, Q continues to drop. Beyond the final V_{bias} of 60 V, at 61V, the device became unable to return to its initial state.

For this device, Q was reduced from a zero-bias value of 5,047 down to a minimum value of 923 at 60 V. Preferably, Q should drop to below 100. This result shows that it's possible

to actuate using small voltages and that analog tuning of the amount of damping (Q) is possible. However, a proper switch demands greater reduction in Q while still allowing a return to the on state than this low stiffness actuator can generate. Either adhesion force must be reduced or the restoring force must be raised.

Remarks on Reliability: Avoiding Stiction and Breakage

Attaining a modest number of switching cycles, the result of section 5.1 is promising for a prototype device. Still, further development work remains to attain mean operating lifetimes of billions of cycles, or more, as would be needed for most practical applications. Switch reliability improvements are enabled through identifying and addressing potential failure mechanisms. Some possible modes of failure for a switchable capacitive-piezo resonator include electrode fracture, disk detachment from the anchor, and stiction.

Electrode fracture is a concern for designs subjected to excessive bending moments during actuation. Fractures can be avoided during switching by only using designs for which stresses during actuation do not approach the fracture strength of Si, which is 7,000 MPa [84], anywhere on the structure. Galvanic corrosion, which was observed to occur during HF release when using two or more dissimilar conductors, may also increase the likelihood of electrode breakage by creating regions of more highly concentrated stress. Disallowing the use of differing top and bottom electrode materials eliminates the possibility of galvanic corrosion during release.

Disk detachment from the anchor must be avoided during electrode pulldown. Large shear stresses can arise at the stem attachment location, which presents a potential problem if the stem's attachment to the disk is weak, as may have occurred for the device of section 5.1 due to a lithography problem during fabrication. Although making a small stem opening in the AlN disk is desirable to maximize Q, the stem attachment area between poly-Si and AlN on the top of the disk should be made substantially larger than the opening in the AlN disk to strengthen the attachment without affecting Q, thus making the device more resilient against stem detachment.

Total removal of liquid etch byproducts from the hydrofluoric acid release is needed to avoid unwanted liquid surface tension based pull down. Devices of dies that were not cleaned properly after release succumbed to stiction, which also degrades Q in the on-state. In our experiments, devices were rinsed in water followed by methanol, dried using supercritical CO_2, and heated to over 200°C to avoid this problem.

Solid-to-solid adhesion forces (Van der Waals forces) can also cause stiction. Adhesion forces are evident in the hysteresis of the IV curves of micromechanical relays and must not exceed restoring forces when the switching voltage is removed [85]. However, micromechanical relay devices performing electrical switching easily overcome these forces with switching voltages of ≈8 V and readily demonstrate switching lifetime cycle counts in the range of 10^6 to 10^9. For such devices, the limiting failure mode is that the on-state resistance R_{on} increases to unacceptable levels over time, which can occur, for example, due to oxidation when using tungsten electrodes [86]. As an advantage, switchable capacitive-piezo resonators

do not have a conductivity requirement at the point of contact; however, they do require greater contact area and downforce to extinguish resonance. To reduce adhesion at the interface between the AlN and the switching electrode, further study on the benefits of using a low-adhesion electrode material, adding a thin non-stick coating to the AlN, or reducing the contact area through the use of dimples is needed.

5.2 Integrated Capacitive Frequency Tuning For Capacitive-Piezoelectric Disk Resonators

Voltage controlled frequency tuning of AlN micromechanical resonators allows one to compensate unwanted resonance frequency shifts due to either temperature or manufacturing variations, thus ensuring proper operation. Although numerous frequency tuning methods for piezoelectric resonators have been previously demonstrated, none simultaneously achieves integration of the tuning element and the resonator, negligible DC power consumption, and continuous (non-discrete) tuning. Capacitive-piezoelectric transduction, on the other hand, can realize all three while also allowing for higher Q's than piezoelectric resonators with attached electrodes.

Prior AlN Microresonator Tuning Work

Ovenized Tuning

Frequency tuning through microscale ovenization, even using optimized thermally isolating supports, consumes significant DC power. Such devices also require thermal codesign of a heater and resonator. The work of [87] consumes up to 2.8 mW of DC power to achieve a broad tuning range of ≈4,500 parts per million (ppm) on an AlN micromechanical resonator. Although the tuning range is sufficient, the mW-level power consumption of ovenization is undesirable for ultra-low power portable applications.

Switched Capacitor Tuning

As another approach, AlN FBAR oscillators can be tuned through adding capacitance in parallel with the FBAR to reduce parallel resonance frequency, f_p. The work of [32] uses two parallel switched capacitor banks in a Pierce oscillator topology to tune f_p according to a digital control word to effect very wide frequency shifts, up to 7,250 ppm, while sustaining oscillation, attributable to an AlN FBAR's large C_x/C_0 of ≈5%. Although switched capacitor tuning in CMOS is readily suitable for tuning a large FBAR with a low capacitance tuning sensitivity, attofarad-level unit capacitance would be needed for VHF contour mode resonators given their much smaller typical sizes.

Varactor Tuning

Varactor based tuning, in contrast, offers a continuous range of voltage controlled tuning capacitance, albeit with a smaller tuning ratio, C_{max}/C_{min}, than is achievable in CMOS using switched-cap tuning. The work of [88] reports varactor based frequency tuning of AlN as an improvement over ovenization citing the advantage of virtually zero power consumption. Here, an off-the-shelf varactor is connected to one or more electrodes of a 13 MHz resonator to effectively stiffen the device and increase its series resonance frequency f_s. The varactor-tuned resonators achieve ≈600 ppm of frequency tuning when one tuning electrode is used (out of four) and ≈1,500 ppm when two tuning electrodes are used. Notably, these tuned devices have rather large motional capacitances C_x's and tuning capacitances C_{min}'s of several fF and several pF, respectively, due to their operating frequency. To increase resonance frequencies towards VHF and UHF, such resonators, and hence their varactors too, would typically need to be scaled down in size dramatically, and would thus need very tight integration of tuning elements and resonators to mitigate parasitics, e.g., either by flip-chip bonding or co-fabrication on the same die. Since contour mode resonators are advantageous primarily due to their layout-defined resonance frequencies, one can envision a multi-frequency system utilizing corrective capacitive tuning on many such resonators, for which numerous variable capacitors, varactors or otherwise, would be needed, consuming considerable space or chip area. For increased compactness, reduced cost and improved ease of design, it would be preferable if the variable capacitor were integrated into the resonator itself and properly sized.

Structure and Operation of Frequency Tunable Capacitive Piezoelectric Disk Resonators

Figure 5.6 depicts a 300 MHz radial contour mode capacitive-piezo disk resonator which is specially designed for effective frequency tuning [74]. The distinguishing feature of this device, which otherwise operates similarly to the one of fig. 5.2, is its compliant folded-beam top electrode suspension, which allows for low actuation voltages while minimizing bending of the top electrode plate.

Figure 5.7 presents the voltage-controlled top electrode pull-down phenomena used to tune series resonance frequency via the cross sections of (a) an untuned and (b) a tuned capacitive piezoelectric AlN radial contour mode disk resonator. Introducing top and bottom gaps g_t and g_b, and hence series capacitances C_{gt} and C_{gb}, above and below the AlN resonator imparts a gap dependent frequency shift to the resonator. Frequency tuning is effected via the voltage controlled reduction of either g_t, as is shown in fig. 5.7, or g_b. The AlN disk, shown in dark gray, is suspended between a pair of top and bottom polysilicon electrodes, shown in light gray, by a central stem. The top electrode, which appears to be floating in the illustrations, is supported by the compliant suspension utilizing folded beams of fig. 5.6. To tune the device, an applied bias voltage V_{tune} generates an attractive force between the

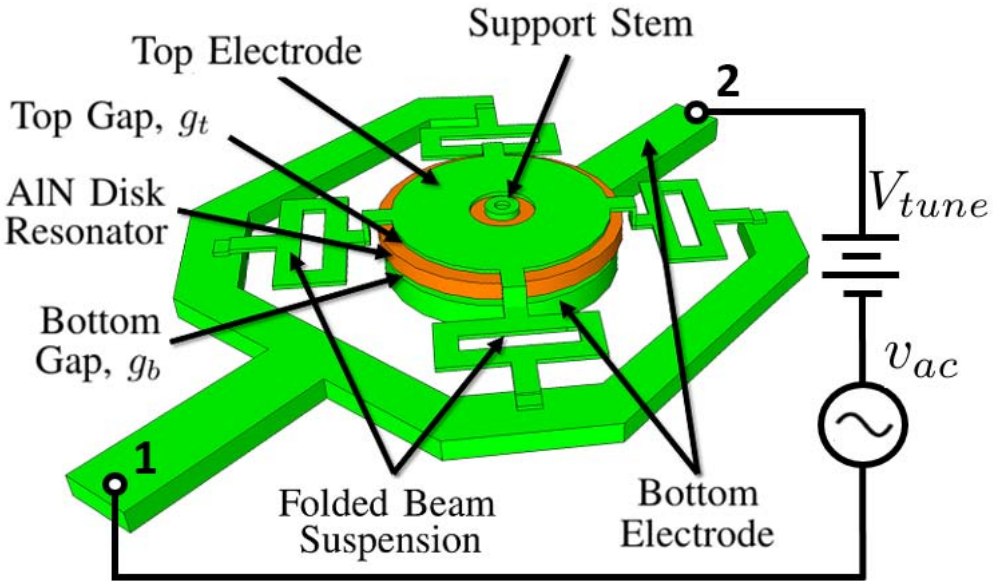

Figure 5.6: Illustration of a frequency tunable 300 MHz capacitive-piezo disk resonator. The device's top electrode suspension is made more compliant by using folded beam supports, enabling vertical actuation with minimal bending of the electrode.

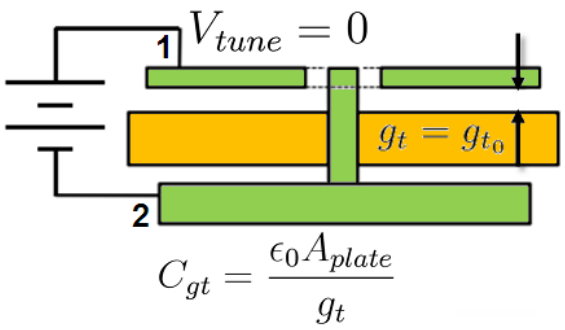

(a) An untuned capacitive piezo disk resonator for which $V_{tune} = 0$ and for which top electrode vertical displacement is zero.

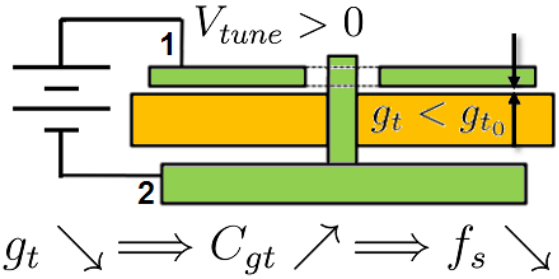

(b) A tuned resonator for which $V_{tune} > 0$. Descent of the top electrode increases series capacitance, C_{gt}, and decreases series resonance frequency, f_s.

Figure 5.7: Cross sections of an (a) untuned and a (b) tuned capacitive-piezoelectric AlN radial-contour-mode disk resonator. Here, the top gap g_t is reduced by V_{tune}.

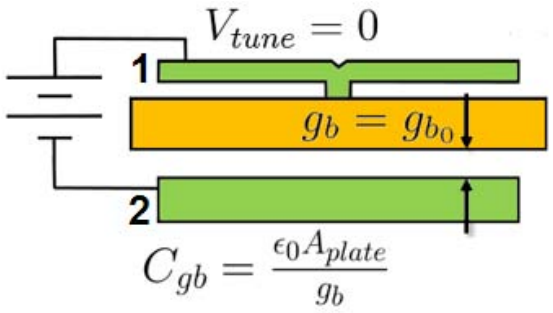

(a) An untuned top-electrode-supported bottom gap actuated resonator for which $V_{tune} = 0$ and for which downward displacement is zero.

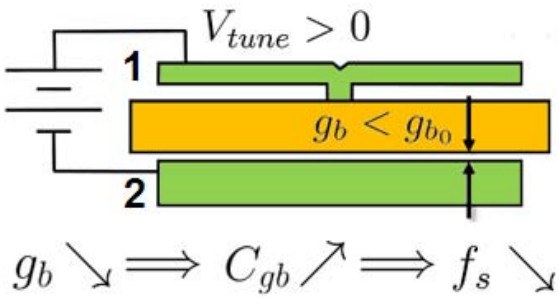

(b) A tuned resonator for which $V_{tune} > 0$ and for which nonzero resonator displacement causes gap reduction.

Figure 5.8: Illustration of bottom gap tuning, with which the AlN disk moves with the top electrode. Cross sections are included for an (a) untuned and a (b) tuned capacitive-piezoelectric AlN radial-contour-mode disk resonator using a top electrode anchor. Here, the bottom gap g_b is reduced by V_{tune}.

electrodes that pulls down the top electrode, as is illustrated in fig. 5.7b. The reduced gap increases series capacitance C_{gt}, thereby decreasing the series resonance frequency, f_s.

Top Gap Tuning vs. Bottom Gap Tuning

The device shown in fig. 5.7 is an instance of a top gap tuned resonator, for which the top electrode moves relative to the resonator. One can also make a bottom gap tuned resonator, c.f. fig. 5.8, by anchoring the resonator to the top electrode rather than the substrate. Thus, when the top electrode descends, the resonator moves with it, and the bottom gap g_b changes. A top electrode supported resonator allows for complete electrode coverage in our fabrication sequence, thus offering better electromechanical coupling and increased tuning range. Whether C_{gb} or C_{gt} is tuned, what ultimately matters for frequency tuning is the variation in total equivalent series capacitance of the top and bottom gaps, C_g, which depends on the total gap spacing g_{total}.

$$C_g = \frac{C_{gb}C_{gt}}{C_{gb} + C_{gt}} = \frac{\epsilon_0 A_e}{g_t + g_b} = \frac{\epsilon_0 A_e}{g_{total}} \tag{5.1}$$

Top Electrode Suspension Design

The top electrode suspension is designed to do the following: (a) have a low enough stiffness to enable reasonably low tuning voltages; (b) allow for vertical movement of the top electrode while ensuring uniform displacement over the plane of the electrode; (c) have

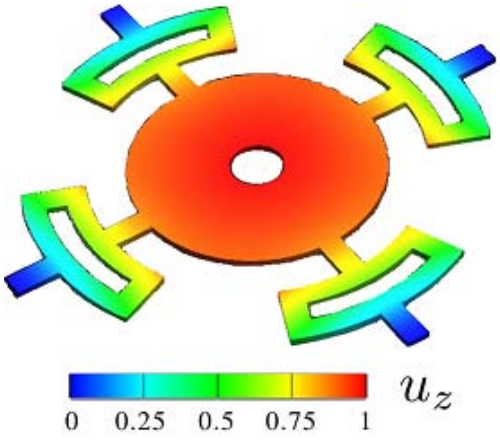

(a) A 3D rendering in COVENTOR of the chosen top electrode suspension design. Anchors are shown in blue. Color indicates displacement u_z due to a downward force on the electrode.

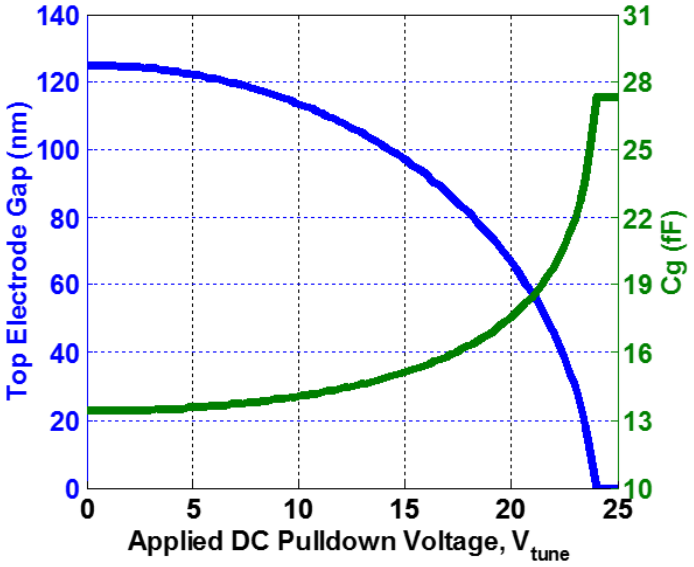

(b) Top electrode gap (blue) and gap capacitance C_g (green) vs. V_{tune} for the suspension of fig. 5.9a for a 1.6-µm-thick capacitive-piezo AlN disk resonator with 125 nm initial top and bottom gaps.

Figure 5.9: Top electrode suspension (a) illustration and (b) displacement and capacitance vs. V_{tune} simulation.

minimal degrees of freedom to avoid unwanted rotations; (d) have a low enough electrical resistance to avoid loading Q; (e) be compact enough to allow multiple $\lambda/2$-coupled devices to exist side-by-side with each having its own suspension; and (f) have lithographically resolvable critical features. Meeting these requirements, the design of fig. 5.9a was chosen and its suspension was FEM simulated to determine its displacement profile in response to a distributed force. Notably, design criterion (b) is met since the coloring of the circular plate, which indicates its vertical displacement, is quite uniform. The suspension consists of four axially-symmetric folded-beam springs and is entirely contained within the desired compact form factor. Using finite element analysis, the vertical stiffness of the device, k_z, is calculated to be 89 N/m for a 300 nm thickness. To predict gap tuning as a function of V_{tune}, one solves eq. (5.2):

$$F_z(u_z) = \frac{1}{2}\frac{\mathrm{d}C_g}{\mathrm{d}u_z}V_{tune}^2 = k_z u_z \tag{5.2}$$

Through plotting gap size vs. V_{tune} as is shown in fig. 5.9b, the voltage at which electrode to resonator contact occurs is predicted to be 24V. Notably, over half of the gap tuning occurs within the narrow range of 20-24V.

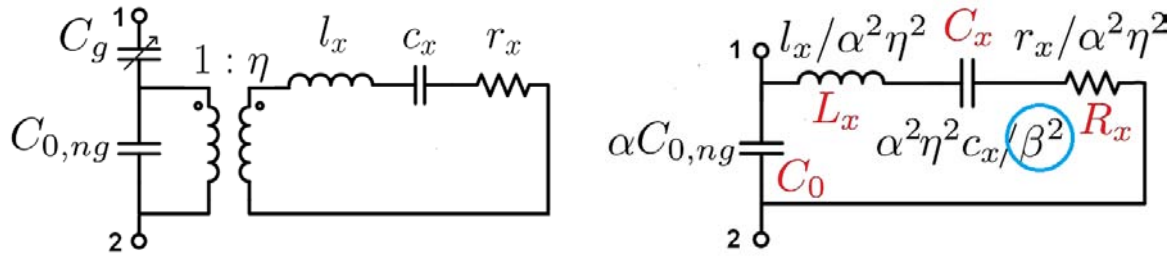

(a) Electro-mechanical circuit for a capacitive-piezo resonator

(b) Equivalent Butterworth Van Dyke (BVD) circuit

Figure 5.10: Equivalent models for a tunable capacitive-piezo resonator. The series resonance frequency tuning term β is encircled.

Frequency Tunability is Described by the Effect of C_g on the Equivalent Circuit

Frequency tunability in a capacitive-piezo resonator is described by the effect that a variable series capacitance has on the resonator's equivalent BVD circuit. The frequency tuning term β, which is a function of C_g, affects the motional capacitor, C_x, while leaving the motional inductor L_x unaffected.

Figure 5.10 presents two equivalent circuit models for a tunable capacitive-piezo resonator with a single transducer. This model was presented previously in Chapter 3. Here, in fig. 5.10a, we emphasize that the equivalent series capacitance due to the gaps, C_g, is *tunable*. As previously shown, this circuit is behaviorally equivalent to the circuit of fig. 5.10b having Butterworth Van Dyke (BVD) circuit component values, C_0, L_x, C_x, and R_x, and for which C_x is tuned by $1/\beta^2$. To account for the changes introduced by capacitive gaps, two factors α and β are introduced to modify the component values, as follows:

$$\alpha = \frac{V_{AlN}}{V_{in}} = \frac{C_g}{C_g + C_{0,ng}} = \frac{t_{AlN}}{t_{AlN} + \epsilon_{r,AlN}(g_b + g_t)} \tag{5.3}$$

$$\beta = \sqrt{\frac{C_g + C_{0,ng} + c_x\eta^2}{C_g + C_{0,ng}}} = \sqrt{1 + \frac{C_{x,ng}}{C_g + C_{0,ng}}} \tag{5.4}$$

These two parameters, which were introduced in Chapter 3, are key to understanding frequency tuning. In eq. (5.3), α is the factor by which input voltage in the piezoelectric is reduced by the gaps through capacitive division. Although α does not describe the amount of tuning, we see that, at least for a single transducer device, coupling and frequency tuning are directly linked together. In eq. (5.4), β is the factor by which f_s is tuned. Here, β is slightly greater than one and depends on total gap size. For example, if β equals 1.001, frequency is tuned upward by 1000 ppm. Both α and β approach one as g_t and g_b drop to zero. Solving the BVD circuit for the frequency of minimum impedance, f_s takes the form:

$$f_s = \frac{1}{2\pi}\sqrt{\frac{1}{L_x C_x}} = f_{s,ng}\beta = f_{s,ng}\sqrt{1+\frac{C_{x,ng}}{C_{0,ng}+C_g}} \tag{5.5}$$

As C_g drops from infinity to zero, f_s rises between the natural eigenfrequency of the resonator $f_{s,ng}$ and the gap independent parallel resonance frequency f_p. The electromechanical coupling, $k_{eff}^2 = C_x/(C_0+C_x) \approx C_x/C_0$ of this circuit, a performance metric gauging both maximum fractional resonator tuning range and fractional filter bandwidth, derives from the relationship between f_p and f_s as follows:

$$f_p = f_s\sqrt{1+\frac{C_x}{C_0}} \rightarrow \frac{C_x}{C_0+C_x} = \frac{f_p^2 - f_s^2}{f_p^2} = k_{eff}^2 \tag{5.6}$$

Resonator Tuning Range

The available capacitive frequency tuning range for this device is the frequency difference between its minimum possible f_s, and maximum possible f_p values. Thus, to determine the largest tuning range one can attain, one can simulate the performance of a capacitive-piezo resonator with gaps reduced below 1 nm, yielding the gapless series resonance frequency, $f_{s,ng}$. As eq. (5.7) shows, $C_x/2C_0$ for a resonator is a convenient expression for the maximum possible fractional tuning range.

$$\frac{\Delta f_{max}}{f_{s,ng}} = \frac{1}{2}\left(\frac{2(f_p - f_{s,ng})}{f_{s,ng}}\right) = \frac{1}{2}\frac{C_{x,ng}}{C_{0,ng}} \tag{5.7}$$

Simulation of Theoretical Maximum Tuning Range

Our model of the 300MHz 11.2-μm-radius capacitive-piezo disk of this work having full electrode coverage and 1 nm gaps predicts $C_x/C_0 = 2.2\%$. Thus, a maximum fractional frequency tuning range of 1.1% (11,000 ppm) is available. To illustrate the wide available tuning range, fig. 5.11 presents multiple simulated S_{21} frequency characteristic plots for a capacitive piezo disk resonator having g_b=1nm and a widely actuatable top electrode gap, g_t. Here, g_t is varied from 1 nm to 10 μm. The plot legend lists the nine different values of total gap size included in the simulation and their corresponding frequency shifts from the zero gap state.

Constraints on Making Large Gaps for Tuning

Frequency tuning with large gaps involves several undesirable tradeoffs. For example, excessive values of $g_{total} = g_t + g_b$, e.g., beyond 500 nm, can greatly diminish electromechanical coupling. Also, gap tuning efficiency, $\frac{d\Delta f_s}{dg_{total}}$, drops as g_{total} increases, eventually becoming quite small at large gap sizes. Gap tuning efficiency drops from 60 ppm/nm at 0 nm to only 3.8 ppm/nm at 500 nm. Third, accommodating a large range of motion would likely result

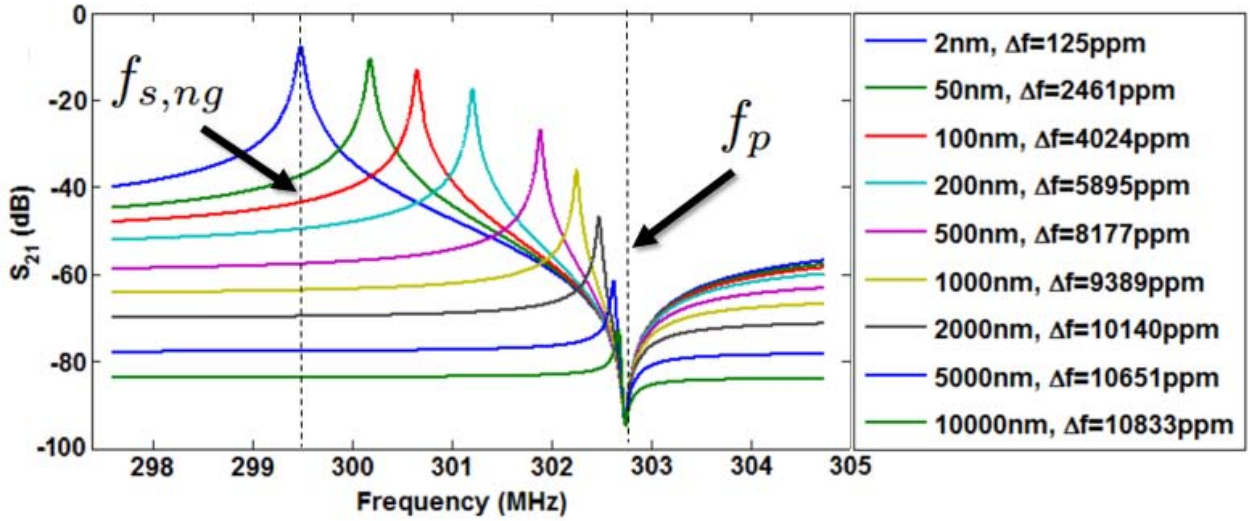

Figure 5.11: Simulated gap reduction based frequency tuning for an 11.2-μm-radius, 1.6-μm-thick, AlN radial contour mode resonator demonstrating a maximum tuning range of ≈11,000 ppm. Nine frequency characteristics are shown at various values of g_{total} ranging from 2 nm to 10 μm.

in reduced fine gap tuning accuracy at small gap sizes. In view of these considerations, one should keep gap sizes below a judicious value of $g_{total,max}$.

Constraints on Making Small Gaps for Tuning

Choosing to fabricate capacitive-piezo resonators with very small gaps also involves undesirable tradeoffs. First, under imperfect deposition conditions, bending moments in AlN thin films can arise, typically causing structures to bend upward. Such strain gradients set a minimum limit on top gap sizes if electrode contact is to be avoided. Beyond stress concerns, reducing both g_b and g_t very aggressively may also lead to fabrication difficulties related to stiction, post-release cleaning, sacrificial layer pinholes, and/or surface roughness. Also, due to the need to overetch AlN with the current fabrication process, a thick bottom sacrificial oxide eases concerns of excessively overetching the bottom electrode interconnect layer. One should thus avoid scaling g_{total} too aggressively simply to ensure proper operation.

Optimal Sizing of Gaps

In this work, top and bottom gaps of 120 nm were chosen to attain a respectable tuning range of ≈1,600 ppm without risking device failure. Here, the chosen tuning ratio, C_{max}/C_{min}, is 2. Larger tuning ratios may be attained by reducing the size of the stationary gap or increasing size of the actuated gap. To examine the relationship between g_{total} and $\Delta f_s = f_s - f_{s,ng}$, refer to fig. 5.12. Overlaid on the plot are annotations showing the designed

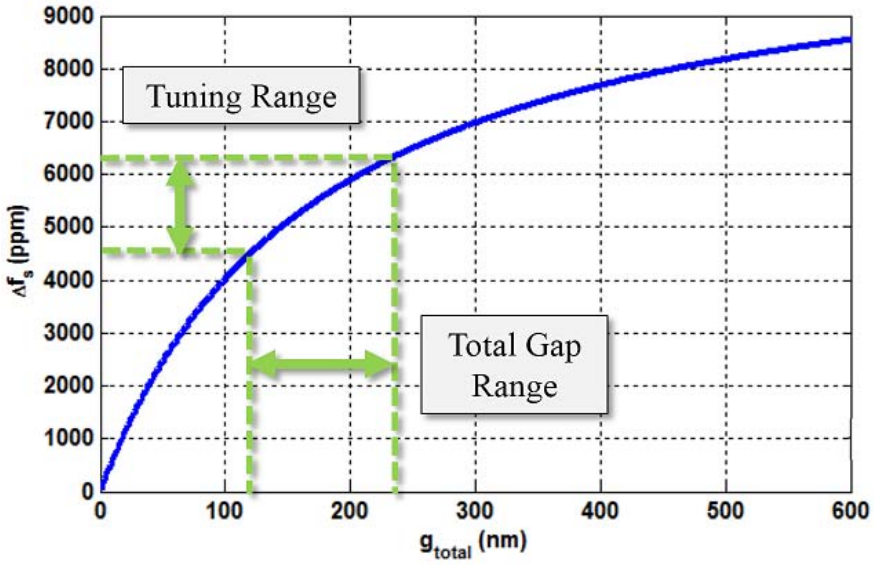

Figure 5.12: Simulated fractional frequency shift from zero-gap state vs. g_{total} for an 11.2-μm-radius, 1.6-μm-thick, radial contour mode capacitive-piezo AlN resonator with reducable capacitive gaps. Included in the plot are annotations showing the achieved gap range of this work and its corresponding tuning range.

gap range for our device and its associated tuning range of 1600 ppm. Considering possible future performance improvements, through using a wider range of g_{total} values, e.g., with a fixed g_b of 70 nm and a variable g_t between 0 nm and 430 nm, 5,200 ppm of tuning would be attained, representing a potential threefold improvement. Additional design iterations will determine the true limits of this technology.

Dedicated Tuning Transducers

Two gap reduction based capacitive tuning methods are explored in this work: tuning through an input/output (I/O) transducer, which affects the I/O coupling, α, of eq. (5.3); and tuning through a separate tuning transducer, which does not. Our analysis so far has emphasized tuning for single transducer devices for which I/O transduction and tuning transduction occur through the same electrode pair. Single transducer capacitive-piezo resonators advantageously minimize R_x and maximize C_x/C_0; however, the achieved values do not stay constant over the tuning range. If R_x and C_x/C_0 change too much through tuning f_s, some oscillator or filter designs may not function properly. Additionally, single transducer tuning often requires putting a tuning voltage in the I/O signal path, which can require a bias tee [71]. Using a dedicated tuning transducer outside the I/O signal path circumvents these issues, allowing one to tune f_s while R_x and C_x/C_0 stay constant.

A dedicated capacitive-piezo tuning element, the circuit model of which is shown in fig. 5.13, allows a voltage controlled variable capacitance linked to an electromechanical

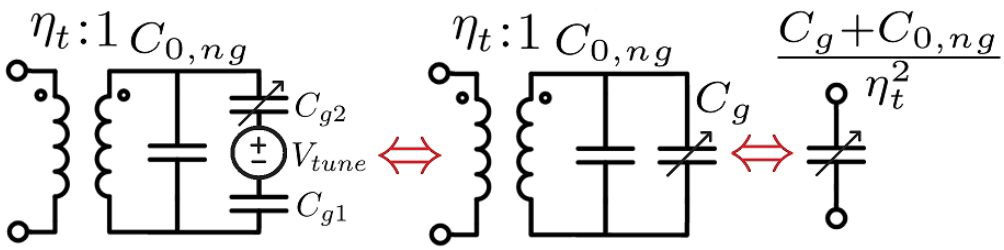

Figure 5.13: Electromechanical circuit model for a dedicated capacitive piezo tuning element and its equivalent series compliance seen by $c_x = 1/k_r$, the inverse stiffness of the resonator.

transformer with transduction factor η_t to effectively act as a variable compliance, i.e., an inverse stiffness having units of [m/N]. This tuning element acts in series with the l_x, c_x, and r_x elements of fig. 3.7a, adding to resonator stiffness. To calculate the frequency tuning for the overall resonator, simply substitute $c_{x,tuned}$ of eq. (5.8) for c_x in both fig. 3.7a and β of eq. (5.4):

$$c_{x,tuned} = \frac{c_x(C_g + C_{0,ng})}{c_x\eta_t^2 + (C_g + C_{0,ng})} \tag{5.8}$$

As an example of the performance tradeoff of switching from I/O gap reduction based tuning to separated tuning, if the electrode configuration of a single transducer device is modified to instead allocate 50% of its area to dedicated I/O and 50% to dedicated tuning, hence reducing η and η_t, holding all else constant, R_x will increase by a factor of four and C_x/C_0 (and hence tuning range) will drop by a factor of two.

Experimental Results

We report experimental tuning demonstrations at 300 MHz of (a) a single transducer bottom-gap-tuned resonator to verify maximum tunability and minimal R_x and (b) a two transducer top-gap-tuned resonator to verify constant R_x tuning. Both devices were tested in a vacuum probe station using a properly calibrated network analyzer with a 50Ω termination at both ports. Transmission scattering parameter (S_{21}) measurements were collected and plotted for various values of V_{tune} to verify operation.

Single-Transducer Tuned Resonator

fig. 5.14 presents frequency tuning of a top-supported single-disk device with one transducer for both tuning and input/output transduction. The measurement setup of fig. 5.3 is used. The measurement plot includes a series of 2-port transmission (S_{21}) measurements taken with various values of V_{tune} ranging from 0 to 24V. Here, the measured tuning range is 1547 ppm. The R_x of this device is showed to decrease as V_{tune} is increased, agreeing with the model. Note that f_p stays relatively fixed, as is simulated in fig. 5.11. If variable

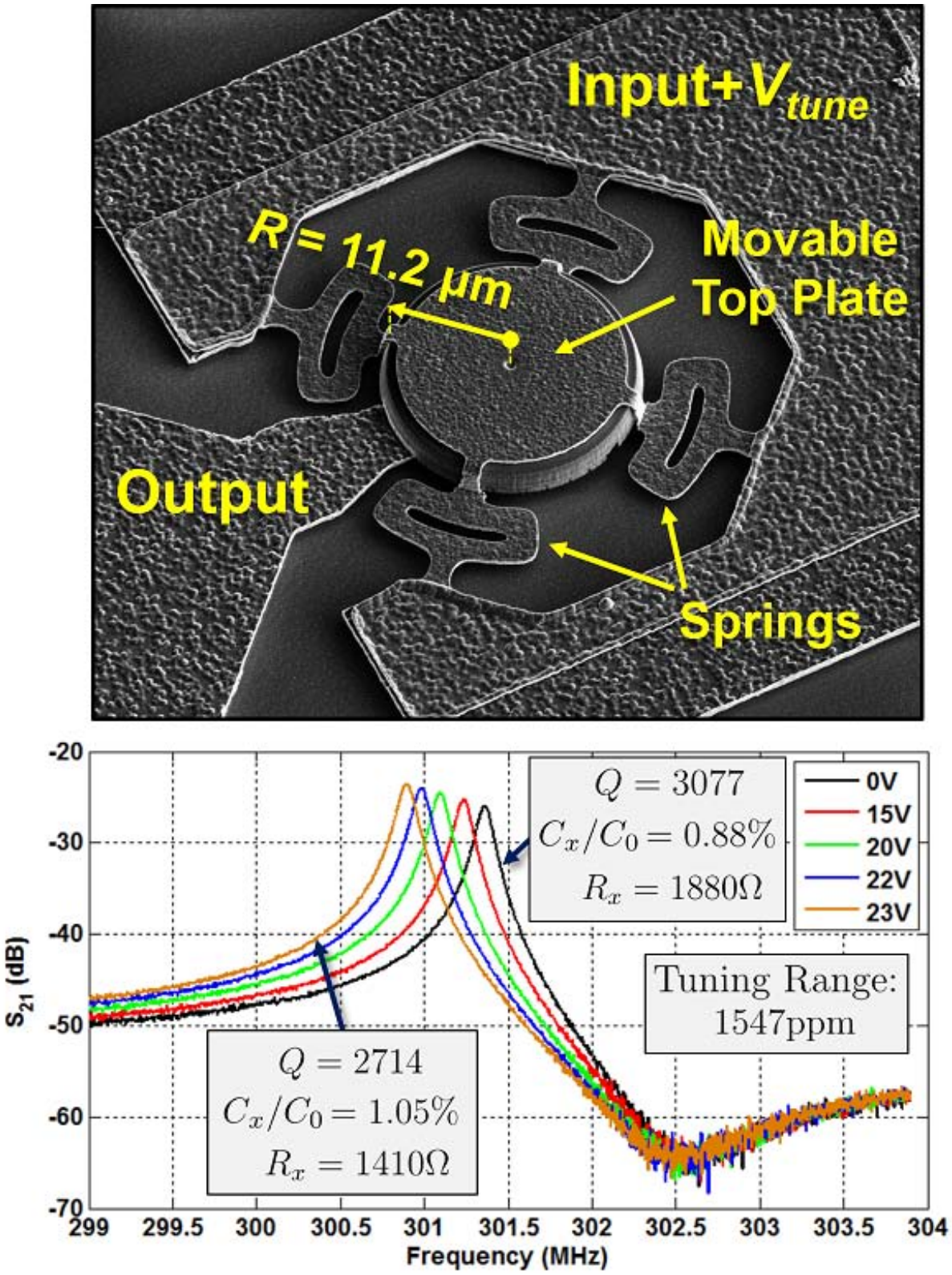

Figure 5.14: Single transducer tuning demonstration. Gap reduction causes frequency tuning and an increase in coupling.

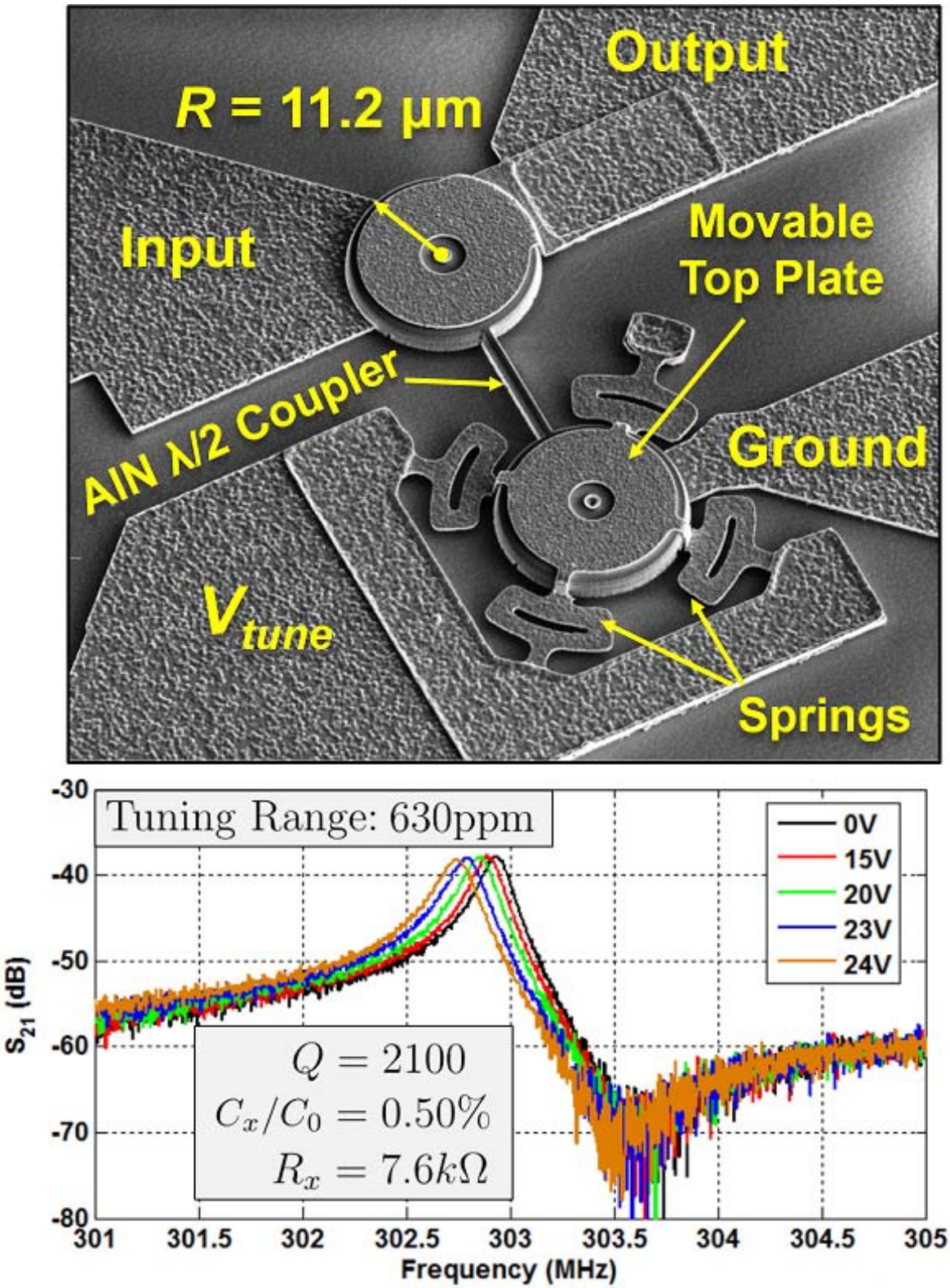

Figure 5.15: A dedicated tuning transducer shifts the resonance frequency of a two-disk structure without affecting the coupling strength of the input/output transducer.

coupling is problematic, then alternatively, a dedicated tuning electrode may be used, at the cost of reduced tuning range.

Two Disk Array Resonator With a Dedicated Tuning Transducer

fig. 5.15 presents tuning of a two-disk device utilizing one electrode pair for I/O transduction and a separate electrode pair for top gap reduction tuning. As shown in the SEM, two radial contour-mode resonators are mechanically coupled using an extensional mode 800-nm-wide coupling beam of acoustic length $\lambda/2$ to form a single degree of freedom resonant system. The upper resonator is surrounded by an I/O transducer electrode pair through which its S_{21} magnitude vs. frequency is measured. Surrounding the lower resonator is the same tuning transducer shown in fig. 5.13, consisting of a grounded bottom electrode and bias voltage (V_{tune}) actuated spring-supported top electrode. The frequency characteristic is shown to uniformly shift downward in frequency as V_{tune} is increased, with no changes in R_x, Q, and C_x/C_0, as expected.

Verification of Model Using Experimental Results

A summary of capacitive-piezo tunable resonator model parameters that correctly predict tuning behavior of our demonstrated devices is included in table 5.1.

Table 5.1: Tunable Resonator Model Parameters

Model Parameter	**Single Disk Resonator**	**Two Disk Resonator**
r_x	9.3×10^{-7} kg/s	2.75×10^{-6} kg/s
l_x	1.535×10^{-12} kg	3.070×10^{-12} kg
c_x	1.840×10^{-7} s^2/kg	9.20×10^{-8} s^2/kg
η, η_t	4.90×10^{-5} C/m	4.50×10^{-5} C/m
$C_{0,ng}$	$1.99 \times 10^{-14} F$	1.88×10^{-14} F
$g_{tot,IO}$ [min, max]	[136 nm, 240 nm]	[240 nm, 240 nm]
$g_{tot,tune}$[min, max]	(same as IO)	[150 nm, 240 nm]
α [max, min]	[0.56, 0.42]	[0.42, 0.42]
β [min, max]	[1.00488, 1.00639]	[1.0029, 1.0029]
$c_{x,tuned}/c_x$[min,max]	N/A	[0.9943, 0.9956]
Δf_s	-1510 ppm	-650 ppm

Remarks on Tuning

Voltage controlled gap reduction has now been shown as an effective means for passively controlling the resonance frequencies of capacitive-piezo AlN micromechanical resonators.

Placing integrated variable capacitances directly inside of VHF AlN resonators also enables higher Q's with strong coupling. We have demonstrated 1547 ppm of tuning at 300 MHz using a single transducer and 630 ppm of tuning using a dedicated tuning electrode to maintain constant R_x. Though these initial results are impressive, analysis shows that through optimizing gap sizes, a substantial increase in the tuning range will be feasible. Frequency modulation, passband correction of channel-select filters, and filter tunability may also be implemented using this technique.

We believe that the tuning method presenting in this work will be useful for improving accuracy or reducing temperature induced frequency shifts in capacitive-piezoelectric resonators, for which measured TCF's of -15 ppm/K are typical. A study on the frequency variability of capacitive piezoelectric disk resonator arrays in [89] found that the manufacturing precision of four disk arrays at 300 MHz has a standard deviation of 160 ppm–the six-sigma range is thus 960 ppm. To compensate for both manufacturing variability and temperature induced shifts over the military range of -55°C to 85°C, a total tuning range of 3660 ppm is needed, which could be attained by shrinking the non-varying gap size to 70 nm.

5.3 C_x/C_0 Control

The ability to reduce g_t or g_b via voltage controlled electrode actuation enables control over the electromechanical coupling strength, ($k_{eff}^2 = C_x/C_0$) through the modification of α of eq. (5.3), as fig. 5.14 demonstrates. Analysis shows that C_x/C_0 is proportional to α, while R_x is inversely proportional to α^2. Tuning the electromechanical coupling of capacitive-piezo resonators enables the use of three novel techniques which improve performance and control.

Gap Reduction Below Manufactured Gap Sizes

First, reducing a capacitive gap using V_{bias} to be smaller than manufactured allows for greater coupling than is otherwise achievable, which benefits filter or oscillator performance. For example, if a sustaining amplifier for an oscillator were unable to sustain oscillation using its manufactured gap size, it might otherwise be able to oscillate if it had better coupling and reduced R_x due to a reduced gap. As a demonstrated performance improvement, the motional resistance of the single disk device of fig. 5.5 was reduced from 934 Ω to 785 Ω via the application of a 34 V bias. As another approach, to improve manufacturing yields, it may be desirable to manufacture intentionally large gaps to aid cleaning after release. A given V_{bias} could be used to turn the devices on–reducing the gaps and restoring strong coupling.

Decoupling Based Switching

Secondly, control over the amount of coupling also enables the intentional *de*coupling of a device, which could be used as an alternate (or complementary) switching mechanism to the one presented in **??**. Switching may be attained via increasing the gap to a very large value, rather than decreasing it to zero, to transition between the on and off states. To motivate this technique, one obstacle that the switching architecture of fig. 5.1b presents is that quenching the resonance peaks of multiple filters in parallel does not eliminate the unwanted feedthrough and shunt capacitances of off-state devices; however, decoupling them eliminates unwanted reactances. Such parasitics must otherwise be eliminated using inductors. Decoupling based switching, particularly when used in tandem with pulldown based quenching, could potentially offer an effective integrated single chip solution for a multi-frequency filter bank. A proof of concept for this method was demonstrated in [90]; however, the method relies on electrode contact for the on state which limited Q to about 200, which is, interestingly, the off state for our method introduced in section 5.1. For maximum Q, the electrode would be brought in close proximity to, but not contact, the resonator.

Dynamic Coupling without Frequency Tuning

A third aspect of coupling control predicted by theory, which has not yet been demonstrated experimentally, is the potential to dynamically alter the amount of coupling without affecting resonance frequency. Via combining the two effects demonstrated in fig. 5.14 and fig. 5.15, varying the coupling without changing resonance frequency requires actuating the electrodes for dedicated tuning and input/output transduction in opposite directions. Variable coupling could find utility in increasing the allowable dynamic range of capacitive-piezo based signal processors. For high power received signals, the coupling could be reduced to avoid driving the resonator into nonlinear vibration. For low power signals for which greater sensitivity is needed, the coupling could be increased.

5.4 Two-Port Capacitive-Piezo Resonant Systems with Voltage Actuated Electrodes

Resonant capacitive-piezoelectric systems with separated transducers for input and output offer reduced feedthrough capacitance compared to single transducer devices. A two-port configuration may thus be used to make capacitive-piezoelectric microelectromechanical filters with highly discriminating transfer functions. To illustrate the essential elements of such a device with voltage actuated electrodes, fig. 5.16 presents a simple two disk device which shows two transducers sharing an ac-grounded terminal for V_{bias}. A mechanical coupling beam transmits vibrations between input and output. Since V_{bias} is placed outside of the signal path, two-port capacitive-piezoelectric resonant systems do not require a bias tee for electrode actuation of the transducers. For this three terminal device, signal transmission

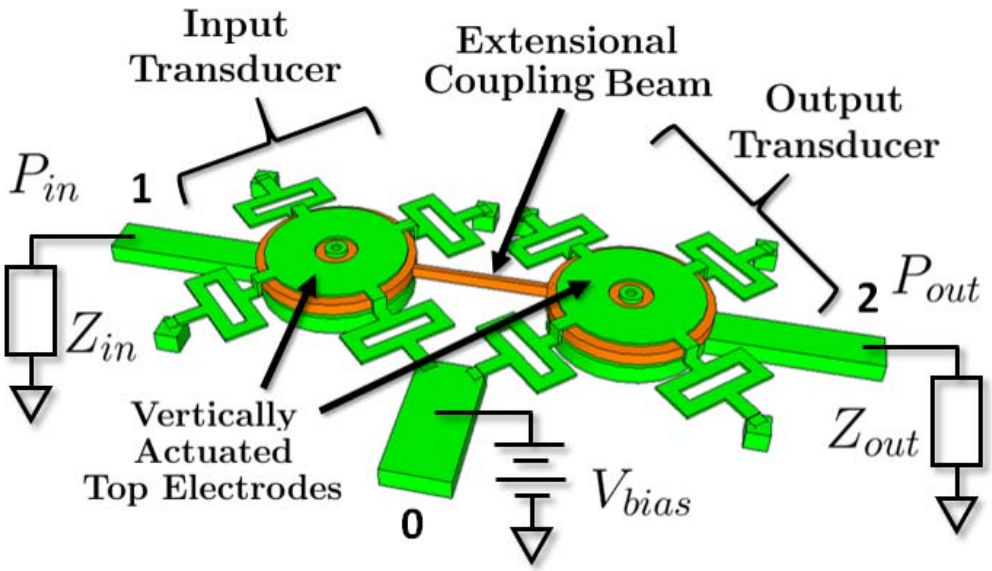

Figure 5.16: A simple implementation of a three terminal capacitive piezoelectric resonator with separate transducers for input and output and a shared terminal for voltage controlled electrode actuation.

between terminals 1 and 2 can be turned on and off via V_{bias} at terminal 3. When used as an analog control variable, V_{bias} can tune electromechanical coupling strength and resonance frequency, as was demonstrated with a single transducer. The same large tuning range which is available to a single capacitive-piezoelectric transducer is available to this three terminal device.

Voltage Actuated Two Port Capacitive Piezo Disk Arrays

While the device of fig. 5.16 serves as a working example of a capacitive-piezoelectric system with separate transducers for input and output, a more practical design uses multiple disks per transducer in order to reduce motional resistance, increase power handling, and improve manufactured frequency precision [89]. Multiple disks, formed into arrays, vibrate in phase by means of mechanical extensional mode coupling beams of acoustic length $\lambda/2$. VHF disk filter systems have been previously demonstrated utilizing a large number of capacitively transduced disks, e.g., 60, as well as thin beams to couple the devices together [48].

The acoustic length of the extensional coupling beam shown in fig. 5.16 that links the input resonator to the output resonator has a strong effect on the operation of the circuit. A beam of acoustic length $\lambda/4$ can be used to evoke a multi-pole resonant response, which is useful for implementing a filter [79]. The fractional bandwidth of the filter is proportional to the width of this coupling beam.

Experimental Results

To demonstrate switching and tuning capabilities of two-port capacitive-piezoelectric disk resonator systems, a number of such devices were fabricated alongside the single transducer devices previously demonstrated. Although lithography and etch problems during fabrication caused some performance degradation, two demonstrations are included.

Two-Port Switchable Disk Array Filter

Figure 5.17 presents an annotated layout view and on/off frequency characteristics for a two-port 3rd order 300 MHz capacitive-piezo switched filter. The device consists of three disk arrays of nine disks each. The three array composite resonators are mechanically coupled in series using two extensional coupling beams of length $3\lambda/4$ to evoke a three pole response. Figure 5.17a includes a color key denoting the four lithography layers used in the device as well as annotated locations of the RF input and output terminals (1 and 2), the V_{bias} terminal (0), electrical ground (GND), and the two coupling beams of length $3\lambda/4$. For switching, this device uses voltage actuated electrode quenching on its center resonator to attenuate signal transmission. This device has top and bottom gaps g_t and g_b of 180 nm and 120 nm, respectively.

For Z_{in} and Z_{out}, 2000 Ω terminating resistors are used. The fractional bandwidth (FBW) of 0.5% is larger than designed, via the coupling beam width, by 2×, which is possibly due to a problem with the fabricated coupling beams, which are connected to the interconnect by thin unwanted stringers present in this fabrication run. Such stringers also degrade Q. Some of the insertion loss observed is due to insufficient coupling due to the larger than expected bandwidth and hence could potentially be compensated using inductors.

The device is switched using a V_{bias} value of 60 V, which was the highest value that could be reached before failing to return to the on state. The S_{21} magnitude for the filter decreases by 15 dB in the off state as compared to the on-state, thus demonstrating the feasibility of two-port switching, while leaving room for performance improvements in future renditions.

Two-Port Frequency Tunable Disk Array Filter

Figure 5.18 presents an annotated layout illustration and frequency tuning measurements for a 150 MHz frequency tunable two port capacitive-piezoelectric filter consisting of two mechanically coupled four-disk arrays, each in a two by two arrangement. The filter is shown to tune the center frequency of its passband by 1140 ppm, from 153.18 MHz to 152.92 MHz. The 3-dB bandwidth of the untuned filter is 525 kHz, representing a 0.34% fractional bandwidth. The decreased tuning voltage of only 10 V is attributable to the reduced stiffness of the electrode due to its larger radius of 22.4 μm.

One limitation of large disks using capacitive-piezo transducers is the increased likelihood of electrode contact due to strain gradients in the film which cause vertical displacements. Larger AlN disks are more likely to contact the electrodes at the edges even without bias, since vertical displacement vs. radius follows a square law. Electrode contact reduces Q,

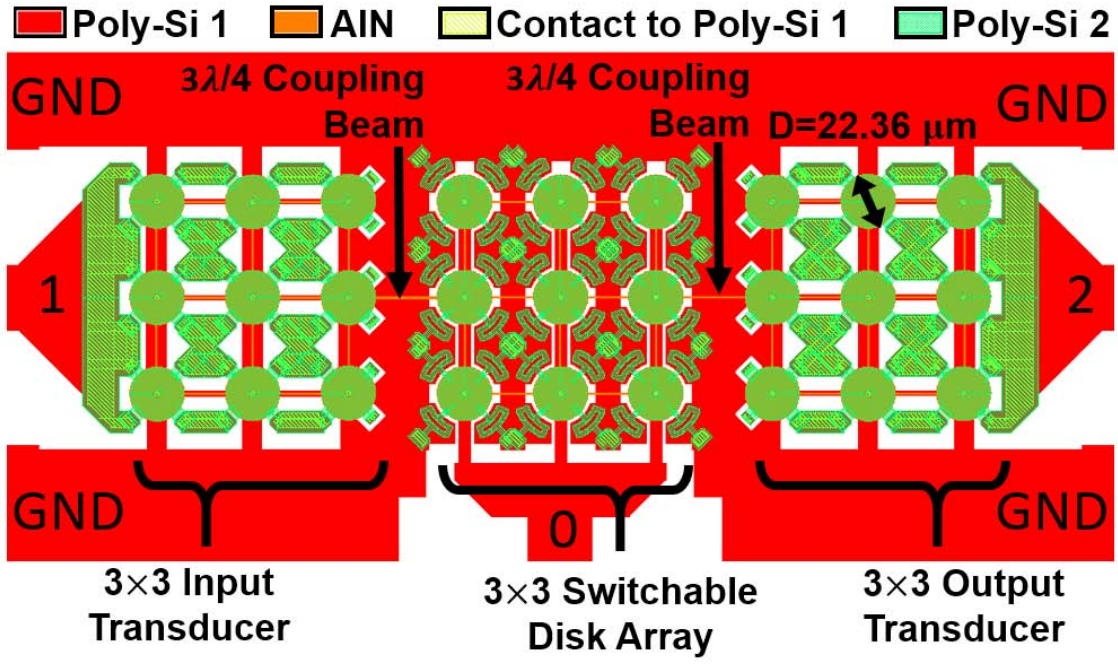

(a) Annotated layout illustration of a 300 MHz 3rd order switched filter.

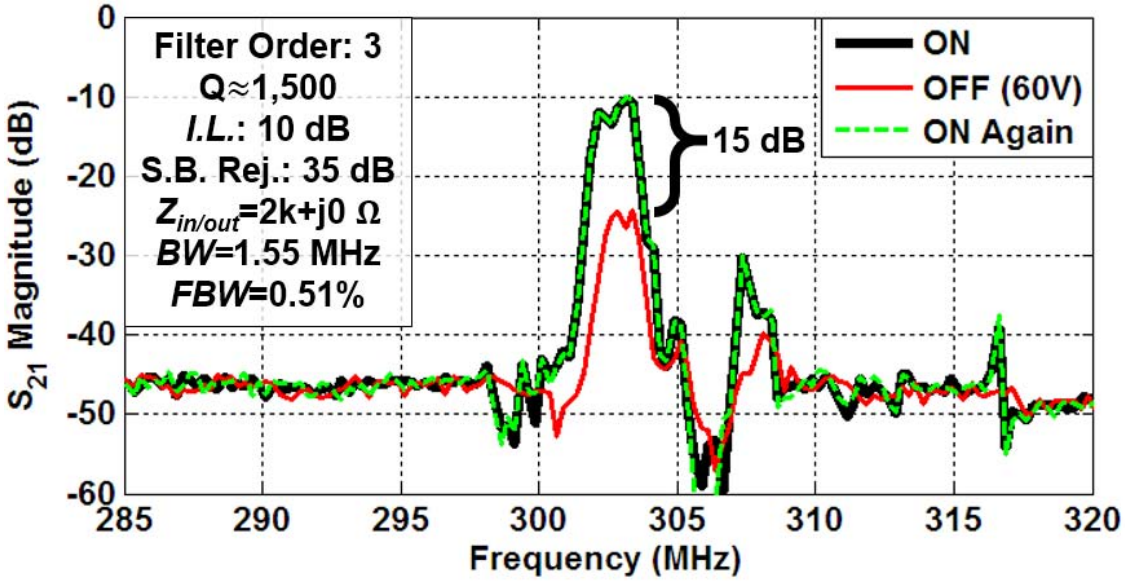

(b) Filter information and S_{21} magnitude frequency responses for the on, off, and on again states.

Figure 5.17: Self-switching demonstration of a two-port capacitive-piezo filter.

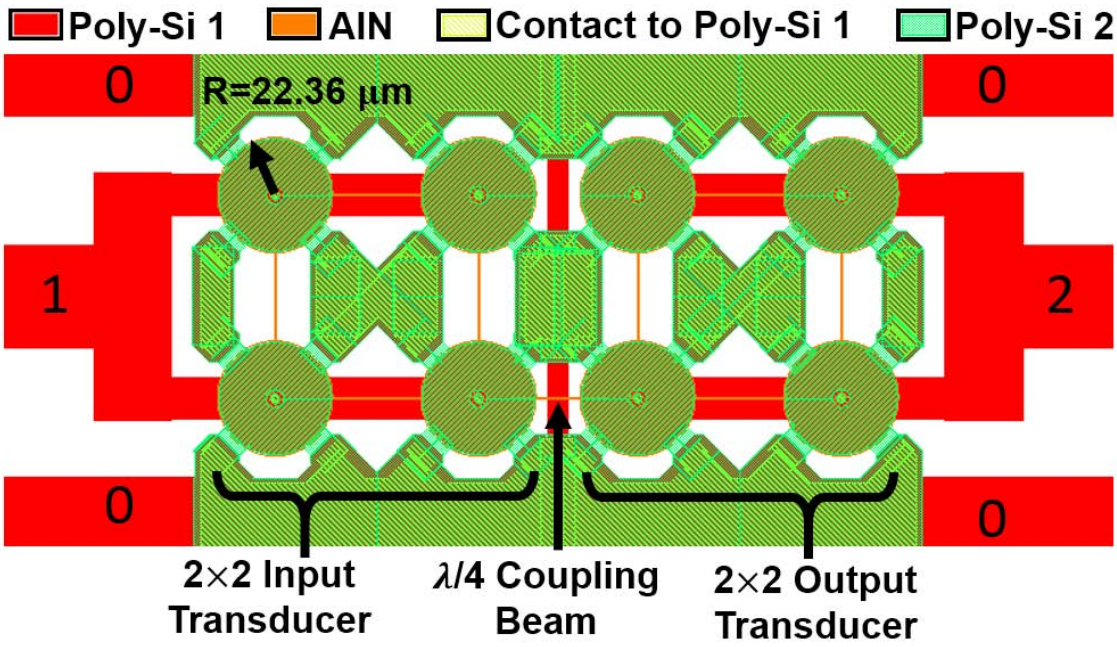

(a) Annotated layout illustration of a frequency tunable 150 MHz 2nd order capacitive-piezo disk array filter.

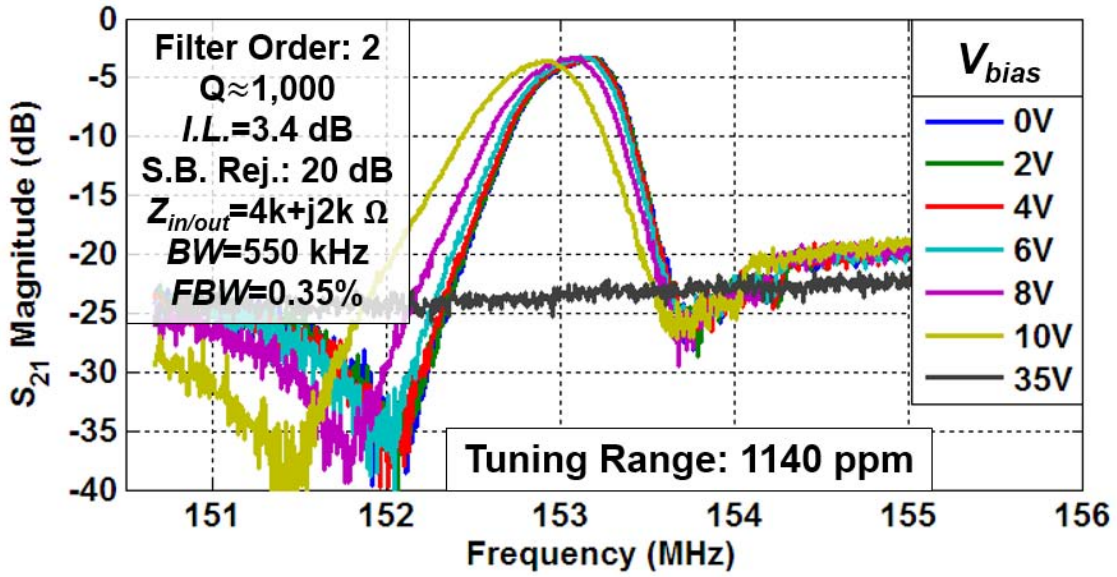

(b) Frequency tuning demonstration for a capacitive-piezo disk array filter.

Figure 5.18: Frequency tuning demonstration of a two-port capacitive-piezo filter

degrading insertion loss. Reducing the strain gradient of the AlN film is a targeted fabrication process improvement for future renditions of these devices.

Remarks

There are several paths forward for further improving the performance of the demonstrated two-port capacitive-piezo resonators. Larger array sizes, smaller bandwidths, and stronger electromechanical coupling through using smaller capacitive gaps will reduce needed filter termination impedances to more reasonable levels of several hundred ohms. Additionally, higher on-state Q's, e.g. 8,800 instead of 1,500, will reduce insertion loss. Such Q's have already been demonstrated on the same fundamental device used to make the arrays, and arrays with Q's as high as 5,000 have so far been demonstrated [89]. For the switched resonators, a lower off-state Q is also needed. A stronger downforce in tandem with an electrode with higher stiffness and more mass, as was used in section 5.1, would generate more effective quenching and hence a larger reduction in transmission in the off state. Additionally, capacitive isolation between input and output is key to maximizing stopband rejection. Stopband rejection as high as 50 dB has been demonstrated in a similar capacitive piezoelectric filter, and can be further improved using additional ground shielding between input and output transducers, stronger electromechanical coupling, or even differential operation. Lastly, eliminating stringers should help smooth out the passbands and minimize spurious responses by ensuring proper operation of coupling beams, which do not perform ideally when physically connected to the substrate.

5.5 Conclusions

Voltage actuation of the top electrode of a capacitive-piezoelectric transducer has been shown to enable quenching-based on/off switching, frequency tuning, and coupling control. Beyond the devices demonstrated here, there exists significant potential for implementing more complex resonant systems, made from AlN, with unprecedented capabilities which take advantage of high Q values, frequency tuning for temperature compensation, switchability, the ability to both decouple a filter and to increase its coupling, and multi-frequency capability on the same chip. Although refabrication will be needed, capacitive-piezoelectric disk array technology is capable of creating, for example, an individually addressable channel selecting filter bank, without needing common external components including switches and tuning varactors to control the device.

Chapter 6

Fabrication

This chapter begins with a detailed walkthrough of the fabrication sequence used in this thesis to make capacitive-piezoelectric micromechanical resonators. Device cross sections at each step of the process flow are presented to illustrate what is happening.

Dedicated sections are also provided specifically for aluminum nitride (AlN) deposition, aluminum nitride etching, and lithography.

As one might expect, many unanticipated problems were encountered in the development of a working fabrication process. These challenges, and more importantly, the lessons learned from them, are reported to give insight into many of the fabrication-related obstacles one might face and pitfalls one should avoid, when possible.

All fabrication of micromechanical resonators in this work was performed in the UC Berkeley Marvell Nanofabrication Facility in Sutardja-Dai Hall. For more information about specific pieces of equipment, one can visit http://nanolab.berkeley.edu/labmanual.

6.1 Capacitive-Piezo Fabrication Process Flow

A sequence of illustrated cross sections for a capacitive-piezo disk resonator at each step of the optimized fabrication process of this work is included in fig. 6.1. The process begins with an n-type 150 mm (6") Si wafer which is pirhana cleaned, rinsed and dried. The wafer is put into an oxidation and annealing furnace (Tystar4) running a thermal oxidation program to achieve a target thickness of 3.0 μm. The result at this point is the cross section of fig. 6.1a. This oxide film serves the purpose of electrically insulating the devices from the conductive Si wafer. A thick oxide layer is used because increasing the distance between the devices and the underlying substrate decreases parasitic capacitance.

After oxidation, the wafer is then directly transferred into a silicon nitride furnace (Tystar17) to deposit a 500 nm thick film of low-stress, i.e., silicon-rich or non-stoichiometric, silicon nitride, resulting in the cross section of fig. 6.1b. The thickness of the low-stress silicon nitride film is chosen so as to provide a sufficiently thick film to provide an overetching buffer in a subsequent plasma etching step. At the final step of the fabrication process, the nitride

(a) 3µm of thermal oxide is grown on a 150mm Si wafer.

(b) 500 nm of low-stress silicon nitride is deposited.

(c) 3.0 um of undoped polysilicon is deposited (CVD) followed by a phosphorous (n-type) doping step.

(d) Polysilicon interconnected is etched using the first masking layer (clear field: POLY1).

Figure 6.1: Optimized fabrication process for the capacitive-piezoelectric resonators and filters of this work. The process continues on the following page.

film must remain sufficiently thick to protect the underlying oxide from a hydrofluoric acid etch step. The oxide and nitride films are collectively referred to as *isolation layers*.

Refer to fig. 6.1c for a cross section of the wafer after doped polysilicon deposition. The wafer is put into a polysilicon deposition furnace (Tystar16) to provide the film that comprises the interconnect layer for the devices. To reduce total deposition time, an *undoped* polysilicon deposition is performed for a target thickness of 3.0µm, followed by a two hour $POCl_3$ (phosphorous) doping in Tystar13 at 1000°C to ultimately realize a polysilicon film with a sheet resistance of 4 Ω/□. Alternatively, an "in-situ doped" deposition can be performed, but the deposition speed is 10× slower.

Lithography using the first mask layer of four, POLY1, a clear-field pattern, is used in etching the polysilicon to achieve the result of fig. 6.1d. Refer to section 6.2 for a dedicated lithography discussion. The resist thickness used at this step is 900 nm; for more information about this resist refer to **??**. The polysilicon etching is performed using the advanced silicon etch process of the *STS2* deep reactive ion etcher. The *Smooth Sidewall 1* etch recipe is used, having an etch rate of approximately 1.5 µm per minute and a PR selectivity of ≈50. This etch recipe uses alternating 5s/7s cycles of passivation and etching respectively to achieve straight sidewalls. Process pressure is maintained at 18 mTorr. The passivation cycle consists of a 100 sccm flow of C_4F_8 with a coil power of 600 W. The etch step consists of a 130 sccm flow of SF_6 and a 13 sccm flow of O_2. Coil power is held at 600 W. Additionally, a 20 W RF Bias is applied at 13.56 MHz during the etch step. After etching is completed, photoresist is stripped using an O_2 plasma at 300 W for several minutes. Etch completion is typically verified using the Alpha-Step IQ Surface Profiler, *ASIQ*.

After polysilicon etching, a 3.5 µm-thick high-temperature oxide (HTO) layer is deposited in Tystar17, resulting in the cross-section of fig. 6.1e. HTO is used at this step for two reasons: better fill conformity in narrow trenches than achievable with LTO and lower intrinsic stress than LTO. If a large amount of HTO is removed from one side of the wafer, wafer bow can remain minimized. The thickness is chosen to be slightly larger than the interconnect

(e) 3.5 µm of high temperature oxide is deposited.

(g) 125 nm of high temperature oxide is deposited.

(f) The oxide is chemically mechanically polished to achieve a flat surface, exposing the POLY1 layer.

(h) 1.6 µm of AlN is sputter deposited.

Figure 6.1: Optimized fabrication process for the capacitive-piezoelectric resonators and filters of this work. The process continues on the following page.

thickness of 3.0 µm.

Chemical mechanical polishing is used to achieve the flattened and polished surface of fig. 6.1f. Using CMP is necessary to eliminate the surface topography that otherwise would be presented to the AlN deposited in a subsequent step. Additionally, on the nanoscale, a polished substrate upon which to sputter is preferable for achieving a highly oriented and strongly crystalline AlN film. Backside polishing of approximately the same duration as that on the front of the wafer is performed to balance out stresses to consistently minimize wafer bow to under 10 µm. The approximate etch rate of the CMP step was 100 nm/minute. CMP was performed until polysilicon was exposed under the HTO as verified using a multimeter. Since the center of the wafer is polished slightly faster, approximately 4 minutes of overetching was performed to expose the polysilicon of the entire wafer. After completion of the CMP, wafers are rinsed using a deck hose and scrubbed using a Mr. Clean magic eraser to remove residual CMP slurry particles while continuously rinsed. The wafers are rinsed using a quick dump rinser and dried.

To form the bottom sacrificial layer, 125 nm of high-temperature oxide (HTO) is deposited in Tystar17. A standard furnace clean cycle is performed prior to deposition. The post-deposition cross-section is included in fig. 6.1g. HTO is used to form the sacrificial layer due to its higher quality and conformality– it is presumably less likely to contain pinholes or other defects than LTO.

A 1.7-µm-thick aluminum nitride (AlN) film is reactively sputter deposited to achieve the cross section of fig. 6.1h. For a detailed explanation of proper aluminum nitride film processing methods, including wafer pre-treatments, sputter deposition, stress control, and etching methods, please see section 6.3. To etch the AlN, an LTO hard mask is used because the AlN etch selectivity to photoresist extremely poor, i.e., much less than 1. The deposited 1.0-µm-thick hard mask is depicted in the cross section of fig. 6.1i. Since the wafer now has an exposed AlN film on it, the pre-furnace cleaning step in preparation for the hard mask does not use piranha, since piranha etches AlN at a rate of 100 nm/min. The wafer is

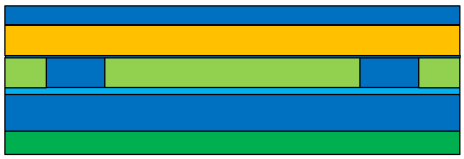

(i) A 1.0-µm-thick low-temperature oxide hard mask is deposited.

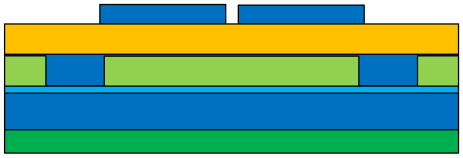

(j) The oxide hard mask is etched using the second masking layer (clear field: ALN).

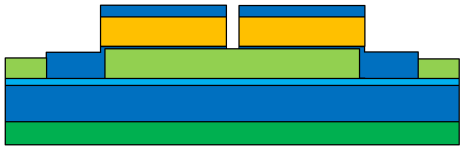

(k) AlN is dry etched while protected by the LTO hard mask.

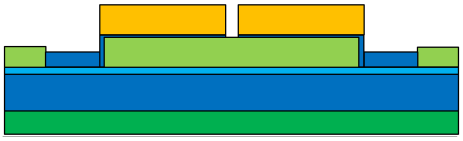

(l) The remainder of the oxide hard mask is dry etched until gone.

Figure 6.1: Optimized fabrication process for the capacitive-piezoelectric resonators and filters of this work. The process continues on the following page.

instead placed in a bath of resist stripper SVC-14 for 10 or more minutes at 60° C. This is the standard pre-furnace metal clean for the Nanolab. Following the SVC-14 bath, the wafer goes through a quick-dump-rinse DI water cleaning cycle, followed by a spin-rinse-dry cycle. The standard undoped LTO recipe is used to deposit the hard mask at a rate of 10.4 nm/min.

Following the hard mask deposition, the second lithography step is performed, using the clear-field pattern titled *AlN* using 900-nm-thick DUV resist. The LTO is then etched using the Centura MxP oxide etcher's "Oxide Spacer Etch with Endpoint" recipe, having an etch rate of 250 nm/min. A 25 percent overetch is performed after endpoint detection to ensure truly vertical sidewalls of features and full wafer etch completion. A cross section depicting the etched hard mask is shown in fig. 6.1j.

AlN etching commences after a quick O_2 plasma PR strip at 300 W lasting several minutes. The AlN is etched in a 90/10/100 sccm gas flow mixture of Cl_2, BCl_3, and Ar at 10 mTorr, a 500 W plasma, and a 70 W RF bias, in the Centura-MET etching tool, using the *ALNVAR* recipe. The etch rate is approximately 250 nm/minute, although the etch rate has been shown to drop to as low as 100 nm/minute. Etching selectivity of AlN to LTO is roughly 4. A strong overetch is performed to further improved the AlN sidewall angle, to eliminate skirting at the bottom of AlN features, and to eliminate stubborn AlN features in the field. The AlN etch rate is non uniform on a microscopic level, so small features several microns wide resembling islands will remain in the field once the majority of AlN has been cleared in the field. The fabrication cross section after AlN etching is shown in fig. 6.1k. Note that due to overetching, the polysilicon interconnect layer is thinned somewhat in the field since the chorine based etch chemistry also attacks Si. The slightly sloped sidewalls due to non-ideal etching are not explicitly shown in the drawn cross section but are nonetheless generally present. Note that SEM inspection is useful during this etch to ensure both straight

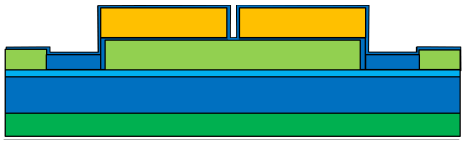

(m) 150 nm of high temperature oxide is deposited to form the top sacrificial layer.

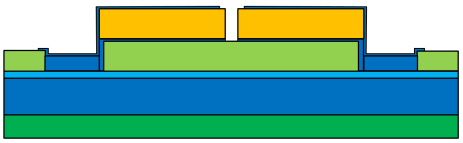

(n) Oxide is etched in certain areas to expose underlying AlN and Poly1 using the third masking layer (dark field: ANCHOR)

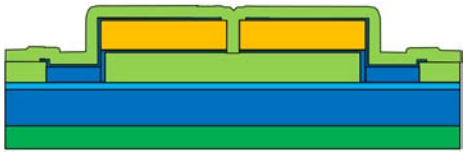

(o) 600 nm of in-situ doped polysilicon (n-type) is deposited forming the top electrode and support stem for the disk.

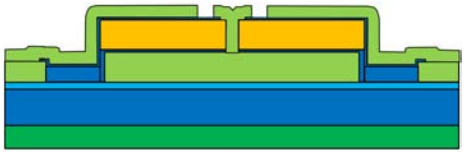

(p) The top polysilicon layer is dry etched using the fourth masking layer (clear field: POLY2).

Figure 6.1: Optimized fabrication process for the capacitive-piezoelectric resonators and filters of this work. The process concludes on the following page.

sidewalls and the proper amount of overetch.

As shown in fig. 6.1l, the remaining oxide hard mask is etched away in the Centura-MxP oxide etcher until the AlN is exposed. This is done so that the top oxide sacrificial layer can be defined precisely and uniformly using a dedicated oxide deposition.

In preparation for a second oxide sacrificial layer deposition, the wafer is cleaned using the standard metal clean cycle to avoid etching AlN. The wafer is put into either an LTO or HTO furnace for a 150 nm thick oxide deposition, yielding the cross section of fig. 6.1m.

Once the top sacrificial layer is deposited, it is necessary to form a contact to the polysilicon interconnect via dry etching. This contact allows for electrical contact between the top and bottom electrode layers as well as direct contact between the AlN layer and the top electrode layer for structural anchoring and support. The third masking layer, a dark field pattern, called *ANCHOR*, is used to lithographically pattern 3.0 μm thick photoresist to create this contact. Thicker photoresist is used to ensure an even coating over the large AlN topography and also to provide a thick enough resist layer for a long etch with finite selectivity between oxide and PR. Refer to table 6.1 for more information on processing the thick resist. A long oxide etch is performed, enough to etch 2.0 um, to allow for the complete removal of vertical oxide stringers in holes. After the etch is completed, the thick PR is stripped in an acetone pool squirted onto the top of the wafer, and sped along using gentle swabbing. A quick-dump-rinse de-ionized water cleaning cycle and a spin-rinse-dry cycle are performed prior to inspection to verify a clean surface in preparation for another deposition. The cross section at this point is shown in fig. 6.1n.

Once anchor contacts have been opened and the wafer is properly cleaned, a pre-furnace metal clean cycle is performed, and the wafer is put into the polysilicon deposition furnace

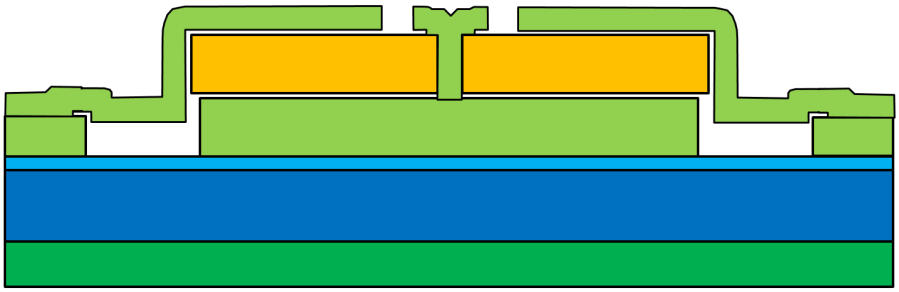

(q) The device is released through etching exposed oxide in hydrofluoric acid for 7 minutes.

Figure 6.1: Optimized fabrication process for the capacitive-piezoelectric resonators and filters of this work. Continued from the previous page.

(Tystar16). An in-situ doping deposition is performed c.f. fig. 6.1o. Post deposition, a dopant activating anneal for one hour at 1000° C is shown to be beneficial for reducing the resistivity of in-situ-doped polysilicon by ≈10×. This anneal is postponed until the final step before singulation (perhaps unnecessarily) to avoid creating additional wafer bow that could lead to lithography challenges.

The final lithography step is performed on the wafer. Thick photoresist is spun and reduced in thickness to 2.5 µm using O_2 plasma. Exposure is performed at 30 mJ/cm^2. After development, a 90° C hard bake is performed for 30 minutes. The wafer is etched using the "Smooth Sidewall" recipe in the STS2 deep silicon etch chamber for 3.0 µm worth of etching to ensure that no stringer structures remain on the sides of AlN features. Thick PR is stripped using an acetone pool and mild swabbing for five minutes, resulting in the cross section of fig. 6.1p. The wafer is rinsed and cleaned using the prefurnace cleaning for metals. Finally, the wafer is annealed in N_2 inside Tystar3 for 60 minutes at 1000°C. Wafers are then manually singulated using a carbide tipped pencil. Structures are released in 49% concentration hydrofluoric acid for 7 minutes, resulting in the cross section of fig. 6.1q.

To conclude and to provide a sense of scale for the wafer level fabrication used and the very small device sizes, fig. 6.2 presents four images of completed capacitive-piezo resonators at the wafer, die, filter, and individual disk levels.

6.2 Lithography

All lithography was performed using an ASML deep-UV model 5500/300 stepper utilizing a 248 nm KrF excimer laser source. The reticle (mask) is a 6"×6" quartz plate with patterned chrome at a 4 to 1 projection ratio. Reticles are ordered from Compugraphics, Inc. Each mask can accommodate 4 lithography layers and a maximum die size of 1.06 cm × 1.06 cm.

This stepper uses alignment marks called PM marks to precisely align layers with an accuracy of better than 100 nm. Thus, PM marks must be exposed in the photoresist and developed in the first lithography step. To save time and cost, the same photoresist film

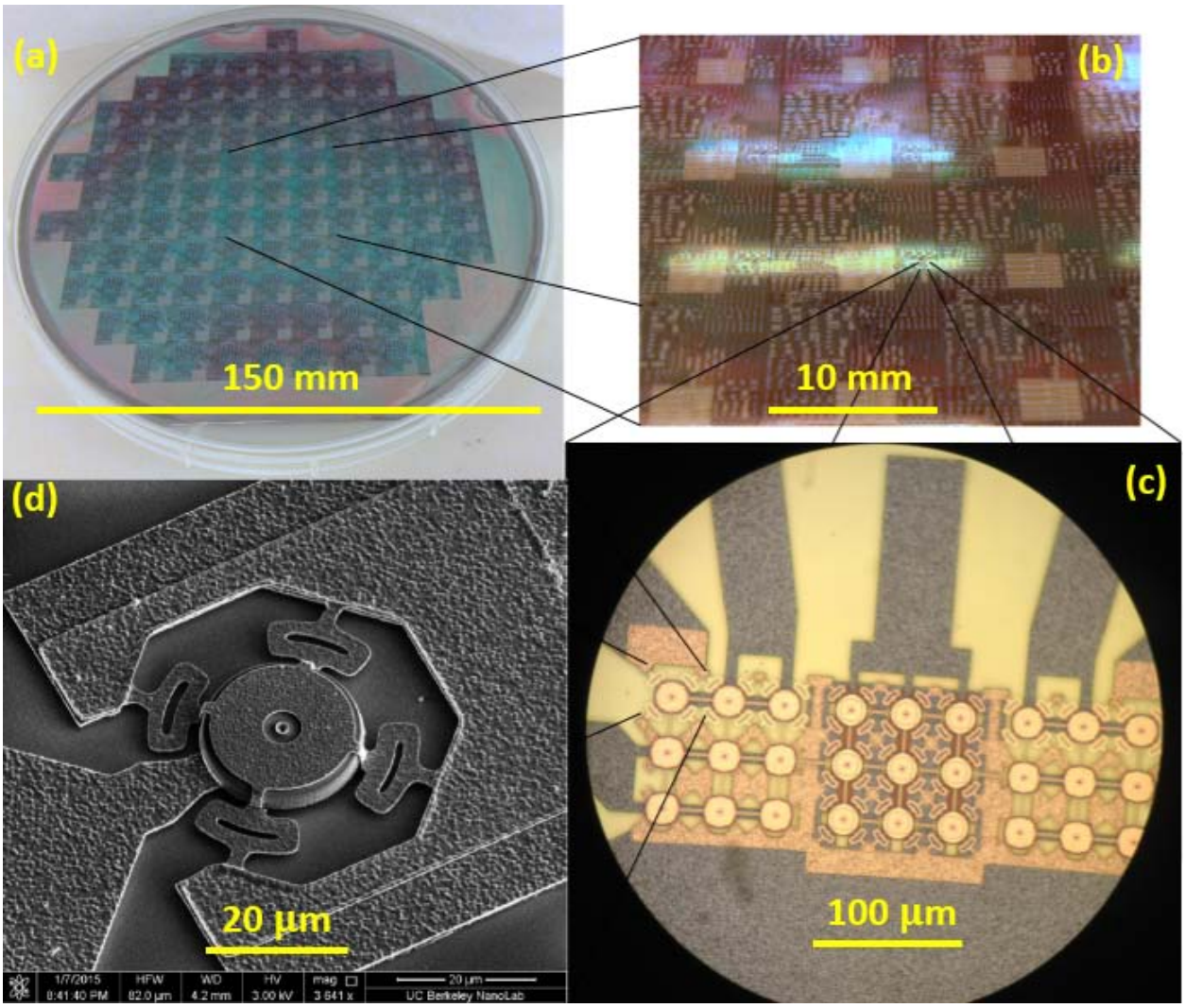

Figure 6.2: Photographs of fabricated devices at four different magnifications. (a) 6" wafer after completion of capacitive-piezo fabrication process. (b) Zoom-in of individual dies. (c) Optical micrograph of an unreleased filter. (d) SEM of a released resonator.

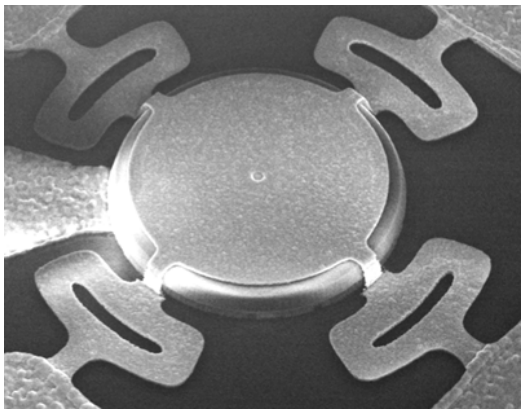

(a) The lithography for the top electrode spring supports, using 3.6 μm resist, resulted in poor pattern fidelity.

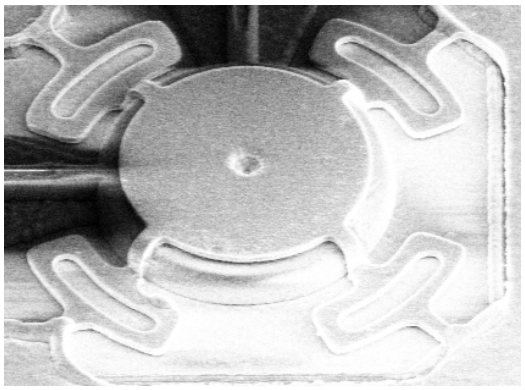

(b) Using thinned 2.5 μm resist, better pattern fidelity in the springs is achieved.

Figure 6.3: Comparison of pattern quality between a wafer which used unoptimized lithography with thicker photoresist and optimized lithography with a thinned resist.

can be exposed/developed twice at this point, i.e., PM marks developed in the photoresist are used as alignment markers for the first pattern. This technique eliminates an additional sequence of hard bake, etch, strip, and coat steps. This technique may cause a marginal decrease in lithographic resolution but is still sufficient for reliably resolving feature sizes of 1000 nm in the first layer, and thus met the needs for this project.

Two thicknesses of deep ultra violet (DUV) photoresist were used in this work: 900 nm and 2500 nm. Notably, a thicker resist is preferable for offering better coverage over large topographic features (such as 1.6-μm-thick AlN structures) and better protection during long etches. However, using a thicker photoresist also entails poorer minimum feature sizes and so should be used only when necessary. The thick photoresist offered by the nanolab was thicker than desired for the needs of this project at a nominal thickness of 3.6 μm. To obtain better resolution for higher performance devices, the resist was thinned to 2.5 μm using a new technique whereby a timed low power O_2 plasma etch is performed at low power to slowly thin the resist while avoiding elevating its temperature enough to affect its properties. The technique proved successful, thus allowing for the proper resolution of small stems and anchor holes which were otherwise not resolvable or were otherwise misshapen. As shown in the side-by-side comparison of fig. 6.3, top electrode spring support pattern fidelity was improved using a thin resist.

Additionally, high aspect-ratio resist patterns, i.e., those that are several times taller than they are wide, can lean to one side or, in the worst case, fall over. A thinner resist is less affected by resist droop and is thus preferable for fine patterns.

Refer to table 6.1 for a comparison of the two types of resist used with regard to spin speeds, softbake temperatures, exposure energies, post-exposure bake temperatures, hard bake method, and smallest resolvable features.

Table 6.1: Comparison of deep UV photoresists used

	900 nm resist	**2.5 μm resist**
Resist Type	Dow UV 210-0.6	Dow UV 26-3.0
HMDS Prime	60 s	60 s
SVGCoat6 Program #	2	3 (custom)
Spin Speed	1480 rpm	5000 rpm
Softbake Temp. and Time	130.0° C, 60 s	135.0° C, 180 s
Thickness After Spinning	900 nm	3.6 μm
O_2 Plasma Thinning	None	15 min., Technics-C, 60 W
Final Thickness	900 nm	2.5 μm
Exposure Energy	12 mJ/cm^2 (CF)	30 mJ/cm^2 (CF); 40 mJ/cm^2 (DF)
Post Exposure Bake	130.0° C, 60 s	110.0° C, 60 s
Developer	MF-26A	MF-26A
Hard bake	UV-Bake, Program U	90°C oven bake, 30 minutes
Strip Method	O_2 Plasma	Acetone or PRS-3000
Min. Linewidth Resolved	400 nm	600 nm
Min. Hole Radius Resolved	400 nm	800 nm
Mask Layer #'s (4 total)	1, 2	3, 4

Lastly, it was found that running an internal quality control (IQC) correction on the ASML300 stepper, requiring staff login credentials, was greatly beneficial to and even necessary before critical lithography steps. For example, when it had been more than 24 hours since the previous IQC, tool parameter drift was significant enough that resolution was too poor to resolve features at 1 μm or smaller. It is thus recommended to perform an IQC correction before critical litho steps.

Although the thick lithography program achieved satisfactory results at least once, repeatedly resolving fine features proved to be challenging. An SEM of properly exposed and developed thick photoresist is included in fig. 6.4. Often, it was necessary to strip the resist after failed lithography and try again, even when using process parameters that had worked previously. Another significant challenge is the apparent exposure and development of features when inspecting using optical microscopy, only to find that the resist had not cleared all the way down to the bottom. Thus, SEM inspection was needed to verify proper resolution of features. Clearing the resist in the holes of AlN disks proved particularly difficult, because it was difficult to verify even when using an SEM.

6.3 Aluminum Nitride Deposition

The operating principle of the AlN deposition tool in the Nanolab, the state of the art *Endeavor AT* by Tegal Corporation, and now OEM group, is sputtering an aluminum target

Figure 6.4: SEM inspection of hard-baked 3-μm-thick photoresist after patterning and before etching the top electrode.

with Ar and N_2 present in the process chamber. This sputtering process is an example of *reactive* sputtering, where an added gas precursor chemically reacts with sputtered ions to deposit a desired compound on a substrate. Reactive AC *magnetron* sputtering, where magnetic fields are used to improve the plasma localization close to the target, has become the preferred method for thin-film AlN deposition in industry because of the favorable combination of high deposition rate, low deposition temperature, good crystal structure and superior stress control.

Depositing high-quality AlN is a complex art due to the large number of process parameters that can be tuned. Opportunities for further optimization remain. AlN deposition is challenging because a deposited film's stress, strain gradient (i.e., curvature after release), crystallinity, and thickness uniformity should all be within specification for a deposition to be considered successful. Additionally, wafer-to-wafer repeatability is a concern that must be properly managed. Deposition parameters can shift in the day-to-day short term, thus the need for both conditioning wafers and a "first" wafer; in the week-to-week medium term as an Al target wears and shielding changes are performed; as well as in the month-to-month long term as targets are switched out. AlN film quality depends somewhat on the materials present on the sputtering surface of the wafer, and trace amounts of unwanted gases in the chamber, in particular O_2 and H_2O, will adversely affect crystallinity. Nonetheless, by following proper procedures as will be described, one can reliably obtain reasonably good AlN film using this tool. Up to this point, stress, crystallinity, thickness uniformity can be well controlled. Attempts to eliminate strain gradient at Berkeley by the author and previous researchers have had some success, although further improvement is desired.

For an account of many useful experiments one researcher performed to characterize and optimize AlN deposition using the *Endeavor AT*, refer to the dissertation published in 2013 by Dr. Fabian Goericke from Prof. Pisano's research group at Berkeley [91]. The AlN deposition chapter includes a detailed report of findings based on several hundred film depositions. In particular, his reports on the first wafer effect and effects of gas flows on film stresses were helpful in their predictive accuracy. They were confirmed to be accurate in this author's own experimental studies.

AlN Stress Characterization and Control

Here, AlN's film stress refers to the *net* value of stress throughout the film as measured by its effect on wafer bow. It is desired to measure the amount of stress present in a film for a given set of deposition parameters, specifically gas flows, and to compensate the unwanted stress in future depositions through adjusting the gas flows appropriately. Film stress must be controlled to avoid excessive wafer bow and unwanted changes in resonator behavior.

Stress Characterization

AlN stress is characterized using a Flexus thin film stress measurement system. Using a laser interferometer, this system measures wafer curvature, which in turn is used to calculate the stress. The following expression is used:

$$\sigma = \frac{E}{1-\nu}\frac{h^2}{6t}\left(\frac{1}{R_f} - \frac{1}{R_i}\right) \tag{6.1}$$

Here, σ refers to the film stress in Pascals (N/m^2), $\frac{E}{1-\nu}$ is the biaxial Young's modulus of the silicon substrate (180.5 GPa), h is the substrate thickness, R_i is the wafer's pre-deposition (initial) radius of curvature, R_f is the wafer's post-deposition (final) radius of curvature, and t is the film's thickness.

Thus, for a 1.6-μm-thick film, each 100 MPa of stress will result in about 25 μm of wafer bow. It is fairly straightforward to keep AlN stress levels within +/-100 MPa, under proper operating conditions, and often, to within +/-50 MPa. Stress is either tensile or compressive. Here, a tensile stress, one that causes a concave top surface on the wafer, is considered positive.

In addition to minimizing the stress of the AlN film, it is also desirable to minimize the absolute value of the wafer bow to under 60 μm throughout the fabrication process to ensure that the stepper can accept the wafer for lithography. If the wafer bow is too high at any point due to unbalanced stresses then the bow must be compensated, either by etching/CMP or a deposition on the backside.

Stress Compensation

AlN stress can be controlled by adjusting gas flows by appropriate amounts. Chamber pressure is determined by the flow rates of Ar and N_2 gases into the chamber because neither vacuum pump speed nor chamber size changes during deposition. Since higher gas flow rates translate into higher partial pressures and modified deposition dynamics in the process chamber, gas flows affect stress.

Additionally, if the Endeavor AT has been inactive for many hours, successive AlN films deposited in the tool have been shown to have stresses that vary as a function of the order in which they are deposited. The "first wafer effect" hypothesis for this tool states that for a 1.0 μm AlN thickness, a deposited film's stress is on average ≈45 MPa more compressive (standard deviation≈18 MPa) on a first wafer than it is on a second wafer [91]. The difference in stress between second and third wafers was not shown to be significant.

Collecting precise data to model the effects of gas flows on stress at 1.6 μm was not performed as it would require an excessive number of depositions and be costly. Additionally, such trends might not even be applicable after a target or shielding change. Nonetheless, a rough estimate of this effect is given. At a thickness of 1.6 μm and gas flow rates for N_2 and Ar at 7±3 and 21±9 sccm respectively, the following trend, based on data from [91] (1.0 μm AlN thickness) and the author's experience (1.6μm AlN thickness), roughly holds.

- Adding 1 sccm of Ar causes stress to become ≈80 MPa more tensile.
- Adding 1 sccm of N_2 causes stress to become ≈30 MPa more tensile.

The process, then, to achieve minimal stress is to adjust gas flows iteratively based on wafer bow measurements until the stress meets specification, while one also accounts for the first wafer effect.

Notably, deposited film stress also depends on the substrate material. Thus, for an AlN deposition over oxide, oxide wafers, rather than bare silicon wafers, should be used for characterization.

AlN Strain Gradient Characterization and Control

It is possible (and common) for an AlN film to have a low amount of overall stress while still being compressive at the bottom and tensile at the top, thus creating a bending moment. It was found that deposited films would consistently bend upwards after release, creating a problem for centrally-supported disk structures with small gaps. If top electrode contact is to be avoided, then the strain gradient should be made small enough so that vertical displacement at the edge of an AlN structure is smaller than the size of its top sacrificial gap. Disk bending also limits the gap range over which frequency tuning can be performed. Refer to fig. 6.5a for an example of an AlN structure which has curled up to contact its top electrode. Electrode contact in such devices leads to undesired modal distortion and

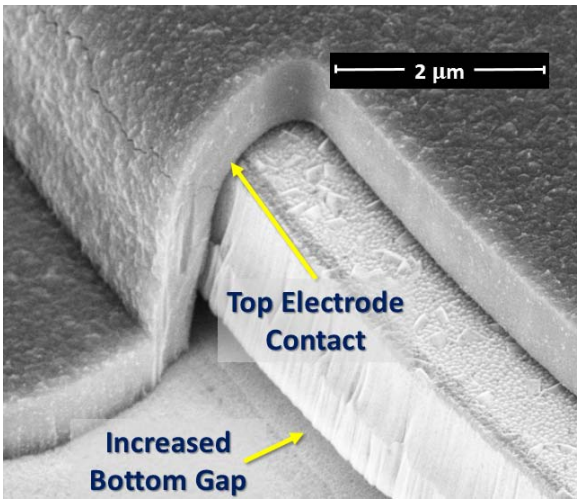

(a) An SEM of an example device where a significant AlN strain gradient resulted in top electrode contact between the resonator and top electrode.

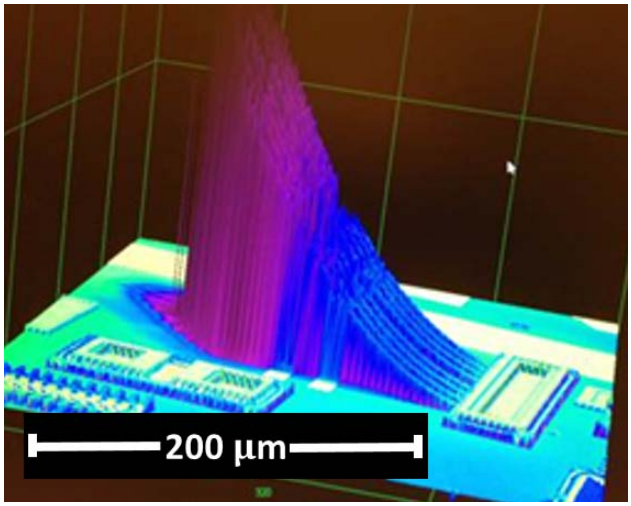

(b) A confocal microcope's topographical model of an inspected surface. Released AlN cantilevers are shown to deflect upward.

Figure 6.5: *Left:* SEM demonstrating a need for AlN stress gradient compensation. *Right:* a screenshot demonstrating how one can precisely measure a released AlN structures's curvature.

mechanical friction which lowers Q–in some cases even completely eliminating a detectable resonance peak. Strain gradient control is thus essential.

Strain Gradient Characterization

Stress gradient is more difficult to characterize than stress because one cannot measure AlN curvature for a sample until additional wafer processing has been completed–one must first pattern and release an AlN structure. One useful way to determine the AlN material's curvature on a released sample is to use a 3D confocal laser microscope, e.g., the Olympus LEXT OLS4000 3D Confocal Laser Microscope available in the Marvell Nanolab. As is shown in fig. 6.5b, this microscope allows for 3D rendering of an inspected microscopic sample, e.g., here, 100-µm-long AlN cantilevers. This rendering is possible through stitching together snapshots taken over a range of focal planes using blue laser light. Here, a color-mapping is placed on the rendering to indicate height above the substrate. Curvature can be accurately calculated based on deflection as a function of position along a measurement line specified along a cantilever's length.

For the purpose of characterization and optimization, the vertically oriented curvature of a released AlN cantilever is assumed to be proportional to that of a centrally supported disk. Reducing the curvature in cantilevers will result in reduction of curvature of disks by a proportional and similar amount, leading to better performance. The measurement of

fig. 6.5b gives a radius of curvature estimate of 836 μm.

Vertical deflection as a function of position for small deflections can be found once radius of curvature, or second derivative, is known. For example:

$$\frac{\mathrm{d}^2 u_z}{\mathrm{d}x^2} = \frac{1}{R} = \frac{1}{836 \times 10^{-6}\mathrm{m}} \tag{6.2}$$

This derivative can be integrated twice to obtain vertical displacement as a function of position, e.g., distance, x, from a fixed point.

$$u_z(x) = \frac{1}{2R}x^2 \tag{6.3}$$

For example, using eq. (6.3), at a distance x of 11.2 μm, the radius of a 300 MHz disk resonator, and using the measured R value of 836 μm for the sample of fig. 6.5b, vertical deflection is estimated to be 75 nm.

Multi-Step-Deposition Method for Strain Gradient Reduction

To reduce the upward bending moment that a single recipe deposition inevitably yields in this tool, the recipe was broken up into parts so the beginning of the recipe becomes less compressive and the latter part becomes less tensile.

Many deposition parameters in the Endeavor AT affect stress, but for various reasons, only a subset of them should be varied during deposition to affect stress gradient, as follows:

- RF Bias negatively affects crystallinity. (Don't vary)
- SAU makes a film more tensile, but can't be changed during deposition. (Don't vary)
- N_2 flow affects stress, but it is a precursor to the deposition. (Don't vary)
- Ar flow affects plasma kinematics and is not a precursor to the deposition. (Vary)
- Substrate temperature. (Vary)

Experiments by V. Felmetsger of OEM group have shown that increasing argon flow and temperature in the beginning of a deposition is effective for compensating stress gradient while maintaining good crystallinity and near zero stress in sub-quarter-micron thick AlN films for nanoactuators [92].

The following multi-recipe wafer flow was outlined to reduce AlN's stress gradient for a 1.6 μm-thick film: Heat the wafer using the maximum heater power available (resulting in a wafer temperature of ≈ 500°C) for the first quarter of the deposition while using an elevated argon flow rate of 7 sccm. Wait at least 10 minutes for the wafer to cool, perhaps flowing nitrogen to cool the wafer faster. In the second quarter of the deposition, deposit at ambient temperature with only a slightly elevated amount of Ar (6.5 sccm). In the third and fourth quarters of the deposition, use a slightly reduced and an even more reduced amount of Ar,

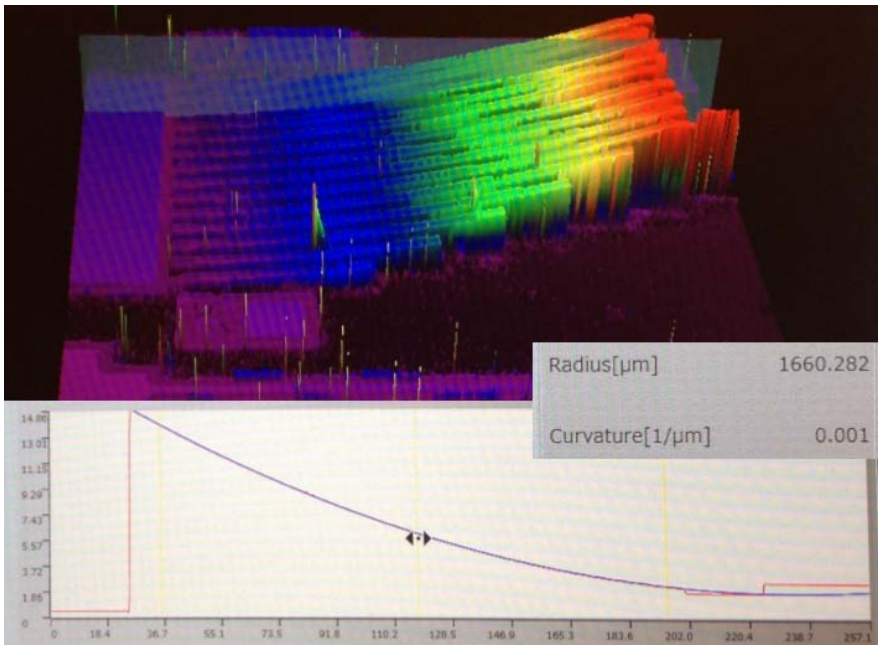

Figure 6.6: Demonstration of AlN strain gradient reduction from a fitted radius of curvature of 836 μm (previous mark) up to 1660 μm (larger is better).

respectively, (6 and 5 sccm). Nitrogen flow is held constant through all four deposition steps at 22 sccm, but should be used as a knob to fine tune the overall stress.

Using this technique, the strain gradient radius of curvature was increased from 836 to 1660 μm, as demonstrated in fig. 6.6, ultimately resulting in reduced vertical displacements in released structures by about 2×. Further iteration would be highly desirable to reduce the vertical bending even more, but due to the numerous fabrication steps needed to achieve released cantilevers, doing so would be cost and time prohibitive.

AlN Crystallinity Characterization and Optimization

Sputtered AlN is a polycrystalline film. For a maximal piezoelectric coefficient, one must ensure that the grown crystals are all vertically oriented in the same way. Deposition conditions not conducive to proper crystal growth can result in a dramatically reduced piezoelectric coefficient, hence reduce electromechanical coupling. To illustrate the vast difference between good and poor AlN film, a comparison between measurements of a strongly coupled and weakly coupled resonator is made in fig. 6.7. Here, two resonators of the same design, but fabricated on different wafers, and having the same Q of 4.6k, are compared side-by-side and are shown to have vastly differing amounts of coupling.

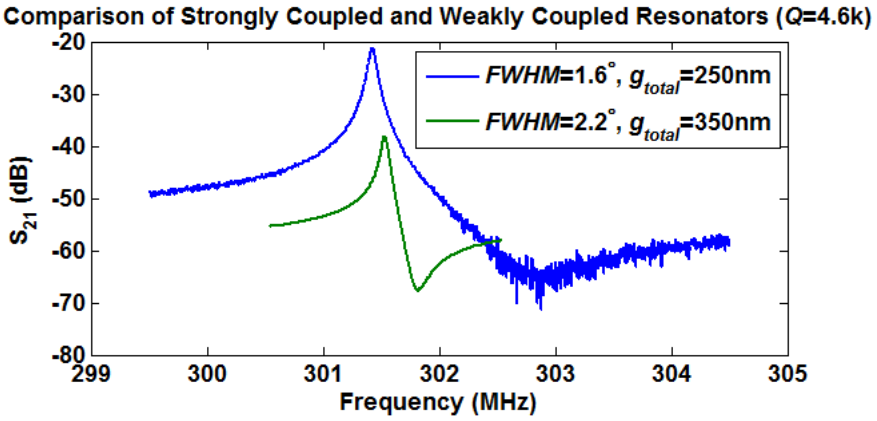

Figure 6.7: Measured frequency characteristics of a strongly coupled disk resonator (blue) and a weakly coupled disk resonator (green), each with a Q of 4,600. Much of the difference in coupling strength is due to differences in AlN crystallinity.

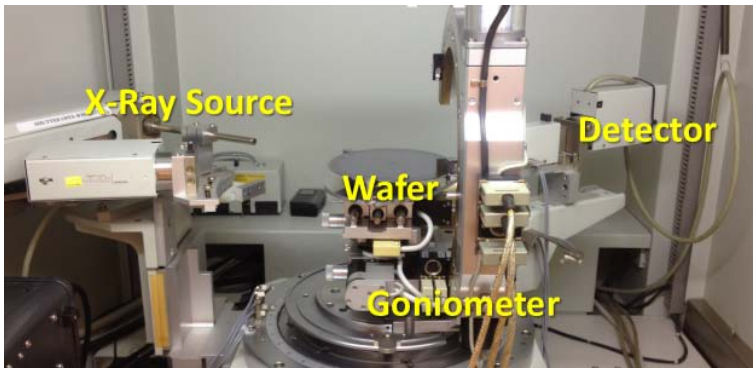

(a) Labeled photograph of essential parts of the Siemens D5000 X-Ray Diffractometer. Note: Wafer changes orientation during measurement.

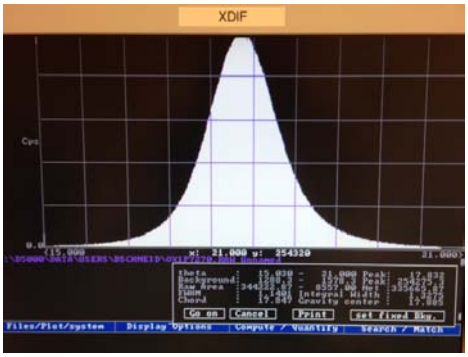

(b) Rocking curve as shown on GUI for best measured FWHM of 1.14°

Figure 6.8: X-ray diffractometer system photograph and sample measurement of a 1.7 µm-thick AlN film deposited on thermal oxide.

X-Ray Diffraction Rocking Curve Measurement of AlN Crystallinity

The crystallinity of thin-film reactive sputtered AlN is evaluated by a Siemens D5000 X-Ray Diffractometer, a photograph of which is included in fig. 6.8. Use of this tool requires passing online radiation safety training through the Office of Radiation Safety, being an authorized user on the radiation use authorization (RUA) form at the tool, and wearing a dosimetry ring on one's finger. These restrictions are in place because the X-ray source can potentially offer a lethal dose of radiation in a fraction of a second if used improperly or when malfunctioning. Of course, the D5000 has a number of interlocks for safety so when properly used, there is only a rare chance of imminent danger to the user.

X-Ray diffractometry relies on Bragg's Law:

$$\lambda = 2d \sin\theta \tag{6.4}$$

Hence, when the crystalline lattice spacing of d is very uniform throughout the material, a strong X-ray signal is diffracted at a specific angle θ, which is situated around 18.1° for AlN. If there is variation in this spacing, then instead of detecting a delta function, the peak is spread out in a gaussian distribution about the mean spacing. Thus, a narrow FWHM and a strong detected signal strength, as measured by counts per second, is an indicator of good crystal quality.

AlN Crystallinity Optimization

Optimizing proper AlN crystallinity depends on several factors. At first, it was assumed that the AlN deposition tool would consistently put out a good film when proper procedure was followed according to the laboratory manual. Actually, it is necessary to take a number of additional steps to achieve very good quality. Early iterations of capacitive-piezo resonators made by the author did not undergo tests for crystalline quality using an X-Ray diffractometer due to the lack of an RUA. Here, we focus on optimizing the crystallinity for an AlN film deposited on oxide.

First, it is helpful to heat the wafer in a vacuum environment to bake out water trapped in the oxide. This is best implemented through the modification of the deposition recipe to first use the quartz lamp in the process module itself before deposition. Heating above 300° C for ten minutes in a process chamber under vacuum (PM2) with a cryo pump specially suited to trap and remove water molecules was very helpful for reducing measured FWHM's and seemed to be sufficient for adequately dehydrating the wafer. Water molecules are harmful to AlN crystallinity during deposition.

Secondly, a flat surface with very low surface roughness is desirable upon which to deposit the AlN film. Polishing the oxide is key. Depositing an oxide film of less than 200 nm thickness on a polished surface was also acceptable for maintaining low surface roughness. HTO (high temperature oxide) is a high quality oxide and is preferred over its low temperature counterpart, LTO. Thermal oxide gave very good results as well but is not compatible with our fabrication process.

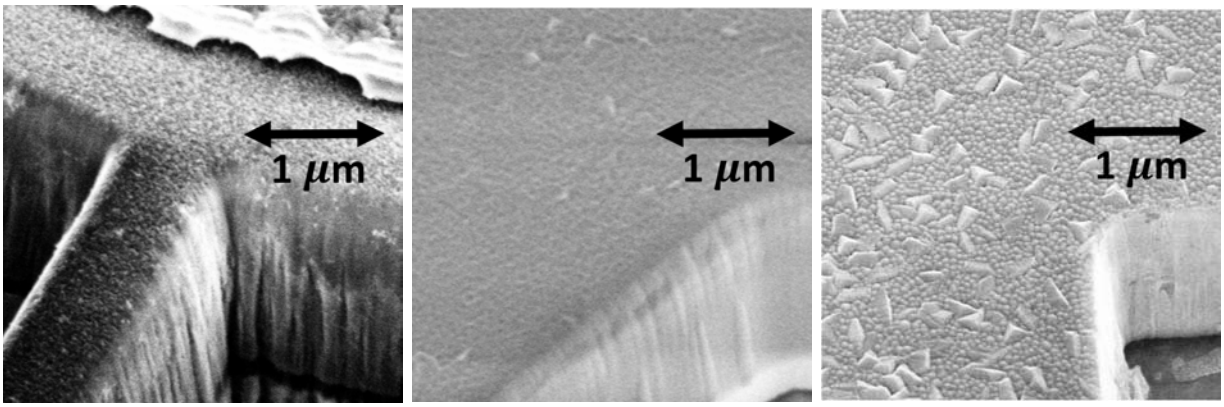

(a) High quality AlN film with uniform proper c-axis orientation. $FWHM = 1.60°$

(b) Decent quality AlN film with mostly good c-axis orientation. $FWHM = 1.70°$

(c) Poor quality AlN film with many poorly-oriented crystals. $FWHM = 2.3°$

Figure 6.9: Comparison of SEM's of 1.7 μm-thick AlN films with varying degrees of proper crystalline orientation.

Third, a large number of conditioning depositions (approximately 10) is needed after any time the chamber is opened up to atmosphere, i.e., for a shielding or target change, to properly prepare the target and chamber to deposit the best film. The measured FWHM of AlN has been observed to gradually improve as a function of wafer number after a shielding change by the author and others.

By implementing these improvements, the FWHM was reduced to an adequate level of 1.60º from 2.3º, or worse. As a visual comparison of multiple AlN films with varying degrees of crystal orientation, fig. 6.9 compares three SEM's of AlN films. One can observe that the poorly oriented AlN in fig. 6.9c has visible improperly oriented crystals visible on the surface.

Finally, to show how signal strength and FWHM are related, fig. 6.10 shows two superimposed measurements. Stronger signal strength is associated with a reduced FWHM. For a FWHM greater than 3.0º, the peak is barely detectable over the noise level.

Rapid AlN Wet Etching

It is useful to be able to strip an AlN film in case of poor material properties, and also to allow for the recycling of wafers used for test and conditioning depositions. For example, if the stress is too high or the crystallinity is poor on a process wafer, one can strip the film and attempt deposition again rather than discard the wafer. It was found that using MF-319 microposit developer was effective for stripping AlN deposited over SiO_2. A five minute dip in MF-319, heated to 60° C as measured by a digital thermometer, was sufficient to remove a 1.6 μm-thick film, although 10 minutes was generally used to ensure complete removal. Note that a heater temperature setpoint greatly exceeding 100° C is used to heat

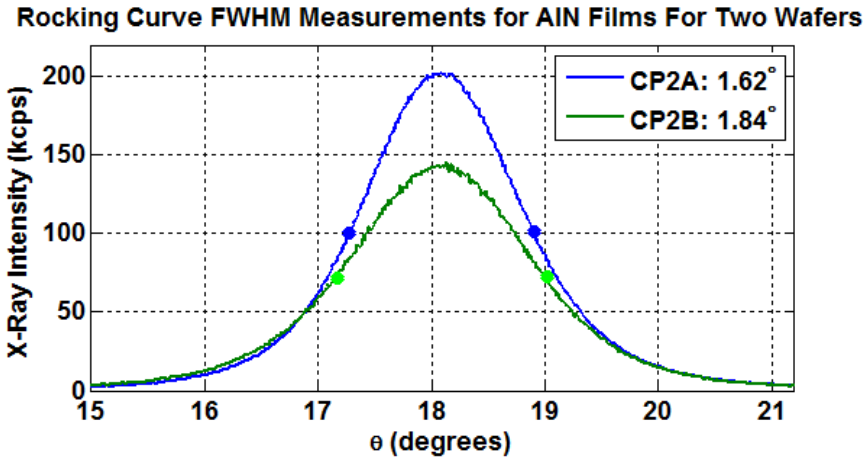

Figure 6.10: A comparison of two superimposed rocking curve measurements of two process wafers to show how signal strength and FWHM are related.

up the water bath and developer to the proper temperature.

This removal technique was used repeatedly on a single process wafer until satisfactory film qualities were achieved.

6.4 Choices for Electrode Materials

The bottom electrode interconnect and top electrode/stem materials were selected to meet performance requirements while avoiding pitfalls. High electrical conductivity, low deposition temperature, and fast deposition time are compelling benefits of using metal electrode materials, but problems with film adhesion, stress variations, and galvanic corrosion can arise if not properly averted. Galvanic corrosion occurs when dissimilar conductors are placed in electrical contact in an electrolyte, e.g., poly-Si and Mo in a hydrofluoric acid (HF) release, thus it is safest to use the same material for both top and bottom electrodes. The electrode material pair was changed between early implementions and latter ones from a mismatched Mo/poly-Si pairing to a matched poly-Si/poly-Si pairing to avoid observed corrosion.

To meet design requirements, the top electrode material is required to conform to the 1.7-μm-tall sidewalls of AlN structures, to provide rigid mechanical support for suspended electrode plates and AlN disks while also serving as a conductive pathway to the interconnect layer. The need for deposition conformality rules out sputtering or evaporation of metals as feasible deposition methods at this step. Since a conformal metal deposition such as CVD tungsten was not available to try during fabrication, poly-Si was selected as the top electrode material. Chemical-vapor deposited doped poly-Si is conformal around outer sidewalls, permeates narrow holes, may be deposited to thicknesses of several microns or more with low stress, is adequately conductive and rigid when thick, and adheres well to nitrides of both

silicon and aluminum.

6.5 AlN Etching

The plasma etching of aluminum nitride with acceptable selectivity and steep sidewall angles requires the use of a hard mask and carefully controlled etch conditions. A hard mask is needed because photoresist's selectivity to AlN was found to be less than 1. Additionally, the developer used for lithography was found to isotropically etch AlN at several hundred nanometers per minute, hence standard lithography over AlN is problematic for achieving an anisotropic etch profile.

Choice of Hard Mask

Before a better alternative hard mask material was selected, a lifted off nickel hard mask was attempted, which used a reverse polarity (dark field) mask pattern. The resolution and maximum hard mask thickness were found to be limited when using liftoff to about 1 μm and 150 nm, respectively. An additional difficulty of using liftoff is that the edges of lifted off patterns are very thin, thus non-ideal selectivity leads to sloped sidewalls. A sputtered and plasma etched molybdenum hard mask was also attempted, but photoresist residue would adhere strongly to the molybdenum, and using a wet etch to strip the hard mask is undesirable. Ultimately, an oxide hard mask was found to be the best choice for the etching of aluminum nitride due to its steep sidewalls, sufficient thickness, and good pattern fidelity. Low temperature oxide is preferred due to its superior selectivity, but plasma assisted chemical vapor deposition (PECVD) oxide, which is deposited at a lower temperature is also sufficient. The oxide hard mask is 25% overetched after endpoint. Photoresist used to define patterns in the oxide was stripped in an O_2 plasma before starting AlN etching.

Etching Process

The AlN is etched in a 90/10/100 sccm gas flow mixture of Cl_2, BCl_3, and Ar at 10 mTorr, a 500W plasma, and a 70W RF bias, in the Centura-MET etching tool, using the *ALNVAR* recipe. This etch was optimized by Chris Zhao of Prof. Al Pisano's group working with Microlab Process Engineer Matthew Wasilik several years prior to the beginning of this project. The verified etch rate is approximately 250 nm/minute. Etching selectivity of AlN to LTO is roughly 4, thus a hard mask thickness of 1 μm is used. A strong overetch is performed to attain a satisfactory AlN sidewall angle, to eliminate skirting at the bottom of AlN features, and to eliminate stubborn AlN features in the field. As fig. 6.11a indicates, the AlN etch rate can be non uniform on a microscopic level around grain boundaries, so small "island-like" features several microns wide will remain in the field once the majority of AlN has been cleared in the field. These particles detach and disappear during release, so their presence is tolerable, but they are undesirable. Note that due to overetching, the

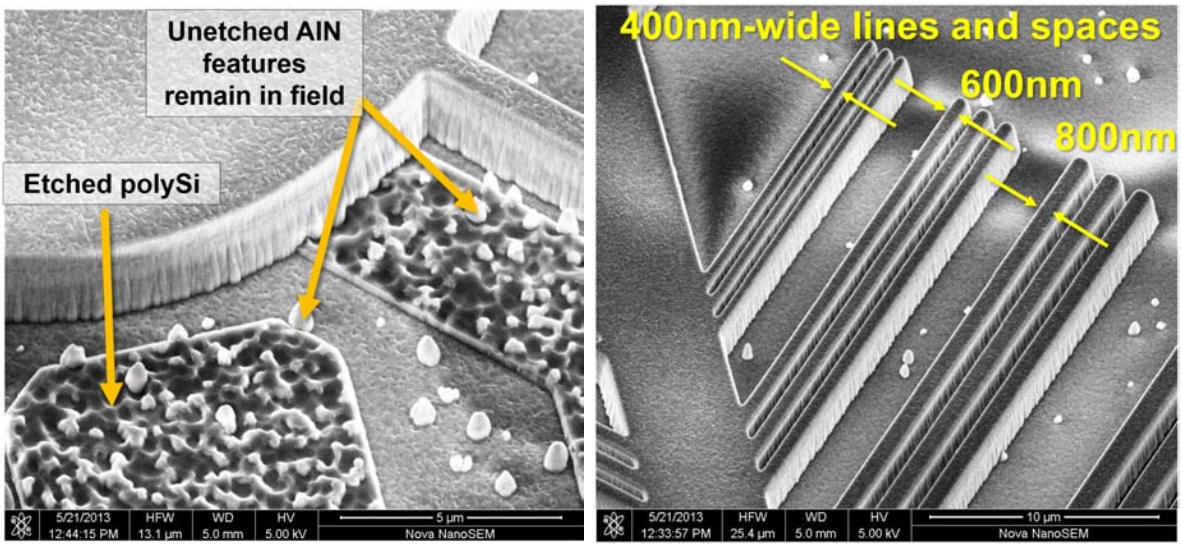

(a) An SEM of an etched AlN structure atop its bottom electrode which is also partially etched due to strong overetching.

(b) SEM of AlN lines and spaces of 400nm, 600nm, and 800nm having sidewall angles steeper than 80°.

Figure 6.11: SEM's of AlN structures demonstrating etch results.

polysilicon interconnect layer is thinned somewhat in the field since the chorine based etch chemistry also attacks Si. SEM inspection is useful during this etch to ensure both straight sidewalls and the proper amount of overetch.

Best AlN Etching Results

An SEM showing the best achieved AlN etching result is included in fig. 6.11b, where linewidths of 400nm were patterned into the AlN over a 1.6 µm thickness. Here, the sidewall angle is estimated at 83°. The hard mask has been removed. This result was achieved in 2013 on the second of five total fabrication runs; however, AlN was used on the substrate as a barrier layer, which led to poor input/output isolation, and electromechanical coupling was poor due to suboptimal AlN film quality.

Intermittent AlN Etching Problems

Although the etching result of fig. 6.11b is quite good, when using the same recipe one year later, the achieved sidewall angle was repeatedly found to be worse than previously attained. Stringers also formed. This adverse outcome is believed to have been caused by a significant leak up rate in the etching chamber, thus the chemistry of the etch is modified from the ideal process by the presence of air.

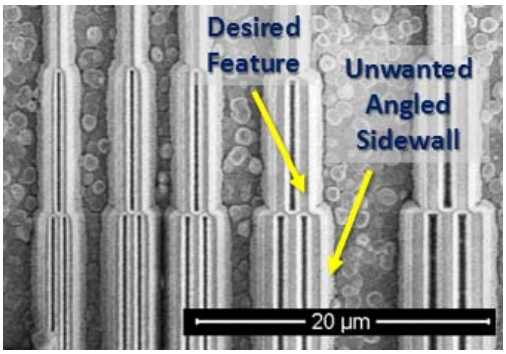

Figure 6.12: SEM of an AlN etch trial with a very poor side wall angle.

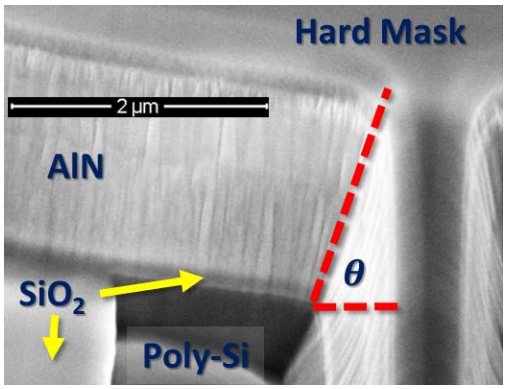

Figure 6.13: Close-up SEM after the AlN sidewall etch during fabrication of a capacitive-piezo resonator with tunable electrodes. The result is improved over that of fig. 6.12

Poor Sidewall Angles Due to Etcher Air Leak

Near vertical sidewalls are key to proper performance, yet some devices were comprimised due to nonreliability of the etching process. For example, fig. 6.12 presents an etch result from when the chamber leak was present and at its worst. The sidewalls are clearly largely angled, estimated to be 70° or worse. If the angle is poor enough, small holes in the centers of the disks cannot be opened and the process completely fails.

After Nanolab staff noticed and fixed one main cause of the leak, the etch angle improved somewhat, but not to the point of being as good as it was in fig. 6.11b. A close up SEM of a sample device to illustrate the final attained sidewall angle for many of the strongly coupled devices in this thesis, which were fabricated more recently, is included in fig. 6.13. Here, the oxide hard mask is visible, as well as oxide below the device. The pit region is where the polysilicon electrode was etched for about 0.5 µm during the overetch. Fortunately, it is made thick enough to be able to sustain such an overetch. Additionally, the electrode is unaffected directly beneath the device, which is important to keeping the proper gap spacing.

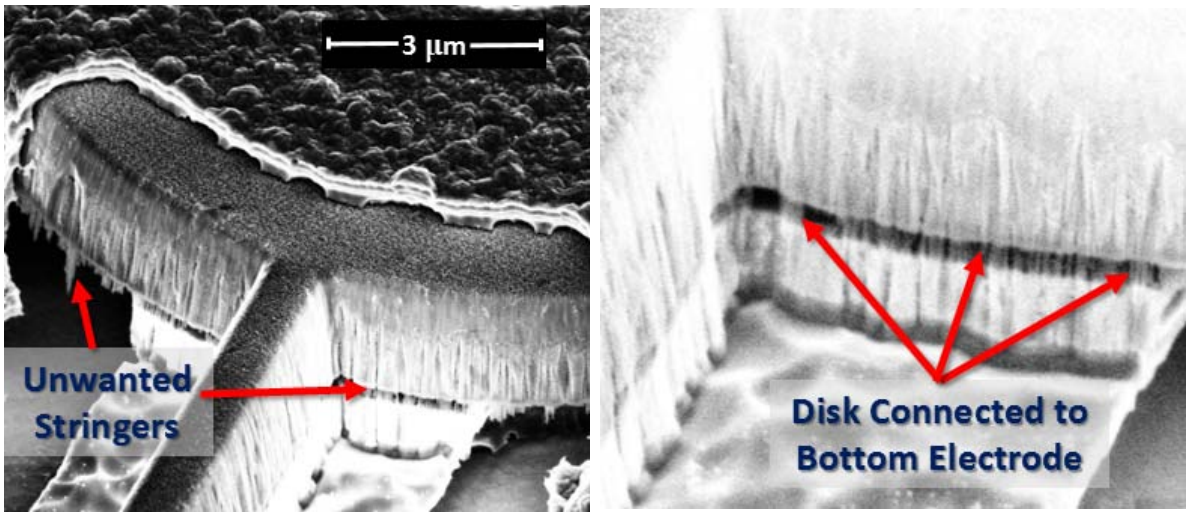

(a) Zoomed out. (b) Zoomed in.

Figure 6.14: SEM's showing the presence of stringers below a released capacitive piezo device. The AlN etch did not perform ideally.

Unwanted Stringer Formation

A second potential difficulty associated with the etching of AlN structures is the unwanted formation of stringers which are unremovable in piranha or polymer removing solutions. Although good results were obtained previously, after the etcher stopped working properly, stringers were found to be present, as presented in the SEM of fig. 6.14a which portrays a released device. The stringers were problematic because they connected the AlN structures to the underlying bottom electrode, as presented in the zoomed in SEM of fig. 6.14b. Thus, instead of a free boundary, the resonator would lose energy to the substrate and have increased stiffness, affecting modal behavior and reducing Q.

Remarks

Despite some encountered intermittent problems with etching, it has been shown that good results can be achieved. It would be very interesting to see how the performance of demonstrated devices would be improved by better etching, particularly for arrays and filters. Both Q's and modal characteristics should improve, allowing for more ideal filter responses.

6.6 Hydrofluoric Acid Release

The selective isotropic etching of silicon dioxide using hydrofluoric acid, while seemingly straightforward, must be performed on devices meeting certain requirements to avoid difficulties. Two situations were encountered which were unanticipated but which should be

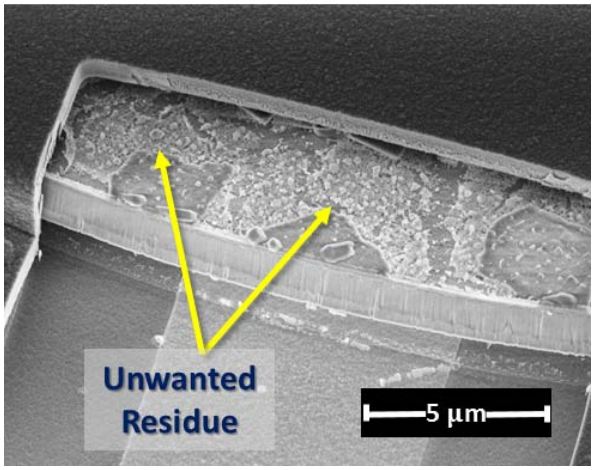

(a) SEM of a disk resonator coated in phosphoric acid residue left over from the HF vapor release of phosphosilicate glass.

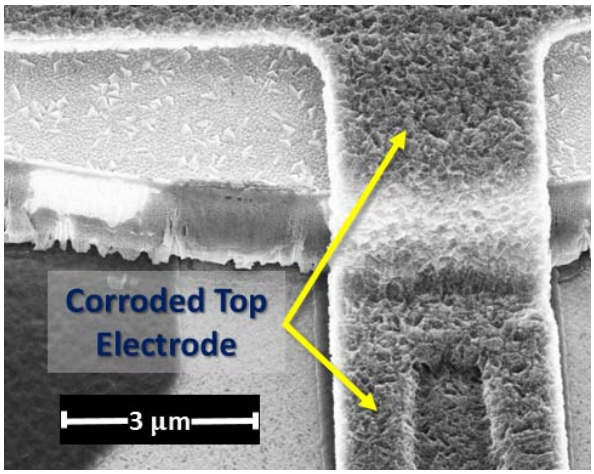

(b) A disk resonator with a corroded polysilicon top electrode due to the formation of a galvanic cell between molybdenum and polysilicon during liquid HF release.

Figure 6.15: SEM's of two situations in which HF release led to undesirable results.

avoided in future renditions of devices. First, the use of HF vapor release with phosphorous-doped silicon dioxide (PSG) was found to leave a water soluble residue on the surface of the AlN structures, as is shown in fig. 6.15a. This problem can be avoided by using undoped oxides. Secondly, galvanic corrosion can occur if dissimilar conductors are in electrical contact in the electrolyte, such as liquid HF. For example, in the SEM of fig. 6.15b, the polysilicon shown is corroded while molybdenum, the bottom electrode, is plated. The result is that the polysilicon is brittle and damaged. Avoiding this issue was the rationale for switching to a polysilicon interconnect layer to form the bottom electrode so as to match the top electrode material. In summary, using undoped oxides and polysilicon bottom and top electrodes was sufficient to get good release results. Using 49% HF acid, the 300 MHz structures, having a radius of 11.2 µm, were released in about 7 minutes.

6.7 Post Release Cleaning

To get the highest Q's, the devices must be cleaned after release. Unwanted release byproducts and other residuals can attach to the resonator and become difficult to remove. For example, with the devices of Run A, due to an unexpected reaction between vapor HF etch precursors and doped oxide sacrificial layers, a water dip was required to dissolve water soluble etch byproducts. Annealing at 500°C for 5 minutes in an N_2-purged chamber was also effective for cleaning surfaces of devices, via vaporization of byproducts, as evidenced by observed dramatic improvements in Q's after annealing, e.g., typically from 4,000 to 8,000. For resonators with very high aspect ratio gaps, material transport out of the gaps becomes

more limited, and hence devices take longer to clean. Critical point drying, which uses liquid CO_2 to replace the methanol or IPA in which a released device is submerged, which is then heated and pressurized above the critical point, 1030 psi and 30° C, allows for the removal of liquid etch products while avoiding stiction forces. Using CPD followed by heating or annealing provided very good results.

6.8 Summary of Targeted Process Improvements

While the fabrication sequence generates functional devices, improving several elements of the fabrication process would lead to better performance and reliability.

AlN Strain Gradient Reduction

Heating the wafer to an estimated temperature of 500° C during sputtering and using a multi-step gas flow recipe to tune stress as a function of deposition thickness was found to aid in improving the FWHM of the AlN film and reduce the residual strain gradient which leads to bending. Still, further optimization is desired to eliminate electrode contact based limits on minimum gap sizes.

AlN Etch Sidewall Angle Improvement

For small contour mode devices, resultant non-vertical sidewall angles from non-ideal plasma etching can impact the mode shape of the device and hence the behavior of coupling beams in arrays, which develop a shear wave component due to slanted boundary conditions at disk attachment points, thus altering effective acoustic wavelength. SEM measured AlN sidewall angles using our etcher range from 70° to 83°.

Improved Lithography For the Support Stem and Top Electrode

The third and fourth lithography steps, which define the oxide opening at the center of the AlN disk and the stem coverage of poly-Si, present an obstacle to the ultimate miniaturization and reliable fabrication of the support stems. Scaling down anchor size, while desirable, can be challenging lithographically in the presence of large topography due to the need to use thick photoresist. A process modification allowing for lithographic definition of smaller features, through the use of thinner resist, is desired to reliably attain well defined anchors and scale down the size of the device. A second oxide backfill and CMP step to eliminate topography after AlN etching could enable this improvement.

Better Cleanliness

To maximize yield and Q's, the devices must be kept as clean as possible during fabrication, release, and testing. Stubborn photoresist after etching proved difficult to remove, and

created non-volatile compounds that stuck to surfaces. Improved chemical cleaning methods at intermediate steps during fabrication can lead to better performance.

Chapter 7

Capacitive Piezoelectric Narrowband Filters

In Chapter 1, we described why RF and IF filters are important components for radios: they allow for spectral coexistance of signals with different operating frequencies. As discussed, in a typical RF environment, among many interferering signals is a lone desired signal. The purpose of a bandpass filter is to heavily suppress unwanted signals at frequencies outside of the passband. Additionally, the filter should add little to no attenuation in transmitting the desired signal between input and output. High resonator Q, electromechanical coupling C_x/C_0, and low motional resistance R_x are all key towards achieving good filter performance.

Each one of the several MEMS filter technologies described in section 1.3 has its own unique advantages and drawbacks. Making capacitive-piezoelectric AlN filters is a compelling area of research for the following reasons:

- They can potentially attain higher Q's than attached electrode AlN resonators.
- They can be fabricated so as to have multiple frequencies on chip.
- They can be fabricated to have variable bandwidths.
- They can be switched on and off through resonance quenching.
- They can be decoupled through top electrode lifting.
- They are frequency tunable.
- They have much stronger electromechanical coupling than capacitively transduced resonators.
- They are aptly suited for narrowband filter applications between 0.1% and 1% fractional bandwidth.

In this chapter, we will explain operating principles, provide a model, provide automated design tools, and present experimental results pursuant towards realizing high performance capacitive-piezoelectric narrowband filters.

7.1 Transfer Functions for Resonators and Filters

A MEMS filter is an example of a linear, time-invariant (LTI) system. The transfer function $H(s)$ for any LTI system allows one to determine how the system will respond to an arbitrary input signal, $x_{in}(t) = \mathcal{L}^{-1}\{X_{in}(s)\}$. Here, t represents time, s is the complex angular frequency Laplace variable, and $\mathcal{L}\{\cdot\}$ represents the Laplace transform operator. The output signal $y_{out}(t) = \mathcal{L}^{-1}\{Y_{out}(s)\}$ can thus be predicted when the input signal and transfer function are known. To calculate the system response in the time domain due to an arbitrary input, one simply takes the inverse Laplace transform of the product of the transfer function and the Laplace transform of the input:

$$y_{out}(t) = \mathcal{L}^{-1}\{H(s)X_{in}(s)\} \tag{7.1}$$

The transfer function is thus equal to the Laplace transform ratio of an LTI system's output signal to its input signal:

$$H(s) = \frac{Y_{out}(s)}{X_{in}(s)} \tag{7.2}$$

An alternative route to finding an LTI system's time domain response is to convolve $(*)$ its input signal with its impulse response, called $h(t)$. One familiar example of an impulse response is the sound heard when one strikes a bell.

$$y_{out}(t) = x_{in}(t) * h(t) \tag{7.3}$$

For an underdamped (high Q) system, sinusoidal input signals that resemble the impulse response in having frequency content at one or more of the natural frequencies of the system will incite more strongly amplified responses than non resonant input signals. In terms of the convolution occurring, maximal integrated area overlap for the time-reversed impulse response superimposed on the input signal occurs when an excitation and a system's underdamped eigenfrequencies match. This is the essence of what leads to resonance–the excitation of an underdamped system's natural frequency. The choice of whether it's better to describe an LTI system using its transfer function or its impulse response depends on whether the inputs to the system are more impulsive or oscillatory in nature. Transfer functions are generally more useful in filter design since they process oscillatory signals.

Frequency Response

If one is interested in the frequency response for a system one can substitute $j\omega$ for s to find the (complex) value of the transfer function at a frequency of interest:

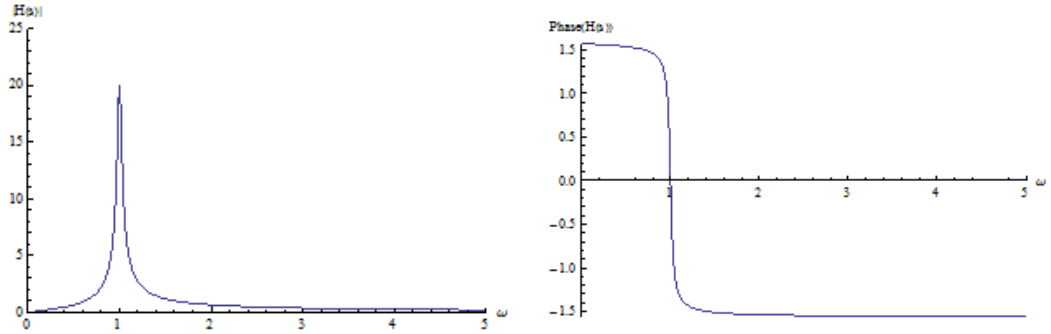

(a) Magnitude plot: $|H(j\omega)|$

(b) Phase plot: $\angle H(j\omega)$

Figure 7.1: Simulated frequency response of the force to velocity transfer function for a single DOF resonator.

$$H(j\omega) = |H(j\omega)|e^{j\angle H(j\omega)} = Ae^{j\theta} \tag{7.4}$$

The output signal will simply be a scaled and shifted version of the input signal at the same frequency–scaled in magnitude by $A = |H(j\omega)|$ and phase shifted by $\theta = \angle H(j\omega)$. A single DOF "mass-spring-damper" resonator has the following force to velocity transfer function:

$$H(s) = \frac{\dot{u}(s)}{F(s)} = \frac{1}{k/s + c + ms} = \frac{1/k}{1/s + 1/(\omega_0 Q) + s/(\omega_0^2)} = \frac{s\omega_0^2/k}{\omega_0^2 + (s\omega_0)/Q + s^2} \tag{7.5}$$

Thus the frequency response of the velocity transfer function is given by:

$$H(j\omega) = \frac{\omega_0^2/(j\omega)}{-\omega^2 + (j\omega\omega_0)/Q + \omega_0^2} \tag{7.6}$$

A magnitude and phase plot for this frequency response are included in fig. 7.2. The peak height of the frequency response magnitude is determined linearly by the Q factor of the resonator. Likewise, the slope of the phase of the transfer function is also linearly proportional to Q.

Poles and Zeros

Key to understanding filter behavior is an awareness of the role that poles and zeros in the transfer function play in determining the frequency response. A zero is a complex value of s which makes the numerator of the transfer function equal zero; a pole is one which makes the denominator equal zero. Generally, the transfer function can be expressed as a rational function of polynomials in s. Often, poles and zeros exist as complex conjugate pairs. To illustrate the effect that poles and zeros have on the frequency response, fig. 7.2b presents a

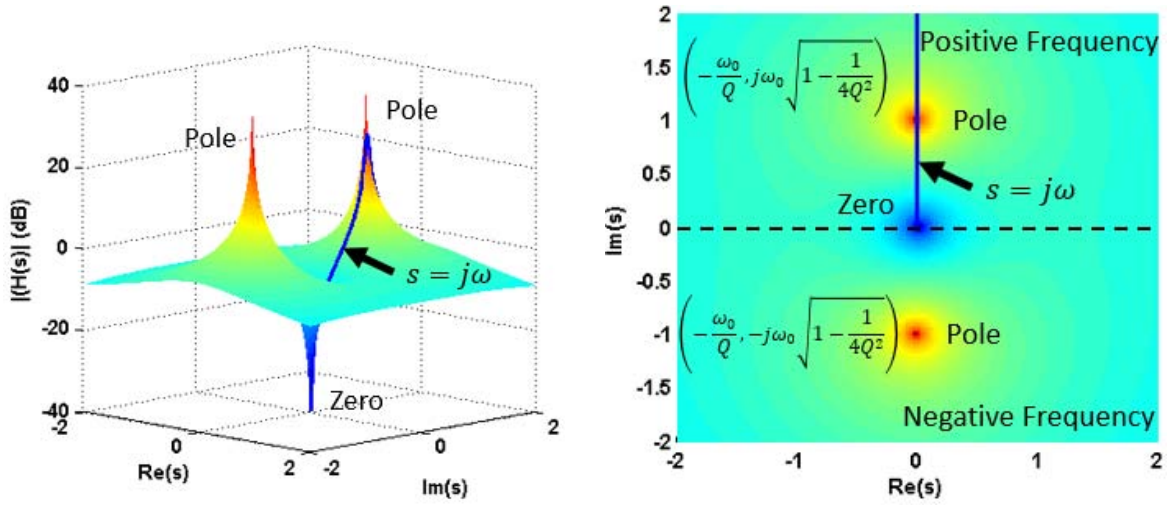

(a) 3-dimensional surface plot of the complex frequency response. The blue trace indicates the frequency response magnitude as a function of frequency. Peak height is determined by the proximity of the pole to the blue trace.

(b) 2-dimensional color plot of the complex frequency response magnitude with annotated poles, zero, and pole-coordinates. The proximity of the positive-conjugate pole to the blue line determines the peak height at resonance.

Figure 7.2: Force to velocity transfer function magnitude in complex frequency space for a single DOF resonator with a Q of 20, ω_0 of 1 rad/s, stiffness k of 1 N/m, and max velocity to force ratio of 20 m/(N·s).

surface plot which indicates the locations of poles and zeros in a manner that also intuitively shows how the "tent" height along $s = j\omega$ axis, which yields the curve shown in fig. 7.1a, depends on their locations. For example, increasing Q causes the poles to move closer to the $s = j\omega$ axis and increase the resonance peak height. The colored surface plots of fig. 7.1a are rendered using MATLAB's surf function.

Using Multiple Resonators to Create Tailored Passbands

Although a single pole transfer function is effective for use in an oscillator, the frequency response shown on the blue curve of fig. 7.2a for a single degree of freedom resonator is not sufficient to meet the needs of most filtering applications. What is needed instead is a somewhat flat passband over a finite bandwidth which exhibits desirable properties such as constant group delay (linear phase) throughout the passband, or constant magnitude, so that the filter preserves signal integrity rather than cause distortion or dispersion. To achieve these desirable properties, one can design a filter's transfer function through proper placement of multiple poles in the vicinity of the passband. Having more than one pole is key to creating a passband with a desired bandwidth which is not entirely dependent on Q.

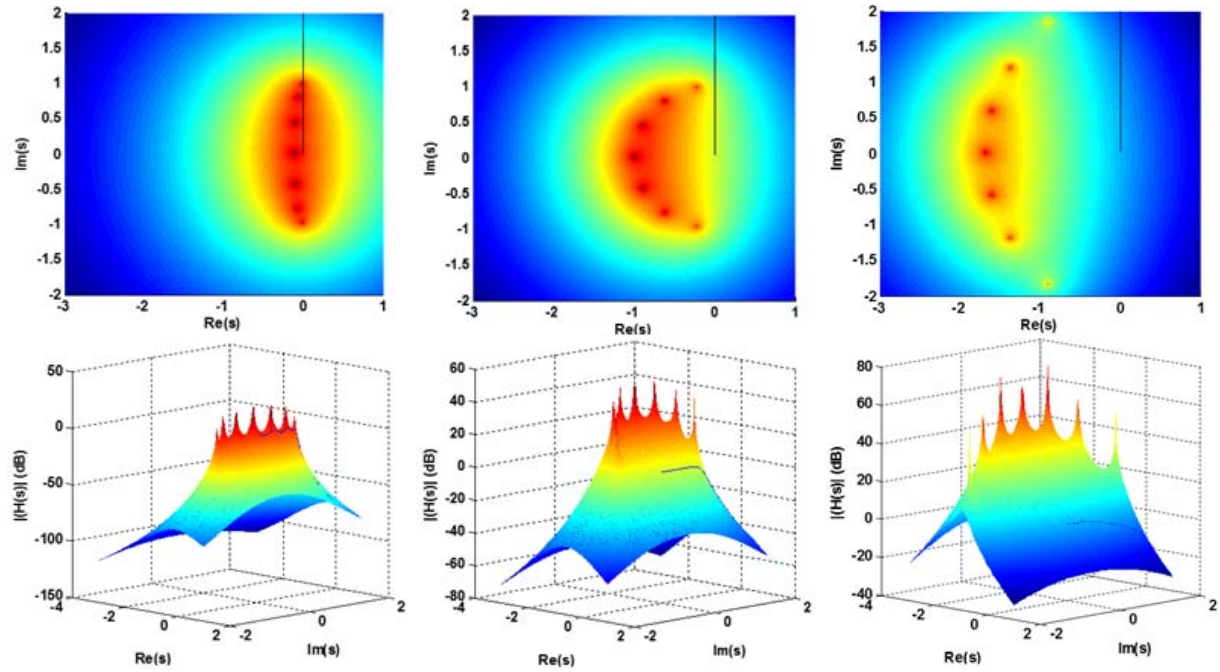

(a) *Chebyshev*. Designed for steep rolloff; has ripple.

(b) *Butterworth*. Designed for a maximally flat passband.

(c) *Bessel*. Designed for maximally flat group delay.

Figure 7.3: Comparison of three 7th order prototype filter frequency responses: Chebyshev, Butterworth, and Bessel.

Using more than two poles allows for fast stopband rolloff. Additionally, zeros can be placed just outside of the passband can help to further steepen stop band rolloff, as will be shown.

Before introducing ways in which to couple multiple resonators together, it's instructive to examine how ideal bandpass filter transfer functions are constructed mathematically. A real filter can be designed to mimic as closely as possible an ideal transfer function which is optimized to obtain desired characteristics.

Prototype Filter Transfer Functions

The first principle of bandpass filter design to understand is the concept of a transfer function for a prototype filter. A prototype filter is a low pass filter with a normalized resonance frequency of one rad/s which can be used as a stepping stone towards creating a bandpass filter at a desired center frequency and fractional bandwidth. For the prototype function, the filter order is the number of poles. For example, fig. 7.3 presents pole-zero plots in complex frequency space for three different types of 7th order, i.e., 7-pole, prototype filters.

The prototype transfer functions are mathematically designed to have certain mathematical properties. For example, to create an nth order Chebyshev transfer function $H(s)$, the

following values are used:

$$\varepsilon = \sqrt{10^{Ripple/20} - 1} \tag{7.7}$$

$$\theta_m = \frac{\pi}{2}\frac{2m-1}{n} \tag{7.8}$$

$$\alpha = \frac{1}{n}\sinh^{-1}\left(\frac{1}{\varepsilon}\right) \tag{7.9}$$

$$s_m = -\sinh\alpha\sin\theta_m - j\cosh\alpha\cos\theta_m \tag{7.10}$$

$$H(s) = \frac{1}{(2^{n-1}\varepsilon)\prod_{m=1}^{n}(s - s_m)} \tag{7.11}$$

An nth order Chebyshev polynomial is bounded to ± 1 within the domain of $[-1, 1]$ and, by definition, attains the largest possible leading polynomial coefficient–thus, Chebyshev filters maximize stopband rolloff. For the prototype filter, the boundary is limited to a general variable called *Ripple* which can be made small to limit magnitude variations in the filter's passband. A Butterworth or maximally flat response is a Chebyshev filter with a *Ripple* value set to zero. A Bessel response is designed to achieve linear phase in the passband. Similar procedures for computing pole locations for Bessel and Butterworth responses can be readily found in literature [93] and were used to create the plots of fig. 7.3.

Transformation from the Prototype to a Bandpass Filter

To implement a bandpass filter using the transfer function of a lowpass prototype, a substitution is made for every s in the transfer function as follows:

$$s \to \frac{1}{FBW}\left(\frac{s}{\omega_0} + \frac{1}{Q} + \frac{\omega_0}{s}\right) \tag{7.12}$$

Where Q is the assumed Q-factor for every resonator in the system, FBW is the fractional bandwidth of the filter (e.g. 0.0025), and $\omega_0 = 2\pi f_0$ is the center frequency of the filter.

A sample bandpass filter, having a wide bandwidth of 30% for the purpose of illustration is included in fig. 7.4. Note that the 8th order bandpass filter transfer function has 16 total poles, with 8 poles in the vicinity of $+j\omega_0$ which act to shape the passband. In the transformation, mirrored and scaled copies of the original pole grouping appear centered around $\pm\omega_0$.

Frequency Responses for Ideal Chebyshev, Butterworth, and Bessel Passband Filters

Included in fig. 7.5 is an array of plots which show magnitude, phase, and group delay vs. frequency for the three filter types mentioned previously. To illustrate the effects of

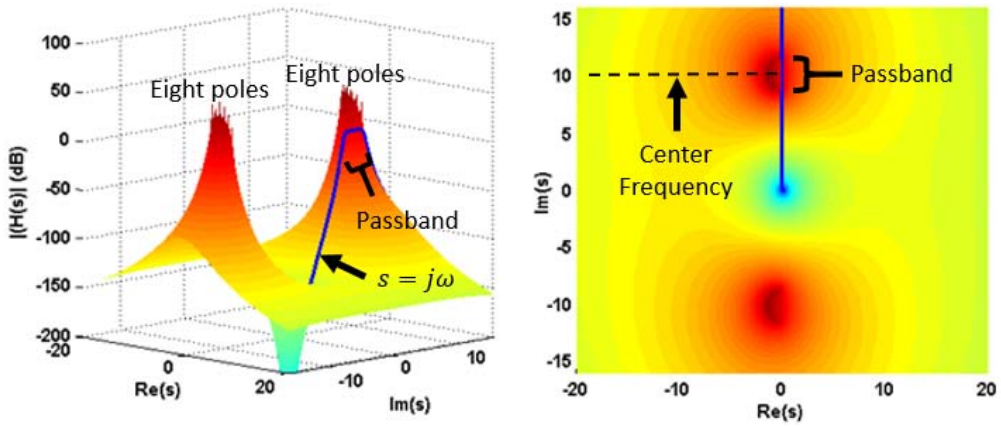

Figure 7.4: Transfer function magnitude in complex frequency space for an 8th order Butterworth bandpass filter with $Q = 500$, 30% FBW, ω_0=10 rad/s as constructed from a transformed prototype filter.

increasing filter order, plots are generated for filter orders ranging from n=1 to n=7. The plots included have center frequencies of 300 MHz and fractional bandwidths of 0.25% to resemble filters that are implemented in this project. Figure 7.5 illustrates the differences between the three filter types. The Chebyshev filters have excellent stopband rolloff, but the group delay variation is high, which can lead to dispersion, or inter-symbol interference. There is also 1 dB of passband ripple. However, filters at adjacent frequencies can easily coexist next to each other. The Butterworth filters have a relatively flat passband as well as less group delay variation. The Bessel filters have very flat group delay vs frequency, which is good for eliminating inter-symbol interference. However, rejection of nearby frequencies is not as strong.

Based on a desired application, designers can choose among these and other filter designs to best meet a system's needs. For example, FBAR duplexers use a custom filter transfer function, using a high order ladder topology, to allow for close proximity to adjacent frequencies by taking advantage of very steep passband skirts like those of the Chebyshev filter. They also take advantage of using zeros in the stopband for increased loss.

Using the idealized transfer functions, simulations of physical designs can be created which are verified to match the desired performance. In the following section, we will introduce methods to compute the transfer functions in terms of physical design parameters.

7.2 Computer Aided Design of Mechanically Coupled Capacitive-Piezo Bandpass Filters

Capacitive-piezoelectric filters may be implemented in several ways, such as by using a ladder topology or through mechanically coupling multiple resonators in series. Either way,

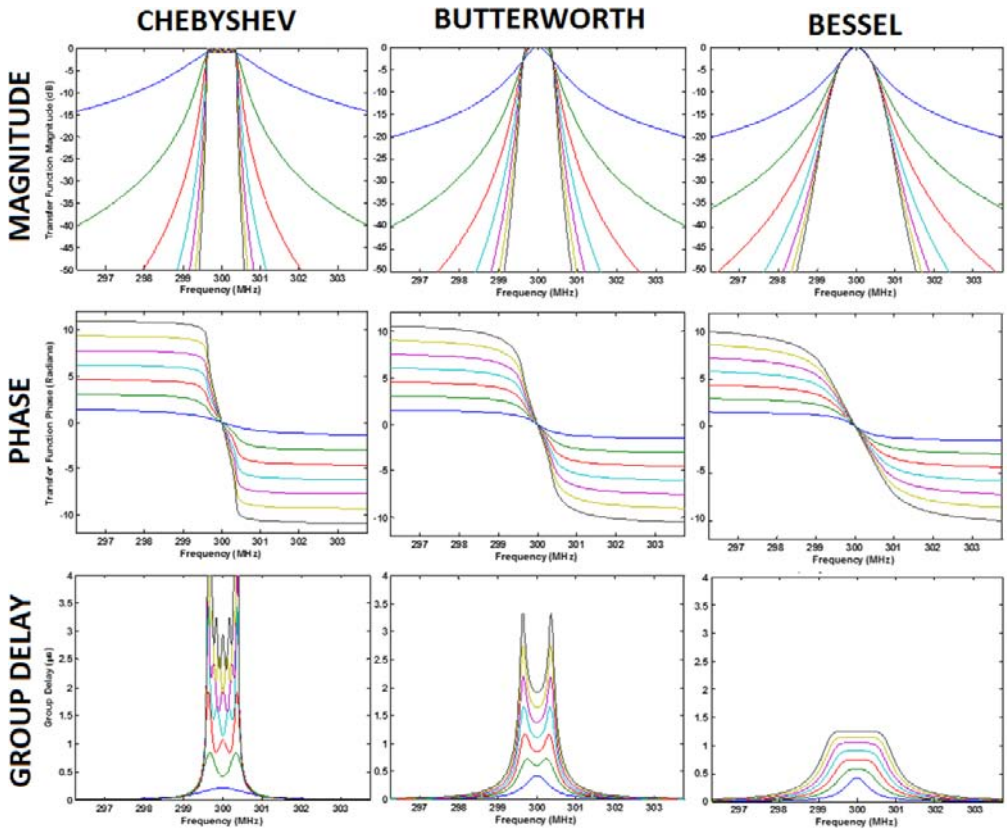

Figure 7.5: Transmission magnitude, transmission phase, and group delay vs frequency for 1-dB ripple Chebyshev, Butterworth, and Bessel simulated ideal 0.25% bandwidth filter responses for n=[1,2,...,7]

computer techniques are key in the design process. In this section, we outline a complete computer aided design flow for making coupled resonator filters.

When n multiple resonators are coupled together so that they have n degrees of freedom, they can form a bandpass system with exceptional shape factor, particularly as n increases beyond 2 or 3. The design of such a system requires knowledge and/or control over a large number of parameters, including resonator motional impedance, 0.5-λ-coupled resonator array size (if necessary), resonator stiffness, filter fractional bandwidth, resonance frequency, resonator frequency accuracy (and tunability if required), parasitic capacitances, resonator Q, coupling beam stiffness(es) and width(s), coupling beam lengths, desired filter order, filter type, and input and output terminating impedances. Needless to say, it helps to have a computer program to account for all the variables that must work together to generate a proper filter. This work automates and expands on many of the filter design principles described in [56], [55], and [48] which were previously applied to making capacitively transduced micromechanical filters at lower frequencies.

A MATLAB filter design kit consisting of four modules was implemented to streamline

the process of making capacitive-piezoelectric filters. Additionally, the designs can also be validated in Agilent's Advanced Design System (ADS) software. Many of the techniques developed in this section would also be applicable to capacitive and piezoelectric transduced filters in addition to capacitive-piezoelectric resonator based micromechanical filters.

MATLAB-Based Filter Coefficient Generator

A MATLAB filter design tool was created to aid filter synthesis in an efficient manner. The first module of the simulator takes as inputs the desired filter order, the filter type, resonator Q-factor, and filter fractional bandwidth and returns as outputs the filter design parameters needed to implement the desired specification. The outputted (dimensionless) parameters include k_{ij} coupling coefficients, q_1 and q_n resonator termination factors, as well as the expected insertion loss that the design will have. The k_{ij} factors are used to determine coupling beam widths while q_1 and q_n determine the input and output resistances used to terminate the filter. Here, IL is the predicted insertion loss for the filter which depends on q_0, filter order, and filter type.

Filter design parameters are determined via automated linear interpolation of the lookup tables of Anton Zverev's *Handbook of Filter Synthesis* [15]. The lookup table for each type of filter up to an order of four is stored in memory so that that for an exact value of $q_0 = QBW/f_0$, accurate values for insertion loss IL, q_1, q_n and the k_{ij}'s can be given. These parameters are selected so as to create coupled resonator filters with transfer functions that match those that are described in section 7.1

For example, if a 0.2%-bandwidth 3rd order 0.5-dB ripple Chebyshev filter using resonators with Q-factors of 8,700 is desired, the simulator first calculates q_0 as 17.4. The simulator then loads the appropriate lookup table into memory as shown in the sample of code below. A look up table exists for each filter order, e.g., 2/3/4/5, and filter type, e.g., Chebyshev, Butterworth, or Bessel.

```
if n==3
    % Chebyshevy Order 3, ripple 0.5db, Zverev p350
    q_0vec=[200 37.273 18.636 12.424 9.318 7.455 6.212 5.325];
    ILvec=[0 .92 1.96 3.14 4.51 6.13 8.11 10.66];
    q1vec=[1.864 1.616 1.577 1.568 1.577 1.5974 1.6275 1.6674];
    qnvec=[1.8636 2.3388 2.5962 2.8158 3.0140 3.1949 3.3584 3.5011];
    k12vec=[0.6474 .6182 .5943 .5680 .5387 .5055 .4667 .4197];
    k23vec=[.6474 .6718 .6884 .7051 .7224 .7407 .7606 .7825];
end
```

Interpolation is performed via the 'interp1' command for each vector as

```
XX=interp1(q_0vec, XXvec, q0)
```

Table 7.1: MATLAB Generated Filter Parameters for a 3rd order 0.2%-BW 0.5-dB ripple Chebyshev filter made of resonators with Q-factors of 8,700.

Filter Parameter	**Outputted Value**
q_0	17.4
IL	2.1948
q_1	1.5752
q_n	2.6399
k_{12}	0.5891
k_{23}	0.6917

The outputs are then returned as shown in table 7.2.

The next module of the filter design system takes the filter parameters and uses them, in cooperation with the resonator simulator, to generate coupling beam widths and termination impedances needed to implement the filter.

MATLAB-Based Coupling Beam Width and Input/Output Termination Impedance Generator

To set the filter's bandwidth, which is determined by the spacing of poles in the transfer function, the stiffness(es) of the coupling element(s) between resonators must be computed. The model for extensional coupling beams, and the expression for stiffness, were described in section 2.10 in Chapter 2. Intuitively, stiffness is proportional to width, and higher stiffness equates to larger bandwidth. Just like in the two degree of freedom coupled resonator example of fig. 2.3, larger coupling beam stiffness leads to increased spacing of modal frequencies.

Calculating coupling beam dimensions and termination impedances requires the parameters of a fully characterized resonator in addition to the filter coefficients calculated previously. The terminating impedances, $R_{q,in}$ and $R_{q,out}$ are calculated as follows:

$$R_{q,in} = R_x \left(\frac{q_0}{q_1} - 1 \right) \tag{7.13}$$

$$R_{q,out} = R_x \left(\frac{q_0}{q_n} - 1 \right) \tag{7.14}$$

Here, R_x is the motional resistance of an equivalent uncoupled end resonator, which is assumed to be matched in frequency and stiffness to all other resonators. The transduction strength η is assumed to be equal at input and output. Interestingly, since q_0 is dependent on Q, the relationship between R_x and $R_{q,in/out}$ does not depend on Q. Thus, Q affects insertion loss but not the optimal termination resistance.

The extensional coupling beam widths, w_{ij}'s, are calculated as follows. First, a standard beam width, w_0, is defined.

$$w_0 = \frac{k_r BW}{\omega_0 t_{AlN} \sqrt{E\rho} f_0} \tag{7.15}$$

Where k_r is the modal stiffness of an individual resonator array, BW is desired bandwidth, ω_0 is modal angular frequency, t_{AlN} is the beam's vertical thickness, E is AlN's Young's modulus, ρ is AlN's density, and f_0 is the operating frequency. This standard beam width is modified by the stiffness coefficients to calculate individual coupling beam widths between the i^{th} and j^{th} resonators.

$$w_{ij} = w_0 k_{ij} \tag{7.16}$$

If the resulting w_{ij}'s are smaller than the minimum linewidths available lithographically and/or termination impedances are too high, then array size should be increased until a valid design is found. Thus, as another benefit not mentioned in Ch. 4, disk arrays are necessary and useful for achieving small fractional bandwidths given lithographic constraints.

Using the simulator with 25-disk arrays of 300 MHz capacitive-piezo disk resonators having 80 nm transduction gaps ($g_{total} = 160nm$) and maximal electrode coverage, the outputted filter design parameters are presented in table 7.2. The R_x of a single disk in this array is 509 Ω and the array R_x is 20.35Ω.

Table 7.2: MATLAB Generated Filter Parameters for a 3rd order 0.2%-BW 0.5-dB ripple Chebyshev filter made of resonators with Q-factors of 8,700.

Filter Parameter	**Calculated Value**
$R_{q,in}$	204.5 Ω
$R_{q,out}$	113.8 Ω
w_{b12}	1.59 μm
w_{b23}	1.87 μm

Using the calculated coupler dimensions one can now proceed to generate layout for the filter design. The locations of many resonators and coupling beams must be specified. It is thus useful to have an automatically generated mapping of where to place all of the components, particularly when multiple resonator arrays are placed side by side.

Automated Filter Layout

An automated filter layout generator is used to aid the process of laying out disk resonators. Disk arrays of standard sizes are plotted, such as 2×2, 3×3, 4×4, or 5×5 configurations. Disk arrays are represented as multiple drawn circles of a specified radius drawn such that they are separated in the x and y directions by coupling beams of length $\lambda/2$. The coordinates of the centers of the arrays are drawn on the printout. Although not yet implemented, it would be even more desirable to directly write to a gds2 file rather than a

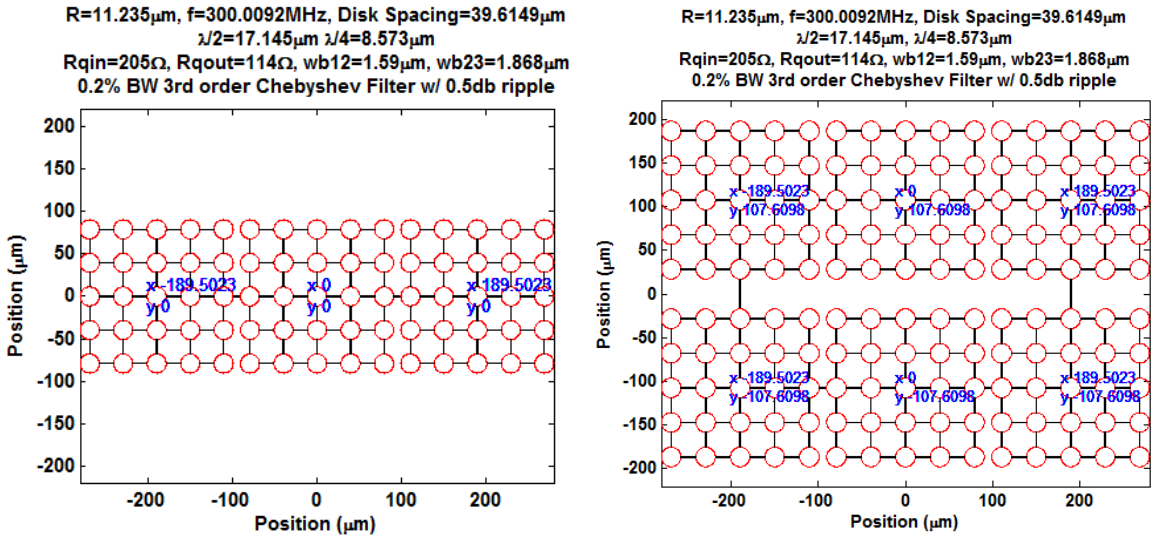

(a) Single-ended version.

(b) Differential version.

Figure 7.6: Auto-generated layout for the simulated 3rd order filter.

MATLAB plot. Nonetheless, it is useful to have the coordinates for placing individual arrays as a quick verification of proper layout for a newly generated filter design.

In addition, the filter layout generator can accommodate differential designs, where two single ended filters are adjoined using coupling beams that are one extensional wavelength long. A sample of generated layout for the differential version of the filter of fig. 7.6a is included in fig. 7.6b.

The final step of the filter design process is to verify that the calculated parameters will indeed manifest the desired filter response. A filter response simulator was implemented to simulate the frequency response for the generated network.

Filter Response Simulator

A filter's response can be modeled and plotted in simulation using an equivalent 2-port network representation for the network which is terminated with the desired impedances at input and output. The most convenient 2-port model for using MATLAB to simulate a coupled resonator filter is one constructed using ABCD parameters, as they easily allow adjacent circuit building blocks to be joined together to form an equivalent cascaded network. The S_{21} response at each frequency can then be calculated using the following expression, where R_{01} and R_{02} represent the real components of terminating impedances, Z_{01} and Z_{02}.

$$S_{21} = \frac{2\sqrt{R_{01}R_{02}}}{AZ_{02} + B + CZ_{01}Z_{02} + DZ_{01}} \tag{7.17}$$

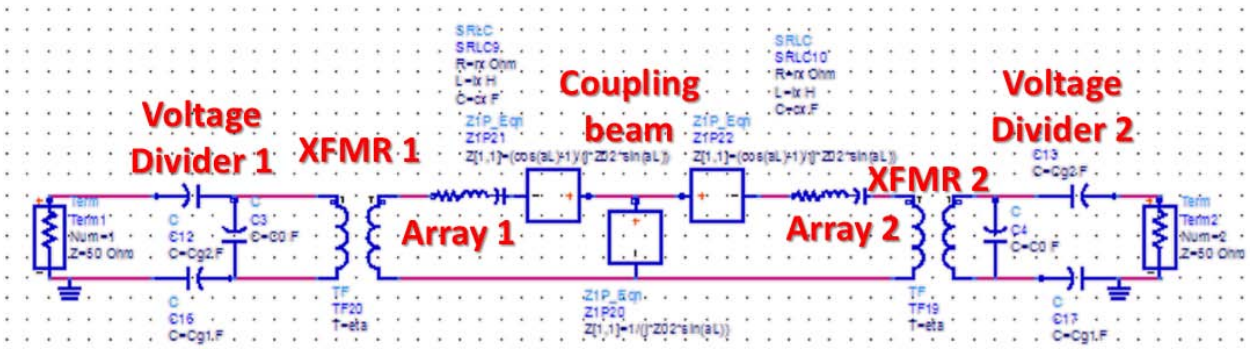

(a) Circuit schematic for a 2nd order capacitive-piezo mechanically-coupled filter.

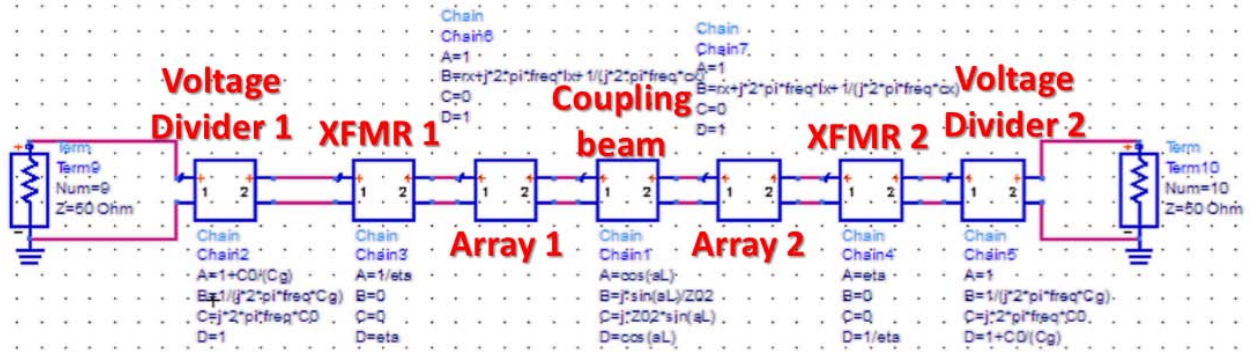

(b) Equivalent cascaded chain of ABCD 2-port networks.

Figure 7.7: Equivalent ADS circuit models for a two resonator capacitive-piezo filter.

ABCD 2-port parameters are defined as follows, where positive currents are defined as entering a port.

$$\begin{bmatrix} v_1 \\ i_1 \end{bmatrix} = \begin{bmatrix} A & B \\ C & D \end{bmatrix} \begin{bmatrix} v_2 \\ -i_2 \end{bmatrix} \tag{7.18}$$

To join two (or more) cascaded 2-port networks into a single equivalent network, the ABCD matrices for cascaded blocks are simply matrix multiplied together. Thus, a system consisting of cascaded blocks including capacitances, transformers, resonators, and mechanical coupling beams can be modeled as a single "black box" 2-port network through performing multiple matrix multiplications. For example, the coupled resonator circuit of fig. 7.7a can be equivalently modeled as seven cascaded blocks of ABCD parameters, as is shown in fig. 7.7b. The outer two blocks represent the input and output capacitive voltage dividers, the next two inner blocks represent represent the electromechanical transformers, the next two inner blocks represent the mechanical impedances of the two resonators, and the middle block represents the extensional coupling beam.

$$\begin{bmatrix} A_{eq} & B_{eq} \\ C_{eq} & D_{eq} \end{bmatrix} = \begin{bmatrix} 1+\frac{C_0}{C_g} & \frac{1}{j\omega C_g} \\ j\omega C_g & 1 \end{bmatrix} \begin{bmatrix} \frac{1}{\eta} & 0 \\ 0 & \eta \end{bmatrix} \begin{bmatrix} 1 & Z_{R1} \\ 0 & 1 \end{bmatrix} \ldots$$
$$\ldots \begin{bmatrix} \cos(\alpha L) & \frac{j\sin(\alpha L)}{Z_{0a,cb}} \\ j\sin(\alpha L) Z_{0a,cb} & \cos(\alpha L) \end{bmatrix} \begin{bmatrix} 1 & Z_{R2} \\ 0 & 1 \end{bmatrix} \begin{bmatrix} \eta & 0 \\ 0 & \frac{1}{\eta} \end{bmatrix} \begin{bmatrix} 1 & \frac{1}{j\omega C_g} \\ j\omega C_g & 1+\frac{C_0}{C_g} \end{bmatrix} \quad (7.19)$$

A fourth order filter would contain ABCD matrices for all the building blocks of eq. (7.19) in addition to four more blocks representing the 3rd and 4th resonators and the 2nd and 3rd coupling beams.

Addition of feedthrough capacitance to the filter response

To account for port to port feedthrough capacitance C_f in the filter, which acts in parallel to the cascaded ABCD network, the ABCD network can be converted to Y-parameters with an added parallel admittance ($X = j\omega C_f$), and then reconverted, as follows. A typical feedthrough capacitance value for our filters is 1 fF. This capacitance can be further reduced through ground shielding between input and output and differential operation. Reducing feedthrough is key to achieving strong stop band rejection.

```
X=1i*omega*Cf;
Y11=D/B+X;
Y12=(B*C-A*D)/B-X;
Y21=(-1/B)-X;
Y22=A/B+X;
A=-Y22/Y21;
B=-1/Y21;
C=(Y12*Y21-Y11*Y22)/Y21;
D=-Y11/Y21;
```

Through allowing MATLAB to calculate the ABCD parameters for the equivalent circuit networks, the filter responses can be quickly generated. For the filter design generated by the previous filter simulator modules, fig. 7.8 presents the generated unterminated and terminated filter responses, as well as the single resonator 50 Ω terminated response, to confirm that the filter design is valid.

Monte Carlo Analysis

Random frequency mismatches, due to manufacturing variations, in coupled resonator filters can corrupt a frequency response by either a tolerable or an unacceptable amount. To meet performance specifications, it must be determined whether frequency tuning techniques are needed and to what degree. Generally, wideband filters are more tolerant of frequency

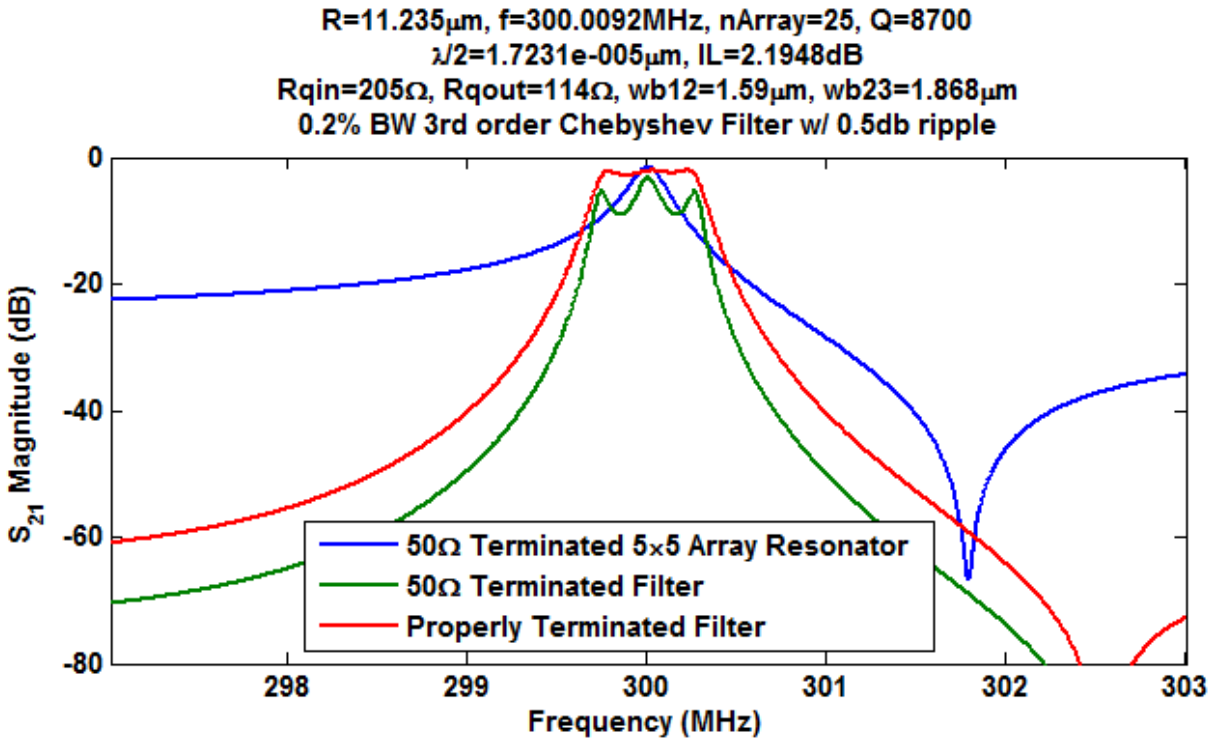

Figure 7.8: MATLAB auto-generated simulated filter response and design parameters based on desired resonator technology, array size, desired filter type, order, and fractional bandwidth.

mismatches and likely do not require electrical tuning techniques, whereas narrowband filters require strict frequency matching, thus generally requiring tuning.

The filter response simulator can be run on a system for which the resonator sizes are multiplied by a random Gaussian error term so as to result in unmatched resonant frequency such as would occur due to imperfect manufacturing tolerances, which unfortunately do not scale well with frequency. As features are made smaller, approaching lithographic limits, fabricated dimensions can become larger or smaller than desired due to the line-edge roughness of lithographic patterns, or due to under or over exposure of photoresist.

Based on the results of fig. 4.7, the frequency error standard deviation σ_1 for a single 11.2-μm-radius (300 MHz) contour mode disk resonator is assumed to be 320 ppm, based upon measurements of 4-disk arrays, for which the standard deviation of frequency error was determined to be σ_4= 160 ppm through measurement.

Invoking the central limit theorem of statistics, the frequency error standard deviation for a coupled array of n disks, σ_n, is reduced as

$$\sigma_n = \frac{\sigma_1}{\sqrt{n_{disks}}} \tag{7.20}$$

σ also depends on the size of the disk resonator. It is postulated that the frequency error

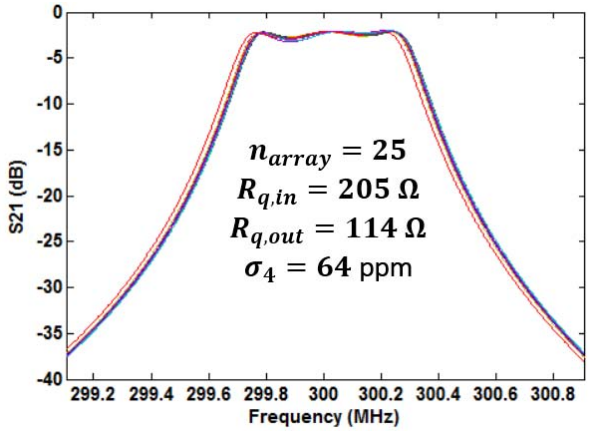

(a) 25 disk arrays have acceptable frequency variation. Resonator manufacturing precision is very good.

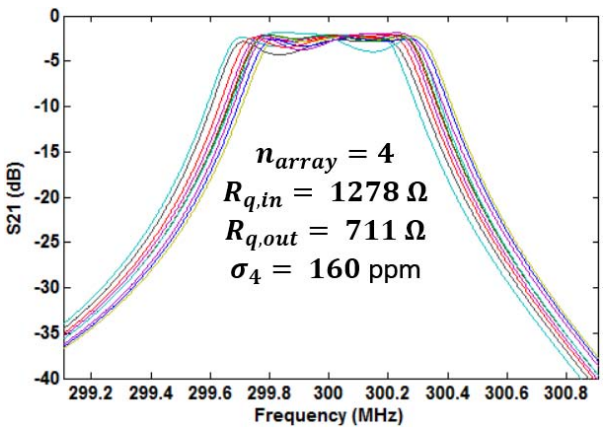

(b) 4 disk arrays have more frequency variation. Precision is marginally acceptable but may require tuning.

Figure 7.9: Comparison of Monte Carlo simulations for a 3rd order filter for 5×5 disk arrays and 2×2 disk arrays.

scales in proportion to $R_{disk}^{-1.5}$, thereby becoming worse for higher resonance frequencies. A given line edge roughness for a circle causes a larger fractional change in radius for small radii ($1/R$ contribution), and is averaged out over a shorter circumference for small radii ($1/\sqrt{R}$ contribution).

The general expression for σ for an array consisting of n resonators having nominal radii equal to R_{disk} may thus be expressed as:

$$\sigma_n \approx \left(\frac{11.2\ \mu\text{m}}{R_{disk}}\right)^{1.5} \frac{320\ \text{ppm}}{\sqrt{n_{disks}}} \tag{7.21}$$

A randomly selected fractional frequency change, δ, obeying the normal distribution with standard deviation σ_n for a resonator is manifested as a change in mechanical lumped element parameters as follows:

$$\delta = \sigma \cdot \text{normrnd}(0, 1) \tag{7.22}$$

$$r_x' = r_x(1 - \delta) \tag{7.23}$$

$$l_x' = l_x(1 - 2\delta) \tag{7.24}$$

$$c_x' = c_x \tag{7.25}$$

To illustrate the predicted effect of array size on frequency variation as it affects a filter design, fig. 7.9 presents a comparison of Monte-Carlo simulations for the 3rd order filter

constructed from 25-disk arrays, and one which uses 4-disk arrays instead. The large array size filter is advantageous due to its reduced terminating resistances and frequency standard deviations.

In either case, the filter's shape is well preserved and likely would not *mandate* frequency tuning for a usable filter, although the filter using 25 disk arrays has certainly has less variation and is preferable. Of course, it's possible that nonideal modal properties are worse for larger array sizes when fabrication does not go well. More investigation is needed into just how large array sizes can be and still operate properly.

7.3 Measurements of Fabricated Capacitive-Piezoelectric Filters

In addition to the switchable and tunable filters presented in Section 5.4, other capacitive piezoelectric filters have been fabricated and measured and are reported in this section. Although further fabrication improvements are needed to fully realize the potential of capacitive-piezo disk resonator array technology, this work provides pioneering examples of feasibility and performance. We present key filter results to show current progress.

2nd Order Capacitive Piezo Disk Array Filter at 300 MHz

Figure 7.10 presents one of the first capacitive-piezoelectric filter results obtained in this study. Here, fig. 7.10a shows an image of the device under test while connected to GSG probes. The filter consists of two 3×3 disk arrays which are mechanically linked to one another by an extensional coupler of acoustic length $\lambda/4$ at a design frequency of 300 MHz. The two mode shapes for this structure are depicted via COMSOL modal simulations in fig. 7.10b and fig. 7.10c. The two peaks of the underterminated filter response correspond to two modes of vibration for the overall structure: one in which the two arrays vibrate out of phase, allowing for minimal deformation of the coupler, and the other in which the coupler deforms, which adds extra stiffness and occurs at a slightly higher resonance frequency. Notably, the spacing of these two peaks is 0.2%, exactly as was designed. Here, bandwidth is determined by the ratio of the coupling beam's stiffness k_c as compared to that of the array's stiffness k_r.

The 50 Ω terminated S_{21} measurement for this device is included in fig. 7.10d. The unloaded Q's of the two resonant modes are measured at 3,500, and single disk R_x's of 14 kΩ are estimated based on insertion loss. What went notably well in this fabrication batch is the AlN etching step, which provided nearly ideal sidewall angles (as shown in fig. 6.11b), thus providing nearly ideal modal characteristics of the filter, for which bandwidth and resonance frequency are set by CAD definable resonance frequencies.

Shortcomings of this fabrication batch included poor electromechanical coupling due to poor AlN film quality, anchor adhesion difficulties affecting Q's and yields, large fabrication gaps, and large amounts of both unwanted power loss and feedthrough due to the use of

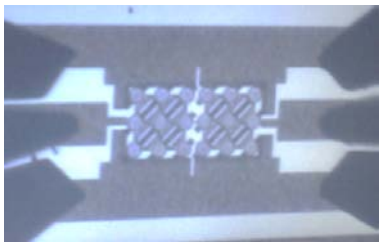

(a) Optical micrograph of a 0.2 % bandwidth 300 MHz 2nd order filter with GSG probes in place for testing.

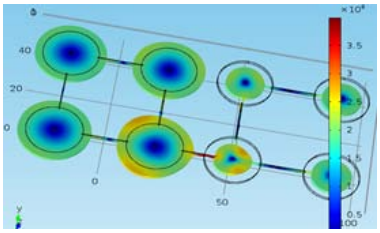

(b) COMSOL simulated mode shape for first resonance peak. (2×2 arrays)

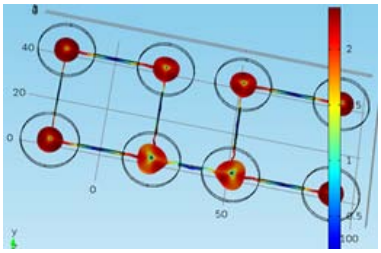

(c) COMSOL simulated mode shape for second resonance peak. (2×2 arrays)

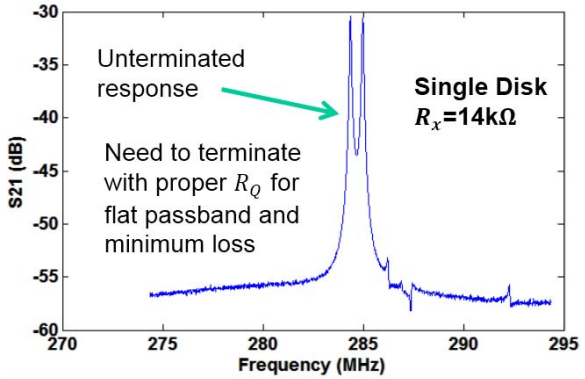

(d) Underterminated (50Ω) frequency response for the 2 pole filter.

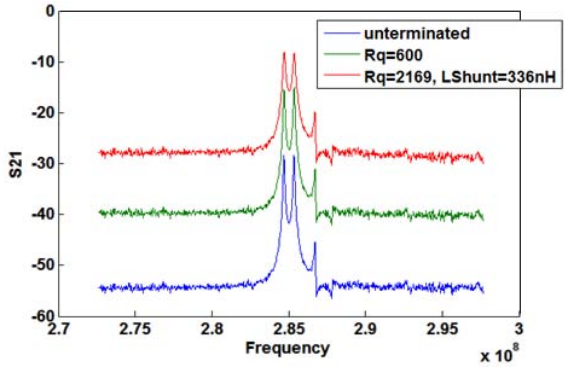

(e) Attempted proper termination of a 0.2 % bandwidth 300 MHz 2nd order filter.

Figure 7.10: 2nd order capacitive piezoelectric filter demonstration.

a 1.6 μm thick AlN film as a substrate protecting barrier layer over which the devices were built. These issues are detrimental to the stopband rejection: low Q (as compared to 8,800) increases passband insertion loss, acoustic radiative power (due to the ill-fated AlN barrier layer) into the substrate adds insertion loss to both the stopband and passbands, and radiative and capacitive power transmission between input and output raised the filter's feedthrough floor.

Attempting to eliminate insertion loss of the filter through increasing termination impedances to the proper values, as is shown in fig. 7.10e, proved unsuccessful due primarily to the use of AlN above the substrate to insulate the electrodes from the conductive Si substrate. The minimum insertion loss attained is 8 dB which required extra inductance and a 2.2 kΩ termination. The minimum insertion loss without using any inductance was attained at a termination resistance of 600 Ω, for which 16 dB of minimum insertion was attained.

The device of fig. 7.10e differed slightly from that measured fig. 7.10d in that its disks were marginally modified in radius by 0.5% while keeping the pitch between devices the same, thus changing coupling beam size. This indicates that the spurious mode of fig. 7.10e is due to a slightly nonideal coupling beam size but can be corrected, since the spurious

mode is reduced in fig. 7.10d.

Remarks

To markedly improve the performance of the filter of fig. 7.10, the following changes should be implemented: don't use AlN as a substrate isolation layer, increase resonator Q, and increase k^2_{eff}. With these changes, termination resistance for a flat passband would be below 500 Ω and would require no inductance. Insertion loss would be under 3 dB and stopband rejection should exceed 50 dB.

2nd Order Capacitive Piezo Ring Filter at 400 MHz

As another approach, it is also possible to make a similar filter to that of fig. 7.10 using ring resonators, as is shown in fig. 7.11. Ring structures have resonance frequencies that depend on the difference between the outer and inner diameters of the ring structures. Refer to [43] for equations to determine modal frequencies of ring resonators. Here, four spokes are used to support each ring that are an odd integer multiple of $\lambda/4$ in length to minimize anchor loss and maximize Q. For large rings, vertical displacement of the ring from the anchor point can cause top electrode contact, thus limiting the maximum ring size that can be used. For this structure, the top electrodes extend over from the outside of the rings, as is enabled by a conformal electrode deposition. The AlN ring structure has inner and outer radii of 45 μm and 53.2 μm, respectively. Due to the high number of spurious modes of ring structures and the difficulty of scaling the structure in size to reduce impedance, disk array structures, with their distributed anchoring and compact form factors, seem advantageous for making filters.

4th Order Capacitive Piezo Disk Array Filter at 200 MHz

Figure 7.12 presents a disk array filter with four poles at a design frequency of 200 MHz. Four 3×3 disk arrays are mechanically coupled in series, creating four distinct modes of vibration for the overall structure. Each disk has a radius of 16.8 μm, and $\lambda/2$ coupling beams are 25.7 μm long. The frequency response of the 50 Ω terminated filter exhibits a very high shape factor. High order filters are advantageous due to their steep stopband rolloffs, but require higher Q's for a given fractional bandwidth to obtain the same level of insertion loss as a comparable low order filter.

The filter structure of fig. 7.12 requires several design improvements to achieve better performance. First, the inner resonators are not frequency matched to the outer ones because the frequency shift of capacitive-piezo transducers was not accounted for in their design. Inner resonators should have both top and bottom electrodes grounded to effect the same frequency shift experienced by the input/output resonators. Additionally, the same coupling beam width was used for the three coupling beams, but proper filter design uses different

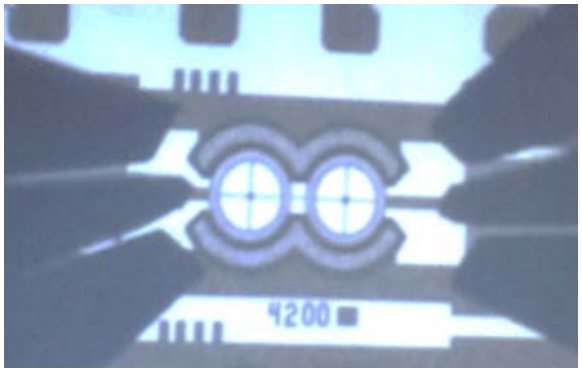

(a) Optical micrograph of the device under test.

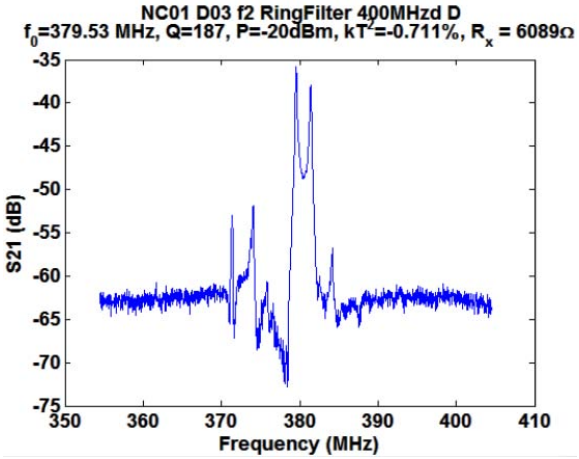

(b) S_{21} magnitude measurement showing the frequency response with 50 Ω terminations.

Figure 7.11: 2nd order capacitive piezoelectric filter demonstration.

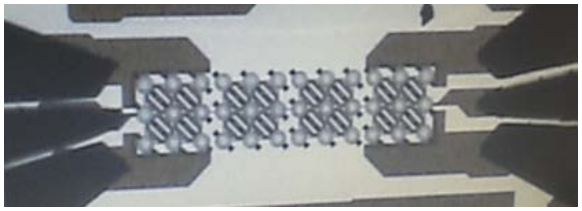

(a) Optical micrograph of the device under test.

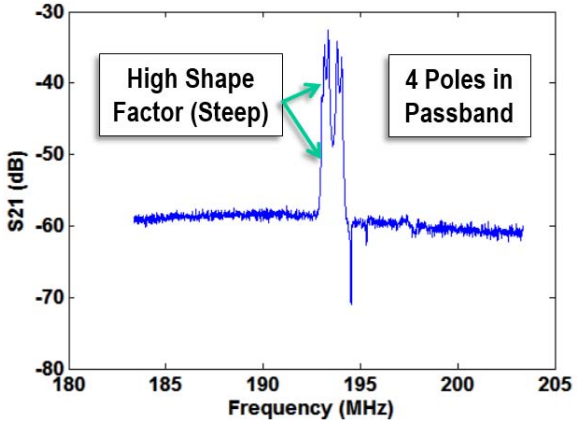

(b) S_{21} magnitude measurement showing the frequency response with 50 Ω terminations.

Figure 7.12: 4th order capacitive piezoelectric filter demonstration.

values to achieve an optimized passband. Lastly, tuning of the individual resonators would allow for fine-tuning of an ideal passband. Aside from design improvements, the same fabrication improvements and corrections mentioned section 7.3 are needed to achieve optimal performance.

Strongly Coupled 433 MHz Disk Array Filters

The three prior filter demonstrations exhibit a need for increased electromechanical coupling and reduced feedthrough. Pursuant to better performance, the capacitive gaps were

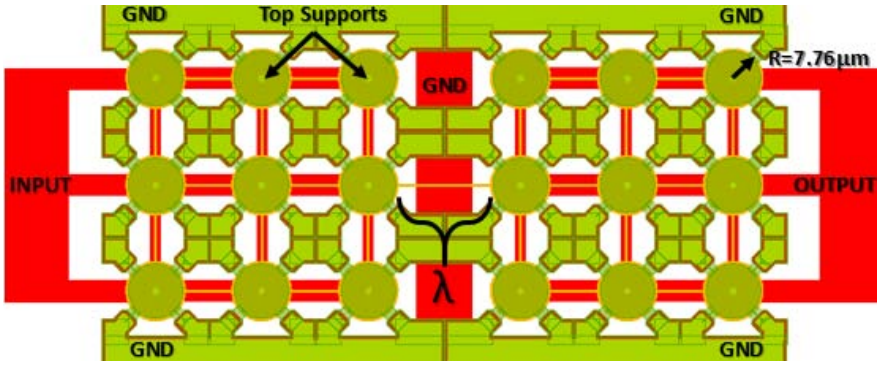

(a) Layout.

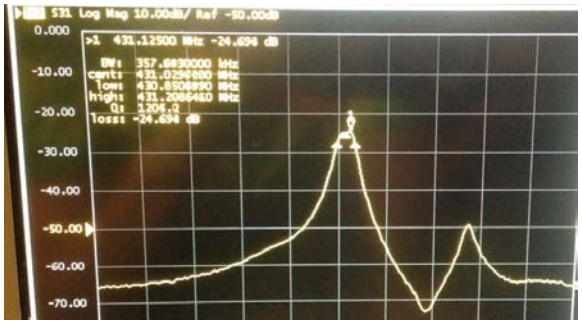

(b) Network analyzer screenshot of a strongly coupled filter-like response.

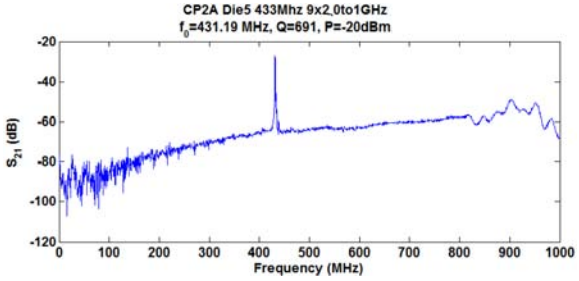

(c) Wideband frequency response of the filter over a 0 MHz to 1.0 GHz range showing very good rejection over the stopband.

Figure 7.13: A 433 MHz strongly coupled filter response demonstration.

reduced, AlN film quality was improved, a ground line was introduced between input and output, and the AlN isolation layer on the substrate was eliminated. However, new fabrication issues arose, including: (a) stringers connecting the coupling beams to the interconnect and (b) electrode-resonator contact. These two effects degrade Q's, and even more detrimentally, proper operation of the coupling beams of the devices. Nonideal couplers introduce spurious modes and reduce coupling strength due to enforced phase variations at the boundaries of adjacent resonators which reduce modal displacement. The reduced Q and reduced transduction strength (η) lead to smaller motional currents, and hence higher motional resistance (R_x), than is ultimately possible with ideal devices.

Nonetheless, fig. 7.13 presents a demonstration at 433 MHz of a strongly coupled disk array structure which exhibits a 2 pole frequency response. Remarkably, this device, the layout for which is presented in fig. 7.13(a), isn't even designed to function as a filter (with its λ-length coupling beam instead of a more appropriate $\lambda/4$- or $3\lambda/4$-length beam) but still demonstrates a strongly coupled response with two closely spaced poles forming a passband. Calculations indicate that the properly functioning device, with a 1000 Ω predicted single disk R_x, could have an unloaded motional resistance of only 222 Ω, and thus an insertion loss of 12.7 dB when loaded by 50 Ω terminations, in which case the stopband rejection would

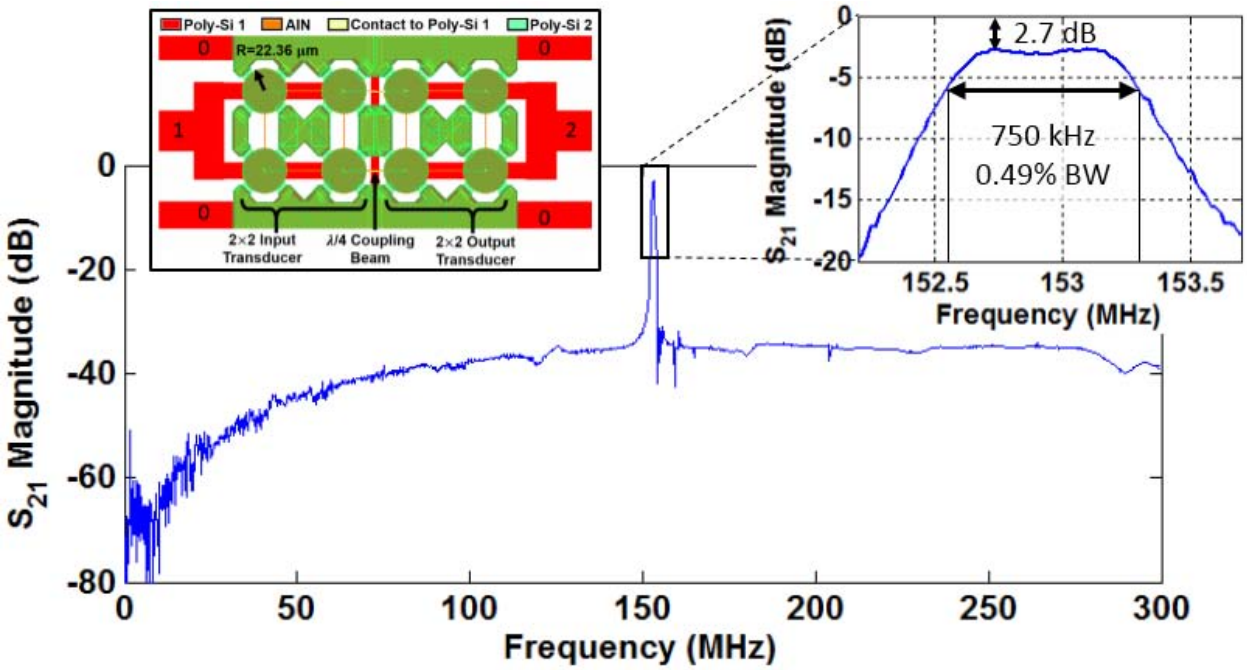

Figure 7.14: A 0.5% bandwidth, 2nd order filter response with 2.7 dB of insertion loss.

be over 55 dB with the given feedthrough level of -68 dB. Figure 7.13c shows the wideband filter response between 1 MHz and 1.0 GHz to illustrate that the filter only responds at the design frequency within this frequency range. With proper coupling beams, the spurious mode at -50 dB will also be suppressed.

150 MHz Filter with 2.7 dB of Insertion Loss

The prior demonstrated filters in this chapter have had significant insertion loss due to low terminating resistances of only 50 Ω. Figure 7.14 presents an optimally terminated response for a 0.5% bandwidth filter at 153 MHz that posts an insertion loss of 2.7 dB. The array has a stiffness of k_r=2.38 N/m while the coupling beams have a combined stiffness of 0.119 N/m, which corresponds to the stiffness of two 0.8 µm wide beams.

7.4 Capacitive-Piezo Filters with Individually Tunable Resonators

Figure 7.15 presents a filter design capable of frequency tuning its three individual resonators independently. This structure is predicted to be capable of total passband correction when properly fabricated. Individual resonator tuning for passband correction is essential for narrowband filters with resonator frequency precision standard deviation that is greater than

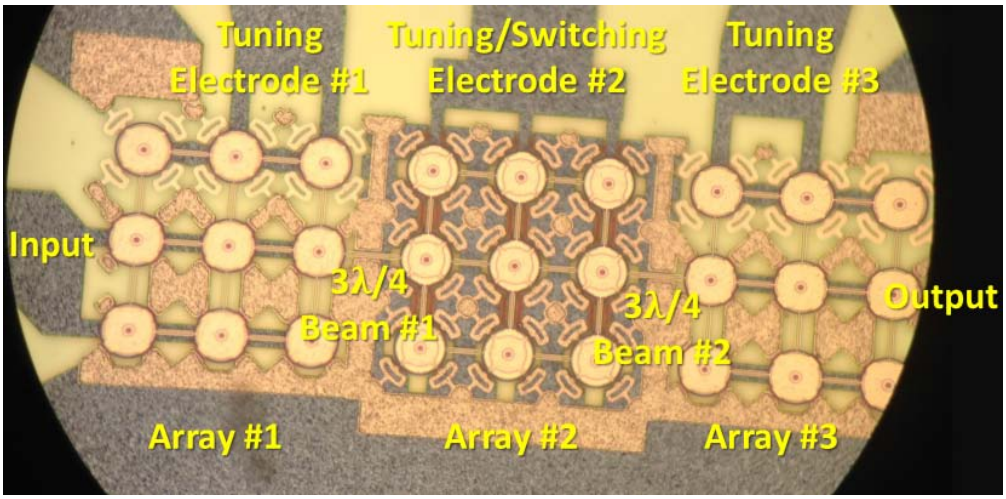

Figure 7.15: Optical micrograph of a third order disk array filter with individually tunable resonators.

one tenth size of the passband. Automated passband correction has recently been demonstrated at 455 kHz by Henry Barrow on a fourth order MEMS filter using an automated tuning protocol [94]. Although the filter peaks in the device of fig. 7.15 responded somewhat to tuning in measurement, it was not enough to overcome the previously discussed fabrication difficulties, which posed more serious problems than resonator mismatch. Nonetheless, the design could prove useful in the future as an important facet of a research effort to realize a narrowband filter with a correctable passband at ultra high frequencies.

7.5 Remarks

The new design tools and experimental results of this chapter aim to support the realization of switchable and tunable narrowband filters for RF channel selection at ultra high frequencies with competitive performance at low cost. We have shown key results including filter model verification, demonstration of proper modal characteristics, a four-pole filter demo, a filter with strong stop band rejection, a filter with strong electromechanical coupling, a filter with low insertion loss, and a design which allows for individual tuning of resonators. Thus, the individual requirements for proper operation have all been satisfied, but not all at the same time yet. Refabrication and further development will surely lead to even more compelling demonstrations.

Chapter 8

Conclusions and Future Work

This closing chapter provides an evaluation and summary of key results and proposes additional research. Although further development work will enable even better devices, based on what has been demonstrated here, high-Q frequency tunable capacitive-piezo narrowband filters and frequency synthesizers have potential to provide a lasting contribution for society's ever-growing need for low power wireless connectivity.

8.1 Summary of Key Results

This section summarizes the most compelling findings of the previous five chapters. The topics include: capacitive-piezo disk resonator optimization, disk arrays, voltage controlled electrode actuation of capacitive-piezo transducers, fabrication, and capacitive-piezo filters.

Capacitive-Piezoelectric Disk Resonators with High Q, Strong k_{eff}^2, and Low R_x

In Chapter 3, the capacitive-piezoelectric AlN disk resonator was introduced as a higher-Q alternative to attached-electrode contour-mode resonators. The Q of 8,757, achieved through anchor minimization and very good cleaning, sets a new bar at 300 MHz for AlN resonators, (a 4.2× improvement), and shows that under very good fabrication and design conditions, one can more closely approach the intrinsic Q limit of sputtered AlN, the true value of which can only be determined via experimentation, by using unattached electrodes. The electromechanical coupling k_{eff}^2 of the AlN capacitive-piezo disk resonator was increased to 1.05% through electrode coverage maximization, gap reduction, and film quality improvements, from an initially demonstrated value of 0.1%. No AlN capacitive-piezoelectric resonator at any frequency had ever achieved $k_{eff}^2 > 0.3\%$ before this work. The best achieved single disk R_x in this work is 785 Ω, using partial gap reduction with a bias voltage, with an unloaded Q of 4,570. If the same device were to instead have a Q of 8,757, as the best device achieved, its R_x would be only 410 Ω. Capacitive-piezoelectric transduction additionally al-

lows for thicker electrodes than are possible when attached directly to the AlN, which can be helpful for both eliminating electrode vibration and for minimizing interconnect resistance based Q loading, which is especially beneficial for high Q devices with low R_x's.

High Q Disk Arrays for Area Scaling of Capacitive-Piezoelectric Resonators

In Chapter 4, mechanically-coupled arrays of capacitive piezo-electric disk resonators were shown to enable reduced R_x's and increased power handling. Connecting multiple disks in parallel electrically reduces R_x by a discrete factor equal to the number of disks. A unique benefit of area scaling with disk arrays is that they utilize distributed anchoring of the resonators and their electrodes, thus enabling high Q's even on large structures which would otherwise succumb to large vertical displacements, hence electrode contact, due to strain gradients in thin films. For example, Q's of 6.5k, 4.9k, and 3.7k were achieved on array sizes of 2×2, 3×3 and 5×5, respectively at 300 MHz. It is also possible to achieve very small R_x's using this technique. For example, using reduced gap sizes, an R_x of 225 Ω was achieved on a 4×4 array, albeit with a low Q of 765. Although Q's were poor due to stringers in the run with the strongest demonstrated electromechanical coupling, 20 Ω motional resistances should be attainable using this approach upon refabrication. Another benefit of using array resonators is to reduce manufacturing variations in resonance frequency. For 2×2 disk resonators, standard deviation of manufacturing frequency precision was measured at 160 ppm. Even better precision should be available on larger structures.

Voltage Actuated Capacitive-Piezoelectric Transducers

Capacitive-piezoelectric transduction offers additional appealing capabilities beyond offering high Q and strong electromechanical coupling, both of which are desired for filters and oscillators. Through voltage-controlled electrode actuation of the capacitive-piezoelectric transducer itself, Chapter 5 presented three distinct capabilities. First, a capacitive-piezoelectric resonator may be switched on and off through a resonance quenching mechanism based on electrode collapse. With a thick electrode, a 220 V switching voltage was sufficient to quench resonance while allowing for a reliable return to the on-state. Thinner electrodes led to reduced switching voltages of 60V, but stiction can be more problematic when restoring force is weakened. Secondly, modifying the capacitive gap sizes allows for frequency tuning over a demonstrated 1,500 ppm range, which is potentially increasable up to an 11,000 ppm theoretical limit. Additionally, it was shown that it is possible to frequency tune without affecting electromechanical coupling by using a dedicated tuning transducer, which would be a preferred method for filter passband correction. Third, gap reduction enables improving the electromechanical coupling to a level greater than initially manufactured, which also allows for large off-state gaps, if desired. These three functions consume no operating power and may be implemented without the use of a bias tee by using separate transducers for input and output, thus enabling self-switched and frequency tunable single-pole or multi-pole

filters with reduced feedthrough capacitance. To demonstrate the efficacy and benefits of using multiple transducers, filters were demonstrated with tunable center frequencies as well as quenchable passbands using electrode actuation for the first time.

Fabrication

Device fabrication methods used in this thesis require fewer overall steps than prior capacitive-piezo processes. They also allow for more versatile designs due to fewer restrictions on possible electrode configurations. The capacitive-piezo resonators of this work utilize a simple four-mask fabrication process. The chemical vapor deposited polysilicon electrodes allow for conformality of electrodes over sidewalls as well as the simultaneous formation of anchor stems, which can contact both the AlN and bottom interconnect layers. Pursuant towards better results, improving the fabrication process over multiple iterations ultimately led to substantial gains in Q's, k_{eff}^2's, R_x's, and yields. Although strides were made towards optimized AlN film quality and stress control, it is hoped that further improvements will be possible. Vertical gaps were manufactured to be as small as 120 nm both atop and below the resonator. These gaps should be further reduceable to 80 nm or smaller for stronger coupling. AlN etching achieved mixed results: nearly vertical sidewalls were achieved early on, but latter etches yielded more angled sidewalls due to tool malfunction. Since none of the multiple fabrication processes was completed without at least one non-ideality occurring, refabrication should offer substantial performance improvements over what has so far been demonstrated. The most important targeted process improvements looking forward include improved resolution during thick lithography steps, AlN strain gradient reduction for smaller gaps, and AlN etch improvement.

Capacitive-Piezoelectric Narrowband Filters

Back in Chapter 1, motivation was provided for high-Q filters which allow for better rejection of out of channel interferers and reduced insertion loss, and hence lower power operation and better sensitivity. Capacitive-piezoelectric narrowband filters with voltage actuated electrodes offer a unique and compelling path forward towards an RF narrowband filter bank, offering a favorable combination of capabilities unafforded by any other technology, including: strong coupling, the ability to decouple through electrode lifting, high Q's, frequency tunability, resonance quenching, and CAD-definable resonance frequencies.

Although capacitive-piezoelectric narrowband filters demand a nearly flawless fabrication process to function properly, Chapter 7 presents numerous milestones that were met towards realizing them. First, after some introductory content on the principles of transfer functions and filter design, a fully automated computer-aided design flow is presented which allows a designer to choose desired filter characteristics such as bandwidth, filter order, center frequency, filter type and automatically obtain needed terminating resistances, coupling beam sizes, and the generated layout. Using Monte-Carlo analysis, it was shown that the previously measured frequency error of arrays is small enough to enable the reliable formation of

0.2% bandwidth filters with functional passbands even without corrective frequency tuning. Frequency tuning of individual resonators for passband correction using the demonstrated method of Chapter 5, while not predicted to be mandated except for smaller bandwidths or for frequencies significantly higher than 300 MHz, can accommodate needs for further accuracy improvements.

On the experimental front, capacitive-piezo filter demos confirmed the following: (1) that capacitive-piezo disk array filter bandwidth is set by coupling beam stiffness, exactly as modeled; (2) that high order transfer functions are possible, e.g., with four-poles; (3) that individual resonators can be tuned in a coupled resonator filter using dedicated electrodes for tuning; (4) that high Q filters are possible, e.g., Q's over 5k were measured in a 2×3×3 2nd order filter; (5) that narrowband filters can be made with no spurious modes, e.g., passbands were shown at 433 MHz with a clean spectrum between 0 and 1 GHz; (6) strong stopband rejection can be achieved, e.g., 50 dB at 300 MHz, even without differential operation or aggressive capacitive isolation through ground shielding between input and output; and (7) low insertion losses are attainable, i.e., 2.7 dB, even without the highest Q's previously demonstrated. Looking forward, refabrication will be needed to achieve targeted performance specifications for filters, which will require achieving all the aforementioned milestones simultaneously.

8.2 Unanswered Questions

Some of the fabrication difficulties encountered in this thesis were due to preventable problems related to tool malfunctions. However, even under the best achieved process conditions, recurrent obstacles arose, including: material stresses, lithographic limits, and etching sidewall angles. We seek to know whether further development will: (1) lead to reduced residual stresses (and stress gradients) to reduce unwanted deformations, (2) improve the resolution of finer features, and (3) allow for the etching of AlN with 90° sidewalls. Whether or not these solutions can be found will have an impact upon the realization of ideal structure geometries and performance. Additionally, sacrificial gap releases become more challenging as gap sizes decrease; so whether or not smaller gaps will be attainable will depend on both stress mitigation and cleaning capabilities.

Additional practical questions remain to be answered beyond what has been addressed in this thesis. Although it may be possible to make devices with "ideal" geometries that perform properly under certain conditions, whether or not they can (1) reliably withstand large amounts of transmit power, (2) withstand large temperature shifts, (3) withstand shocks, and (4) have lifetimes of many years, remains to be seen. Fabrication issues that currently impact yields such as stiction, device damage, and contamination must also be eliminated. The devices must be also manufacturable at low cost and sold at high enough margin to be commercially viable.

Regarding arrays specifically, it is unknown how many disks can be practically be made to vibrate synchronously without phase deviations in the mode shape which affect proper

operation. Thin coupling beams are desirable for not loading the mode shape of the disks, but it is unknown how thin the coupling beams can be made. If stresses are present in the structures, it is unknown how coupling beam propagation velocity will be affected, thus new spurious modes could be introduced by this effect. Additionally, it is unknown if coupling a very large disk array to another with a single $\lambda/4$-beam will distort the mode shapes of the resonators too highly–this could be investigated with FEM simulations.

A final open question is to know how much the voltage actuated resonance quenching method of Chapter 5 can benefit from further development. Whether or not this method can be used reliably with voltages far below the 220 V needed to actuate the thick electrode and not succumb to stiction is currently unknown. Although micromechanical relays operate with voltages of ≈10V and have very long lifetimes, quenching resonance may take much greater contact forces than are needed to create a conductive path.

8.3 Future Work

Although questions remain over how much capacitive-piezo disk array technology can be further improved, results obtained thus far indicate that useful systems are already possible using the current devices.

Frequency Synthesizers

UHF oscillators made from capacitive-piezo disk resonator arrays could offer very good phase noise, start up time, and low power performance at low unit fabrication cost due to their high-Q, strong electromechanical coupling, multifrequency capability, minimal capacitive feedthrough (which helps to reduce needed transconductance to sustain oscillation), integrated frequency tunability, and potentially exceptional aging stability. Removing the electrodes from the device may offer better aging performance, as was demonstrated with BVA resonators [66], although further study will be needed. Such devices potentially could be used to power the Internet of Things (IOT) revolution at lower cost than quartz counterparts which offer state-of-the-art stability and accuracy but which require a phase-locked loop (PLL) and cannot be fabricated on chip.

Tunable and Switchable Filters and Filter Banks

The devices in this thesis have been shown to enable filters with tunable and switchable passbands. Refabrication will offer better performance. It would be interesting to explore filter bank architectures which utilize all the capabilities afforded by electrode actuation of capacitive piezo transducers, while harnessing high Q and strong coupling, to ultimately improve the frequency agility and sensitivity of radio front ends.

Bibliography

[1] C. E. Shannon, "Communication in the presence of noise," *Proceedings of the IRE*, vol. 37, no. 1, pp. 10–21, 1949. [Online]. Available: `http://ieeexplore.ieee.org/stamp/stamp.jsp?tp=&arnumber=1697831` (cit. on p. 2).

[2] John R. Vig, "Quartz crystal resonators and oscillators for frequency control and timing applications - a tutorial," 2014, [Online]. Available: `http://www.ieee-uffc.org/frequency-control/learning-vig-tut.asp` (cit. on pp. 3, 13).

[3] B. Razavi, *RF Microelectronics*. Prentice Hall PTR, 1998 (cit. on p. 3).

[4] T. H. Lee, *The Design of CMOS Radio-Frequency Integrated Circuits*, 2nd ed. New York: Cambridge University Press, 2004, ISBN: 9780521835398 (cit. on p. 3).

[5] C. Balanis, *Antenna Theory*, 2nd ed. NY: John Wiley & Sons, Inc., 1997 (cit. on p. 5).

[6] J. C. Rudell, J. A. Weldon, J.-J. Ou, L. Lin, and P. Gray, *An Integrated OSM/DECT Receiver: Design Specifications*. Citeseer, 1997. [Online]. Available: `http://citeseerx.ist.psu.edu/viewdoc/download?doi=10.1.1.39.6142&rep=rep1&type=pdf` (cit. on p. 5).

[7] Federal Communications Commission, *FCC enforcement advisory on cell jammers, GPS jammers, and other jamming devices*, 2012. [Online]. Available: `https://apps.fcc.gov/edocs_public/attachmatch/DA-12-347A1.pdf` (cit. on p. 6).

[8] A. M. Mehta and K. S. Pister, "Frequency offset compensation for crystal-free 802.15. 4 communication," in *Advanced Technologies for Communications (ATC), 2011 International Conference on*, IEEE, 2011, pp. 45–47. [Online]. Available: `http://ieeexplore.ieee.org/xpls/abs_all.jsp?arnumber=6027432` (cit. on p. 7).

[9] SiTime, *SiT8209: High frequency ultra performance oscillator data sheet*, Aug. 2, 2012. [Online]. Available: `http://www.sitime.com/products/oscillators/sit8209` (cit. on p. 7).

[10] Aaron Partridge, "Commercial MEMS oscillators: Specifications, applications, and system perspectives (tutorial)," IEEE International Frequency Control Symposium, Denver, Apr. 11, 2015 (cit. on p. 7).

[11] T. L. Naing, T. O. Rocheleau, E. Alon, and C. T.-C. Nguyen, "A 78-microwatt GSM phase noise-compliant pierce oscillator referenced to a 61-MHz wine-glass disk resonator," in *European Frequency and Time Forum & International Frequency Control Symposium (EFTF/IFC), 2013 Joint*, IEEE, 2013, pp. 562–565. [Online]. Available: http://ieeexplore.ieee.org/xpls/abs_all.jsp?arnumber=6702305 (cit. on p. 7).

[12] C. T. Nguyen and R. T. Howe, "CMOS micromechanical resonator oscillator," in *Electron Devices Meeting, 1993. IEDM'93. Technical Digest., International*, 1993, pp. 199–202, ISBN: 0780314506. [Online]. Available: http://ieeexplore.ieee.org/stamp/stamp.jsp?tp=&arnumber=347242 (cit. on p. 7).

[13] D. B. Leeson, "A simple model of feedback oscillator noise spectrum," *Proceedings of the IEEE*, vol. 54, no. 2, pp. 329–330, 1966. [Online]. Available: http://ieeexplore.ieee.org/xpls/abs_all.jsp?arnumber=1446612 (cit. on p. 7).

[14] A. Hajimiri and T. H. Lee, "A general theory of phase noise in electrical oscillators," *Solid-State Circuits, IEEE Journal of*, vol. 33, no. 2, pp. 179–194, 1998. [Online]. Available: http://ieeexplore.ieee.org/xpls/abs_all.jsp?arnumber=658619 (cit. on p. 7).

[15] A. I. Zverev, *Handbook of Filter Synthesis*. New York: John Wiley & Sons, Inc., 1967 (cit. on pp. 11, 159).

[16] R. M. White and F. W. Voltmer, "Direct piezoelectric coupling to surface elastic waves," *Applied Physics Letters*, vol. 7, no. 12, p. 314, 1965, ISSN: 00036951. DOI: 10.1063/1.1754276. [Online]. Available: http://scitation.aip.org/content/aip/journal/apl/7/12/10.1063/1.1754276 (cit. on p. 13).

[17] M. Lewis, "SAW filters employing interdigitated interdigital transducers, IIDT," in *1982 Ultrasonics Symposium*, 1982. [Online]. Available: http://ieeexplore.ieee.org/xpl/articleDetails.jsp?arnumber=1534719 (cit. on p. 13).

[18] C. C. Ruppel, R. Dill, A. Fischerauer, G. Fischerauer, A. Gawlik, J. Machui, F. Muller, L. Reindl, W. Ruile, G. Scholl, *et al.*, "SAW devices for consumer communication applications," *Ultrasonics, Ferroelectrics, and Frequency Control, IEEE Transactions on*, vol. 40, no. 5, pp. 438–452, 1993. [Online]. Available: http://ieeexplore.ieee.org/xpls/abs_all.jsp?arnumber=238094 (cit. on p. 13).

[19] N. Saldanha and D. Malocha, "Low loss SAW RF ID tags for space applications," in *IEEE Ultrasonics Symposium*, IEEE, 2008, pp. 292–295. [Online]. Available: http://ieeexplore.ieee.org/lpdocs/epic03/wrapper.htm?arnumber=4803559 (cit. on p. 13).

[20] W. G. Cady, "The piezo-electric resonator," *Proceedings of the Institute of Radio Engineers*, vol. 10, no. 2, pp. 83–114, 1922. [Online]. Available: http://ieeexplore.ieee.org/xpls/abs_all.jsp?arnumber=1666707 (cit. on p. 13).

[21] K. Shibayama, K. Yamanouchi, H. Sato, and T. Meguro, "Optimum cut for rotated Y-cut LiNbO3 crystal used as the substrate of acoustic-surface-wave filters," *Proceedings of the IEEE*, vol. 64, no. 5, pp. 595–597, 1976. [Online]. Available: `http://ieeexplore.ieee.org/xpls/abs_all.jsp?arnumber=1454450` (cit. on p. 13).

[22] Token Electronics Industry Co., Ltd. (2010). Token SAW filters and SAW resonators, [Online]. Available: `http://www.token.com.tw/pdf/saw.pdf` (cit. on p. 13).

[23] M. Tanaka, T. Morita, K. Ono, and Y. Nakazawa, "Narrow bandpass filter using double-mode SAW resonators on quartz," in *1984 Frequency Control Symposium*, 1984, pp. 286–293. [Online]. Available: `http://ieeexplore.ieee.org/stamp/stamp.jsp?tp=&arnumber=1537710` (cit. on p. 14).

[24] F. P. Stratton, D. T. Chang, D. J. Kirby, R. J. Joyce, T.-Y. Hsu, R. L. Kubena, and Y.-K. Yong, "A MEMS-based quartz resonator technology for GHz applications," in *Frequency Control Symposium and Exposition, 2004. Proceedings of the 2004 IEEE International*, IEEE, 2004, pp. 27–34. [Online]. Available: `http://ieeexplore.ieee.org/xpls/abs_all.jsp?arnumber=1418425` (cit. on p. 14).

[25] K. M. Lakin, K. T. McCarron, and R. E. Rose, "Solidly mounted resonators and filters," in *Ultrasonics Symposium, 1995. Proceedings., 1995 IEEE*, vol. 2, 1995, pp. 905–908. [Online]. Available: `http://ieeexplore.ieee.org/xpls/abs_all.jsp?arnumber=495711` (cit. on pp. 15, 100).

[26] R. C. Ruby, P. Bradley, Y. Oshmyansky, A. Chien, and J. D. Larson III, "Thin film bulk wave acoustic resonators (FBAR) for wireless applications," in *Ultrasonics Symposium, 2001 IEEE*, vol. 1, IEEE, 2001, pp. 813–821. [Online]. Available: `http://ieeexplore.ieee.org/xpls/abs_all.jsp?arnumber=991846` (cit. on pp. 15, 83).

[27] R. Ruby, "Review and comparison of bulk acoustic wave FBAR, SMR technology," in *2007 IEEE Ultrasonics Symposium Proceedings*, 2007. [Online]. Available: `http://ieeexplore.ieee.org/stamp/stamp.jsp?tp=&arnumber=4409835` (cit. on p. 15).

[28] Avago Technologies. (). Data sheet for AV02-0473 FBAR duplexer, [Online]. Available: `http://www.avagotech.com/docs/AV02-0473EN` (cit. on p. 16).

[29] R. Ruby, P. D. Bradley, J. D. Larson III, and Y. Oshmyansky, "PCS 1900 MHz duplexer using thin film bulk acoustic resonators (FBARs)," *Electronics Letters*, vol. 35, no. 10, pp. 794–795, 1999. [Online]. Available: `http://ieeexplore.ieee.org/stamp/stamp.jsp?tp=&arnumber=771422` (cit. on p. 15).

[30] M.-A. Dubois, J.-F. Carpentier, P. Vincent, C. Billard, G. Parat, C. Muller, P. Ancey, and P. Conti, "Monolithic above-IC resonator technology for integrated architectures in mobile and wireless communication," *IEEE Journal of Solid-State Circuits*, vol. 41, no. 1, pp. 7–16, Jan. 2006. [Online]. Available: `http://ieeexplore.ieee.org/lpdocs/epic03/wrapper.htm?arnumber=1564340` (cit. on p. 16).

[31] A. Nelson, J. Hu, J. Kaitila, R. Ruby, and B. Otis, "A 22uw, 2.0 GHz FBAR oscillator," in *Radio Frequency Integrated Circuits Symposium (RFIC), 2011 IEEE*, 2011, pp. 1–4. [Online]. Available: http://ieeexplore.ieee.org/stamp/stamp.jsp?tp=&arnumber=5940708 (cit. on p. 16).

[32] J. Hu, R. Parker, R. Ruby, and B. Otis, "A wide-tuning digitally controlled FBAR-based oscillator for frequency synthesis," in *Frequency Control Symposium (FCS), 2010 IEEE International*, IEEE, 2010, pp. 608–612. [Online]. Available: http://ieeexplore.ieee.org/xpls/abs_all.jsp?arnumber=5556258 (visited on 11/14/2014) (cit. on pp. 16, 105).

[33] G. Piazza, P. J. Stephanou, and A. P. Pisano, "Piezoelectric aluminum nitride vibrating contour-mode MEMS resonators," *Journal of Microelectromechanical Systems*, vol. 15, no. 6, pp. 1406–1418, Dec. 2006, ISSN: 1057-7157. [Online]. Available: http://ieeexplore.ieee.org/lpdocs/epic03/wrapper.htm?arnumber=4020287 (cit. on pp. 16, 75).

[34] B. Kim, R. H. Olsson, and K. E. Wojciechowski, "AlN microresonator-based filters with multiple bandwidths at low intermediate frequencies," *Journal of Microelectromechanical Systems*, vol. 22, no. 4, pp. 949–961, Aug. 2013, ISSN: 1057-7157, 1941-0158. [Online]. Available: http://ieeexplore.ieee.org/lpdocs/epic03/wrapper.htm?arnumber=6506957 (cit. on pp. 17, 18).

[35] M. Rinaldi, C. Zuniga, C. Zuo, and G. Piazza, "Super-high-frequency two-port AlN contour-mode resonators for RF applications," *IEEE Transactions on Ultrasonics, Ferroelectrics and Frequency Control*, vol. 57, no. 1, pp. 38–45, Jan. 2010. [Online]. Available: http://ieeexplore.ieee.org/lpdocs/epic03/wrapper.htm?arnumber=5361520 (cit. on p. 17).

[36] C. Zuo and G. Piazza, "Single-ended-to-differential and differential-to-differential channel-select filters based on piezoelectric AlN contour-mode MEMS resonators," in *Proceedings of the 2010 IEEE International Frequency Control Symposium*, 2010. [Online]. Available: http://ieeexplore.ieee.org/stamp/stamp.jsp?tp=&arnumber=5556383 (cit. on pp. 17, 95).

[37] C. Zuo, N. Sinha, and G. Piazza, "Very high frequency channel-select MEMS filters based on self-coupled piezoelectric AlN contour-mode resonators," *Sensors and Actuators A: Physical*, vol. 160, no. 1, pp. 132–140, 2010. [Online]. Available: http://www.sciencedirect.com/science/article/pii/S0924424710001731# (cit. on p. 17).

[38] A.-C. Wong and C.-C. Nguyen, "Micromechanical mixer-filters ("mixlers")," *Journal of Microelectromechanical Systems*, vol. 13, no. 1, pp. 100–112, Feb. 2004. [Online]. Available: http://ieeexplore.ieee.org/lpdocs/epic03/wrapper.htm?arnumber=1269736 (cit. on p. 18).

[39] T. L. Naing, T. Beyazoglu, L. Wu, M. Akgul, Z. Ren, T. O. Rocheleau, and C. T. C. Nguyen, "2.97-GHz CVD diamond ring resonator with Q¿ 40,000," in *Frequency Control Symposium (FCS), 2012 IEEE International Conference on*, 2012, pp. 1–6. [Online]. Available: `http://ieeexplore.ieee.org/xpls/abs_all.jsp?arnumber=6243723` (visited on 10/04/2012) (cit. on pp. 18, 19).

[40] M. Akgul, R. Schneider, Z. Ren, G. Chandler, V. Yeh, and C. T.-C. Nguyen, "Hot filament CVD conductive microcrystalline diamond for high Q, high acoustic velocity micromechanical resonators," in *Proceedings of the 2011 International Frequency Control Symposium*, San Francisco, CA, 2011. [Online]. Available: `http://ieeexplore.ieee.org/stamp/stamp.jsp?tp=&arnumber=5977877` (cit. on p. 18).

[41] H. Najar, M.-L. Chan, J. Xie, L. Lin, and D. A. Horsley, "Impact of doping and microstructure on quality factor of CVD diamond micromechanical resonators," in *Frequency Control Symposium (FCS), 2012 IEEE International*, IEEE, 2012, pp. 1–5. [Online]. Available: `http://ieeexplore.ieee.org/xpls/abs_all.jsp?arnumber=6243675` (cit. on p. 18).

[42] M. A. Abdelmoneum, M. U. Demirci, and C. T. Nguyen, "Stemless wine-glass-mode disk micromechanical resonators," in *Micro Electro Mechanical Systems, 2003. MEMS-03 Kyoto. IEEE The Sixteenth Annual International Conference on*, pp. 698–701, ISBN: 0780377443. [Online]. Available: `http://ieeexplore.ieee.org/stamp/stamp.jsp?tp=&arnumber=1189845` (cit. on p. 18).

[43] S.-S. Li, Y.-W. Lin, Y. Xie, Z. Ren, and C.-C. Nguyen, "Micromechanical "hollow-disk" ring resonators," in *Micro Electro Mechanical Systems, 2004. 17th IEEE International Conference on.(MEMS)*, IEEE, 2004, pp. 821–824. [Online]. Available: `http://ieeexplore.ieee.org/xpls/abs_all.jsp?arnumber=1290711` (cit. on pp. 18, 169).

[44] W. C. Li, Y. Lin, B. Kim, Z. Ren, and C. T. C. Nguyen, "Quality factor enhancement in micromechanical resonators at cryogenic temperatures," in *Solid-State Sensors, Actuators and Microsystems Conference, 2009. TRANSDUCERS 2009. International*, 2009, pp. 1445–1448. [Online]. Available: `http://ieeexplore.ieee.org/xpls/abs_all.jsp?arnumber=5285815` (cit. on p. 18).

[45] T. O. Rocheleau, A. J. Grine, K. E. Grutter, R. A. Schneider, N. Quack, M. C. Wu, and C. T.-C. Nguyen, "Enhancement of mechanical Q for low phase noise optomechanical oscillators," in *Micro Electro Mechanical Systems (MEMS), 2013 IEEE 26th International Conference on*, 2013, pp. 118–121. [Online]. Available: `http://ieeexplore.ieee.org/xpls/abs_all.jsp?arnumber=6474191` (cit. on p. 18).

[46] J. R. Clark, W. T. Hsu, and C. T. C. Nguyen, "Measurement techniques for capacitively-transduced VHF-to-UHF micromechanical resonators," in *Digest of Technical Papers of the 11th International Conference on Solid-State Sensors and Actuators, Transducers*, 2001, pp. 1118–1121. [Online]. Available: `http://www.eecs.berkeley.edu/`

~ctnguyen/Research/ConferencePubs/2001/diskmeas.trans01.ctnguyen.pdf (cit. on p. 19).

[47] M. Akgul and C. T.-C. Nguyen, "A passband-corrected high rejection channel-select micromechanical disk filter," in *Frequency Control Symposium (FCS), 2014 IEEE International*, IEEE, 2014, pp. 1–6. [Online]. Available: http://ieeexplore.ieee.org/xpls/abs_all.jsp?arnumber=6860009 (cit. on pp. 19, 21, 45, 91).

[48] S. S. Li, Y. W. Lin, Z. Ren, and C. T. Nguyen, "An MSI micromechanical differential disk-array filter," in *Solid-State Sensors, Actuators and Microsystems Conference, 2007. TRANSDUCERS 2007. International*, pp. 307–311. [Online]. Available: http://ieeexplore.ieee.org/stamp/stamp.jsp?tp=&arnumber=4300130 (cit. on pp. 19, 20, 45, 84, 91, 120, 158).

[49] M. U. Demirci and C. T.-C. Nguyen, "Mechanically corner-coupled square microresonator array for reduced series motional resistance," *Journal of Microelectromechanical Systems*, vol. 15, no. 6, pp. 1419–1436, Dec. 2006. [Online]. Available: http://ieeexplore.ieee.org/lpdocs/epic03/wrapper.htm?arnumber=4020264 (cit. on p. 19).

[50] M. Akgul, B. Kim, Z. Ren, and C. T.-C. Nguyen, "Capacitively transduced micromechanical resonators with simultaneous low motional resistance and q¿70,000," Hilton Head Island, SC, 2010, pp. 467–470. [Online]. Available: http://www.eecs.berkeley.edu/~ctnguyen/Research/ConferencePubs/2010/HighQSolidGap.hh10.makgul.ctnguyen.web.pdf (cit. on p. 19).

[51] T. J. Cheng and S. A. Bhave, "High-q, low impedance polysilicon resonators with 10 nm air gaps," in *Micro Electro Mechanical Systems (MEMS), 2010 IEEE 23rd International Conference on*, 2010, pp. 695–698. [Online]. Available: http://ieeexplore.ieee.org/xpls/abs_all.jsp?arnumber=5442311 (cit. on p. 19).

[52] M. Ziaei-Moayyed, E. P. Quevy, J. Hsieh, and R. T. Howe, "Efficient internal electrostatic transduction of the 41st radial mode of a ring resonator," in *Micro Electro Mechanical Systems (MEMS), 2010 IEEE 23rd International Conference on*, IEEE, 2010, pp. 711–714. [Online]. Available: http://ieeexplore.ieee.org/xpls/abs_all.jsp?arnumber=5442307 (cit. on p. 19).

[53] H. G. Barrow, T. L. Naing, R. Schneider, T. O. Rocheleau, V. Yeh, Z. Ren, and C. T.-C. Nguyen, "A real-time 32.768-kHz clock oscillator using a 0.0154-mm^2 micromechanical resonator frequency-setting element," in *Proceedings of the 2012 IEEE International Frequency Control Symposium*, Baltimore, MD, 2012. [Online]. Available: http://ieeexplore.ieee.org/stamp/stamp.jsp?tp=&arnumber=6243740 (cit. on pp. 20, 44).

[54] S. S. Li, Y. W. Lin, Z. Ren, and C. T.-C. Nguyen, "Self-switching vibrating micromechanical filter bank," in *Frequency Control Symposium and Exposition, 2005. Proceedings of the 2005 IEEE International*, pp. 135–141. [Online]. Available: `http://ieeexplore.ieee.org/stamp/stamp.jsp?tp=&arnumber=1573915` (cit. on pp. 20, 98).

[55] F. D. Bannon, J. R. Clark, and C. T.-C. Nguyen, "High-Q HF microelectromechanical filters," *Solid-State Circuits, IEEE Journal of*, vol. 35, no. 4, pp. 512–526, 2000. [Online]. Available: `http://ieeexplore.ieee.org/xpls/abs_all.jsp?arnumber=839911` (cit. on pp. 21, 158).

[56] K. Wang and C. T. Nguyen, "High-order medium frequency micromechanical electronic filters," *Microelectromechanical Systems, Journal of*, vol. 8, no. 4, pp. 534–556, 1999, ISSN: 1057-7157. [Online]. Available: `http://ieeexplore.ieee.org/stamp/stamp.jsp?tp=&arnumber=809070` (cit. on pp. 21, 158).

[57] C. Nguyen, "Micromechanical signal processors," PhD thesis, UC Berkeley, 1994 (cit. on p. 23).

[58] J. Wang, J. E. Butler, T. Feygelson, and C. T. Nguyen, "1.51-GHz nanocrystalline diamond micromechanical disk resonator with material-mismatched isolating support," in *Micro Electro Mechanical Systems, 2004. 17th IEEE International Conference on.(MEMS)*, 2004, pp. 641–644, ISBN: 078038265X (cit. on p. 23).

[59] S. Senturia, *Microsystem Design*. New York: Kluwer Academic Publishers, 2002 (cit. on pp. 24, 34).

[60] F. Ma, *Me273 course notes in oscillations in linear systems*, Nov. 2011 (cit. on p. 29).

[61] C. T.-C. Nguyen, "Frequency-selective MEMS for miniaturized communication devices," *IEEE Trans. Microwave Theory Tech*, vol. 47, pp. 1486–1503, 1999 (cit. on p. 33).

[62] S. H. Chang, N. N. Rogacheva, and C. C. Chou, "Analysis of methods for determining electromechanical coupling coefficients of piezoelectric elements," *IEEE Transactions on Ultrasonics, Ferroelectrics and Frequency Control*, vol. 42, no. 4, pp. 630–640, Jul. 1995. [Online]. Available: `http://ieeexplore.ieee.org/stamp/stamp.jsp?tp=&arnumber=393106` (cit. on p. 42).

[63] R. Johnson, *Mechanical Filters*. New York: John Wiley & Sons, Inc., 1983 (cit. on pp. 46, 95).

[64] D. Pozar, *Microwave Engineering*, 3rd ed. USA: John Wiley & Sons, Inc., 2005 (cit. on p. 46).

[65] L. W. Hung and C.-T. Nguyen, "Q-boosted AlN array-composite resonator with Q¿ 10,000," in *Electron Devices Meeting (IEDM), 2010 IEEE International*, San Francisco, CA: IEEE, 2010, pp. 7.3.1–7.3.4. [Online]. Available: `http://ieeexplore.ieee.org/xpls/abs_all.jsp?arnumber=5703315&tag=1` (cit. on p. 55).

[66] Besson, R.J., "A new "electrodeless" resonator design," in *31st Annual Symposium on Frequency Control*, 1977, pp. 147 –152. [Online]. Available: http://ieeexplore.ieee.org/stamp/stamp.jsp?tp=&arnumber=4558470 (cit. on pp. 56, 178).

[67] L.-W. Hung and C. T.-C. Nguyen, "Capacitive-piezo transducers for higher Q contour-mode AlN resonators at 1.2 GHz," in *Proceedings of the 2010 Solid State Sensor, Actuator, and Microsystems Workshop*, Hilton Head Island, SC, 2010 (cit. on p. 56).

[68] L.-W. Hung and C. T.-C. Nguyen, "Capacitive-piezoelectric transducers for high-Q micromechanical AlN resonators," *Journal of Microelectromechanical Systems*, vol. 24, no. 2, pp. 458–473, Apr. 2015, ISSN: 1057-7157, 1941-0158. DOI: 10.1109/JMEMS.2014.2332991. [Online]. Available: http://ieeexplore.ieee.org/lpdocs/epic03/wrapper.htm?arnumber=6857352 (cit. on p. 56).

[69] L.-W. Hung and C.-C. Nguyen, "Capacitive-piezoelectric AlN resonators with Q¿ 12,000," in *Micro Electro Mechanical Systems (MEMS), 2011 IEEE 24th International Conference on*, IEEE, 2011, pp. 173–176. [Online]. Available: http://ieeexplore.ieee.org/xpls/abs_all.jsp?arnumber=5734389 (visited on 05/10/2015) (cit. on p. 56).

[70] T.-T. Yen, A. P. Pisano, and C.-C. Nguyen, "High-q capacitive-piezoelectric AlN lamb wave resonators," in *Micro Electro Mechanical Systems (MEMS), 2013 IEEE 26th International Conference on*, IEEE, 2013, pp. 114–117. [Online]. Available: http://ieeexplore.ieee.org/xpls/abs_all.jsp?arnumber=6474190 (visited on 05/10/2015) (cit. on pp. 56, 85).

[71] R. A. Schneider and C. T.-C. Nguyen, "On/off switchable high-q capacitive-piezoelectric AlN resonators," in *Micro Electro Mechanical Systems (MEMS), 2014 IEEE 27th International Conference on*, IEEE, 2014, pp. 1265–1268. [Online]. Available: http://ieeexplore.ieee.org/xpls/abs_all.jsp?arnumber=6765879 (visited on 04/21/2014) (cit. on pp. 57, 74, 86, 96, 113).

[72] M. Onoe, "Contour vibrations of isotropic circular plates," *The Journal of the Acoustical Society of America*, vol. 28, no. 6, pp. 1158–1162, Nov. 1956 (cit. on pp. 58, 65).

[73] G. Vigevani, "MEMS aluminum nitride technology for inertial sensors," PhD thesis, UC Berkeley, 2011, 195 pp. (cit. on p. 61).

[74] R. A. Schneider, T. L. Naing, T. O. Rocheleau, and C. T.-C. Nguyen, "Gap reduction based frequency tuning for aln capacitive-piezoelectric resoantors," in *European Frequency and Time Forum & International Frequency Control Symposium (EFTF/IFC), 2015 Joint*, IEEE, 2015, pp. 100–104. [Online]. Available: http://ieeexplore.ieee.org/stamp/stamp.jsp?arnumber=7138938 (cit. on pp. 64, 96, 106).

[75] A. E. H. Love, *A Treatise on the Mathematical Theory of Elasticity*, 3rd. London: Cambridge University Press, 1920, 651 pp. (cit. on p. 65).

[76] R. Tabrizian, M. Rais-Zadeh, and F. Ayazi, "Effect of phonon interactions on limiting the fQ product of micromechanical resonators," in *International Solid-State Sensors, Actuators and Microsystems Conference, TRANSDUCERS 2009.*, 2009, pp. 2131–2134. [Online]. Available: `http://ieeexplore.ieee.org/xpls/abs_all.jsp?arnumber=5285627` (visited on 10/04/2012) (cit. on p. 74).

[77] L. Wu, M. Akgul, Z. Ren, Y. Lin, W.-C. Li, and C. T.-C. Nguyen, "Hollow stems for higher micromechanical disk resonator quality factor," in *Ultrasonics Symposium (IUS), 2011 IEEE International*, IEEE, 2011, pp. 1964–1967. [Online]. Available: `http://ieeexplore.ieee.org/xpls/abs_all.jsp?arnumber=6293678` (cit. on p. 75).

[78] C. Zuo, N. Sinha, and G. Piazza, "Novel electrode configurations in dual-layer stacked and switchable ALN contour-mode resonators for low impedance filter termination and reduced insertion loss," in *Micro Electro Mechanical Systems (MEMS), 2010 IEEE 23rd International Conference on*, IEEE, 2010, pp. 719–722. [Online]. Available: `http://ieeexplore.ieee.org/xpls/abs_all.jsp?arnumber=5442305` (visited on 06/18/2014) (cit. on p. 75).

[79] R. H. Olsson, C. M. Washburn, J. E. Stevens, M. R. Tuck, and C. D. Nordquist, "VHF and UHF mechanically coupled aluminum nitride MEMS filters," in *Frequency Control Symposium, 2008 IEEE International*, IEEE, 2008, pp. 634–639. [Online]. Available: `http://ieeexplore.ieee.org/xpls/abs_all.jsp?arnumber=4623077` (visited on 03/28/2014) (cit. on pp. 75, 95, 120).

[80] M. Rinaldi, A. Tazzoli, J. Segovia-Fernandez, V. Felmetsger, and G. Piazza, "High power and low temperature coefficient of frequency oscillator based on a fully anchored and oxide compensated AlN contour-mode MEMS resonator," in *Micro Electro Mechanical Systems (MEMS), 2012 IEEE 25th International Conference on*, IEEE, 2012, pp. 696–699. [Online]. Available: `http://ieeexplore.ieee.org/xpls/abs_all.jsp?arnumber=6170282` (visited on 04/22/2014) (cit. on p. 82).

[81] Y. Lin, W.-C. Li, B. Kim, Y.-W. Lin, Z. Ren, and C.-C. Nguyen, "Enhancement of micromechanical resonator manufacturing precision via mechanically-coupled arraying," in *Frequency Control Symposium, 2009 Joint with the 22nd European Frequency and Time forum. IEEE International*, 2009, pp. 58–63. [Online]. Available: `http://ieeexplore.ieee.org/stamp/stamp.jsp?tp=&arnumber=5168142` (visited on 09/09/2013) (cit. on p. 93).

[82] E. A. Vittoz, M. G. Degrauwe, and S. Bitz, "High-performance crystal oscillator circuits: Theory and application," *Solid-State Circuits, IEEE Journal of*, vol. 23, no. 3, pp. 774–783, 1988. [Online]. Available: `http://ieeexplore.ieee.org/xpls/abs_all.jsp?arnumber=318` (cit. on p. 95).

[83] G. Hummel, Y. Hui, and M. Rinaldi, "Phase change material programmable vias for switching and reconfiguration of aluminum nitride piezoelectric MEMS resonators," in *Frequency Control Symposium (FCS), 2014 IEEE International*, IEEE, 2014, pp. 1–3.

[Online]. Available: http://ieeexplore.ieee.org/xpls/abs_all.jsp?arnumber=6859996 (cit. on p. 98).

[84] Petersen, K. E., "Silicon as a mechanical material," *Proceedings of the IEEE*, vol. 70, no. 5, pp. 420–457, May 1982. [Online]. Available: http://ieeexplore.ieee.org/stamp/stamp.jsp?tp=&arnumber=1456599 (cit. on p. 104).

[85] T.-J. K. Liu, L. Hutin, I.-R. Chen, R. Nathanael, Y. Chen, M. Spencer, and E. Alon, "Recent progress and challenges for relay logic switch technology," in *VLSI Technology (VLSIT), 2012 Symposium on*, 2012, pp. 43–44. [Online]. Available: http://ieeexplore.ieee.org/xpls/abs_all.jsp?arnumber=6242452 (cit. on p. 104).

[86] Y. Chen, R. Nathanael, J. Jeon, J. Yaung, L. Hutin, and T.-J. K. Liu, "Characterization of contact resistance stability in MEM relays with tungsten electrodes," *Journal of Microelectromechanical Systems*, vol. 21, no. 3, pp. 511–513, Jun. 2012, ISSN: 1057-7157, 1941-0158. DOI: 10.1109/JMEMS.2012.2186282. [Online]. Available: http://ieeexplore.ieee.org/lpdocs/epic03/wrapper.htm?arnumber=6156410 (cit. on p. 104).

[87] B. Kim, R. H. Olsson, and K. E. Wojciechowski, "Ovenized and thermally tunable aluminum nitride microresonators," in *Ultrasonics Symposium (IUS), 2010 IEEE*, IEEE, 2010, pp. 974–978. [Online]. Available: http://ieeexplore.ieee.org/xpls/abs_all.jsp?arnumber=5935635 (cit. on p. 105).

[88] B. Kim, R. H. Olsson, and K. E. Wojciechowski, "Capacitive frequency tuning of AlN micromechanical resonators," in *Solid-State Sensors, Actuators and Microsystems Conference (TRANSDUCERS), 2011 16th International*, IEEE, 2011, pp. 502–505. [Online]. Available: http://ieeexplore.ieee.org/xpls/abs_all.jsp?arnumber=5969665 (cit. on p. 106).

[89] R. A. Schneider and C. T.-C. Nguyen, "Capacitive-piezoelectric aln radial contour mode disk resonator arrays," In Press *JMEMS or TUFFC*, vol. X, no. X, pp. 1–15, 2016 (cit. on pp. 118, 120, 124).

[90] C. D. Nordquist, R. H. Olsson, S. M. Scott, D. W. Branch, T. Pluym, and V. Yarberry, "On/off micro-electromechanical switching of AlN piezoelectric resonators," in *Proc. Microwave Symposium Digest*, Seattle, WA, 2013, pp. 1–4. [Online]. Available: http://ieeexplore.ieee.org/xpl/articleDetails.jsp?arnumber=6931876 (cit. on p. 119).

[91] F. Goericke, "Aluminum nitride sensors for harsh environments," PhD thesis, UC Berkeley, 2013 (cit. on pp. 135, 136).

[92] V. V. Felmetsger, P. N. Laptev, and R. J. Graham, "Deposition of ultrathin AlN films for high frequency electroacoustic devices," *Journal of Vacuum Science & Technology A: Vacuum, Surfaces, and Films*, vol. 29, no. 2, pp. 021014 1–7, 2011, ISSN: 07342101. DOI: 10.1116/1.3554718. [Online]. Available: http://scitation.aip.org/content/

avs/journal/jvsta/29/2/10.1116/1.3554718 (visited on 10/26/2015) (cit. on p. 138).

[93] W.-K. Chen, *Passive, Active, and Digital Filters*, 3rd ed. 2009, 840 pp., ISBN: 1420058851 (cit. on p. 156).

[94] H. G. Barrow and C. T.-C. Nguyen, "A protocol for automated passband correction of high-order microelectromechanical filters," in *Frequency Control Symposium (FCS), 2014 IEEE International*, IEEE, 2014, pp. 1–5. [Online]. Available: http://ieeexplore.ieee.org/xpls/abs_all.jsp?arnumber=6860010 (visited on 09/15/2015) (cit. on p. 173).

Appendix A

Capacitive-Piezo Fabrication Process Traveler

1. Starting Wafer: 150 mm (6") n-type Si
    - Pre-furnace wafer cleaning - Msink6
        - 10 minute piranha clean
        - Quick dump rinse, 4 cycles
        - Spin, rinse, dry
2. Thermal Oxidation
    - Recipe 4WETOXA - Tystar 4
        - Target thickness: 2000 nm
        - Temperature: 1050° C; Recipe uses O_2 and steam (H_2O) for fast oxidation.
        - Time: 11 hours 2 minutes;
3. Silicon Nitride Deposition
    - Recipe LSNSTDA.017 - Tystar17
        - Target thickness: 500 nm
        - Deposition time: 100 minutes (≈5 nm/min)
        - 100 sccm SiH_2Cl_2; 25 sccm of NH_3; 140 mTorr; 835° C.
4. Polysilicon Interconnect Deposition
    - Recipe 16SUPLYA - Tystar16
        - Target thickness: 3000 nm
        - Deposition Rate: ≈10 nm/min
        - Time: 5 hours 0 minutes

  - 615° C; Uses SiH_4 as silicon source

5. Polysilicon Doping
   - Recipe 13POCL3A - Tystar13
     - 1000° C; 1 hour $POCl_3$ doping, 1 hour drive-in anneal
     - $POCl_3$ vapor delivered with an N_2 carrier gas; O_2 is used in the doping step to convert $POCl_3$ vapor into P_2O_5.
6. Interconnect Film Thickness and Conductivity Verification
   - Thickness Measurement - NANODUV
     - Verify $t \approx 3000$ nm
   - Sheet Resistance Measurement - 4PTPRB
     - Verify $R_\square < 10\Omega/\square$
7. Alignment Mark and Interconnect Layer Lithography
   - Spin - SVGCoat6
     - Program #s: 1,2,1 (60s HMDS Prime, 1.8k rpm, 60s soft-bake @ 130°C)
     - 900 nm thickness
   - Expose - ASML
     - Reticle: PM Mark. Exposure Energy: 18 mJ/cm^2
   - Develop - SVGDev6
     - 60s Post-Exposure Bake @ 130°C, 60s Develop Time
   - Expose - ASML
     - Mask Layer 1: POLY1 (Clear Field). Exposure Energy: 18 mJ/cm^2
   - Develop - SVGDev6
     - 60s Post-Exposure Bake @ 130°C, 60s Develop Time
   - Hard Bake Resist - UVBake
     - Recipe U
8. Polysilicon Interconnect Etch
   - Recipe Smooth Sidewall 1 - STS2
     - Target Etch Distance: 3500 nm

  - Etch Rate = 350 nm/cycle. 1 cycle includes 5s passivation and 7s etch.
  - Total Cycles: 10; ≈130 s
  - Passivation: C_4F_8 flow: 100 sccm; 600 W Coil Power
  - Etch: SF_6/O_2 flow: 130/13 sccm; 600 W Coil Power; 20 W Bias Power
- Verify Etch Completion - Multimeter
  - Verify infinite resistance between two probes placed in the field.
- Strip Photoresist - Matrix
  - 2.5 mins, 400 W O_2 Plasma, 250^o C chuck temp

9. Pre-furnace wafer cleaning

- Pre-furnace wafer cleaning - Msink8
  - 10 minute piranha clean
  - Quick dump rinse, 4 cycles
  - Spin, rinse, dry
- Pre-furnace wafer cleaning - Msink6
  - 10 minute piranha clean
  - Quick dump rinse, 4 cycles
  - Spin, rinse, dry

10. High Temperature Oxide Deposition (Field Fill Around Interconnect)

- Recipe HTOSTDA.017 - Tystar 17
  - Target thickness: 3500 nm
  - Temperature: 800^o C
  - Deposition Rate: 266 nm/hour
  - Time: 13 hours 10 minutes

11. Chemical Mechanical Polishing (Lapping)

- Standard 6" Oxide Polish Recipe - CMP
  - Downforce: 4 p.s.i.
  - Removal Rate: ≈150 nm/min
  - Multimeter can verify exposure of interconnect upon completion. Stark color change will be evident as well.
  - Polish backside of wafer for 180 s for every 180 s of frontside polishing.
- Post CMP Rinsing - SinkCMP
  - Rinse thoroughly upon completion of polishing.

  - Use a wet Mr. Clean Magic Eraser to remove CMP slurry particles while rinsing with the deck hose for 60 s. Do not let dry before starting QDR cycle.
  - Quick dump rinse, then dry.

12. Pre-furnace wafer cleaning

- Pre-furnace wafer cleaning - Msink8
  - 10 minute piranha clean
  - Quick dump rinse, 4 cycles
  - Spin, rinse, dry
- Pre-furnace wafer cleaning - Msink6
  - 10 minute piranha clean
  - Quick dump rinse, 4 cycles
  - Spin, rinse, dry

13. High Temperature Oxide Deposition (Bottom Sacrificial Gap)

- Recipe 17SULTOA - Tystar 17
  - Target thickness: 120 nm
  - Temperature: 800° C
  - Deposition Rate: 266 nm/hour
  - Time: 28 minutes 12 seconds

14. AlN Deposition

- Wafer Bow Measurement - Flexus
  - Record Pre-dep wafer bow
- Deposit Aluminum Nitride - AlN2
  - Prior to attempting to deposit AlN on the process wafer, run multiple trial wafers. Verify that crystallinity is acceptable and make adjustments to gas flows in the deposition recipe to reduce stress.
  - For optimal crystallinity, prior to deposition, use the quartz lamp to heat the wafer to ≈300-500° C under vacuum in PM2 for 15 minutes to dehydrate.
  - Multi-step deposition for low stress gradient: Use 22 sccm N_2 throughout and set coil power to 4.5 kW. Ar flow is set to 7 sccm for the first 550 s, then is reduced to 6.5 sccm for another 550 s, then is reduced 6 sccm for another 550 s, and is then set for 5 sccm for the final 550 s of the 2200 total seconds of the deposition. Set heater power to 100% during the first quarter, then remove heat. Target thickness: 1.7 µm.

- Wafer Bow Measurement - Flexus
  - Record post-dep wafer bow. Film stress should be less than ±100 MPa.
- Crystallinity Measurement - Xdif
  - Run a normal coupled scan on the wafer to determine the angle at which to perform a rocking curve measurement (≈18.1°). Use the angle of the peak in a rocking curve measurement. Verify that the full-width half max (FWHM) is less than 1.7°.
- IF NECESSARY: AlN Strip - MSink1
  - If film quality is poor, heat Microposit MF-319 developer to 60° C. Submerge wafer for 5 minutes until AlN is completely stripped. Quick-dump-rinse × 4 followed by spin/rinse/dry. Once wafer is cleaned, deposit a new AlN film.

15. Pre Furnace Cleaning
    - Clean Wafer - Msink1
      - SVC-14 dip, 10+ minutes, 80° C
      - Quick-dump-rinse × 4 followed by spin/rinse/dry
      - Piranha etches AlN. DO NOT USE PIRANHA.
16. Hard Mask Deposition
    - Recipe 12SULTOA - Tystar12
      - Target thickness: 1000 nm
      - Deposition rate: 14 nm/min
      - Deposition time: 1 hour 11 min 25 seconds
17. Lithography for the AlN Hard Mask
    - Spin - SVGCoat6
      - Program #s: 1,2,1 (60s HMDS Prime, 1.8k rpm, 60s soft-bake @ 130°C)
      - 900 nm thickness
    - Expose - ASML
      - Mask Layer 2: AlN (Clear Field). Exposure Energy: 18 mJ/cm^2
    - Develop - SVGDev6
      - 60s Post-Exposure Bake @ 130°C, 60s Develop Time
    - Hard Bake Resist - UVBake

  - Recipe U

18. Hard Mask Etch

    - Oxide Spacer Etch with Endpoint - Centura MXP
      - Target Etch Distance: 1200 nm
      - Etch Rate = 300 nm/minute.
      - Etch Time = 240 seconds
      - Etch: $Ar/CF_4/CHF_3$ flow: 120/10/50 sccm; 200 mTorr; 500 W Power
    - Strip Photoresist - Matrix
      - 2.5 mins, 400 W O_2 Plasma, 250^o C chuck temp

19. Aluminum Nitride Etch Etch

    - ALNVAR - Centura MET
      - Target Etch Distance: 2250 nm
      - Etch Rate = 250 nm/minute
      - Etch Time = 9 minutes; 120 s at a time
      - $Ar/Cl_2/BCl_3$ flow: 100/90/10 sccm; 10 mTorr; 500 W Power; 75 W RF Bias
    - Etch Inspection - FEI-SEM
      - 2.5 mins, 400 W O_2 Plasma, 250^o C chuck temp

20. Pre-furnace wafer cleaning

    - Pre-furnace wafer cleaning - Msink8
      - 10 minute piranha clean
      - Quick dump rinse, 4 cycles
      - Spin, rinse, dry
    - Pre-furnace wafer cleaning - Msink6
      - 10 minute piranha clean
      - Quick dump rinse, 4 cycles
      - Spin, rinse, dry

21. High Temperature Oxide Deposition (Top Sacrificial Gap)

    - Recipe 17SULTOA - Tystar 17
      - Target thickness: 120 nm
      - Temperature: 800^o C
      - Deposition Rate: 266 nm/hour

  - Time: 28 minutes 12 seconds

22. Lithography for the Anchor Etch

    - Spin - SVGCoat6
      - Program #s: 1,3,1 (60s HMDS Prime, 5k rpm, 60s soft-bake @ 135°C)
      - $\approx$ 3500 nm thickness
    - OPTIONAL Thin Down the Resist Thickness - Technics-C
      - 15 minutes Technics-C O_2 plasma at 60 W
      - $\approx$1000 nm of resist removal
      - Can be useful for improving the resolution of the lithography using thick resist.
    - Expose - ASML
      - Mask Layer 3: AlN (Dark Field). Exposure Energy: 40 mJ/cm^2
    - Develop - SVGDev6
      - 60s Post-Exposure Bake @ 110°C, 60s Develop Time
    - Hard Bake Resist - Oven
      - 30+ minutes at 90° C.

23. Anchor Hole Etch

    - Oxide Spacer Etch with Endpoint - Centura MXP
      - Target Etch Distance: 2000 nm
      - Etch Rate = 300 nm/minute.
      - Etch Time = 400 seconds (100 s at a time)
      - Etch: Ar/CF_4/CHF_3 flow: 120/10/50 sccm; 200 mTorr; 500 W Power
    - Strip Photoresist and Prefurnace Cleaning- Msink1
      - Acetone squirt to remove bulk of photoresist
      - Overnight soak in PRS-3000 bath at 80° C to remove photoresist.
      - Quick-dump-rinse $\times$4
      - SVC-14 10 minutes pre-furnace cleaning
      - Quick-dump-rinse $\times$4, spin-rinse dry

24. Polysilicon Top Electrode Deposition

    - Recipe 16SDPLYA - Tystar16

  - Target thickness: 600 nm
  - Deposition Rate: 1.92 nm/min
  - Time: 5 hours 12 minutes

25. Lithography for the Anchor Etch

    - Spin - SVGCoat6
      - Program #s: 1,3,1 (60s HMDS Prime, 5k rpm, 60s soft-bake @ 135°C)
      - ≈ 3500 nm thickness
    - OPTIONAL Thin Down the Resist Thickness - Technics-C
      - 15 minutes Technics-C O_2 plasma at 60 W
      - ≈1000 nm of resist removal
      - Can be useful for improving the resolution of the lithography using thick resist.
    - Expose - ASML
      - Mask Layer 4: POLY2 (Clear Field). Exposure Energy: 30 mJ/cm^2
    - Develop - SVGDev6
      - 60s Post-Exposure Bake @ 110°C, 60s Develop Time
    - Hard Bake Resist - Oven
      - 30+ minutes at 90° C.
    - Verify lithography before etching- FEI-SEM

26. Polysilicon Top Electrode Etch

    - Recipe Smooth Sidewall 1 - STS2
      - Target Etch Distance: 2800 nm (etches vertical stringers, too)
      - Etch Rate = 350 nm/cycle. 1 cycle includes 5s passivation and 7s etch.
      - Total Cycles: 8; ≈130 s
      - Passivation: C_4F_8 flow: 100 sccm; 600 W Coil Power
      - Etch: SF_6/O_2 flow: 130/13 sccm; 600 W Coil Power; 20 W Bias Power
    - Verify Etch Completion - FEI-SEM

27. Strip Photoresist and Prefurnace Cleaning- Msink1

    - Acetone squirt to remove bulk of photoresist

- Overnight soak in PRS-3000 bath at 80° C to remove photoresist.
- Quick-dump-rinse ×4
- SVC-14 10 minutes pre-furnace cleaning
- Quick-dump-rinse ×4, spin-rinse dry

28. Dopant Activation Anneal
    - Recipe 3N2ANNLA - Tystar3
        - Temperature: 1000° C; Time: 90 minutes
29. Singulate Wafer Into Dies - MSink16/18
    - Use a carbide-tipped scribe. Alternatively, use the wafer saw.
30. Release - MSink 16/18
    - Dip die in 49% concentration hydrofluoric acid for seven minutes. Use Teflon tweezers and a Teflon beaker.
    - Transfer die to a water beaker, do not allow to dry. Alternating between two beakers, repeat four times to dilute HF acid, replacing with new de-ionized water each time. Let die soak for several minutes.
    - Remove die from water. Use compressed N_2 gun to dry the die, hold in place with tweezers. Put the die on a hot plate with a 250° C setpoint and let dry for several minutes.
    - As an alternative to the previous step, critical point drying may be used. In which case, transfer from water to methanol without drying. Dry in a Tousimis critical point dryer to avoid stiction.
31. Post release anneal
    - Rapid thermal anneal - RTP3
        - 500° C for five minutes